School Bus Pass
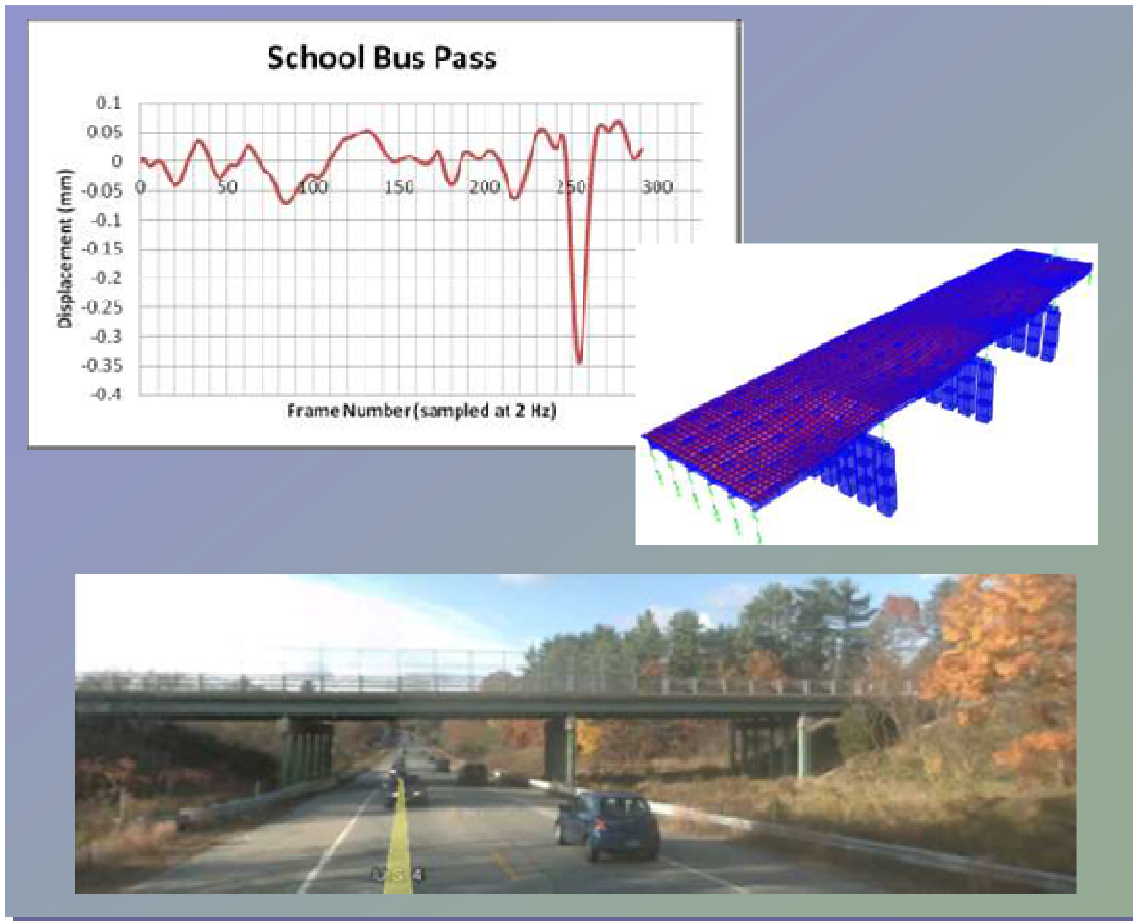

Instrumentation, Digital Image Correlation, and Modeling to Monitor Bridge Behavior and Condition

Final Report

1. Report No. FHWA-NH-RD-15680L	2. Gov. Accession No.	3. Recipient's Catalog No.	
4. Title and Subtitle Instrumentation, Digital Image Correlation, and Modeling to Monitor Bridge Behavior and Condition Assessment		5. Report Date June 24, 2015	
		6. Performing Organization Code	
7. Author(s) Erin Santini Bell, Ph.D., P.E. David Gaylord, M.S. Adam Goudreau, M.S. Daniel White, M.S.		8. Performing Organization Report No.	
9. Performing Organization Name and Address University of New Hampshire Department of Civil Engineering Kingsbury Hall, 33 Academic Way Durham, NH 03824		10. Work Unit No. (TRAIS)	
		11. Contract or Grant No. 15680L, A001(267)	
12. Sponsoring Agency Name and Address New Hampshire Department of Transportation Bureau of Materials and Research Box 483, 5 Hazen Drive Concord, New Hampshire 03302-0483		13. Type of Report and Period Covered FINAL REPORT	
		14. Sponsoring Agency Code	

15. Supplementary Notes

In cooperation with the U.S. DEPARTMENT OF TRANSPORTATION, FEDERAL HIGHWAY ADMINISTRATION

16. Abstract

Bridge managers have historically relied on visual inspection reports and field observation, including photographs, to assess bridge health. The inclusion of instrumentation, including strain gauges, along with a structural model can enhance bridge management. This combination of instrumentation and modeling is commonly classified as Structural Health Monitoring (SHM). Traditional SHM measurements are reference-independent, such as strain gauges. These sensors can be easily installed and provided valuable information for bridge condition assessment, including neutral axis location. The collection of global deflection of a bridge, a reference-dependent measurement, is more difficult to collect as the connection between the bridge structure and a fixed reference is geometrically challenging. A measurement technique that alleviates this issue is digital image correlation. Through recent advances in digital photography and the computational capability of personal computers, Digital Image Correlation (DIC) is a non-contact measurement technique that can be cost-effectively deployed to collect global deflection measurements of a bridge structure. DIC uses multiple digital cameras to photograph a target object to provide structural response information. This project incorporates a DIC system into the bridge instrumentation and testing program for a concrete deck-steel girder composite bridge, Bagdad Road over US Route 4, in Durham, New Hampshire. This report presents the instrumentation selection, sensors location planning and deployment, structural testing, DIC measurement for displacement, and strain measurements in both laboratory and field experiments. This report also includes a detailed structural model that is calibrated with collected field structural response data for bridge decision-making and management.

17. Key Words structural health monitoring, bridge testing, structural modeling, condition assessment, strain measurements, digital image correlation, girder distribution factor and bridge management		18. Distribution Statement No Restrictions. This document is available to the public through the National Technical Information Service (NTIS), Springfield, Virginia, 22161.	
19. Security Classif. (of this report) UNCLASSIFIED	20. Security Classif. (of this page) UNCLASSIFIED	21. No. of Pages 268	22. Price

Instrumentation, Digital Image Correlation, and Modeling to Monitor Bridge Behavior and Condition Assessment

Erin Santini Bell, Ph.D., P.E., Professor and Department Chair,
   Department of Civil Engineering, University of New Hampshire

David Gaylord, M.S. Graduate Research Assistant
   Department of Civil Engineering, University of New Hampshire

Adam Goudreau, M.S. Graduate Research Assistant
   Department of Civil Engineering, University of New Hampshire

Daniel White, M.S., Graduate Research Assistant
   Department of Civil Engineering, University of New Hampshire

DISCLAIMER

Instrumentation, Digital Image Correlation, and Modeling to Monitor Bridge Behavior and Condition Assessment

Submitted by:

Erin Santini Bell, Ph.D., P.E.

Researchers:

David Gaylord, M.S. Thesis Project

Adam Goudreau, M.S. Thesis Project

Daniel White, M.S., Researcher

June 2015

DEPARTMENT OF CIVIL AND ENVIRONMENTAL ENGINEERING

COLLEGE OF ENGINEERING & PHYSICAL SCIENCES

University of New Hampshire

TABLE OF CONTENTS

EXECUTIVE SUMMARY

According to the American Society of Civil Engineers more than one in nine bridges is considered to be structurally deficient (American Society of Civil Engineers 2013). This ranking is based on condition assessment and load ratings from visual inspections, which aim to assess the condition of a bridge but are inherently subjective. It is vital to determine the true structural health of bridges in order to ensure efficient allocation of limited resources for critical infrastructure elements. The purpose of this research is to develop protocol to use performance data recorded from strain sensors and digital imaging as a tool that bridge managers can for an objective assessment of bridge condition. There are three measurements: (1) traditional strain measurement for condition assessment, (2) digital imaging for displacement measurement and (3) digital imaging for strain measurement, related to two bridge performance metrics: (1) neutral axis location and (2) live load girder distribution factors.

The neutral axis of a composite bridge girder provides information relating to the health of both the girder and the concrete deck. Using bonded foil strain gauges, this location may be a useful Structural Health Monitoring metric. Structural health monitoring is an emerging tool that will create safer and more reliable bridge systems. By leveraging technology to investigate the way a structure behaves and degrades over time, the engineering community will gain valuable insight for developing more resilient bridges and can be alerted to damage when it occurs. This research used bonded foil strain gauges to determine neutral axis locations at the Bagdad Road over US Route 4 Bridge in Durham New Hampshire. This project documents the monitoring system design process and evaluates equipment for potential future structural health monitoring applications throughout New Hampshire.

Digital image correlation can be used to measure deflections of bridge girders. In June 2012, digital cameras were used during a pseudo-static load test of the Bagdad Road over US Route 4 Bridge in Durham, NH, to capture bridge deflection. The deflections from this load test were used to calibrate a structural model to determine the impact of boundary conditions on the continuous action of the bridge. This research also assesses the accuracy and limitations of digital image correlation and the value of using deflections to determine load distribution factors to more accurately load rate a bridge and calibrate a structural model that is more representative of the bridge's behavior. In addition, a profile of girder deflections creates a metric for assessing bridge health in the future.

The third goal of this project is to illustrate the opportunity and need for a niche form of structural response testing through the use of a set of synchronized cameras for strain measurement at multiple locations through digital image correlation. This work will demonstrate a cost effective, simply implemented non-contact sensor network using commercially available GoPro® camera for bridge strain measurement demonstrated through laboratory tests at the University of New Hampshire

Research Goals and Activities

Structural Health Monitoring (SHM) uses a blend of instrumentation and science that has the potential to save bridge owners and managers significant amounts of money and manpower through early damage detection. Information from these continuous monitoring systems can help remove uncertainties about the structural condition in bridges by detecting hidden damage or capacity. This research aims to facilitate and accelerate future SHM research projects in New Hampshire conducted by UNH by documenting the design and implementation of both a strain-based and displacement-based structural health monitoring system. Protocols are developed and, instrumentation is deployed at the Bagdad Road over US Route 4 Bridge in Durham NH (NH Bridge Number 114/128) for evaluation of sensors and data acquisition hardware for potential use in future bridge SHM projects.

The sensors and modular data acquisition system purchased for Gilford Bridge deployment was installed at the Bagdad Road over US Route 4 to accelerate future strain-based and displacement-based SHM projects in New Hampshire. The report documents observations made during the development and implementation of a system using bonded foil gauges and digital, installation and operation of bonded foil gauges and a digital image correlation system for monitoring of in-service bridge performance. The report also details the development of a 3D structural model, calibrated with collected structural response data, for the purpose of structural health monitoring.

Goals and Outcomes

- Provide a detailed manual for strain gauge selection, installation and operation.
- Demonstrate the value of structural health monitoring for structural condition assessment via load rating.
- Develop a procedure to calculate neutral axis location for a composite girder using collected strain readings.
- Develop a procedure to calculate live load distribution factors for an in-service bridge using collected bridge responses.
- Recommend foil strain gauge type, installation and data acquisition methods
- Demonstrate the robustness of digital image correlation for collection of bridge deflections and strains

Activities

- Detail the importance of structural health monitoring, specifically foil strain gauges and digital image correlation, for bridge management (Chapter 1)
- Design an instrumentation plan for the Gilford Bridges (Appendix A)
- Design an instrumentation plan for the Bagdad Road over US Route 4 Bridge, including sensor selection (appendix B), sensor installation procedures (Appendix C), data acquisition system (Appendix D) and full instrumentation plan (Chapter 2 and Appendix G)
- Deploy an instrumentation plan at the Bagdad Road over US Route 4 Bridge and use collection strain measurements to determine the in-service neutral axis location (Chapter 2 and Appendices E and H)

- 2012 Loading Testing of the Bagdad Road Bridge over US Route 4, including digital image correlation testing parameters (Appendix F), truck positioning and data collection (Chapters 3 and 5).
- Post-processing of collection information for neutral axis location and live load distribution factor calculation (Chapters 4 and 6 and Appendix H)
- Use of collected structural data for condition assessment and load rating (Chapter 6 and Appendix J)
- Develop and calibrated a 3D structural model of a in-service bridge for load rating and condition assessment (Chapter 6)
- 2015 Laboratory Data Collection via GoPro® cameras (Chapter 7 and Appendix K)
- Recommendations (8)

Development of the Project

This research project began as part of an effort to instrument a bridge in Gilford, New Hampshire to aid in accelerated construction processes. As part of research in the field of rapid deck replacement, UNH has partnered with the New Hampshire Department of Transportation (NHDOT) under the funding of the Federal Highway Administration's Highway's for Life program to investigate the use of precast panels to replace the deck only in 60 hours or less. The goal of this project is to save time. Reduced times will minimize disruptions to traffic flow, and potentially reduce construction site accidents by shortening the number of hours crews will work on projects. The planned instrumentation was intended to monitor the impact of the rapid redecking on the existing steel girders and, investigate potential roles for sensors placed on an existing bridge during maintenance.

Due to a delay in the bidding process and the placement of safety netting underneath the bridge that prevents deck debris from falling on cars in the underpass that also obstructs sensor installation, the project was ultimately delayed. Through discussions with the NHDOT, permission was granted to use sensors and data acquisition equipment purchased by this project on another bridge for SHM. After a review of bridges in the area around Durham, the Bagdad Road over US Route 4 Bridge. The sensor types, foil strain gauges and digital imaging, were both used at the Bagdad Road over US Route 4 Bridge. The structural responses collected were used to validate recommendations for sensor type, installation procedures and data acquisition protocol. The structural responses were post-processed to determine performance metrics, neutral axis location and live load distribution factors, related to load rating and condition assessment.

One of the original goal of this research to evaluate sensors that will be used in the Gilford Bridge Accelerated Bridge Construction (ABC) project was completed and is documented in Appendix A.

1. Introduction

1.1 Bridges: Essential to Societal Prosperity

Bridges have been important to society since the Roman Empire. The Romans were masters at using the arch to create bridges for their road network. The city of Rome greatly profited from the salt trade which was made possible by bridges across the Tiber River (Taylor 2002). Figure 1 shows Pons Aemilius, believed to be the first Roman Bridge across the Tiber in Rome. In addition to serving the capitol's salt trade, the bridges served to transport labor, worshippers, food supplies, trade goods, and communications into and out of the city (Taylor 2002). Bridges throughout the empire allowed for efficient movement of troops, as well as merchants and their goods.

Figure 1: Surviving center span of Pons Aemilius Rome, Italy (credit: Flickr.com).

Though many aspects of the social order fell with the collapse of the Roman Empire, bridges continued to support society in England throughout the Middle Ages and were important to the rise of the industrial revolution. The English realized the importance of bridges to the movement of people and invested in their construction and maintenance. They saw the need to establish safe dry crossings at rivers in order to prevent time intensive detours to a nearby ford (Harrison 2007). A large portion of funding came from charitable donations, but many church lands were given exemption from farming for the king if the people of the lands took liability for the upkeep of bridges (Harrison 2007). These bridges were not just built to suit the ego of a king; they were built to meet a demand (Harrison 2007). Bridge construction and maintenance was expensive, but necessary because of the importance to travelers, and goods (Harrison 2007). For instance, major bridge repairs in 1700 AD cost about £1200 (Harrison 2007). To put that in perspective, according to Gregory King, the average spending per capita per year in England in 1695 was £3.85 (Hearfield 2015). The large network of bridges that existed in England in 1760 was a product of investment in bridges between 750 and 1250 (Harrison 2007). The infrastructure was in place to allow the industrial revolution to take place and advance society.

In the 21st century, bridge maintenance is just as important to society as it had been to the Romans and English. Visual inspection and structural health monitoring (SHM) are aids that provide a way of ensuring that bridges that need repair receive it. Suspension bridges in the 19th

and early 20th century suffered because of light spans and flexible decks which were susceptible to torsional effects from wind loading (WSDOT 2005). The Tacoma Narrows bridge collapse was a disaster because engineers did not design for the vertical forces induced by wind and knew little about the dynamics caused by those forces (Figure 2).
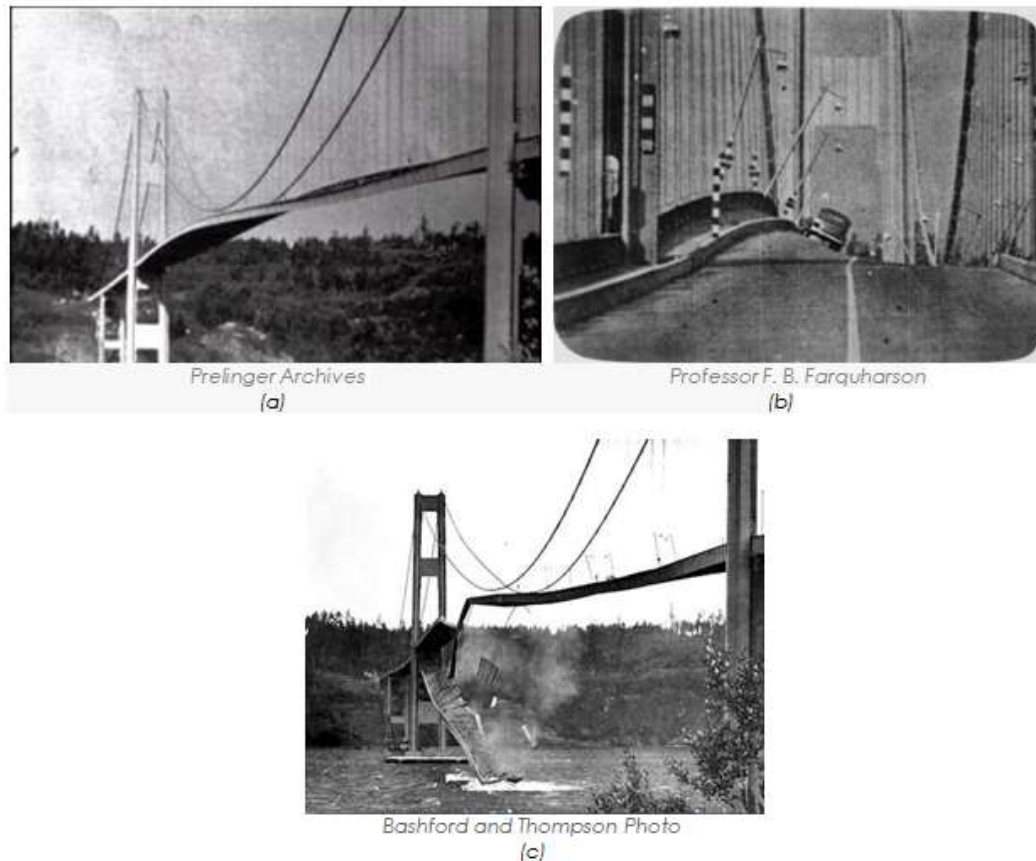
Figure 2: Tacoma Narrows, (a) and (b) show torsional displacements and (c) shows subsequent collapse. (WSDOT 2005)

Most signature bridges have some form of dynamics monitoring. For Instance, the Golden Gate Bridge in San Francisco, CA is equipped with a wireless sensor network to monitor ambient vibrations (Suhun, et al. 2012). However; the standard highway bridge, representing the majority of the bridge infrastructure, needs its own form of monitoring. While typically not vulnerable to dynamic response, they still have a need for monitoring as they provide the backbone of transportation infrastructure.

1.2 Cost of Current Management

In the Unites States bridges are critical infrastructure for delivering goods on time to the markets where they are being consumed. Time and fuel is wasted when trucks and buses have to drive more miles to avoid structurally deficient bridges. This translates to individuals paying more for goods and services, and having less disposable income. In addition there is a shortfall of investment in bridges (American Society of Civil Engineers 2013). Therefore a structurally deficient bridge requires assets that could otherwise be allocated to other infrastructure maintenance needs. The US is spending $12.8 billion annually on bridge construction and

maintenance, but need to invest $20.5 billion annually to eliminate the nations backlog of deficient bridges by 2028 (American Society of Civil Engineers 2013). It is critical that money is spent effectively on critical deficient bridges.

Routine Inspections, or visual inspections, are performed ever two years in accordance with the National Bridge Inspection Standards (NBIS) set by the Federal Highway Administration (FHWA). The standards apply to any public bridge spanning more than 20 ft. The quality of the inspection is based on inspector experience and familiarity with the bridge, as well as field conditions, and a accessibility to components (Graybeal, et al. 2002). As valuable as inspections and non-destructive evaluations are, they are discrete. What happens between inspections or evaluations will not be recorded or responded to until the next individual observation. This may not account for damage that occurs between inspections and these inspections are typically visual, and therefore, structural health related features not visible, like rebar condition can be overlooked. Although these out-of-sight deficiencies may not cause a bridge to fail, they could result in unintentional redistributions of stress that further accelerate bridge deterioration resulting in more frequent and costly maintenance needs. SHM offers a means to provide missing information to bridge engineers, potentially decreasing maintenance costs and further improving safety. Innovative tools can aid in assessing bridge health and allocating funds for bridge maintenance. Bridge deflections have been successfully measured with lasers (Attanayake, et al. 2011). However, the systems are expensive and the high capital cost is difficult to warrant.

1.3 Structural Health Monitoring

Scrutinizing the way a structure responds to loading provides a way to investigate deficiencies that may not be externally visible. Furthermore, continuous monitoring offers a means to catch the deficiencies at first appearance, rather than at the next inspection cycle, allowing for repair before the damage has an opportunity to cause further deterioration to the system. Structural Health Monitoring (SHM) is the process of observing the way a structure behaves with an interest in damage sensitive parameters. By complimenting the current inspection process, it offers a means to provide bridge managers more information about current capacities and the rates at which structures degrade so they may make more accurate predictions of future maintenance needs.

(Farrar, Doebling and Nix, Vibration-based Structural Damage Identification 2001) described a process of vibration based SHM in a report printed in 2001. In the report, they describe a damage detection technique as a statistical pattern recognition process. The four part process is listed below. The process was later used to discuss SHM in general in a report by the Los Alamos National Laboratory. The report, titled "A Review of Structural Health Monitoring Literature: 1996-2001" covered hundreds of SHM articles out of numerous technical literature. In it, the authors chose to categorize SHM research based on the four steps. They broadened the fourth step described by considering damage techniques that did not necessarily rely on a structural model, thus re-labeling the step from *Statistical Model Development* to *Feature Discrimination*.

Four Part SHM Process

1. *Evaluation*
2. *Data acquisition and cleansing*
3. *Feature extraction*
4. *Feature discrimination*

Evaluation is the step that involves researching the structure. It identifies the environmental and operational constraints and establishes the customization of the particular SHM method. Data acquisition and cleansing is the physical data collection. It involves selecting sensors, determining measurement intervals, and normalizing and storing data. Feature extraction is the process of using measurements to determine characteristics of the structure. Feature extraction is used to condense data as significant numbers of measurements are reduced to manageable data sets, multiple accelerometer values may be converted to mode shapes for example. Lastly, feature discrimination is the process of analyzing statistical patterns to identify damage. This process typically requires a model in civil structures as data sets from a damaged structure typically aren't available (Farrar, Doebling and Nix., Vibration-Based Structural Damage Identification 2001). This research includes work in all four of these areas: evaluating the Bagdad Road Bridge for SHM metrics that could be researched, acquiring and post-processing field data, extracting neutral axis location, and using the location to infer the health of a composite section.

A later work identified several challenges in structural health monitoring, as it moves from primarily research efforts to common practices. These challenges include but are not limited to (1) detecting local damage based on global behavior, (2) identification of damaged sensors, and (3) convincing owners that the cost of SHM systems has a benefit (Farrar and Worden, An Introduction to Structural Health Monitoring 2007). These challenges are currently being addressed in several SHM projects, and as their findings are published, SHM is likely to become more broadly utilized. Several SHM research examples pertaining to civil infrastructure are summarized by (Brownjohn 2006).

Multiple short-term studies in the State of Connecticut were summarized in a report and demonstrated significant near-term cost savings. The projects, conducted by the University of Connecticut, showed that short term SHM projects have saved the State over 2.5 million dollars in repair costs (DeWolf, Culmo and Lauzon 1998). Studies generally involved investigating potential crack propagation. One study, for example, noted that stresses in cracked diaphragms were only high enough at center span to cause the cracks to propagate. By demonstrating that cracks did not need to be repaired in the diaphragms at the quarter points, the State was able to save on the renovation costs. The University of Connecticut and the Connecticut Department of Transportation have worked together on several projects to accelerate the field of SHM research. (Cardini and DeWolf, Long Term Structural Health Monitoring of a Multi-Girder Steel Composite Bridge Using Strain Data 2009) stated that in over 20 years of research, roughly 30 bridges have been monitored in Connecticut.

1.4 Future of SHM

As sensor networks become more economical and reliable and SHM metrics develop, long-term continuous monitoring will be able to give engineers more information not only about the condition of bridges but how they behave, as well. Eventually, SHM systems may even help engineers build better structures. A future SHM system may sense a crack propagating at the same time it records a vibrations signature and measures the vehicle driving across and the distance between axles. Using that type of information, researchers will be able to definitively identify the source of damage and compare the structure to other structures that have experienced equal loading without an occurrence of damage. Those types of observations can result in more rugged structures that perform in a more favorable manner under that loading.

Sensor networks combined with advances in modeling and iterative techniques may even be able to locate and quantify damage providing the same sort of information that discrete non-

destructive evaluations give bridge engineers on a continuous and automated fashion. Iterative procedures are being researched at UNH that could be used to create baseline models using measurements of the structures behavior (García-Palencia and Santini-Bell 2012). By updating the baseline model over time so that they react to loading like the real structures, virtual damage in the model may be indicative of real damage. Advanced systems may be able to run these updating routines so regularly that damage is detected immediately after it occurs.

Future sensor networks will be multipurpose and able to reliably provide other information in addition to structural behavior. The SHM network installed in the new Saint Anthony's Fall Bridge, which replaced the I-35 Bridge, contains temperature sensors that are used to trigger the anti-icing system (French, et al. 2011). Bridge weigh-in-motion is being researched as a means to use strain sensors to weigh trucks, expanding the capacity of States to determine non-permitted overload vehicles (Cardini and DeWolf, Implementation of a Long-term Weigh-in-Motion System for a Steel Girder Bridge in the Interstate Highway System 2009). It becomes relatively easy to think about the potential benefits of continuous SHM when considering how an improved continuous health monitoring system would benefit a person. The nervous system in a body is much like current SHM systems, pain can often tell a person that something is wrong, but the person needs to see a doctor to examine why, similar to an early inspection that might be triggered by today's SHM networks. However, future networks may be able to report what's wrong. People would likely eat better, exercise more, and go to bed earlier if they continuously saw metrics about how the decisions they make affect their health. If large amounts of data were available from these systems for doctors, they would make better recommendations to their patients regarding lifestyle choices. And lastly, the monitoring could catch ailments so they may be treated earlier before they grow into larger more damaging afflictions. In a similar way, an SHM system could detect a fatigue crack or delamination in the early stages, when the repair costs are minor.

1.5 Traditional Structural Health Monitoring as Part of This Research

The work conducted as part of this research could be categorized by steps in the SHM process described by (Farrar, Doebling and Nix, Vibration-based Structural Damage Identification 2001). The evaluation and data acquisition steps are described in this section, and the feature extraction and discrimination are described in chapter 6. The bridge was evaluated and the steel girders presented an opportunity to instrument with bonded foil strain gauges to detect neutral axis in a composite section and to deploy digital image correlation to determine live load distribution factors. Data acquisition was conducted by installing strain sensors and reading them for roughly 40 minutes during heavy traffic flow. Neutral axis locations and live load distribution factors were extracted as features, and the discrimination involved comparing the experimentally determined locations to a location determined through structural mechanics.

The full bridge bonded foil strain gauges selected for this research function by combining strains measured in multiple directions. The process, which is further described in Chapter 3, may be sensitive to unintended local effects and, if great enough, the effects could render the gauges unusable for this type of monitoring. Comparisons were made by instrumenting both sides of the beam. The northern face of the beam was instrumented with the full bridge gauges, and the southern face was instrumented with quarter bridge gauges. An image of the full bridge gauges, Omega© model number SGT-4/1000-FB11, is shown in Figure 3a. The quarter bridge gauges, Omega© model number KFG-3-350-C1-11L1M2R, shown in Figure 3b. The thermocouple chosen to measure temperature, Omega© model number 5TC-GG-T-20-36, is shown in Figure 3c. Much more information about comparisons using combinations of sensors is provided in Appendix B.

The details of the installation procedure, data acquisition programming and full instrumentation plan are details in in Appendices C, D and E, respectively.

(a)   (b)   (c)
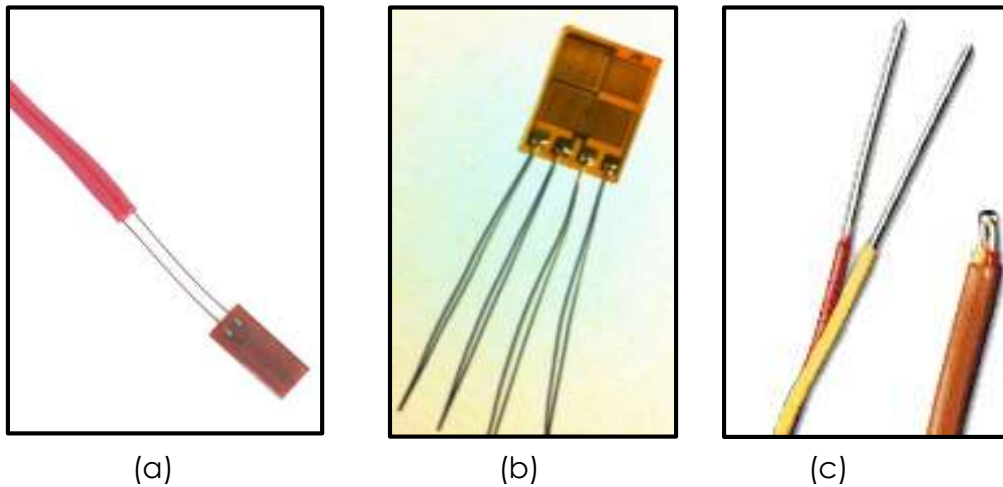
Figure 3: Structural Health Montioring Sensors (a) Quarter Bridge Strain Gauge, (b) Full Bridge Strain Gauge and (c) Thermocouple

1.5.1 Neutral Axis Location from Strain Measurements

The theoretical neutral axis of a beam represents a horizontal plane above which longitudinal stresses act tension or compression and below which stresses act in the opposite. In a doubly symmetric rolled shape with a consistent modulus of elasticity that is in pure bending, the plane is theoretically in the center of the section. Evenly dividing the geometry will balance tension and compressive forces in the beam. In a composite section, the added capacity of the deck moves the neutral axis upward, as shown in Figure E-1. The neutral axis is therefore of particular interest because it is a feature that can indicate changes in the capacity of the deck or the steel as well as changes in the level of composite action. If shear studs became corroded, for example, and the steel beams and concrete deck of a bridge were no longer in full composite action, the calculated neutral axis from strain gauge readings should shift indicating damage.

Figure E-1 shows a composite beam made of a concrete slab and steel rolled shape. When the beam is fully composite it is expected to have a neutral axis higher than half the depth of the beam and closer to the deck. When the beam is fully composite it has a single neutral axis, however, a non-composite beam will have two, a neutral axis for the deck and a neutral axis for the beam. The neutral axis of a rolled shape will be at half the depth of the beam, or lower in cases with an attached bottom cover plate like at the Bagdad Road Bridge. By instrumenting the steel, the location of the neutral axis can be watched over time to see if it moves suddenly from external events, such as impact, or slowly over time indicating degradation of the composite section or behavior.

Generally, the location of the neutral axis is assumed to be relatively static, meaning that it is in the same location regardless of load applied to the beam. The assumption holds true when the beam behaves linearly in the elastic range. However, mechanics show that materials do not behave entirely elastic. Concrete in particular has a non-linear and inelastic stress-strain relationship though it is usually assumed to be linear-elastic at smaller stresses. This indicates

8

that as load increases, the neutral axis may move slightly. Other phenomena such as creep, or section loss, can also cause the location of the neutral axis to change over time. If this movement is tracked with instrumentation, it could be used to access the hidden deck or shear connector health.

Figure 4: Illustration of Neutral Locations in Composite and Non-Composite Sections

Neutral axis research using two strain gauges in a cross section has been conducted by UNH and other universities. Lefebvre designed a system using quarter bridge bonded foil strain gauges at the Powder Mill Bridge in Barre, MA (Lefebvre 2010). This research expands on previous neutral axis based research by using multiple gauges in a cross section to investigate sensor behavior. A potential problem in measuring neutral axis locations is the presence of noise in the strain readings. Ideally only two strain values should be required because that is all that is needed to plot a straight line. Under elastic deformations, longitudinal strains will theoretically vary linearly throughout the depth of the section. Hence the assumptions that plane sections remain plane will hold true. The process of measuring neutral axis can be thought of in two ways that both rely on the assumption of linear strain distribution. The first is using similar triangles, and the second is plotting stain versus depth within the section and solving for the y-intercept of the line it creates. Both methods are mechanical identical using the anatomy of a composite section, as shown in Figure 5, and are used in this research and detailed in Appendix E.
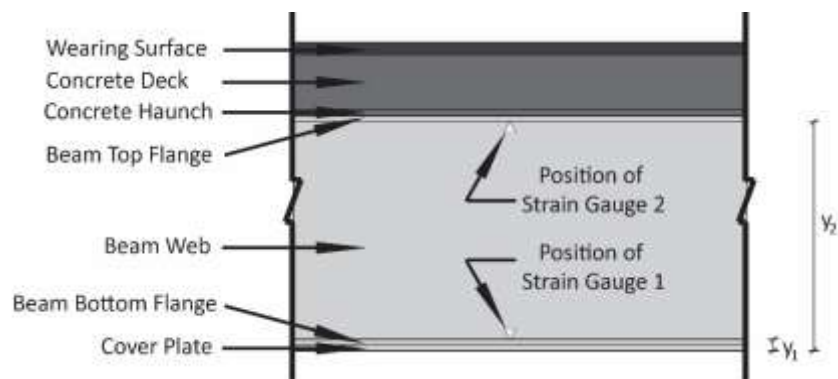
Figure 5: Illustration of Composite Section Instrumented For Neutral Axis Detection Neutral

1.6 Digital Image Correlation Structural Health Monitoring for this Research

This research seeks to take advantage of the emerging use of digital image correlation (DIC) for civil engineering applications. DIC is an optical method for tracking changes from one image to another. For civil engineering, images are recorded during some event, such a truck passing over a bridge, and displacements are obtained. Image processing software analyzes pixel movement from subsequent images and can calculate strain and displacement. In the software, the user defines the length of a known line in the field of view for a given set of images. This calibrates the set of images and allows the software to assign a length to each pixel. The software is able to calculate displacements by assigning a physical length to each pixel in an image and tracking the movement of subsets of pixels. The image processing software also assigns gray values to subsets of pixels. These gray values vary from 0 to 255; 0 is pure black and 255 is pure white. This requires a random speckle pattern so that groups of subsets have a unique pattern of numbers (Figure 6).
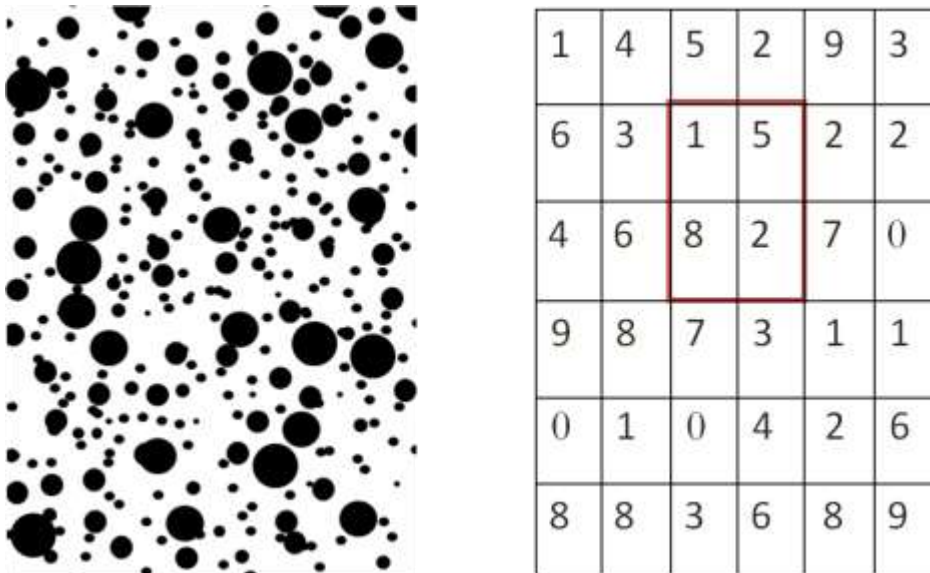
Figure 6: Speckle pattern transformed into a grid of subsets with varying gray values. The red box may be tracked from one image to another.

 DIC has the advantage of making structural health monitoring non-contact. That is, it does not require removal of paint for placement of sensors nor does it require running wire along the bridge to supply power to the sensors. Though not necessary, the image correlation technique works better with some form of target attached to the bridge at locations of interest. This provides a better contrast between the areas of interest and surrounding parts of the bridge, allowing the image processing software to better locate areas of interest and track their movement.

In material laboratory tests and manufacturing applications, the distance from camera to the target, the angle between the camera and the target, and the lighting conditions can be controlled. However, these parameters are difficult to control in the field, particularly when looking to capture multiple targets with a single camera, as detailed in Appendix F. Part of this research investigates the effect these parameters in structural response.

The resolution determines the physical size of a pixel in the image, so the higher the resolution the better the results. Investigating various algorithms and their associated resolutions is beyond the scope of this thesis, but is discussed to show the validity of the results obtained at the given

resolutions. There are advanced algorithms that deliver high resolution through sub-pixel resolution (Waterfall, MacDonald and McCormick 2012). Sub-pixel resolution is the smoothing of the digitally recorded image, effectively reducing pixelation. (Waterfall, MacDonald and McCormick 2012) used cameras with a field of view 2m x 2m. The algorithm used to process the data gave a resolution approximately equal to 1/100000th of the dimension of the field of view (depends on algorithm being used); this corresponded to a 0.02mm resolution for the 2m x 2m field of view.

With coarser resolutions, the peak displacements may be drowned out in the signal-to-noise ratio (Busca, et al. 2012). (Busca, et al. 2012) used three conditions for resolution: maximum zoom with one target in view and a resolution of 0.3mm/pixel, medium zoom with two targets in view and a resolution of 5mm/pixel, and minimum zoom with three targets in view and a resolution of 10mm/pixel. The measurements collected for this thesis were captured at resolutions between 0.22 – 3.21 mm/pixel with the majority falling between 0.30 – 0.80 mm/pixel. In the case of (Busca, et al. 2012) the minimum and maximum zoom provided similar results with respect to the shape and max values of displacement, as shown Figure 7. However, it is difficult to quantitatively compare the two since the results are not plotted on the same graph.

1.6.1 Girder Distribution Factors from DIC

The live load distribution factors play a significant role in the load rating of a bridge. Meaningful load ratings are based on accurate live load distribution factors. There has been a significant amount of research regarding live load distribution factors obtained from finite element modeling studies. This research has led to recommendations for changes to the AASHTO equations for calculating distribution factors.

The AASHTO Standard Specification used the simple "S-over" equations for calculating the girder distribution factors based on girder spacing. For example, the live load distribution factor for moment on a steel stringer with a concrete deck 6" or thicker and two or more traffic lanes is calculated as S/4.5. The equations from the Standard Specification were highly generalized and the current specification (AASHTO LRFD) bases the girder distribution factor on span length (L), beam stiffness (K_g), and deck thickness (t_s) in addition to girder spacing (S). For the same stringer discussed above, the new LRFD equation is shown in equation (1). Still there are other factors that contribute to the distribution of load in a bridge deck and beam system.

$$0.075 + \left(\frac{S}{9.5}\right)^{0.6} \left(\frac{S}{L}\right)^{0.2} \left(\frac{K_g}{12.0Lt_s{}^3}\right)^{0.1} (Eq:1)$$

In this research, an investigation into live load distribution factors reveals that the AASHTO LRFD Bridge Design Specification produces distribution factors that are generally conservative with respect to the measured distribution of live load in a steel girder bridge. This can lead to inaccurate load ratings of existing bridges and inefficient use of time and resources, mainly tax dollars, in bridge maintenance. Cameras can be used to find a load distribution of girders that is representative of the bridges actual behavior. This load distribution can be used to generate more accurate load ratings. More accurate load ratings will ensure that bridges that need rehabilitation will be recognized and placed on the proper list.

The main goal of this research is to develop digital image correlation into an inspection and investigative tool for use by bridge owners. This includes conducting laboratory experiments to increase the confidence in the field application of DIC for bridge response measurement and developing a protocol for the use of the cameras to find the relative girder displacements of a structure and monitor any changes. It also involves generating load ratings from measured deflections.

This research demonstrated a method to validate a structural 3D model of an in-service bridge using digital image correlation and then determine the distribution factors of the bridge using the model. It will demonstrate the difference between moment distribution factors from the AASHTO LRFD Specifications and computer models. This includes assessing the various conclusions about the conservative nature of the distribution factors from the LRFD code relating to steel girder bridges.
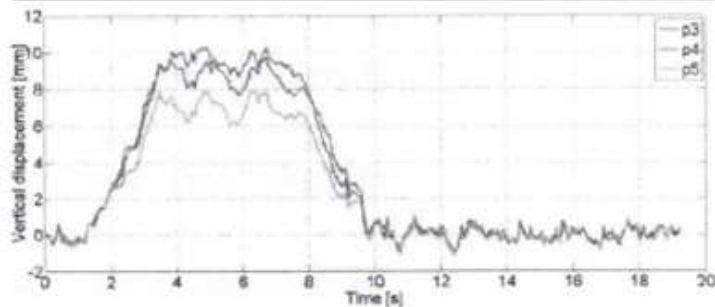
a) targets p3 (mid-span), p4 and p5; b) the corresponding displacement time histories (positive values for downward motion).
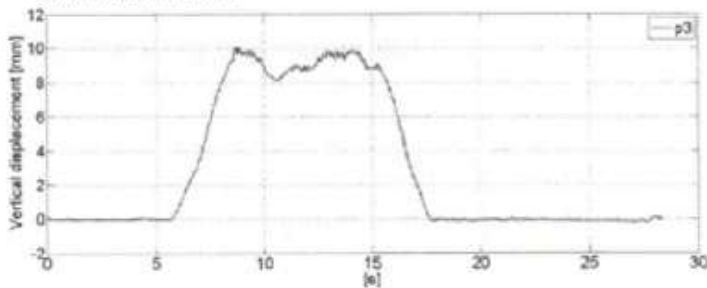
a pass-by test with maximum zoom level and only one target in the field of view (point p3, mid span).

Figure 7: (Busca, et al. 2012) test setup and data. The top graph shows the response from a multiple target field of view with a resolution of 10mm/pixel. The bottom graph shows the response from a single target field of view with a resolution of 0.3 mm/pixel.

2. Structural Health Measurements with Bonded Foil Strain Gauges and Digital Image Correlation

There are two means of structural response measurement used in this research, (1) Bonded foil strain gauges and (2) digital image correlation (DIC), as shown in Figure 8. Strain measurements allow for the calculation of neutral axis location, distribution factors, and curvature. Strain can be measured using a variety of sensor that all have limitations and challenges for use on civil structures, particularly the effects of varying temperature. DIC is a non contact measurement tool that can collect strain, deflection and acceleration. Research in the field of SHM can develop while sensor technology improves by using cost effective instruments and managing errors in post processing.

Bonded foil strain gauges were used in this research because they are cost effective, relatively easy to install. DIC was used in this research because of its cost, flexibility and ease of installation. There is an existing experience base with that type of sensor in the UNH SHM research group (Santini-Bell, et al. 2012).

2.1 Introduction to Strain Measurement

A fundamental of structural engineering is the method of arranging structural members such that applied forces result in elastic stresses in the material allowing the structure to deform rather than permanently displace. These stresses can be compressive or tensile and material can undergo a limited amount of stress before it fails. Stress cannot be measured directly. However a change in stress can generally be calculated from a known applied load as shown in equation 2. The equation shows the calculation of normal stress, meaning the load is applied axially to the cross section of interest. In equation 2, σ is the stress while P is the known load and A is the known cross sectional area the load is applied to.

$$\sigma = {}^{P}/_{A} \qquad \text{(Eq: 2)}$$

When the load is unknown, or the distribution is more complicated, stress is typically measured using strain values. Strain (ε) is the measurement of the deformation that stress has caused. There are two types of strain generally referred to true strain and engineering strain. Engineering strain represents the change in length over the original length as shown in equation 3, where ΔL is the change in length and L is the original length. The value is a ratio and is unitless; however, it is typically referred to in units of length over length. When stresses are relatively low, some materials, such as steel, behave in an elastic fashion and there is a direct correlation between stress and strain. The amount the material strains from elastic loading is given by Young's modulus, an experimentally determined value (Eq. 4). Values of the modulus for frequently used materials are widely published and, for steel, a value of 29,000 ksi is generally utilized.

$$\varepsilon = {}^{\Delta L}/_{L} \qquad \text{(Eq: 3)}$$

$$\sigma = \varepsilon E \qquad \text{(Eq: 4)}$$

By using the relationships between stress and strain, more information can be derived about how a structure behaves and handles load. By mounting vibrating wire strain gauges into concrete girders, (Barr and Eberhard 2001) were able to calculate live load moments and distribution factors. (Johnson and Robertson 2007) demonstrated a method of using strain values at several locations to determine deflected shapes and displacements for a variety of loading and support scenarios. They compared results from numerical models to those of calculations using curvature

and displacement relationships. Although they demonstrated a high correlation, they concluded that signal to noise ratios of sensors poses a major challenge in real world implementation.

Strain can be measured using several devices. Vibrating wire strain gauges use a tensioned wire mounted between two points. When the wire changes length the frequency at which it vibrates changes and an electromagnet reads the change (Geo Instruments 2009). Various fiber optic strain gauges use light refraction in a mounted tube to measure strain. When the two mounts that holds the gauge separate, a fiber optic wire in the tube is pulled away from a reflective end (Sipple 2007). Light that is reflected out of the fiber optics reflect off the reflective end and return back down the optic cable creating varying patterns in the light that are read by an instrumentation system. Digital Image Correlation (DIC) is a process of comparing multiple images of a specimen under strain. Software tracks groups of pixels through the sequence of images and determines strain by the changes between the groups (Peddle 2011). The bonded foil strain gauge is the instrument focused on in this research. The gauges utilize a filament that changes electrical resistance when elongated. The change is then read by electrical equipment to determine strain (Omega Engineering Inc. n.d.).

(a) Example of a Vibrating Wire Strain Gauge (Geo Instruments 2009)
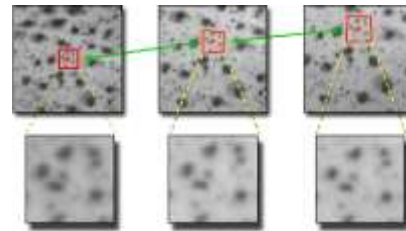
(b) Graphic Demonstrating DIC software process (Peddle 2011)
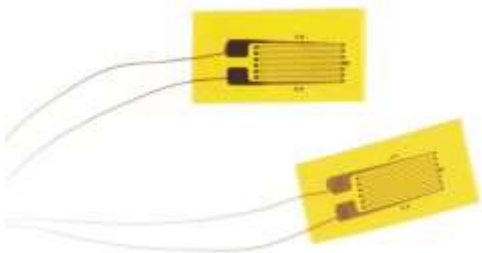
(c) Example of Bonded Foil Strain Gauges (Omega Engineering Inc. n.d.)

(d) Example of a Fiber Optic Strain Sensor (Sipple 2007)

Figure 8: Examples for strain and deflection measurements tool for structural health monitoring.

In order to understand and plan for the types of errors in strain-based monitoring systems utilizing bonded foil strain gauges, researchers need some basic understanding of how they function. This is a big challenge facing civil/structural engineers that serve the role of researchers in the field of SHM. This chapter describes the basics of how strain in the gauge is read as voltage change. It will begin with the basics of voltage measurements, then a description of how the

Wheatstone bridge, the most common circuit in strain measurement, is utilized for different strain measuring needs. Appendix B includes a detailed description of the gauges used in this research and how they function.

2.2 Quarter and Full Bridge Foil Strain Gauges

The types of gauges used in this research are two lead quarter bridge gauges and four lead full bridge gauges, both made with constantan alloy. Constantan is a copper-nickel alloy and is one of the most common alloys used in gauges. It has a significant fatigue life if strains are kept below 1500 Degree F which is much higher than strains expected in SHM for an in-service bridge. Constantan also has a relatively low sensitivity to temperature effects as compared to other alloys, if temperatures are in the range of -50˚ to 150 ℉. Other alloys are available for higher strain or higher temp measurements. (Murray and Miller 1992) Information on other types of gauges can be found in texts such as Murray and Millers book or in technical literature.

Full bridge gauges compensate for temperature effects on conductivity by mounting all four resistors of the Wheatstone bridge on the specimen. Two of the resistors of the Wheatstone bridge have an additive effect on the output voltage of the gauge and two of the resistors have a subtractive effect. Therefore, when a full bridge gauge is used, because all resistors will be at the same temperature, effects of temperature will be added twice and subtracted twice, thus maintaining a balanced condition. This, of course, would also imply that any uniform strain on the resistors would be added twice and subtracted twice negating strain measurements; however the grids that form the gauge are mounted in different directions. Full bridge configurations can involve mounting resistors in different places to remove certain types of strain. The full bridge gauges used in this research were purchased from Omega and locate all resistors on the same carrier as shown in Figure 9.
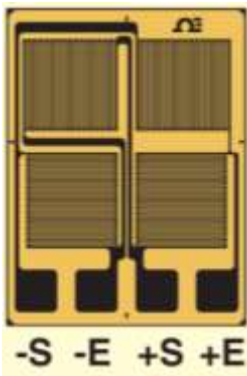
Figure 9a: Full Bridge Axial Strain Gauge on a Single Carrier
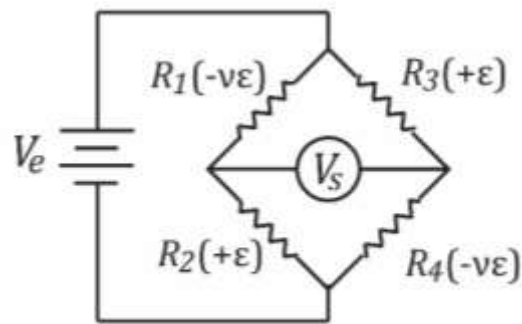
Figure 9b: Diagram of Resistor Strain Measurement Directions on Full Bridge Gauges

The two resistors mounted in the principle stress direction replace resistors 2 and 3 that have the additive effect. The two other resistors replace resistors 1 and 4 which have a subtractive effect. However, since the two resistors are mounted in the perpendicular direction they experience a compressive strain due to Poisson's effect as shown in Figure 10. Therefore, when the specimen experiences axial strain, their resistance change turns out to be additive as well. The combined

effect in turn amplifies the signal. This amplification is illustrated in Figure 10a and further explained by the equations following 10b.
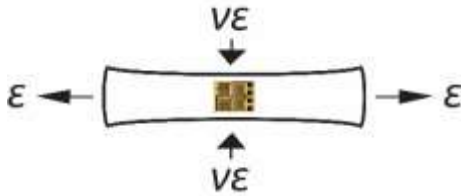
Figure 10a: Illustration of an Instrumented Specimen Under Axial Strain
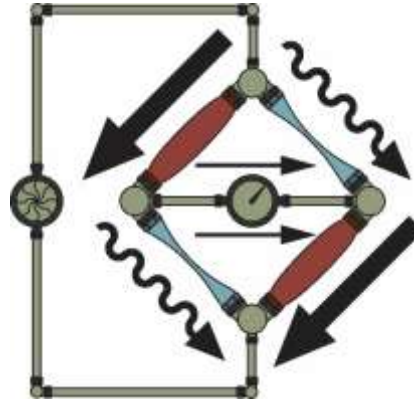
Figure 10b: Hydraulic Wheatstone Bridge of Strained Full Bridge Axial Strain Gauge

The total measured strain is due to the strain measured in each of the gauges:

$$\mathcal{E}_t = +\mathcal{E}_2 + \mathcal{E}_3 - \mathcal{E}_4 - \mathcal{E}_1 \qquad\qquad \text{(Eq: 5)}$$

Resistors 2 and 3 are the resistors mounted in the principle stress direction:

$$\mathcal{E}_2 = \mathcal{E}_3 = \mathcal{E} \qquad\qquad \text{(Eq: 6)}$$

Resistors 1 and 4 are the resistors mounted in the direction experiencing strain due to Poisson's effect:

$$\mathcal{E}_1 = \mathcal{E}_4 = (-v\mathcal{E}) \qquad\qquad \text{(Eq: 7)}$$

The total strain measured by the gage is:

$$\mathcal{E}_t = +\mathcal{E} + \mathcal{E} - (-v\mathcal{E}) - (-v\mathcal{E}) \qquad\qquad \text{(Eq: 8)}$$

These gauges will be monitoring steel, which has a Poisson's ratio of 0.3, simplifying the equation to:

$$\mathcal{E}_t = +\mathcal{E} + \mathcal{E} - (-0.3\mathcal{E}) - (-0.3\mathcal{E}) \qquad\qquad \text{(Eq: 9)}$$

$$\mathcal{E}_t = 2.6\mathcal{E} \qquad\qquad \text{(Eq: 10)}$$

The configuration has benefits of higher sensitivity and resistance to thermal and off axis errors. A potential drawback of the full-bridge gauge is that while it cancels errors due to thermal effects on the conductivity of the gage, it also removes the ability to measure thermal effects of actual expansion and contraction of the material being gauged. The gauges might also be unsuitable for mounting on the web of the beams because of web compression, which would cause strain in the resistors mounted in the direction of Poisson's effect but not the other direction. Temperature effects are discussed in Appendix B. Foil strain gauges require a specific installation procedure and data acquisition system, both are detailed in Appendices C and D, respectively.

2.3 Introduction to Digital Image Correlation

Image correlation has its roots in photogrammetry which surfaced in the 1850's. Gaspard Felix Tournachon took the first know aerial photograph from a balloon in 1858, see Figure (EO-MINERS 2013). In the 1960's and 70's, with the availability of digital images, robotics researchers developed vision-based algorithms to process information and control robots (Sutton 2009).


Figure 11: Aerial photographs of Paris taken by Gaspard Felix Tournachon in 1858 (credit: EO-MINERS).

There was rapid growth of image correlation in the areas of character recognition, microscopy, medicine/radiology, and aerial photography between 1955 and 1979, but during this time period experimental mechanics was focused on laser technologies (Sutton 2009). Research in image correlation related to deformations was nonexistent until the early 1980s.

The auto industry's demand for lightweight materials led researchers to use DIC to investigate the properties of new materials. Since the 1980s, most research has focused on the development of more accurate algorithms for calculating deformations, and materials testing in the lab. Facial recognition relies on correlating digital images to identify a given image from a database of images. Facial recognition was used at the 2001 Super Bowl in Tampa Bay, FL to identify potential terrorists. While no terrorists were discovered, the program was able to identify 19 people from a police database of people formerly arrested (Greene 2001). Many industries including manufacturing, technology, and security have been changed by digital imaging. The field of civil engineering can take advantage of this technology as well, but to rely on it with confidence there needs to be a recommended set of testing parameters for digital image correlation to collect accurate measurements, see Appendix F. In the case of the 2001 Super Bowl, facial recognition was an additional tool for security, so accuracy and reliability were not paramount. The software was worth using if there was a chance of identifying a potential terrorist. In fact, the project was a trial to determine if the police department wanted to purchase facial recognition software (Greene 2001). The same approach is not applicable to civil engineering. If a structure's fate is to depend on its monitoring system, image correlation has to be able to identify the problem. Otherwise, it cannot be relied on for public safety reasons.

2.4 Civil Engineering Application of DIC

DIC has been used in various civil engineering field applications many of which relate to bridges. Researchers in Canada successfully monitored crack propagation in a concrete bridge beam during a load test in order to better understand fatigue behaviors (Kuntz, et al. 2006). Japanese researchers loaded a new simple span steel girder bridge using a 44 kip (196 kN) cargo truck and measured deflections with cameras (Yoneyama, et al. 2007). Figure 12 shows the comparison between camera deflections and displacement transducers. The two methods agreed well.
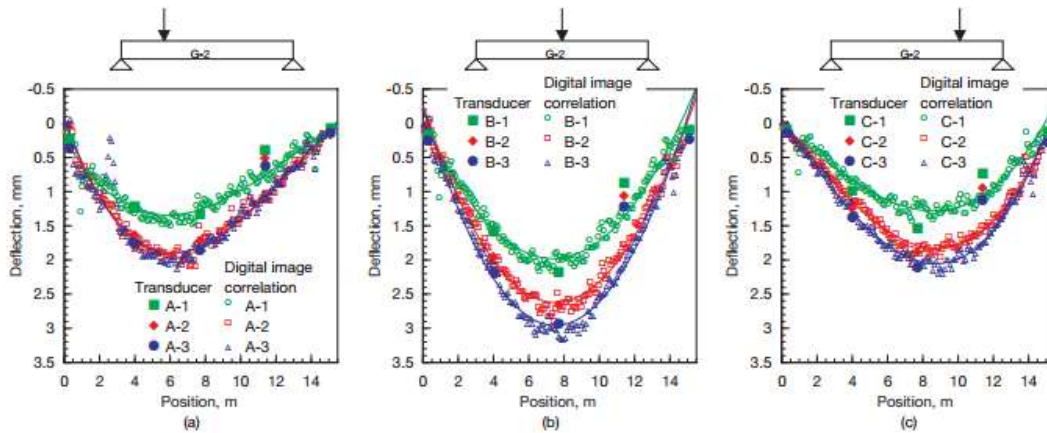

Figure 12: Yoneyama et al. deflection comparison between displacement transducer and DIC (credit: (Yoneyama, et al. 2007)

The test was conducted at night and used artificial light to illuminate the girders of interest. Only deflections in exterior girders were able to be measured.

Digital image correlation research began at the University of New Hampshire with an NSF Career Grant (# 0644683). Under this grant researchers investigated measuring deflections at the Powder Mill Pond Bridge in Barre, MA. The bridge was constructed in 2009, and white magnets were fixed to an exterior girder prior to the girder being placed (Figure 13) (Brogan 2010). The magnets served as a speckle pattern and had strings attached that hung down to ground level. The strings allowed for the magnets to be removed after testing was done. The researchers were able to measure displacements of exterior girders, but with little confidence in the reliability of the results. The deflections measured with DIC were not repeatable.
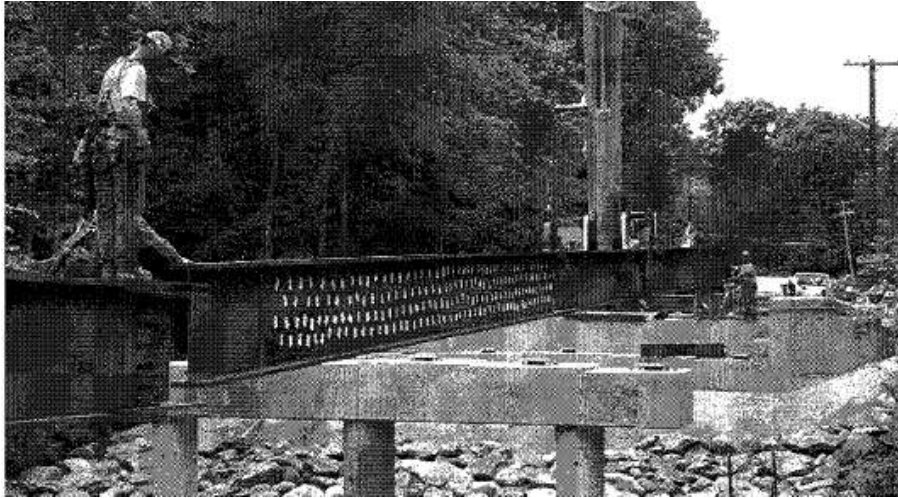
Figure 13: Exterior girder with magnets being placed at Powder Mill Pond Bridge (Brogan, 2010).

The research continued with an NSF PFI Grant (#0650258). This grant furthered the research under the Career Grant by accessing interior girders and focusing on accurate results. A target system using PVC piping and spray painted sheet metal was developed (Figure 14). A typical target was a square of sheet metal attached to one end of the PVC pipe with an adjustable steel clamp and a 2.5 inch (6.35 cm) neodymium magnet glued to the other end. The magnet was used to connect the pipe to the bottom of a steel beam. This system allowed access to interior girders for measurements by measuring the displacement of a rigid target hung from a beam rather than the web of a beam. It also eliminated the need for a speckle pattern to be applied directly on the bridge girders.

Figure 14: PVC target system used beneath the Powder Mill Pond Bridge (credit: Peddle, 2011).

The DIC data collected was compared to linear variable differential transformers (LVDT) at two locations to verify the accuracy of the results (Peddle, 2011). In addition the research focused on a single target to obtain accurate results for each point of interest on the bridge. This required a truck pass for each point of interest in a load test. This method of collecting data is time

consuming and prolongs bridge closings. With the PVC target system researchers began investigating into distribution factors and load ratings (Peddle, 2011).

The project outcomes from the NSF grants were well received by bridge owners, but there were some concerns about the reliability of DIC. This research furthers that work by developing a protocol for rapid use of DIC as a bridge inspection tool. This includes capturing multiple points of interest within a single field of view to reduce the number of truck passes in a load test. An investigation into the effects of lighting, targets, and camera angle on DIC results was needed in order to achieve the research goals. These parameters were tested in the structures laboratory. The results from these tests are detailed in Appendix F.

3.   Bagdad Road Ove US Route 4 Bridge

The Bagdad Road Bridge was chosen for a case study using the optimized testing parameters from laboratory testing. In April 2012, a strain data was collected from the BROUS4 Bridge. The excitation for the data collection was traffic loads. This data was used to determine the neutral axis location. In June 2012, a load test was performed to determine the effect of girder connection on the continuous action of the bridge performance and the live load distribution factor. In addition, the field of view for DIC was expanded to include multiple targets with the goal of collecting multiple points of interest in a single truck pass.

3.1 Background of Bagdad Road Bridge

The Bagdad Road Bridge over U.S. Route 4 in Durham NH was selected for field verification because of its proximity to the UNH campus and previous instrumentation, see Figure 15. The bridge is 2.0 mi (3.22 km) from the UNH engineering building, Kingsbury Hall. The bridge was designed in 1965. The bridge has four spans with two 45 ft (13.7 m) spans at each abutment and two 60 ft (18.3 m) center spans making it symmetric about its center bent. U.S. Route 4 runs beneath the southern 60 ft (18.3 m) span. The northern 60 ft (18.3 m) span crosses over a field of grass and is safely accessible (Figure 16).

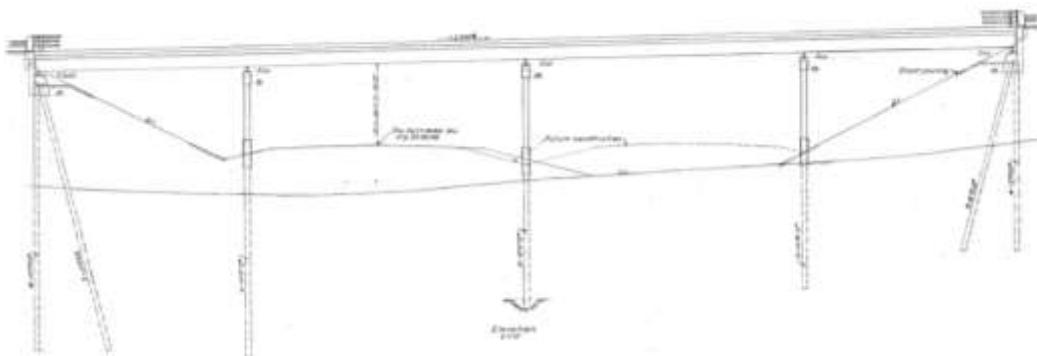**Figure 15 Bagdad Road Over US Route 4**

Figure 16: Elevation View of the Bagdad Road Bridge.

The bridge has six W36x135 steel girders spaced at 8 ft (2.44 m) with a 7.5 in (19.05 cm) reinforced concrete deck. The exterior girders are inset 2.33 ft (0.710 m) from the edge of the bridge. A 36 ft x 10.5 in x 0.5 in (10.98 m x 26.7 cm x 1.27 cm) cover plate is welded to the bottom of each girder in each 60 ft (18.3 m) span. The cover plate begins and ends 12 ft (3.66 m) from each bent. The girders are welded at the bents to form a continuous beam. C15x33.9 steel diaphragms connect the beams transversely at midspan in the 45 ft (13.7 m) spans and at the third points in the 60 ft (18.3 m) spans. In addition, there are diaphragms at each support (Figure 17).
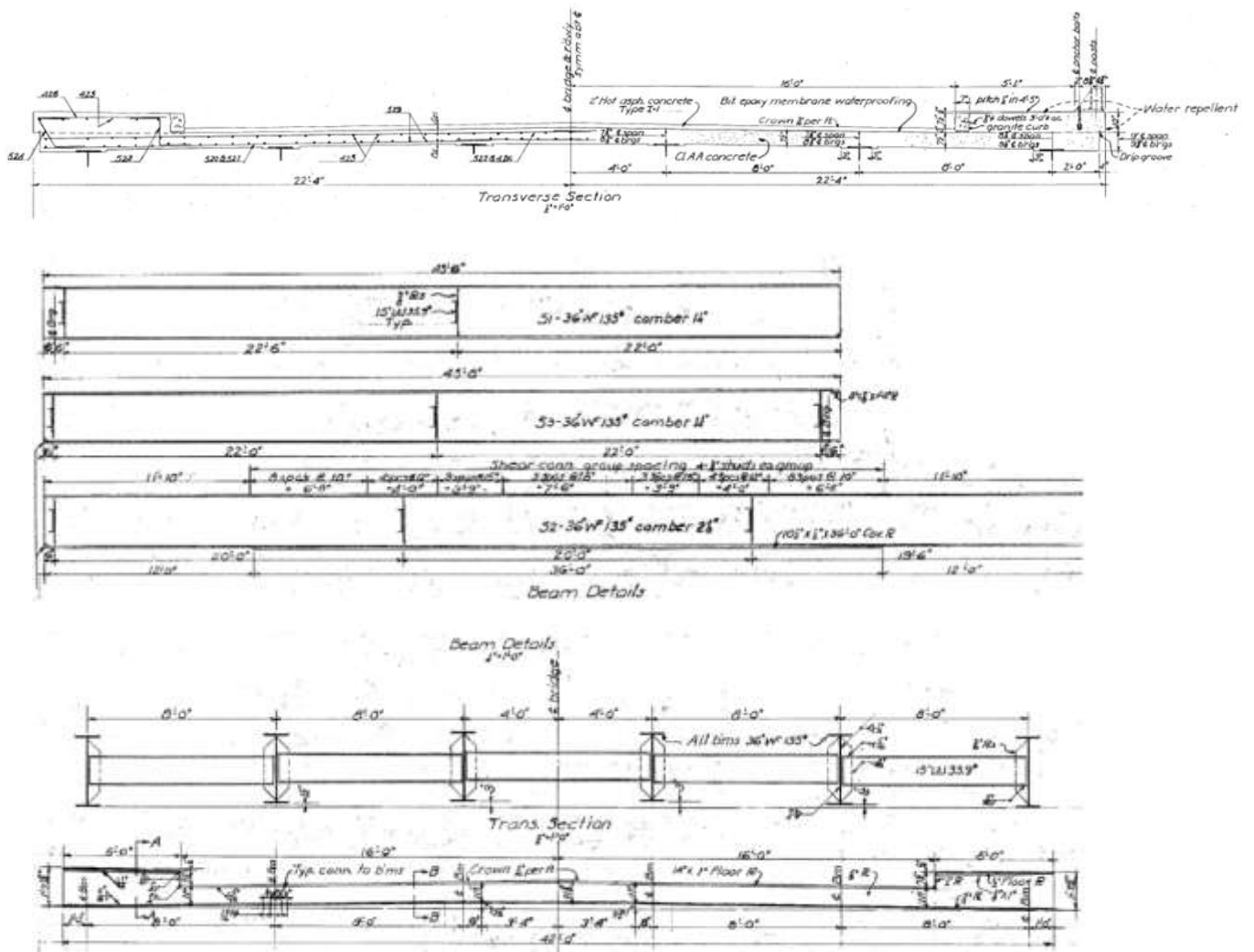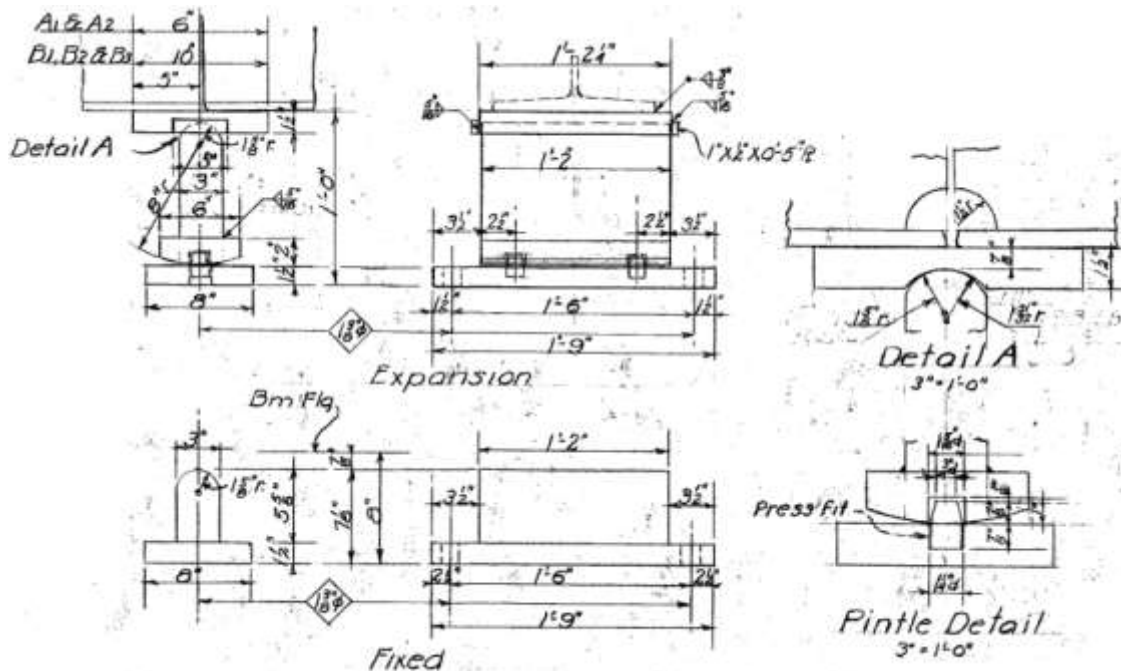

Figure 17: Typical cross sections and beam details.

The girders are supported at each bent with rocker bearings, most of which have tipped to some degree over the years. See Figure 18 for details of the rocker bearings.

Figure 18: Bearing details.

The northern 60 ft (18.3 m) span was chosen for instrumentation because there are no obstructions below it and it is a relatively long span. In addition to the location of the neutral axis from the collected strain measurement and the live load distribution factors from girder deflections, this research also focuses on the nature of the beam splice at each bent cap. This connection was a concern for the NHDOT. Based on the construction technique used to place the beams, the continuous action of the bridge under live loads was unknown. These topics were investigated using bridge deflections measured with DIC. The first goal was to determine whether the bridge acted as a continuous structure, or more like a simply supported structure. See Figure for a depiction of the impact of this on the response of a structure.

This question revolved around the splice made between beams at the bents (Figure 20). The beams were initially placed as simply supported with a camber such that a gap existed between the ends of each beam. Then two plates were welded on the top flange across the beams. Then the deck was cast and with the gap closed the webs were welded together. The NHDOT load rates the bridge as a simply supported structure for dead load, but as a continuous structure for live load. The true effect of the connection on the continuous action of the bridge under live load was unclear
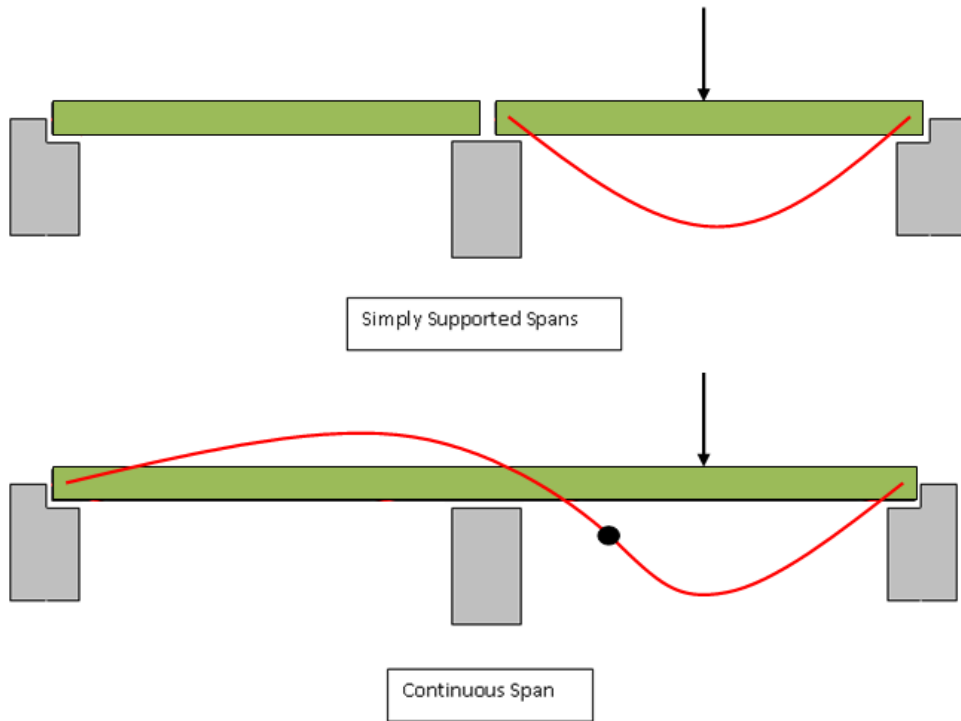
Figure 19: Continuous action versus simply supported. Black dot indicated point of inflection.
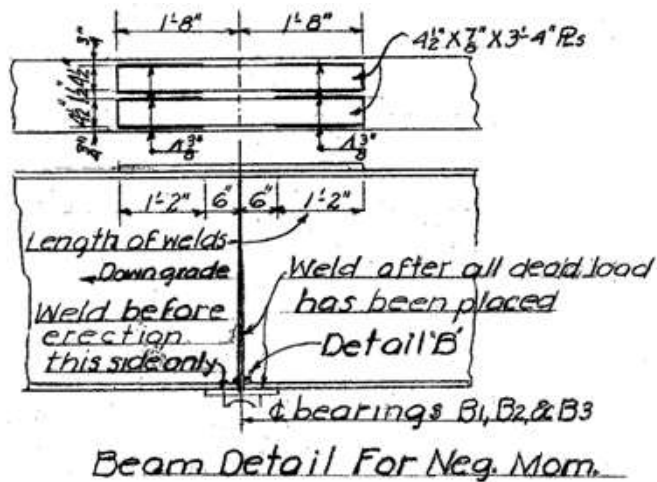

Figure 20: Detail of beam splice at bents. The upper part of the diagram shows the two plates welded to the top of the beam, and the lower part of the diagram shows the weld between the two beams.

3.2 Layout of Sensors

The sensor network at the Bagdad Road Bridge was implemented on a small scale for sensors and data acquisition equipment testing. The full installation plan and procedures are detailed in Appendix G. To meet the needs of strain gauge research, only two beams were prioritized for installation. Interior beams were chosen because they were expected to have a higher response under live loads, given the sidewalks over the exterior beams, and to hide the installation and preserve the aesthetics of the bridge from travelers on US Route 4, below the bridge
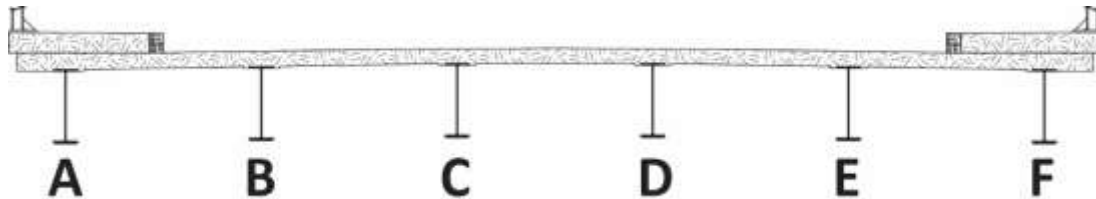

Figure 21: Bridge Section Looking East

Beam D, shown in Figure 21, was chosen for evaluating optimal placement of strain gauges for neutral axis measurements. The impact of flawed measurements in strain, typically due to noise, when using two gauges was also evaluated. Three strain gauges were used to calculate neutral axis using linear regressions and compared to values produced by pairs of strain gauges within the set of the three gauges. The analysis will, therefore, also be able to show what the best locations are when neutral axis locations are made when using a pair of strain gauges. Both sides of the beam were instrumented with three gauges to increase confidence in the results and provide redundancy for the instrumentation system. Two thermocouples were also installed at this location to evaluate the behavior that temperature has on the strain measurements. Layouts of the instrumented cross sections are shown in Figure 22. The purpose of instrumenting Beam E was to evaluate the behavior of the sensors themselves by comparing measurements made from full and quarter bridge gauges. The instrumented location is between the two bridge bents shown in Figure 23. The instrumented locations and beam nomenclature are provided in Figure 24.
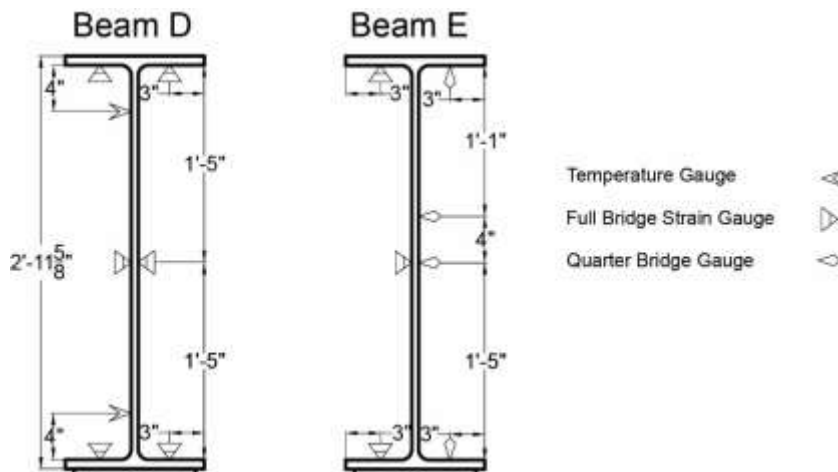

Figure 22: Instrumented Beam Cross-sections at Bagdad Rd.

Figure 23: Photo of the Underside of Span 3 Viewed from Under Span 4

The girders that were ultimately instrumented were girders D and E, both at the center of span 3. The locations are labeled in the structural plan view of the bridge shown in Figure 24. Both faces of Beam D and the North face of Beam E were each instrumented with three full bridge strain gauges, one gage on the inside face of each flange and one gauge on the web. The South face of Beam E was instrumented with three pairs of quarter bridge gauges, corresponding to the same locations full bridge gauges were installed on other beam faces. Two thermocouples were also installed on the web of the North face of Beam D, as shown in Figure 24.
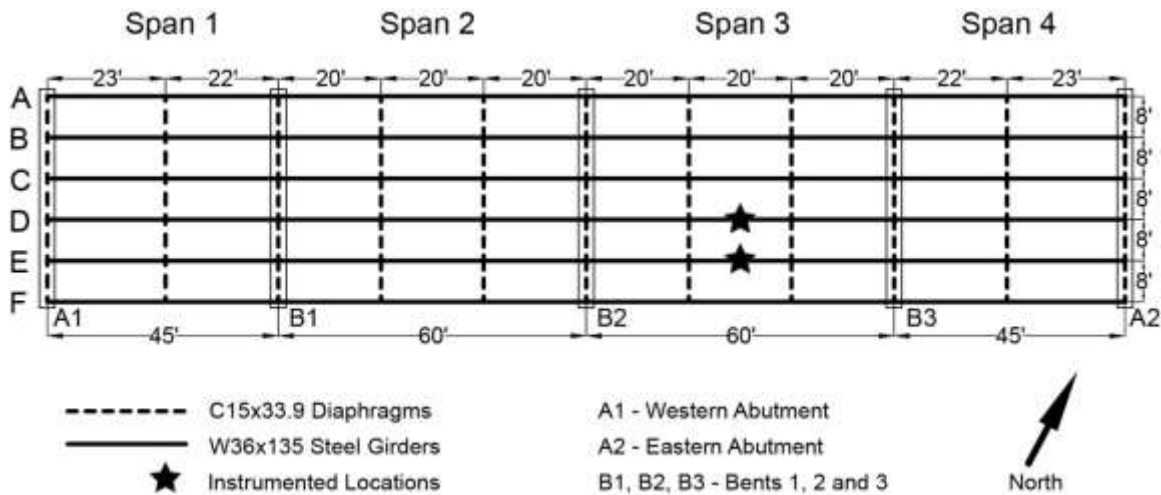
Figure 24: Sensor Layout at the Bagdad Rd. Bridge

Pairs of quarter bridge gauges were oriented with one intended to measure longitudinal strain and one for transverse strain at approximately the same location. Sections of each beam are shown in Figure 22. Note that the quarter bridge gauges oriented in the transverse direction on the flanges are not shown in the section because they are mounted slightly ahead, longitudinally, of the gauges mounted in the longitudinal direction. Gauges on the flange are therefore not technically in the same cross section as the gauges on the web and longitudinal measuring gauges on the flange.

26

3.3 Strain Data due to Traffic Excitation

In April 2012, strain measurements were collected for sensor measurement quality assessment and neutral axis location determination. Several laboratory and field experiments were conducted to insured the quality of the collected strain data from the foil gauges at the BROUS4 bridge. These experiments are detailed in Appendix H. During field data collection, an traffic event that induced a strain response greater than 12 με was determine to be a live load event and the data was used to calculate the composite section neutral axis. The strain reading are included in Appendix H. The resulting neutral axis locations are included in this chapter, while the calculations and additional discussion are included in Appendix H.

Determining the neutral axis frequently over time may be a means to detect sudden damage or track slow degradation of the steel or deck. Neutral axis location, therefore, is a metric that is being researched by the SHM community (Liu, et al. 2008), (Olund and DeWolf 2007), and (Lefebvre, 2009). In those studies, 2 strain gauges were used to determine the location. This research expands on those investigations by using multiple gauges on each beam face to determine the locations. Each group of gauges belonging to a beam face was divided into 3 sets of 2 gauges and 1 set containing all gauges. The measurements from each set of gauges were used to calculate the neutral axis location and are presented in Appendix H and further discussed in section 3.5. Results were compared to expected values to infer the health of the composite section and compared among multiple sets to make observations about gauge placement.

Using a structural mechanics approach, the location of the neutral axis was calculated using transformed section properties and was 31.7" from the bottom of the steel, as shown in Figure 25. The bottom of the steel in this case is the bottom of the cover plate. By hand calculation (see appendix E) both Beams D and E are assumed to have the same neutral axis location because the curb is taken as outside of the effective width of Beam E and, therefore, does not contribute to the cross sectional properties.
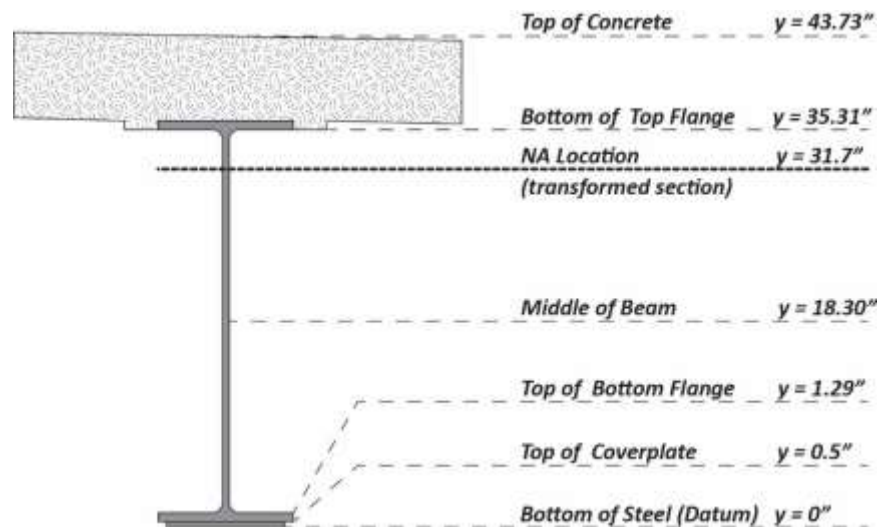

Figure 25: Diagram of Points of Interest Throughout Depth of Composite Section

Neutral axis locations were calculated using data from the Live Load Event Database, as described in Appendix H. The four sets of data used to calculate the position are from the top and bottom flange strain gauge readings, top flange and middle of web strain gauge readings, middle of web and bottom flange strain gauge readings, and a linear interpolation of all three values.

3.4 Sample Neutral Axis Calculation

Sample calculations for all four sets are shown below. The readings are taken from event 2:115, on the south face of Beam D. Results from the event are shown on Figure 26. For a pair of gauges:

$$NA = y_2 - \frac{d\varepsilon_2}{\varepsilon_2 - \varepsilon_1}$$

When considering all 3 gauges:

$$m = \frac{n(\sum xy) - (\sum x)(\sum y)}{n(\sum x^2) - (\sum x)^2}$$
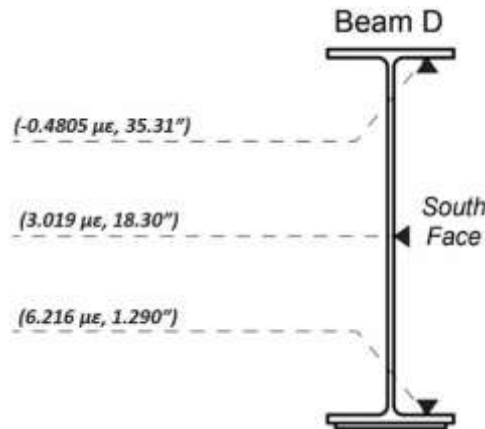
$$NA = \bar{y} - m\bar{x}$$

Figure 26: Data Points for Event 2:115 Illustrated on South Face of Beam D

Top & Bottom Pair (d = 34.02)

$$NA_{top\,\&\,bottom} = 35.31in - \frac{34.02in\,(-0.4805\mu\varepsilon)}{(-0.4805\mu\varepsilon - 6.216\mu\varepsilon)} = 32.87in$$

Top & Middle Pair (d = 17.01)

$$NA_{top\,\&\,middle} = 35.31in - \frac{17.01in\,(-0.4805\mu\varepsilon)}{(-0.4805\mu\varepsilon - 3.019\mu\varepsilon)} = 32.97in$$

Middle & Bottom Pair (d = 17.01)

$$NA_{middle\ \&\ bottom} = 18.30in - \frac{17.01in\ (3.019\mu\varepsilon)}{(3.019\mu\varepsilon - 6.216\mu\varepsilon)} = 34.36in$$

Linear regression of all 3

$$\sum xy = (-0.4805 \times 35.31) + (3.019 \times 18.30) + (6.216 \times 1.290) = 46.30$$

$$(\sum x)(\sum y) = (-0.4805 + 3.019 + 6.216)(35.31 + 18.30 + 1.290) = 480.6$$

$$\sum x^2 = -0.4805^2 + 3.019^2 + 6.216^2 = 47.98$$

$$(\sum x)^2 = (-0.4805 + 3.019 + 6.216)^2 = 76.64$$

$$m = \frac{3(46.29) - 480.6}{3(47.52) - 76.62} = -5.077$$

$$\bar{y} = \frac{1}{3}(35.31 + 18.30 + 1.290) = 18.30$$

$$\bar{x} = \frac{1}{3}(-0.4805 + 3.019 + 6.216) = 2.918$$

$$NA = 18.30 - (-5.18)(2.918) = 33.12in$$

The strain values plotted versus depth are shown in Figure 27. Note that in this instance the reading from the middle gauge value was only 6.20% over expected. If the middle gauge is considered an erroneous value, it can be seen that including it in calculation had a larger impact when combined with the bottom gauge than with the top gauge. This is likely the result of the low readings from the top gauge. Because the reading plotted on the x-axis of the strain diagram is close to zero, the y-intercept of a line plotted using the data point will be close to the y value regardless of the other value or values in the set.
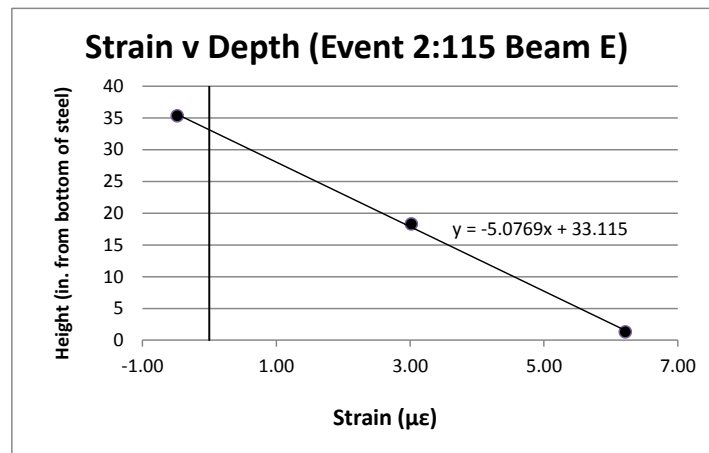

Figure 27: Strain Diagram Corresponding to Event 2:115 on South Face of Beam D

3.5 Results from the Live Load Event Database

The results calculated from each live load events are included in Appendix H. the comparison of the resulting neutral axis values is included here.

### *3.5.1 Comparison of Sets Common to Each Beam Face*

This section uses the data from Appendix H Section 4 to discuss implications from the findings specific to the individual beam faces. Appendix H section 5 presented neutral axis calculations by comparing a given set of gauges, for example top and bottom on the north face of Beam D, to other sets of gauges that used the same gauged locations on other beam faces. By categorizing sets of gauges by location on the beam it was found that the top gauge has a large influence on the resulting neutral axis location. This section categorizes neutral axis locations specifically by the beam face they are calculated for, by placing results from all sets that belong to each face on the same box plot. The box plots are show in Figure 28 through Figure 31. The center of each box represents the media value. The upper bound of the box plot is equal to the third quartile and the bottom bound is equal to the first quartile. The error bars extend to the maximum and minimum values for the set. The horizontal red line on each plot represents the value calculated for the healthy transformed section property, 31.7". Healthy means in this case that there is no section loss in the steel or the cover plate and no cracking in the deck, which has a compressive strength of 3.5 ksi.

The box plots show that, in general, the calculated neutral axis locations are above the value determined by transformed section properties. The sets from the north face of Beam E seem to agree with each other the most, which is to be expected given the results of appendix H section 3 showed that on average the readings from the middle of the web strain gauge, resulted in less than a 1% deviation from the expected value found through linear interpolation between the two gauges. Lastly, the neutral axis location calculated from the quarter bridge strain gauge readings produce the widest range of values, highlighting that results from those gauges can be scattered.

These results have interesting implications for the SHM system at the Bagdad Road Bridge and structural health monitoring systems in general that rely on neutral axis positioning. The positions that were derived using the gauges on the web of Beam D highlight a weakness in SHM systems that use only two gauges per cross section because the readings were shown to be artificially increased through web compression in Appendix H, and yet the resulting feature extractions produced believable values. Beam E is of interest for the system at the Bagdad Road Bridge because the results from the north face indicate the neutral axis is high enough that damage may have occurred, however the south face of the beam indicates a healthy section. This raises questions about the differences that could be occurring on the two faces of Beam E. Two distinct possibilities exist that could be causing the difference; either the top gauge on the north face of Beam E is malfunctioning, or the process of excluding outliers from results using the quarter bridge gauges created samples that on average have erroneously low neutral axis locations.
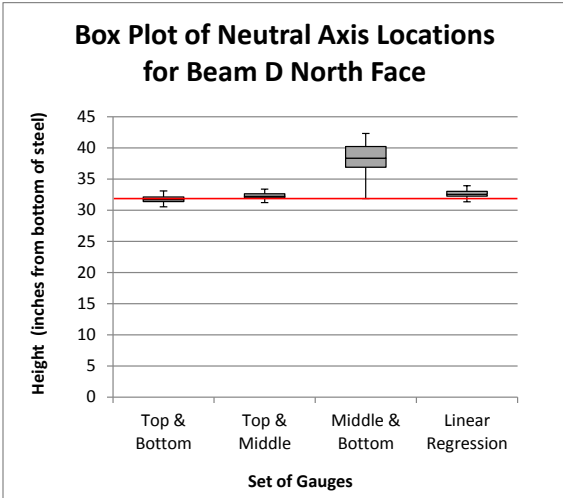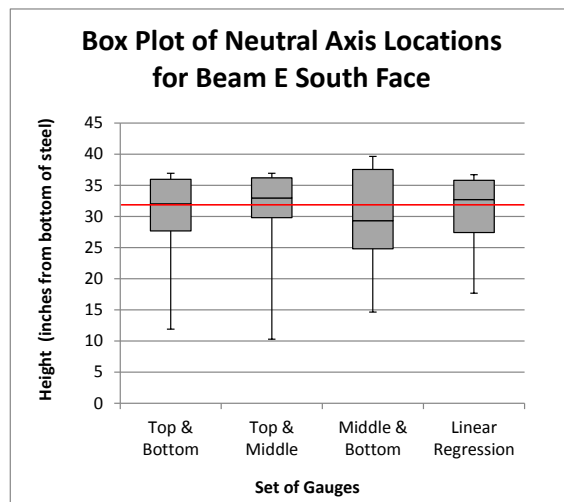
Figure 28: Box Plot of Neutral Axis Locations Calculated for the North Face of Beam D
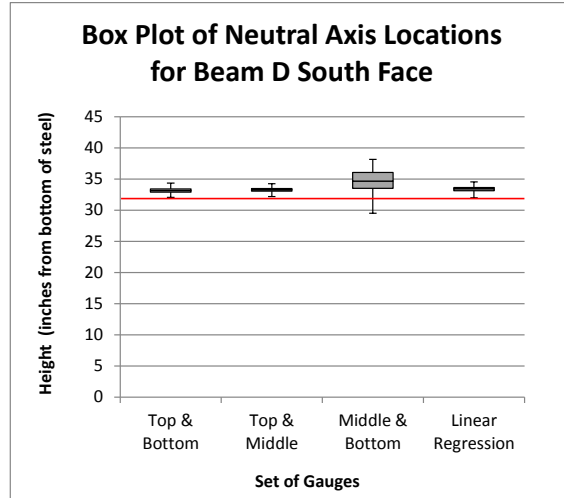
Figure 29: Box Plot of Neutral Axis Locations Calculated for the South Face of Beam D
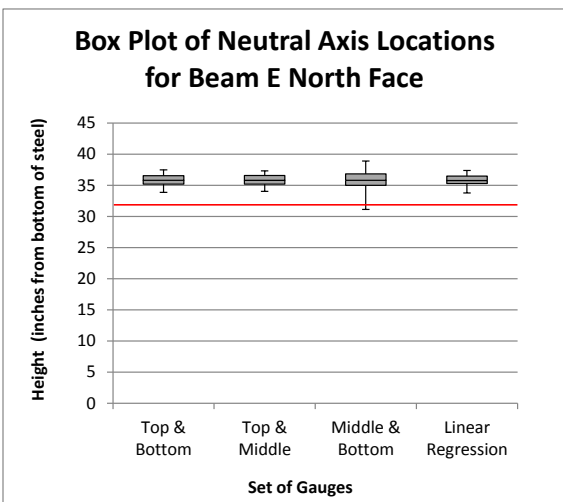
Figure 30: Box Plot of Neutral Axis Locations Calculated for the North Face of Beam E

Figure 31: Box Plot of Neutral Axis Locations Calculated for the South Face of Beam E

The first possibility is supported by the results of Appendix H, where the full bridge gauge on the web of Beam E produced values close to expectations, as opposed to Beam D where both gauges produced readings that exceeded expectations. If the gauge is malfunctioning and constantly reading zero, the expected strain value on the web would be higher than if the gauge produced negative values during bending, and strains that are artificially magnified by web compression could agree with those expectations. Negative values were common during events at Beam D. Unfortunately, the readings on the top flange are generally too small to be reasonably evaluated for consistent behavior considering the high noise to signal ratio in the quarter bridge gauges at low values.

The second possibility is supported by the fact that the majority of outliers excluded from the samples of quarter bridge gauge readings on Beam E were excluded for being above the composite section and not below it. Recall that the upper bound is 12" away from the position in a healthy section and the lower bound is 31.7" away. By including locations between 12" above and 31.7" below the transformed section position, and not in the same range above the position, may have resulted in a lower average that actually hides possible damage. This suggests that improved means of excluding outliers should be developed, which are more sophisticated than simply excluding values that fall outside of the section.

3.6 Neutral Axis during Negative Bending Events

The sample of negative bending events that was described in Appendix H was also used to determine neutral axis locations. Calculating neutral axis locations during negative bending may produce opportunities to investigate structural health parameters that positive bending situations do not. An example would be situations where cracks in the deck do not affect the compressive capacity of deck but reduce the tensile capacity. Conclusions from the sample are difficult to make because it is so small, only 12 occurrences, and the readings during negative bending were significantly smaller and thus had a higher noise to signal ratio.

An example strain diagram is shown in Figure 32 using the negative bending event that caused the largest peak strain in either beam of any negative bending event. As opposed to a positive bending example strain diagram, the strain diagram is drawn on the compressive side during negative bending events, indicated by the negative strain values. Also note that although this was the largest negative bending event of the twelve, it caused less than a three microstrain reading in the bottom flange, which was actually the limit used to remove small, and considered more noise influenced, samples from the Live Load Event Database.

Strain v Depth (Event 5:236 Beam D)

$y = 13.286x + 33.372$

Height (in. from bottom of steel)
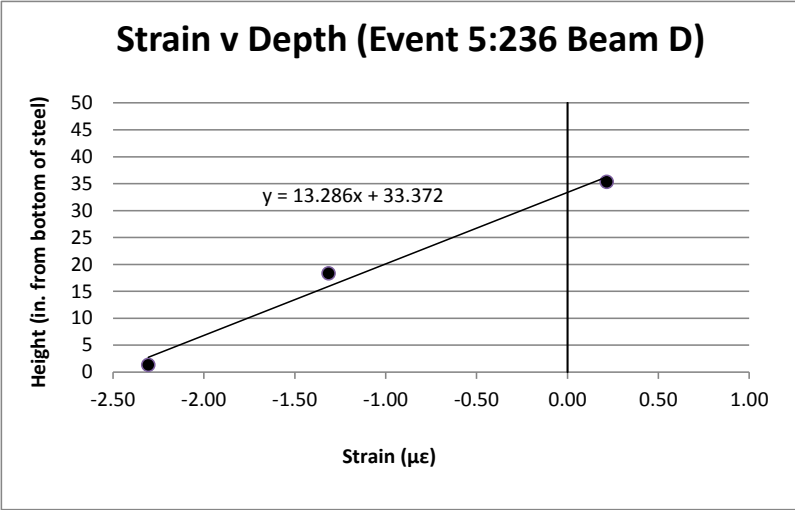
Strain (με)

Figure 32: Example Strain Diagram Derived from a Negative Bending Event

Table 1 shows the averages, standard deviations, and ranges of the calculated neutral axis locations. Although more negative bending events should be collected, initial results are similar to those for positive bending events; the neutral axis location is slightly higher than the position

calculated using transformed section properties when using all sets of gauges on Beam D except the pair of middle and bottom gauges, which were significantly higher. The results from the north face of Beam E indicate possible damage or sensor malfunction, and the results from the quarter bridge gauges are again more varied, which is demonstrated by the large amount of outliers that needed to be excluded from the sample.

Table 1: Neutral Axis Location Results From Negative Bending

| Set	Average	Standard Deviation	Outliers	Range
Beam D: North Face				
Top & Bottom	32.20	0.5644	0	31.20 − 33.29
Top & Middle	32.77	0.5028	0	31.60 − 33.62
Bottom & Middle	42.25	3.658	4	33.77 − 43.37
Linear Regression	33.17	0.6175	0	$31.76 - 34.19$
Beam D: South Face				
Top & Bottom	33.43	0.6112	0	32.31 − 34.53
Top & Middle	33.56	0.6488	0	32.30 − 34.68
Bottom & Middle	37.16	3.611	1	$31.63 - 42.57$
Linear Regression	33.73	0.9029	0	32.29 − 35.51
Beam E: North Face				
Top & Bottom	36.24	0.6391	0	35.43 − 37.32
Top & Middle	36.47	0.8341	0	35.45 − 37.84
Bottom & Middle	30.93	1.709	0	28.19 − 34.29
Linear Regression	35.00	0.6899	0	33.65 − 36.02
Beam E: South Face				
Top & Bottom	40.70	3.583	8	$35.75 - 43.41$
Top & Middle	25.66	7.871	6	$7.871 - 39.52$
Bottom & Middle	27.14	7.23	6	$17.53 - 37.32$
Linear Regression	29.56	12.41	2	2.816 − 42.74

As stated, the pool of samples is too small to draw conclusions from but the process shows that positions can be derived from negative bending events. This could have implications for future research at the bridge. Although it will take much longer to produce a sample of reasonable size,

as only large trucks and school buses may produce satisfactory readings, the results may produce more information from the SHM system using already in place sensors.

3.7 Evaluation of Neutral Axis Results

In general, it can be seen that the readings from the top flange and middle of the web strain gauge pairs, or the top and bottom flange pairs, produced much more consistent results than that of the middle and bottom. The results may be particularly unexpected in Beam D because, as shown in Appendix H, the middle gauges are likely not functioning as intended. Recall that the collected data from the middle of the web strain gauge were consistently over expected values in Beam D. These erroneous values reduce the confidence in the neutral axis location calculated using any pair of strain gauges that include a full bridge strain gauge on the web.

The results from Beam E highlight an interesting concept. If a gauge is placed close to the neutral axis, then the small readings will cause the strain diagram to always pass close to the neutral axis, as shown in Figure 33. The dashed lines in the figure represent strain diagrams produced by erroneous values in a strain gauge located at y_1. The wide range of erroneous values produces a small shift in neutral axis locations. This could pose a problem for SHM systems with strain gauges installed on or near the neutral axis.   In this case, if the strain gauge were to malfunction and no longer collect meaningful values, the calibration routine would zero the strain gauge. This would produce an expected zero value and if movement of the neutral axis actually had occurred for any reason, for example damage, it would go undetected.
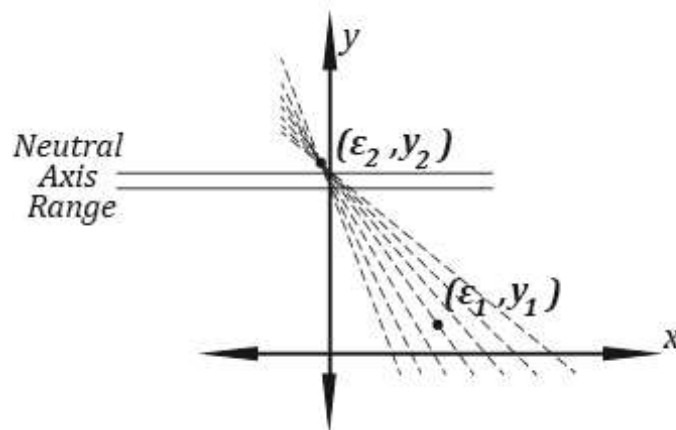
Figure 33: Illustration of Gauge Error on Neutral Axis Location When Strain Gauge is Located Near NA

At this time, this issue is not believed to be occurring in the installation of Beam D, however, it could be occurring in the installation of Beam E. Table 2 shows results from an analysis of the ratios from top to bottom strain gauge readings in a pair. Because plane sections are assumed to remain plane, the ratio of top to bottom strain gauge readings should be consistent. These ratios are from the samples used to derive neutral axis locations using the top and bottom strain gauge readings on each face, therefore, in case of the south face of Beam E, 30 outliers have been excluded from the 101 event sample.

Table 2 shows that the north face of Beam E has a ratio of top to bottom strains that is closest to zero of any beam face because the strain gauge on the top flange produces readings typically were close to zero. The ratio also has a higher standard deviation than both of the full bridge strain gauge pairs on Beam D, which could indicate that behavior of the strain gauge on the top flange of Beam E, event to event, is not consistent. The standard deviation from values on the north face of Beam E is also higher than the two other beam faces instrumented with full bridge gauges, which could support that the top gauge is behaving less consistently than other full bridge gauges. The south face of Beam E contains the largest standard deviation which is likely caused by the quarter bridge gauges, however, it could be an indicator that the behavior of the top flange on Beam E is simply more varied than in Beam D.

Table 2: Ratio of top reading to bottom reading

Beam / Face	Average	Standard Deviation	Range
D / North	-0.1164	0.0202	-0.1636 to -0.0704
D / South	-0.0674	0.0137	-0.1064 to -0.0321
E / North	0.0173	0.0302	-0.0445 to 0.0937
E / South	-0.192	0.3802	-2.203 to 0.1967

Another result that highlights the top strain gauge on the north face of Beam E may not be functioning correctly is the calculated neutral axis location. Table shows that the average calculated neutral axis location was higher on that beam face than any other beam face in all instances where a top strain gauge was utilized.

Table 3: Average Neutral Axis Locations from Pairs Utilizing Gauge on the Top Flange

Gauge Pairs	Beam D: North Face	Beam D: South Face	Beam E: North Face	Beam E: South Face
Top & Middle	32.30"	33.25"	35.99"	32.54"
Top & Bottom	31.77"	33.17"	35.94"	31.81"

Examining the neutral axis locations derived from only full bridge strain gauges shows a higher location in Beam E as opposed to Beam D. This is either caused by the two sections truly having different neutral axis that differ by that large of an amount, or the top strain gauge of the set on the north face of Beam E is malfunctioning. Different neutral axis locations from beam to beam are not expected as hand calculations showed they both had the same location. Therefore, the difference could be the result of damage. There was a minimal level of damage detected during the deck repair conducted in summer2012. .

3.8 Baseline Neutral Axis

It is important to produce a neutral axis location for each beam so the results of this research can serve as a data point in any pool of samples used to track neutral axis position over time. These locations will serve as a baseline neutral axis. The values are expected to change as a result of maintenance and aging. Because the results of Appendix H indicated the full bridge gauges on the web of each beam and the full bridge gauge on the top flange of Beam E may not be producing reliable readings, results from sets using those gauges have been omitted from consideration.

Figure 34 labels the gauges used for determining baselines. The omitted gauges leave the only sets of the top and bottom gauges on both faces of Beam D and all sets on the south face of Beam E. The baseline neutral axis location for Beam D is therefore derived from a sample size of 202 events measured by the pair of top and bottom gauges on each side. The baseline neutral axis for Beam E is determined by using the results from the linear regression of all three readings because combining results from the individual pairs would involve counting some individual readings multiple times, and the set of three readings contains the most amount of data. Furthermore, a single outlier that fell below 12" from the location of the neutral axis determined by structural mechanics, 31.7", was omitted to balance the effect of omitting outliers that were over 12" above the location. This resulted in a sample size of 81.
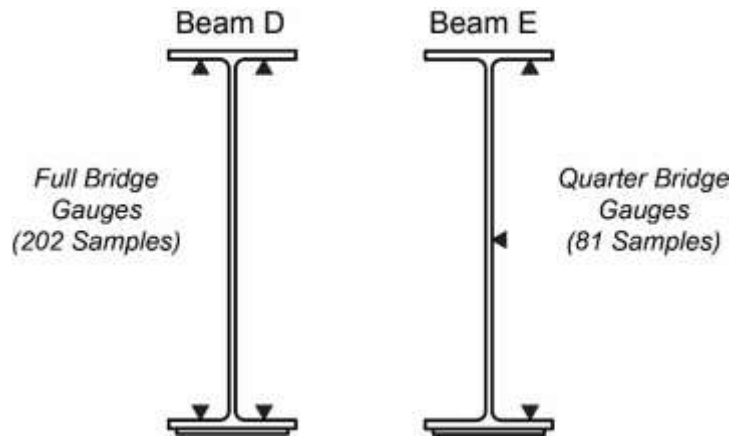
Figure 34: Location of Gauges Used to Determine Baseline Neutral Axis

The baselines consist of 95% confidence intervals. Table 4 shows the intervals for both beams. The locations are shown graphically in Figure 35 and Figure 36. In Beam D, the results are slightly higher than the location calculated using structural mechanics. The higher location could be caused by a deck that has a higher compressive strength than the assumed 3500 psi or could be the result of section loss in the steel over time resulting in a lower area of steel than was used in the hand calculations as no section loss was assumed. In Beam E the range of values is centered on the hand calculated value. This could be the result of uniform capacity loss in the section over time or a section that is not damaged at all.

Table 4: Baseline Neutral Axis Locations (95% CI)

Beam	Number or Samples	Neutral Axis Location (inches)
D	101	$32.35 - 32.59$
E	83	$30.49 - 33.08$
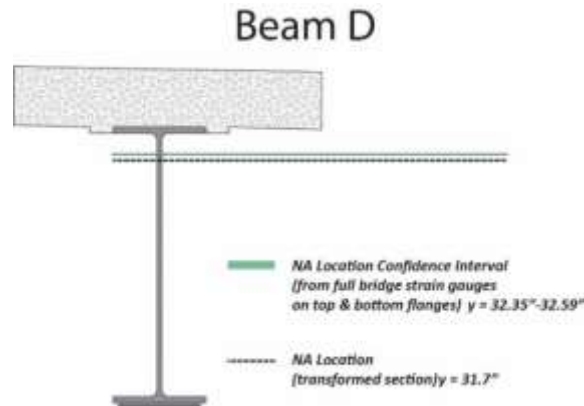
Figure 35: Baseline Neutral Axis Location in Beam D versus Transformed Section
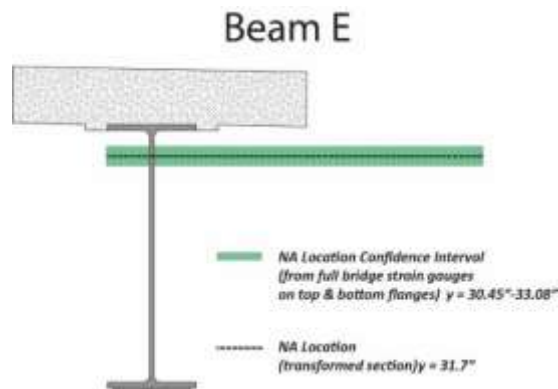
Figure 36: Baseline Neutral Axis Location in Beam E versus Transformed Section

The baseline results do not imply significant damage in either section. Although the quarter bridge gauges produced more varied results, as indicated by higher standard deviations and greater amount of outliers over the full bridge gauges throughout the analysis, the results are still satisfactory enough to draw conclusions from. Neutral axis heights determined at other locations in the bridge where no shear stud exist to connect the deck and the steel beams, such as in negative bending regions or the two outside spans, should contain lower results that can be used to verify this methodology. Comparisons should be made with neutral axis heights at those positions to verify that this method is capable of detecting non-composite or partially composite action. Those comparisons would support the notion that this method can detect damage to the shear studs, which is typically hidden from bridge inspectors.

4. Digital Image Correlation at the Bagdad Road Ove US Route 4 Bridge

4.1 Initial Data Collection

The Bagdad Road Bridge is located adjacent to Oyster River High School and sees school bus traffic twice daily. The buses provide a measurable deflection. Car deflections have been found to be drowned out in the vibrations of the bridge and, therefore, are undetectable. Bus deflection data was collected prior to the load test. A sample of this data is shown in Figure 37.
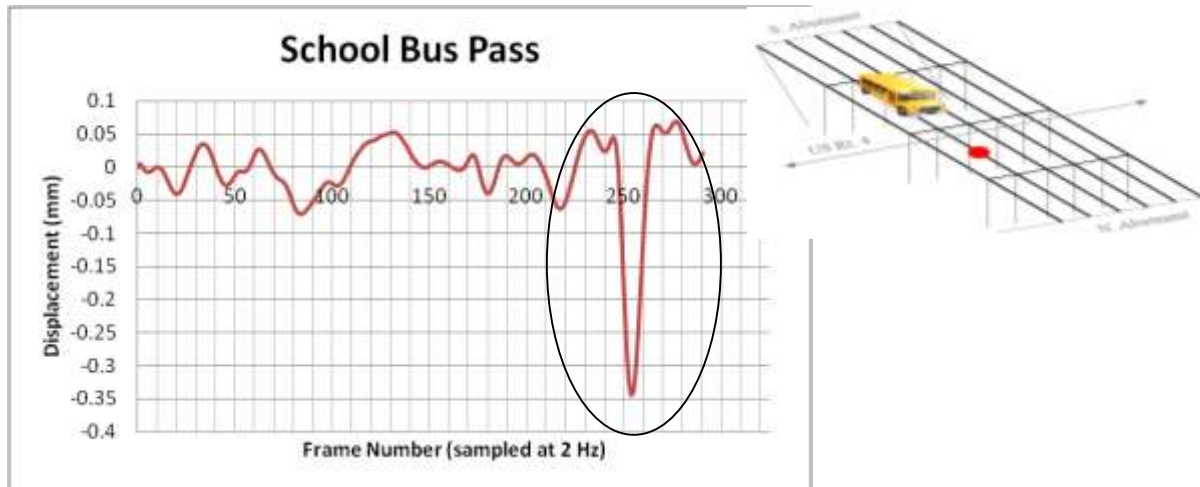
Figure 37: Time history for displacement of interior beam (Station 4 Girder 5) from bus loading.

This collection served as a proof of concept test for using DIC with the new operating parameters, see Appendix F for details, at the Bagdad Road Bridge. It also aided in refining the test setup before performing a load test on the bridge. The data was run through a Butterworth filter to remove noise from vibrations. Successful data shown in Figure gave confidence that a load test would be worthwhile. A conventional school bus is either a Class 6 or 7 vehicle. Therefore its gross vehicle weight (GVW) falls between 19501-33000 lbs (86.7-147 kN). GVW is the maximum weight at which a vehicle can legally operate. This would correspond to a bus fully loaded with adults, which the Oyster River High buses are not. The buses were at most half full, so they were assumed to weigh less than 33000 lbs (147 kN). In addition, a dump truck, the type of truck used for the load test, has a short wheel base compared to a bus's long wheel base. This makes the test truck more of a concentrated load than the bus. The load test truck was a 2002 International 4900 dump truck with crew cab (Figure 38). This is a Class 7 vehicle with a GVW of 26001-33000 lbs (116-147 kN). For the load test, the truck was loaded with sand and was close to its GVW.

Figure 38: NHDOT Test Truck.

4.4 Load Test Plan

After satisfactorily completing the proof of concept tests for DIC, a load test was planned. The research team coordinated with Scott Provost, of the NHDOT, to perform a load test before the deck work in June 2012. Deck work included stripping the asphalt off the bridge, sounding the deck with a steel rod, and repairing delaminated deck sections. The load test plan was created to include load paths, load cases, and any additional instruments installed prior to the load test. The test consisted of 24 runs covering 4 truck paths (Table 5).

Table 5: Load test runs.

| Test			Camera 0	Camera 1	Tilt Meters	BDI Gauges	Foil Gauges
a	Path 1	Pass 1	Sta 4 Girder 5	Sta 1 Girder 5			X
b		Pass 2	Sta 4 Girder 5	Sta 1 Girder 5			X
c		Pass 3	Sta 4 Girder 5	Sta 1 Girder 5			X
d		Pass 4	Sta 5 Girder 5	Sta 2 Girder 5			X
e		Pass 5	Sta 5 Girder 5	Sta 2 Girder 5			X
f		Pass 6	Sta 5 Girder 5	Sta 2 Girder 5			X
g		Pass 7	Sta 6 Girder 5	Sta 3 Girder 5			X
h		Pass 8	Sta 6 Girder 5	Sta 3 Girder 5			X
i		Pass 9	Sta 6 Girder 5	Sta 3 Girder 5			X
j	Path 2	Pass 1	Sta 4 Girder 4	Sta 1 Girder 4	X	X	X
k		Pass 2	Sta 4 Girder 4	Sta 1 Girder 4	X	X	X
l		Pass 3	Sta 4 Girder 4	Sta 1 Girder 4	X	X	X
m		Pass 4	Sta 5 Girder 4	Sta 2 Girder 4	X	X	X
n		Pass 5	Sta 5 Girder 4	Sta 2 Girder 4	X	X	X
o		Pass 6	Sta 5 Girder 4	Sta 2 Girder 4	X	X	X
p		Pass 7	Sta 6 Girder 4	Sta 3 Girder 4	X	X	X
q		Pass 8	Sta 6 Girder 4	Sta 3 Girder 4	X	X	X
r		Pass 9	Sta 6 Girder 4	Sta 3 Girder 4	X	X	X
s	Path 3	Pass 1	Sta 4 Girder 4	Sta 4 Girder 3		X	
t		Pass 2	Sta 4 Girder 2	Sta 4 Girder 4, 3, and 2		X	
u		Pass 3	Sta 4 Girder 3 and 2	Sta 4 Girder 4 and 3		X	
v	Path 4	Pass 1	Sta 4 Girder 2	Sta 1 Girder 2		X	
w		Pass 2	Sta 4 Girder 2	Sta 1 Girder 2		X	
x		Pass 3	Sta 4 Girder 2	Sta 1 Girder 2		X	

For Paths 1, 2, and 4 the runs were repeated two times for each point of interest (POI). This gave three runs for each POI in those paths. Path 3 was designed to evaluate widening the field of view to capture multiple targets. The four truck paths were centered over each interior girder, with the exception of Paths 1 and 4. Paths 1 and 4 were over the first interior girders, and it was not possible to center the truck over the girders because of the sidewalk (Figure 39).
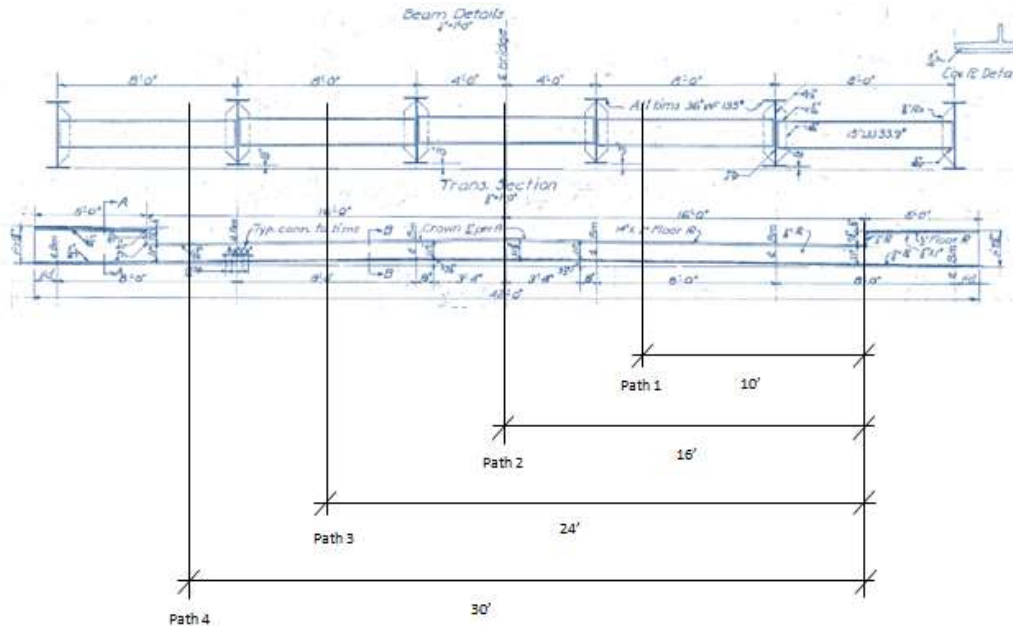
*Measurements to be made from edge of East sidewalk to driver's side tire.

Figure 39: Truck paths showing position of driver's side tire with respect to the bridge cross section. Measurements are from East sidewalk. Truck track width assumed to be 8 ft.

Figure 40 shows the bridge girders and stations instrumented. Station 2 is located 2 ft (0.61 m) north of Bent B3, Station 3 is located 2 ft (0.61 m) South of Bent B3, Station 5 is located 2 ft (0.61 m) north of Bent B2, and Station 6 is located 2 ft (0.61 m) south of Bent B2. For a more in depth description of instrumentation and load test logistics see Appendix G.
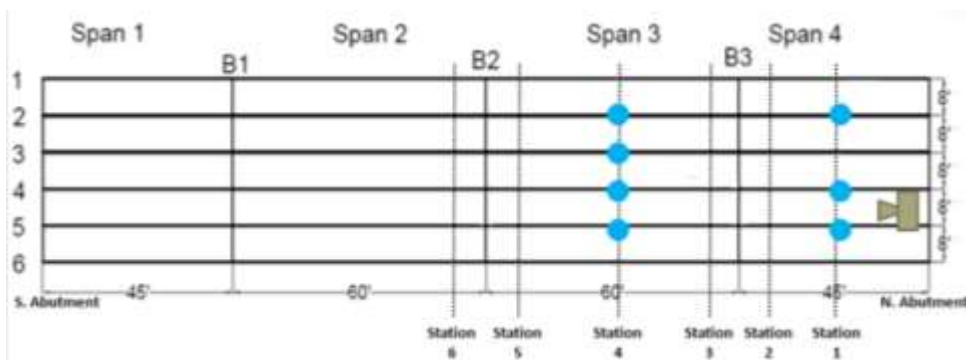
Figure 40: Instrumentation Stations for the Bagdad Road Bridge. DIC locations are denoted with blue circles, and camera location is shown with gray camera.

Using DIC, deflections were measured at midspan of each interior girder at Station 4 and at midspan of three of the four interior girders at Station 1. Deflections were also monitored at

Stations 2, 3, 5, and 6 with DIC; however, the displacements were too small to measure. Only data from Stations 1 and 4 are presented in this research.

4.5 Setup

The equipment involved with deploying the DIC system for this test can be seen in Table 6.

Table 6: DIC equipment used in load test.

Hardware	
Computer	Dell Precision M6400, Intel Core 2 Duo CPU 2.66 GHz, 2GB RAM
Cameras	(2) Point Grey Research Grasshopper 2 Megapixel
Lenses	(2) SIGMA 300mm
Tripod	Manfrotto Carbon Fiber
Cable	6' Belkin 6 to 9 pin firewire cable
Targets	(20) Spray painted steel speckle patterns w/ magnets
Power Supply	Generator, 50 ft 12 GA extension cord
Target Hanger	12 ft modified telescoping pruning stick
Software	
Operating	Microsoft Windows 7
Image Capture	Vic-Snap 2010
Post Processing	Vic-2D 2009

The camera system was set up under the north abutment as level with the bottom flange of the girders as possible. The setup can be seen in Figure 41 and Figure 42. Oyster River High School served as a parking area for load test participants, and a staging area for the truck between runs.

Figure 41: Camera system setup beneath Bagdad Road Bridge for load test.

Figure 42: Targets attached to girders. Note: targets identified by circles; not all targets are shown.

4.6 Data Collection

The load test truck, a 2002 International 4900 dump truck with crew cab, was loaded with sand and weighed 36 kips (160 kN). Weights were determined by Trooper William Burke of the New Hampshire State Police mobile weigh team, see Figure 43. The front axle was 11 kips (49 kN) and the rear axle was 25 kips (111 kN) (Figure 44). The truck drove over the bridge at a crawl speed which corresponded to roughly 150 seconds per truck pass or 1 mph. The camera collected data at 2 Hz and captured an average of 300 frames per truck pass. That is about 1.4 frames per foot (4.6 frames per meter).

Figure 43a: NH State Trooper William Burke weighing the test truck.
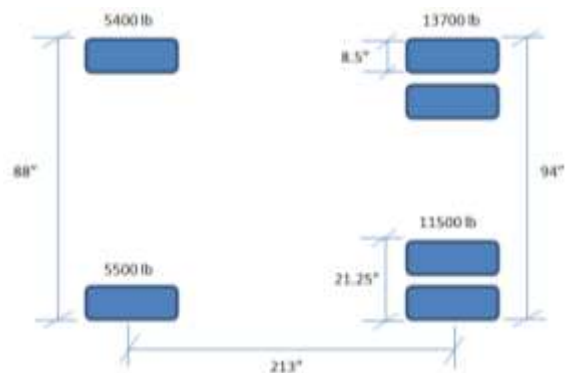
Figure 43b: Truck weights and dimensions.

42

4.7 Load Test Results

The raw data from the displacement results were run through a Butterworth filter in Matlab®. This filter was chosen because it is a low pass filter which allows low frequencies to pass and filters out high frequencies. This allows for removal of ambient vibrations in the bridge (high frequency) and retains the response due to traffic loading (low frequency). The code for this filter can be found in Appendix I.

The results for Station 1 were far less noisy than the results for Station 4. This is attributed to the varying sunlight on the targets at Station 4, as well as the resolution. Though lighting variations were not measured, it was evident from the collected images that the lighting varied significantly on the targets near the fascia of the bridge. It could also be the exaggeration of the camera motions with distance from the camera. Station 4 was further from the camera. If the camera settles an equivalent of 2 pixels then that would correspond to a change in nearly 1 mm at Station 4 (average resolution of 0.48 mm/pixel) and 0.6 mm at Station 1(average resolution of 0.28 mm/pixel).

Each test was run independently of each other. Repeat tests had to be adjusted such that their graphs line up as close as possible. To do this data was removed from the beginning or end of the test when the truck was off the bridge. For example 18 data points were removed from the start of "Test j Camera 0" and 9 data points were removed from "Test k Camera 0" in Figure 44 to produce matching graphs in Figure 45. See Table 7 for list of tests. This was done prior to filtering.
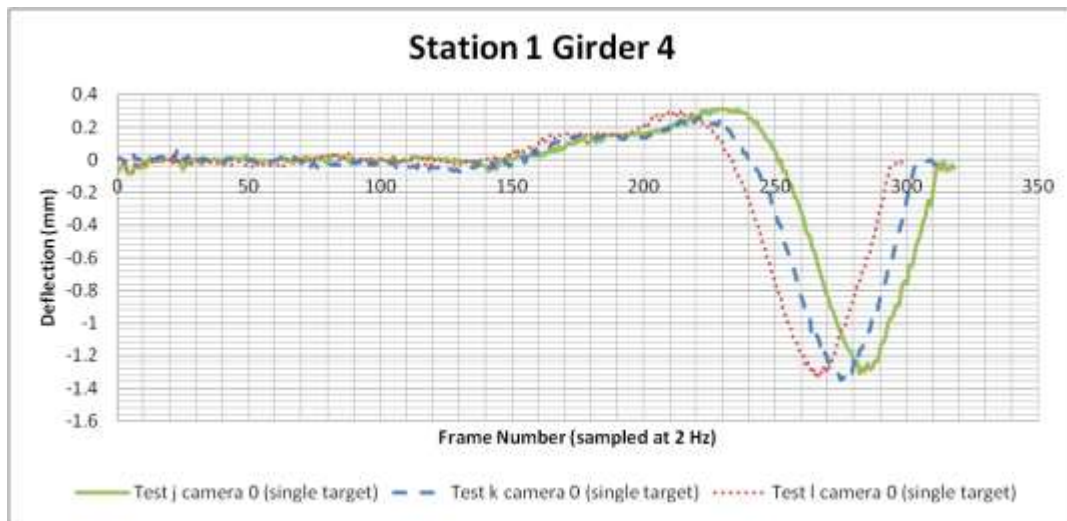
Figure 44: Unprocessed data showing differences in repeat test lengths.
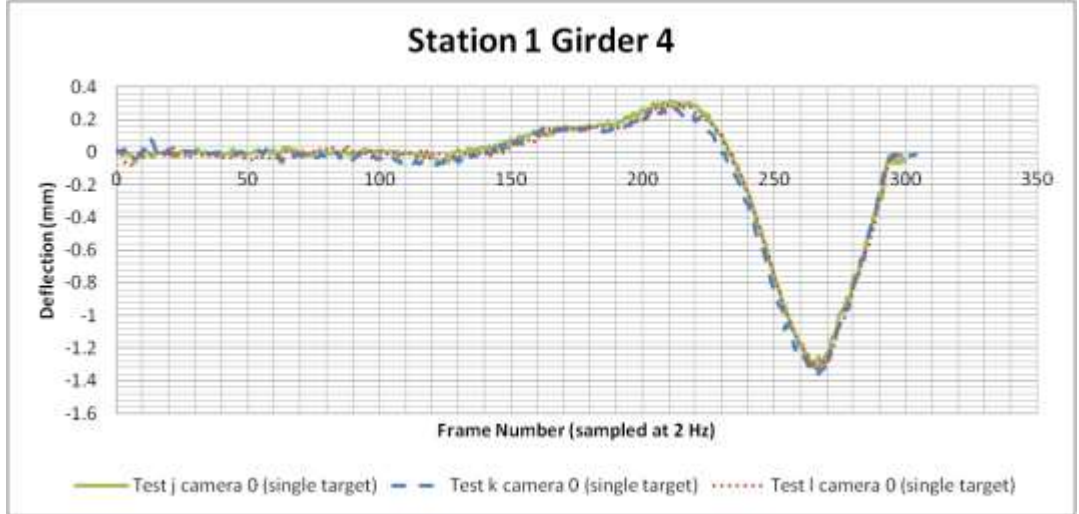
Figure 45: Processed data showing matching test lengths.

The average maximum displacement in at Station 4 was 1.53 mm and 1.14 mm at Station 1. Deflections for each girder and its three runs can be seen in Table **7**. The displacements for Girders 2 and 5 were about the same, which was expected. Girder 2 and Girder 5 are symmetric about the centerline of the bridge. Girder 3 was left out because its deflection was not measured at Station 1 and therefore not comparable to the displacement in Girder 3 at Station 4.

Table 7: Deflections at midspans of Girders 2, 4, and 5.

Truck Path	Station	Girder	Test	Max Measured Deflection (mm)
1	4	5	a	1.57
			b	1.57
			c	1.72
2	4	4	j	1.35
			k	1.49
			l	1.48
4	4	2	v	1.46
			w	1.57
			x	1.60
1	1	5	a	1.12
			b	1.04
			c	1.04
2	1	4	j	1.26
			k	1.33
			l	1.30
4	1	2	v	0.985
			w	1.15
			x	1.06

44

Figure 46 through Figure 50 show the displacements at Station 4. The graphs are essentially influence lines for the load test truck. Girder 5 has the most variability at this station. This is attributed to its proximity to the exterior of the bridge and exposure to variable lighting conditions. Overall, the filter improved the clarity of the data, as shown in Figure 46 and Figure 50. However, even after filtering, Station 4 Girder 5 still produced erratic data when the truck was in the spans preceding and following the span of interest. The average deflection of the filtered data for Station 4 Girder 5 is 1.62 mm.
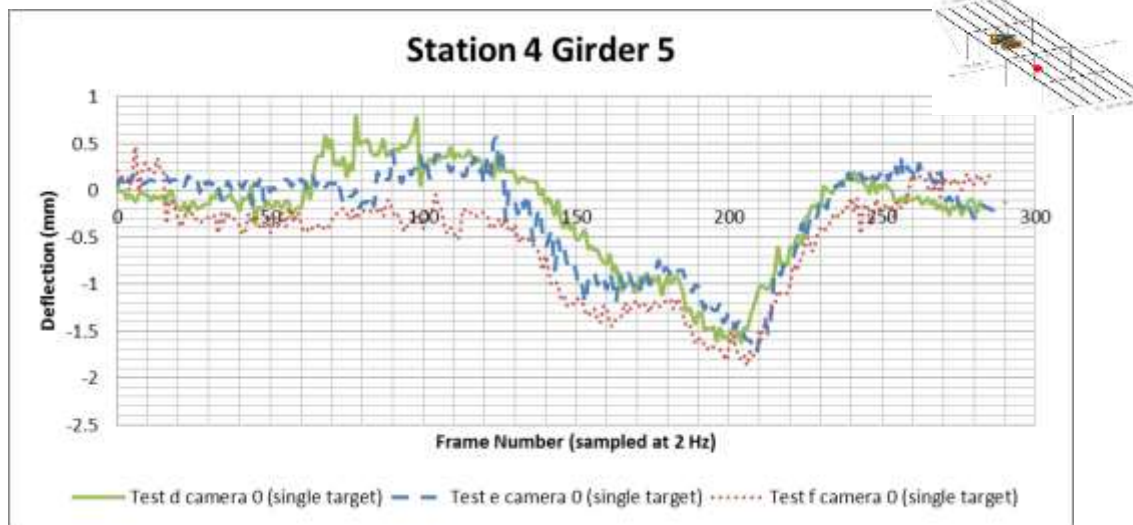
Figure 46: Raw displacements from Bagdad Road load test for Station 4 Girder 5.
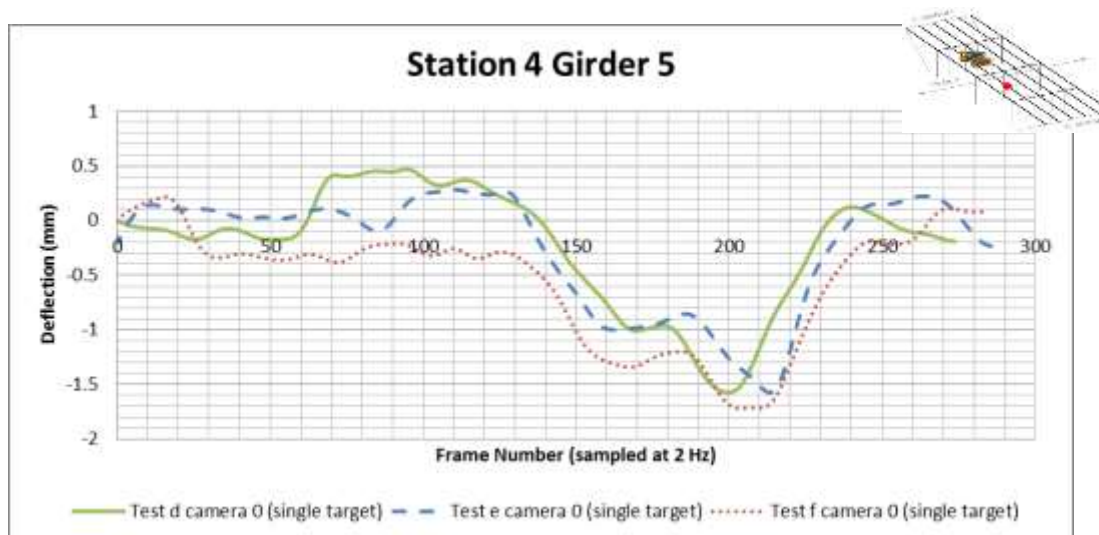
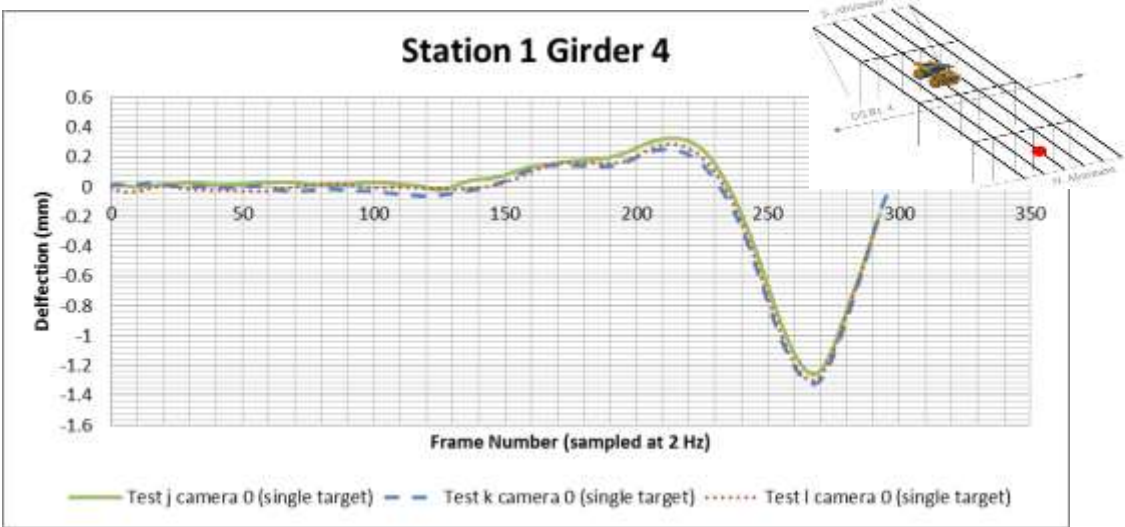
Figure 47: Filtered and shifted displacements from Bagdad Road load test for Station 4 Girder 5.

The average deflection of the filtered data for Station 4 Girder 4 was 1.44 mm. For "Test 0 Camera 1" (see Table 5 for list of tests) there appeared to be an initial drift downward in the data before

the truck entered the bridge. The displacement did not return to zero after the truck left the bridge, suggesting a permanent deformation. This change was most likely due to some environmental influence such as temperature. June 20th 2012 was a typical late spring day with a low of 62 degrees F and a high of 96 degrees F producing a daily swing o 30 degrees F. The deformation may also have been caused by someone bumping into the camera system and tilting the camera upward. Since the focus of this data is on the response of the live load, the initial deformation was removed from the data. The average of 10 data points from just before the truck entered the bridge was subtracted from each data point within the test in order to remove the initial downward drift.
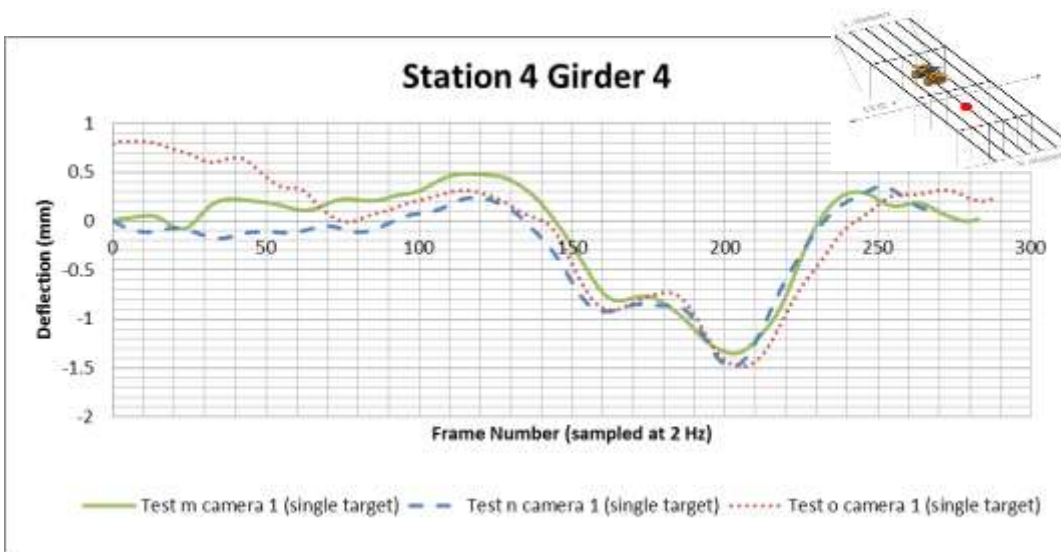
Figure 48: Filtered and shifted displacements from Bagdad Road load test for Station 4 Girder 4.

Girder 2 was the most consistent girder at Station 4. The target on this girder was well protected from variable light exposure. The girder showed definitive evidence of continuous beam action under live load. It clearly experiences uplift when the truck is in adjacent spans. The average deflection of the filtered data for Station 4 Girder 2 was 1.54 mm.
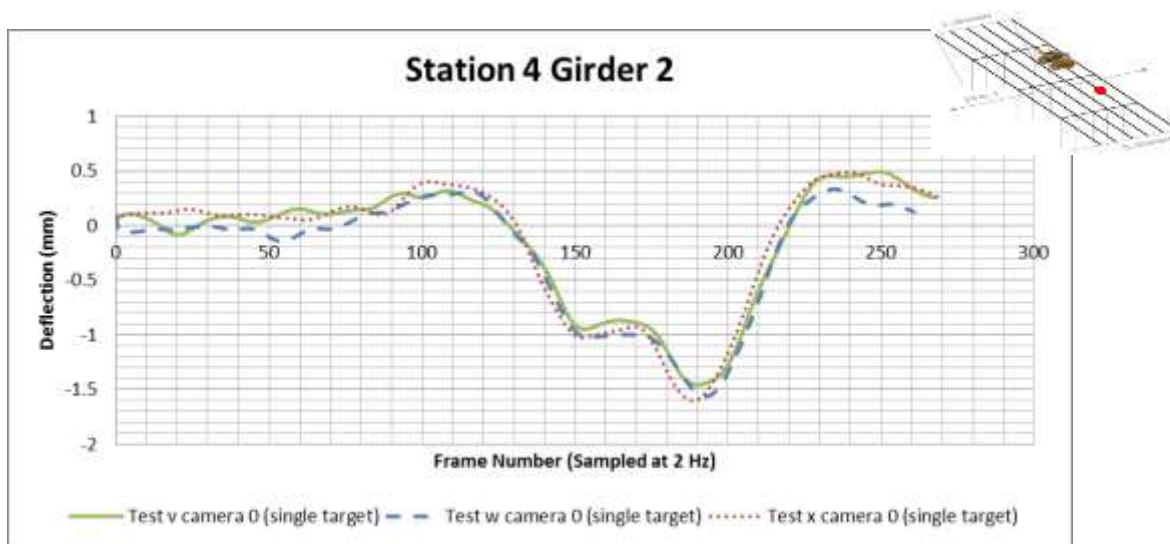
Figure 49: Filtered and shifted displacements from Bagdad Road load test for Station 4 Girder 2.

Figure 50 through Figure 52 show the displacements at Station 1. This station shows significantly less noise than Station 4. This is attributed to its proximity to the camera system. The camera was setup beneath the North Abutment about 20 ft (6.1 m) from Station 1 and about 72 ft (22 m) from Station 4; therefore the resolution was better for Station 1. All three girders in this span experienced uplift when the truck was in the previous span. This confirmed the bridge's continuous action under live load. Again Girder 5 shows the most noise. The average displacement for Station 1 Girder 5 is 1.07 mm.
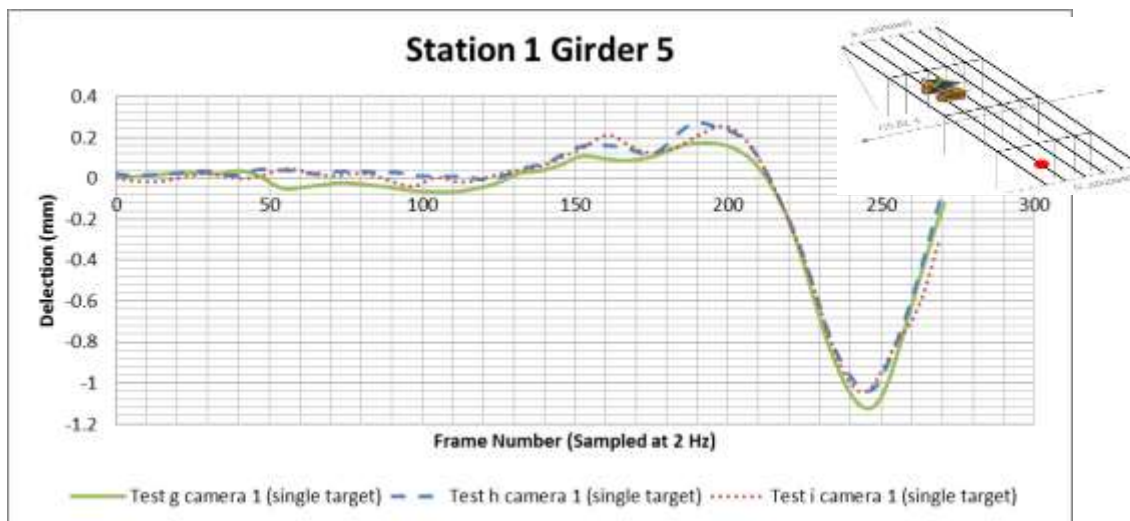
Figure 50: Filtered displacements from Bagdad Road load test for Station 1 Girder 5.

Station 1 Girder 4 was the closest target to the camera system and provided the cleanest data. It is so clear that the slight downward displacement from the truck being two spans away is visible. The average displacement of filtered data for Station 1 Girder 4 was 1.30 mm.

Figure 51: Filtered displacements from Bagdad Road load test for Station 1 Girder 4.

The average deflection of filtered data for Station 1 Girder 2 was 1.07 mm. This exactly equals the average deflection for Station 1 Girder 5. This is encouraging. It shows that despite variables such as truck position and lighting conditions the DIC technique can provide reliable results. The average maximum displacement in Girders 2 and 5 at Station 4 did not match perfectly (1.54 mm in Girder 2 and 1.62 mm in Girder 5). This difference is attributed to the resolution and clarity of the data.
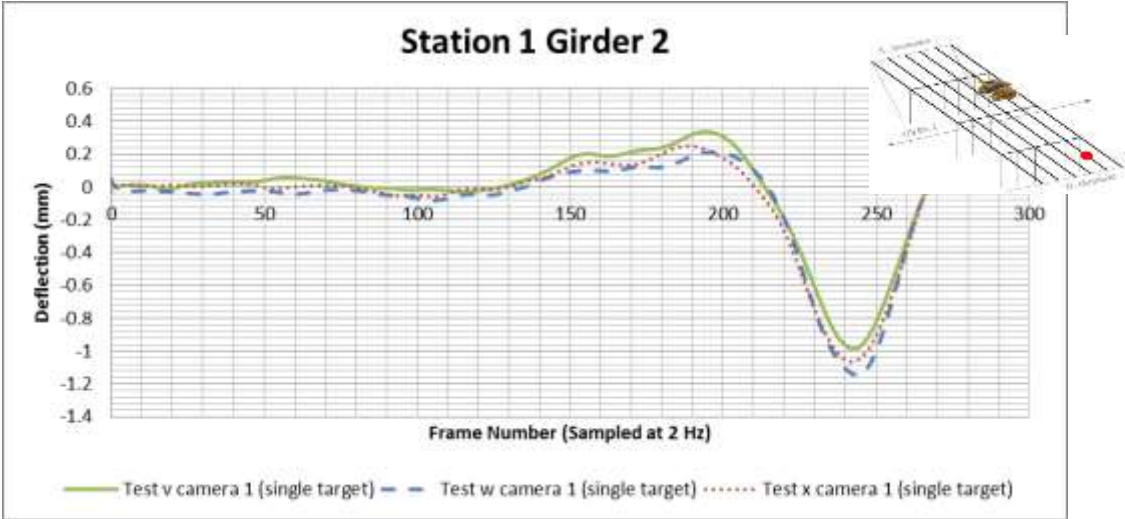
Figure 52: Filtered displacements from Bagdad Road load test for Station 1 Girder 2.

4.8 Evaluation of Multiple Target Field of View

Traditionally, the cameras have only focused on one location at a time to ensure the most accurate results. Another goal of the load test was to assess the number of targets that could be captured in one field of view and still obtain accurate results. This was limited by the distance between the camera and the targets. Three targets were the most that could fit in a frame while keeping the cameras beneath the bridge. The accuracy issue is not so much single target versus multiple targets, rather, the distance between the target and the camera. This distance determines the resolution of the target within the picture frame. The largest issue is that when the camera is far from the target, small vibrations/movements of the camera setup are amplified. This is because at a far distance each pixel represents a larger physical length.

Waterfall et al. (2012) and Zappa et al. (2012) support that the resolution is the key to getting accurate results. The resolution determines the physical size of a pixel in the image, so the smaller the resolution the better the results.

For the maximum displacement, the percent difference between a single target and full field displacement varies from 3-20 percent, with an average of 7.7 percent. Table 8 shows the percent difference for each test using multiple targets. This is only based on three tests and needs to be examined further, but it appears as though full field measuremnts are sufficiently accurate.

Table 8: Percent differences between single target and multiple target fields of view.

| Location	Test	Camera Number	Number of Targets in FOV	Max Displacement
Station4 Girder4	S	1	1	-1.029
	T	0	3	-1.06
	U	0	2	-1.105
% Difference	S and T	1 and 0	1 and 3	3.0
	S and U	1 and 0	1 and 2	7.1
Station4 Girder3	S	0	1	-1.503
	T	0	3	-1.606
	U	0	2	-1.653
	U	1	2	-1.57
% Difference	S and T	0 and 0	1 and 3	6.6
	S and U	0 and 0	1 and 2	9.5
	S and U	0 and 1	1 and 2	4.4
Station4 Girder2	S	1	1	-1.341
	T	0	3	-1.291
	U	1	2	-1.102
% Difference	S and T	1 and 0	1 and 3	3.8
	S and U	1 and 1	1 and 2	19.6
			Average % Difference	**7.7**

All data collected for evaluating multiple target fields of view was from Truck Path 3. The diagrams above the following graphs indicate the path of the truck and the location of the point of interest. The data presented in Figure 53 and Figure 54 are time histories of displacements.
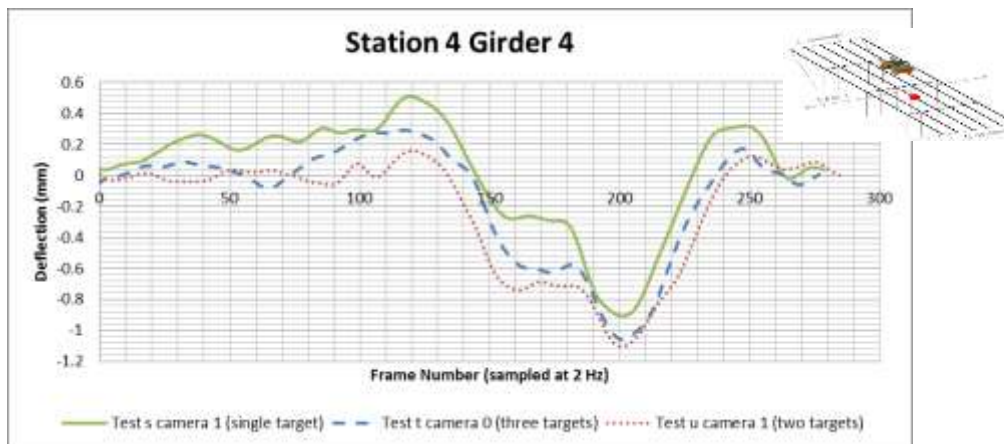
Figure 53: Filtered displacements from Bagdad Road load test for Station 4 Girder 4 using a multiple target field of view.

The three target test appears to have provided a smoother curve than the single or two target test; however this may have been due to over filtering the data. All of the data was filtered using the same parameters for the Butterworth filter. These parameters were determined by removing the noise from the data at Station 1 when the truck was not on the bridge.
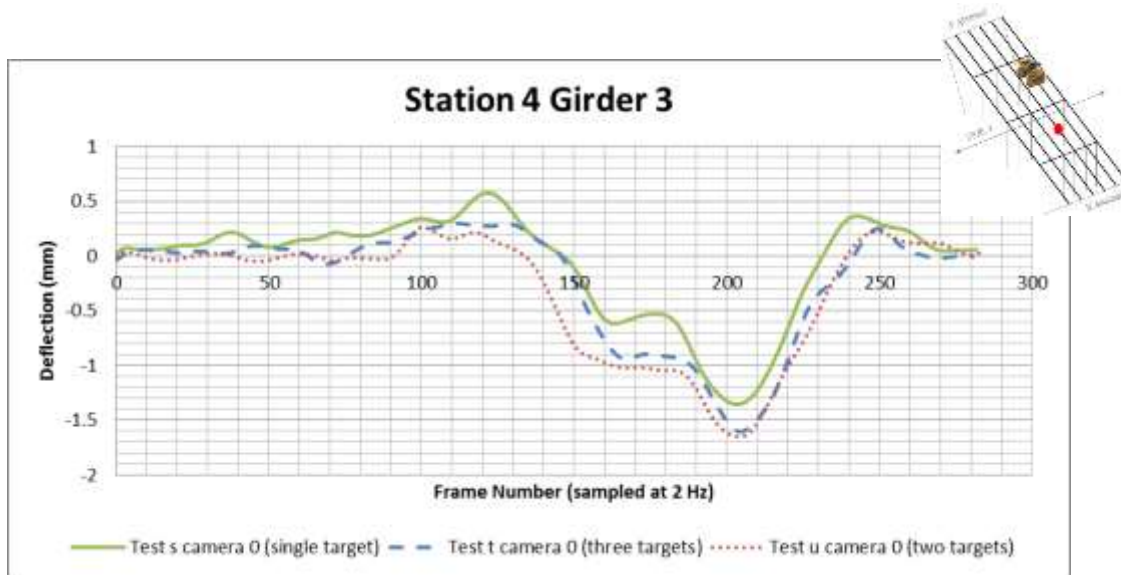
Figure 54: Filtered displacements from Bagdad Road load test for Station 4 Girder 3 using a multiple target field of view.

4.9 Remarks

The results show negative bending when the test truck was in spans adjacent to the span of interest. For instance in at Station 4 (in Span 3)the displacements were upward when the truck was in Span 2 and Span 4, and at Station 1 (in Span 4) the displacements were upward when the truck was in Span 3. This indicates that the bridge acts continuously under live loads (Figure). This is consistent with the way the bridge has been evaluated for load rating. The dead loads are evaluated under simply supported conditions, since the girders and deck were constructed in that manner, and the live loads are evaluated continuously under live load, which this data supports.

For small deflections with low resolution, the noise to signal ratio is high and determining the true deflection is difficult. More research needs to be conducted to investigate resolution and a minimum detectable deflection. The difficulty in calculating a minimum arises because of the sub-pixel resolution of VIC-2D. The software is able to detect movements less than a pixel in size, the question is how much movement? Also, factors such as tripod settlement and slight vibrations on the camera have a larger impact on small displacements.

The data was cleaner when distances between the target and camera were smaller. For 2-D displacements only a single camera is needed. However, it would be difficult to capture all six girders of the case study bridge with a single camera because of the required distance to open up that wide of a field of view. The required distance would lower the resolution and increase the noise in the data. However, if it is the load distribution that is of interest then the noise is a trivial

issue because it will be there every time the bridge is tested. That is assuming that the testing parameters (camera system, targets, distance to target, etc.) remain constant from year to year. With two cameras, each collecting data for three girders, deflections could be captured for all six girders within a cross section of the Bagdad Road Bridge. This would allow DIC to directly determine the load distribution in the bridge. More cameras could be added to a monitoring system as the cost of cameras comes down, and distribution factors could be found at multiple locations along the bridge. This shows that DIC can be used with confidence to collect data for an objective measure of load distribution.

In response to thiese findings, multiply GoPro® camera were deployed at the Bagdad Road Bridge in June 2015 after significant laboratory testing, as detailed in Chapter 7. The results of these tests will be submitted as an addendum to this report, as they were not included in the original scope of this project but are related to the topics covered by this project.

5. Structural Model Creation and Calibration for the Bagdad Road over US Route 4 Bridge

5.1 Model Creation

A structural model was created in CSiBridge® to compare the results. CSiBridge® is a bridge wizard program that operates within SAP2000®. It is a user interface that compiles the components necessary to efficiently create a structural model of a bridge, and all of the components of the wizard can be found within SAP2000®. The two programs are made by Computers and Structures Inc. and are capable of performing the same analyses. The Bridge was modeled using frame elements since displacement was the only parameter of concern. See Figure 55 for an extruded view of the model. This model was named Base FEM.
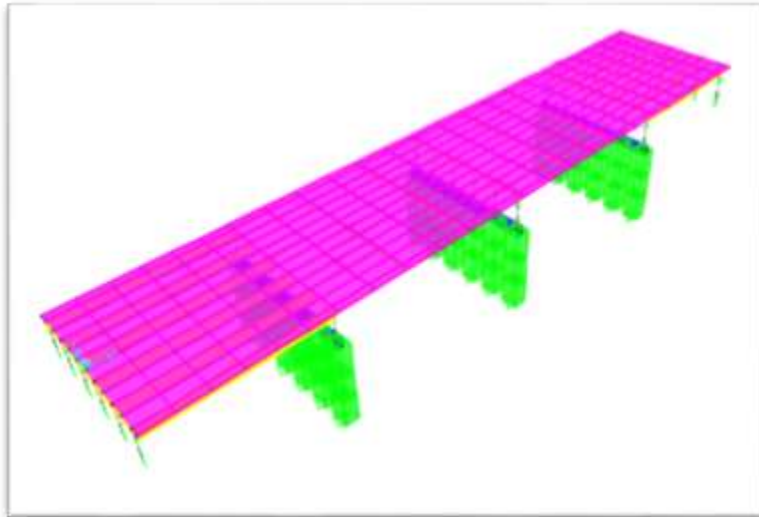
Figure 55: Structural model of Bagdad Road Bridge created in CSiBridge® 15.

5.1.1 Layout Line

The layout line was created with a 2.303 percent grade. Its end station was 2520" (64 m) to account for two 45' (13.7 m) and two 60' (18.3 m) spans. The bearing line was left at the default setting of N90°E.

5.1.2 Materials

Class AA concrete was used in the deck. Class A concrete was used in the bents and abutments. The structural steel was A36 grade steel. The material properties can be found in Table 9.

Table 9: Materials used to create model in CSiBridge®.

| Material	Strength in ksi (Mpa)	Modulus of Elasticity in ksi (GPa)
Steel	36 (250)	29000 (200)
Concrete (AA)	3.5 (24)	3400 (23)
Concrete (A)	3.0 (21)	3200 (22)

5.1.3 Frame Sections

A concrete column section consistent with the structural drawings was created for the bent caps. A C15x33.9 section was added for the diaphragms. These diaphragms were applied to the abutments, bents, at midspan of Spans 1 and 4, and at third points of Spans 2 and 3 (see Figure for span labels). A W36x135 section was added for the beams. This was applied to the deck section used in Spans 1 and 4. A W36x135 section with a 10.5" x 0.5" (26.7 cm x 1.27 cm) cover plate was created using the "built-up Steel: Cover Plated I" option within the section modeler of CSiBridge®. This was incorporated into the deck section used in Spans 2 and 3. The beams were modeled with supports attached to the base of the beams, not the neutral axis.

5.1.4 Deck Sections

A deck section was created using the 3500 psi (24 MPa) concrete. Four interior girders were added. The total width of the section was 536" (1360 cm). The depth of the section was 7.5" (19 cm). A 28" (71 cm) overhang was used to account for the distance from the centerline of the exterior beam to the outer edge of the deck. A thickness of 8.75" (22.2 cm) was used for the deck overhang. The sidewalk was ignored structurally, and since displacements were only measured for live load, the dead load of the sidewalk was ignored as well.

5.1.5 Bearings

Rocker (Expansion) bearings were defined for the bents and the North Abutment. This included fixing the translational restraints (U1, U2, and U3) and releasing the rotational restraints (R1, R2, and R3). The South Abutment bearing was defined as fixed, so all restraints (U1, U2, U3, R1, R2, and R3) were set to fixed (Figure 56).
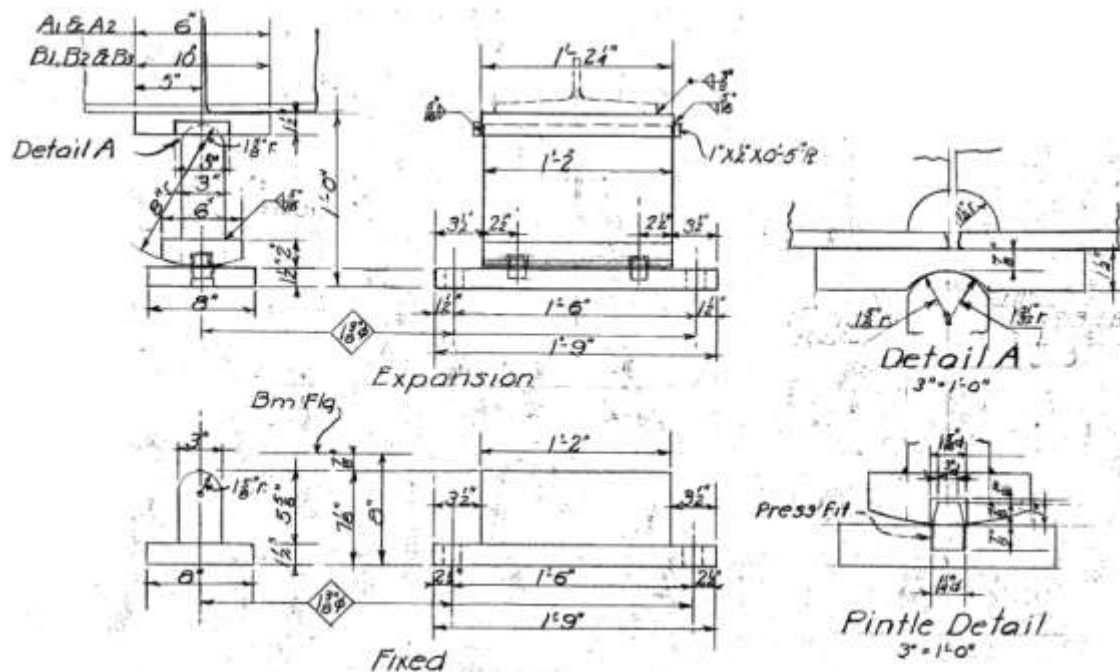
Figure 56:"Expansion" and "Fixed" bearing details

5.1.6 Bents

The bent cap section previously defined was used for the bent caps. The cap length was set to 516" (1310 cm). The bents consisted of 6 columns. A single bearing line was used to be consistent with the continuous nature of the structure. Bents were defined at 540" (1372 cm), 1260" (3200 cm), and 1980" (5029 cm) along the layout line.

5.1.7 Results

Lanes were defined consistent with the actual load test lanes (see Figure 39). The simulated test truck was created with weights and axle spacings consistent with those in Figure 44. The model was run for each lane. The average displacement calculated by the computer model at Station 4 was 1.69 mm, and the average percent difference between the measured and model displacements was 10.4 percent. At Station 1 the average displacement was 0.86 mm, and the average percent difference between the measured and model displacements was 27.3 percent. The model was further refined based on measured camber and more detailed modeling of the girders on the major spans.

5.3 Refinements to Bridge Structural Model

Two models were created that further refine the parameters of the first model. The results from each model were compared to the digital image correlation results from the Bagdad Road Bridge Load Test. The three models are named Base FEM, Refined FEM, and Calibrated FEM. Base FEM is the original structural model created in CSiBridge®. Refined FEM is a refinement of BaseFEM to include the camber in each span and adjust the cover plate in Spans 2 and 3. Base FEM has the cover plate covering the full length of the steel girder in the Spans 2 and 3. In Refined FEM the cover plate was removed from the first and last 12 ft (3.66 m) of the steel girder in those spans. This was done to more accurately reflect the physical structure where the cover plate only

covers the middle 36 ft (11 m) of the two major spans. Figure 58 shows an envelope deflected shape for Refined FEM.
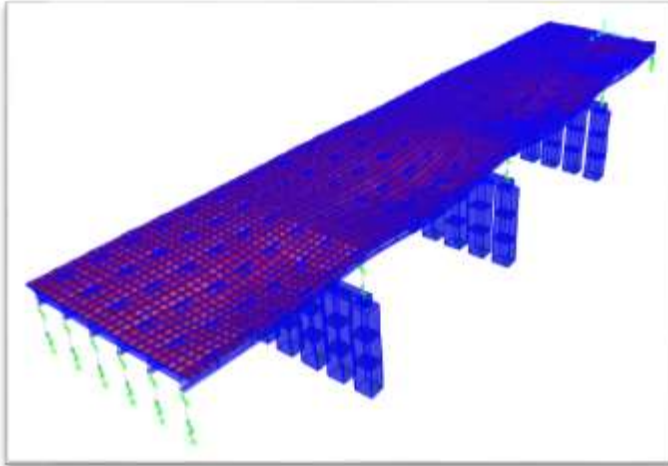
Figure 58: Enveloped deflected shape of Refined FEM structural model.

The results of Refined FEM did not significantly differ from the results of Base FEM. The deflections for Station1 remained roughly the same, and therefore the percent difference between the DIC results and the model for the average maximum displacement was 34 percent for this span. The deflections for Station 4 decreased by about 0.25 mm, and the percent difference between the average of the maximum displacements decreased from 10.4 to 7.7 percent. Calibrated FEM is a further refinement of Refined FEM. See Figure 59   for an extruded view of the Calibrated FEM model.
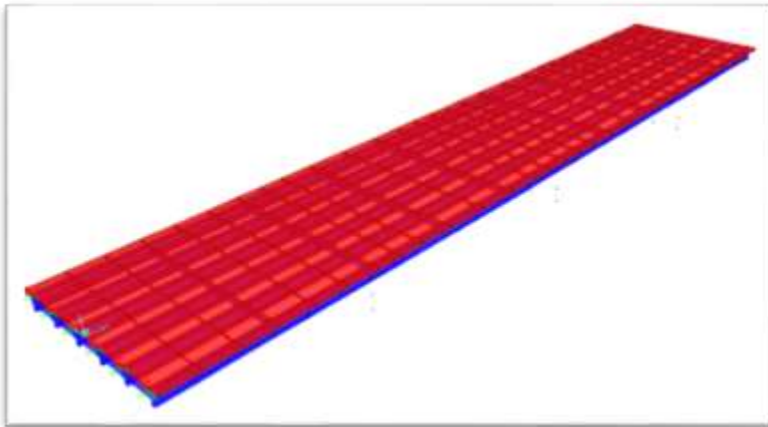
Figure 59: Calibrated FEM. This model includes the camber, cover plate, and rotational spring refinements. Note that the supports were removed to add the foundation springs.

Calibrated FEM was created by removing the foundational supports and replacing them with springs. A summary of the refinements made to each model can be seen in Table 10.

Table 10: FEM models and their respective refinements.

Model	
Base	Representative of bridge plans, with the exception that the cover plate spans the entire length of the 60 ft
Refined	Includes measured camber in girders; removes cover plate from ends of 60 ft spans, leaving cover plate only on the middle 36 ft of the span
Calibrated	Removes foundation supports and replaces with springs; translational fixities kept constant, rotational fixities changed to 4.0 x 10^6 k/in

The idea was to reasonably adjust the rotational fixity of the rocker bearing supports until the displacements resembled the measured displacements. Given that the rocker bearings were mostly tipped at the bents, it is logical that the supports provide more rotational restraint than a roller support. The condition of the rocker bearings has been documented in NHDOT inspection reports since 2006 and is visible in Figure 60.

Figure 60: Fully tipped rocker bearings at North Abutment.

The original model was modeled as fixed at the south abutment and with rollers at all other supports. The refinements in Calibrated FEM are meant to account for the change. The rotational stiffness added to the supports at each bent was 4.0 x 10⁶ k/in (7.0 x 10⁶ kN/cm). This was slightly greater than the rotational stiffness of the W36x135 steel beam (3.4 x 10⁶ k/in or 6.0 kN/cm). Adding this amount of stiffness to the support produced the same results as if the structure were modeled with fixed supports at the bents. The increase in stiffness seems large but is not unrealistic given the severity of the tipped rockers. When a rocker is fully tipped, the support is has difficulty rotating. The results of Calibrated FEM along with the results of Base FEM and Refined FEM can be seen Table 11, Table 12, and Figure 61 through Figure 63. Note that downward displacements are indicated by positive numbers in Figure 61 through Figure 63.

Table 11: Comparison of measured deflections and deflections from the three CSiBridge® models.

| Span	Girder	Measured Deflection (mm)	Base FEM Deflection (mm)	Refined FEM Deflection (mm)	Calibrated FEM Deflection (mm)
60'	Station 4 Girder 5	1.57	1.66	1.41	1.65
		1.57	1.66	1.41	1.65
		1.72	1.66	1.41	1.65
60'	Station 4 Girder 4	1.35	1.67	1.44	1.61
		1.49	1.67	1.44	1.61
		1.48	1.67	1.44	1.61
60'	Station 4 Girder 2	1.46	1.73	1.48	1.57
		1.57	1.73	1.48	1.57
		1.60	1.73	1.48	1.57
45'	Station 1 Girder 5	1.12	0.84	0.84	1.24
		1.04	0.84	0.84	1.24
		1.04	0.84	0.84	1.24
45'	Station 1 Girder 4	1.26	0.86	0.88	1.23
		1.33	0.86	0.88	1.23
		1.30	0.86	0.88	1.23
45'	Station 1 Girder 2	0.985	0.89	0.87	1.18
		1.15	0.89	0.87	1.18
		1.06	0.89	0.87	1.18

**Table 12: Percent differences between CSiBridge® models and the measured results.**

Span	Girder	Percent Difference Base FEM	Percent Difference Refined FEM	Percent Difference Calibrated FEM
60'	Station 4 Girder 5	5.6	10.7	5.0
		5.6	10.7	5.0
		3.6	19.8	4.2
60'	Station 4 Girder 4	21.2	6.5	17.6
		11.4	3.4	7.7
		12.1	2.7	8.4
60'	Station 4 Girder 2	16.9	1.4	7.3
		9.7	5.9	0.0
		7.8	7.8	1.9
	Average:	**10.4**	**7.7**	**6.3**
45'	Station 1 Girder 5	28.6	38.5	10.2
		21.3	38.5	17.5
		21.3	38.5	17.5
45'	Station 1 Girder 4	35.5	35.4	2.4
		40.7	35.4	7.8
		38.5	35.4	5.5
45'	Station 1 Girder 2	12.4	28.0	18.0
		27.7	28.0	2.6
		19.7	28.0	10.7
	Average:	**27.3**	**34.0**	**10.3**
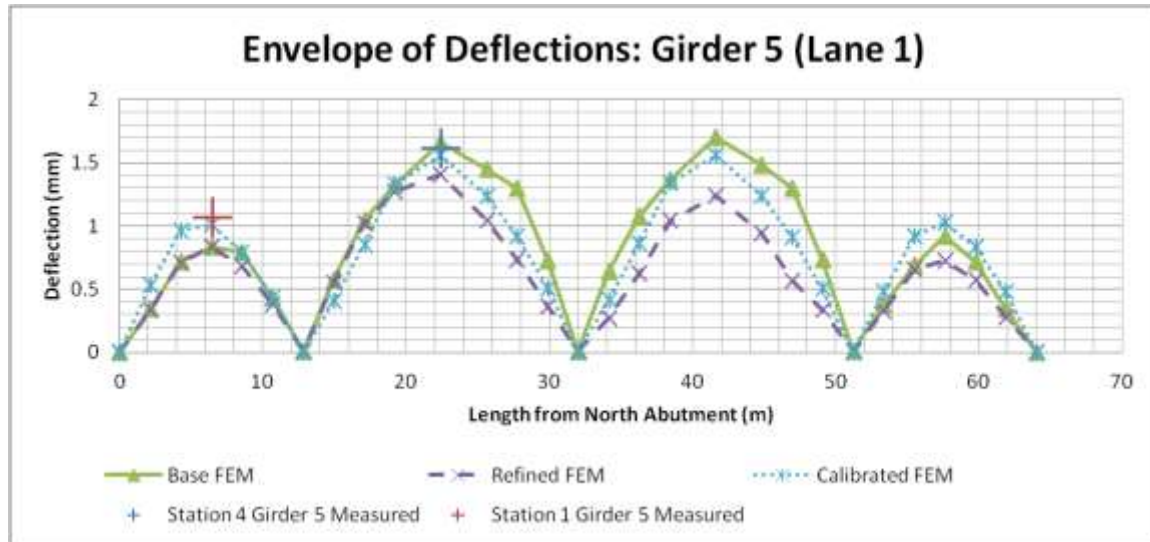
Figure 61: Envelope of deflections from model for Girder 5. Measured points are indicated with crosses. Note, positive value indicates downward displacement.
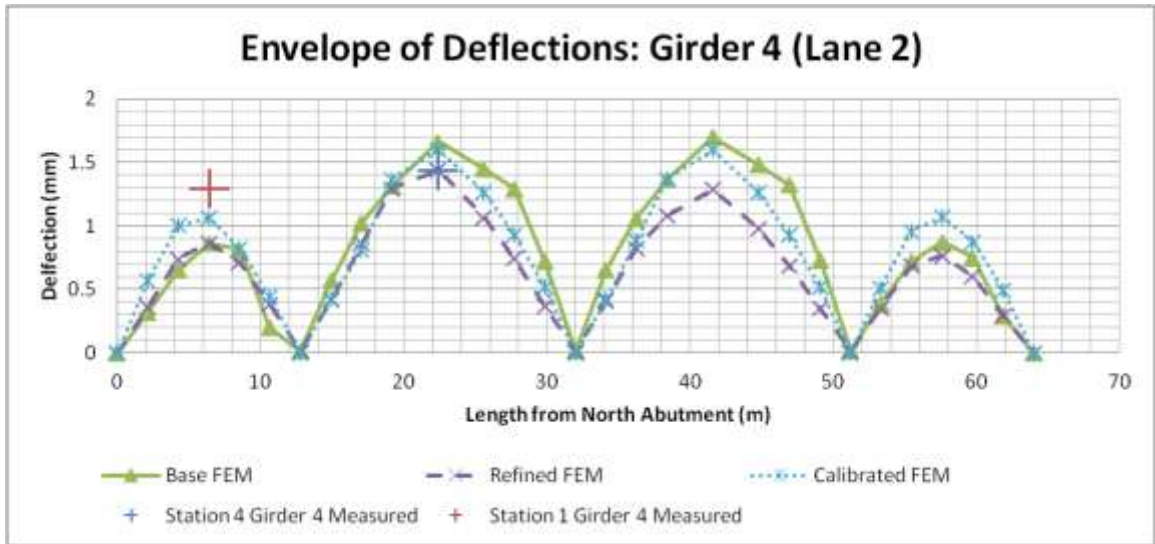
Figure 62: Envelope of deflections from model for Girder 4. Measured points are indicated with crosses. Note, positive value indicates downward displacement.
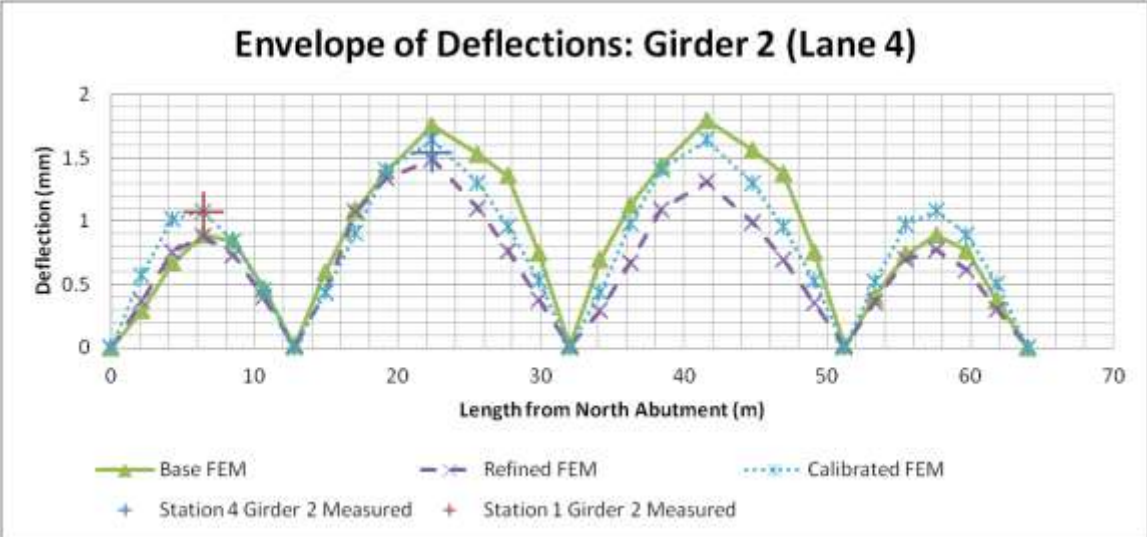
Figure 63: Envelope of deflections from model for Girder 2. Measured points are indicated with crosses. Note, positive value indicates downward displacement.

No one computer model perfectly represents the data collected by DIC. The base model was a good representation of the bridge in accordance with the construction plans. It was close to matching DIC deflections at Station 4 Girder 5, but was far from matching the results at any other location. The Refined FEM was the best match for Station 4 Girder 4 and Station 4 Girder 2, but it did not match the rest of the data well. The Calibrated FEM was the best match for Station 4 Girder 5, Station 1 Girder 4, and Station 1 Girder 2, and was closely matched with results at other locations as well. The goal was to minimize the percent difference between the model and DIC for all collected data points, and move forward with load rating using a single model. The Calibrated FEM fits best to the data set as a whole, so it was used to determine the distribution factors for load rating. Future research should collect more data in order to do a statistical analysis and compare the model data at multiple points with the confidence intervals of the collected data.

60

5.2 Camber Survey

The bridge was surveyed using a Topcon AT-G2 Auto Level in order to determine the residual camber in the girders. The level rod used had an accuracy to the nearest hundredth of an inch. The survey was conducted to provide information for enhancing the structural model with the idea that the models deflections may be more reflective of the measured data.

The auto level was setup on the west side of the bridge for Span 3. To record the location of the instrument, swing ties were measured to the nearest corners of the bent foundations (40.5 ft (12.3 m) to Bent 3 and 30.0 ft (9.15 m) to Bent 2). In addition the height on the instrument was recorded (HI = 62.75" (159 cm)). The auto level was setup beneath the north abutment between Girders 4 and 5 for Span 4. Swing ties were measured to the center of the nearest bolts of the rocker bearings (85.5" (217 cm) to Girder 4 and 71.5" (182 cm) to Girder 5; HI = 26" (66 cm)). In Span 3 measurements were taken at the pier caps, midspan, and the locations of the diaphragms. In Span 4 measurements were taken at the pier cap and at midspan. It was not possible to survey this span at the abutment. The level rod did not fit within the low clearance between the girder and the ground. The total camber in Span 3 was 0.33" (0.838 cm) and in Span 4 was 0.62" (1.57 cm). Spans 1 and 2 could not safely be measured, but, due to the symmetric geometry of the bridge, Span 1 was assumed to have a camber of 0.62" (1.57 cm) and Span 2 was assumed to have a 0.33" (0.838 cm) camber. The model refinements, Refined FEM and Calibrated FEM, account for the residual camber in the girders. The intention was that including the camber in the model would provide deflection results more consistent with the DIC data.

6. Digital Image Correlation for Bridge Load Rating and Assessment.

A bridge load rating determines if a bridge is capable of carrying its design live load. The most common method of rating is Load and Resistance Factor Rating (LRFR) which is consistent with Load and Resistance Factor Design. Other methods include Allowable Stress Rating (ASR) and Load Factor Rating (LFR) (AASHTO, 2011). There are load ratings for each component of the bridge, i.e. deck, girders, and bearings. The bridge's overall load rating is the lowest rating of any component. A member's load rating is calculated by subtracting the dead load from its capacity then dividing by the design live load. If the rating is greater than 1.0, then the bridge is ok. If the rating is less than 1.0, then further assessment is needed

Each bridge should be load rated at the Inventory and Operating levels. An Inventory level assessment takes into account the existing condition of the structure and results in a live load that can safely use the structure indefinitely. If the Inventory rating is greater than 1.0 for the HL-93 load case, then the bridge should be able to handle that loading indefinitely. The Operating level assessment results in the maximum permissible live load the structure may experience. This determines the weight limit, or posting, of the bridge. It is a load that the bridge can see on occasion, but should not experience on a regular basis.

There are three stages of rating. The first is Design load rating. This stage evaluates whether the bridge can support the AASHTO HL-93 Design Load. The second stage is Legal load rating. This is required if the bridge fails the Design load rating at the Operating level. The AASHTO Legal Loads are defined in Figure 64. The third stage is Permit load rating. This checks the safety of a bridge to carry a load greater than the legally established weight limit. It is used in issuing special

permits to trucks. It should only be used on bridges that are capable of carrying AASHTO Legal Loads.

This research focuses on LRFR Design Load rating at the Inventory and Operating levels for the Strength I Limit State, see Table 13 for additional limit states and load factors. It also focuses on ratings for composite beam members. Other elements are not examined in this research. The following equation is used for load rating accordingly, as shown in Equation 11

$$RF = \frac{C - \gamma_{DC}(DC) - \gamma_{DW}(DW) \pm \gamma_p(P)}{\gamma_L(1+IM)(LL)}$$
(Eq:11)

Where:

RF is the rating factor

C is the capacity of the member of interest

DC is the dead load of components on the member of interest

DW is the dead load of wearing surfaces on the member of interest

P is the permanent loads other than dead loads (effects from post-tensioning)

1+ IM is the dynamic load allowance

LL is the live load

γ is the load factor as defined by Table

For the Strength 1 Limit State Inventory level, the equation becomes Equation 12.

$$RF = \frac{C - 1.25(DC) - 1.50(DW) \pm 1.0(P)}{(1.75)(1.33)(LL)}$$
(Eq: 12)

And for the Strength 1 Limit State Operating level, the equation becomes Equations 13.

$$RF = \frac{C - 1.25(DC) - 1.50(DW) \pm 1.0(P)}{(1.35)(1.33)(LL)}$$
(Eq: 13)

APPENDIX D6A—AASHTO LEGAL LOADS

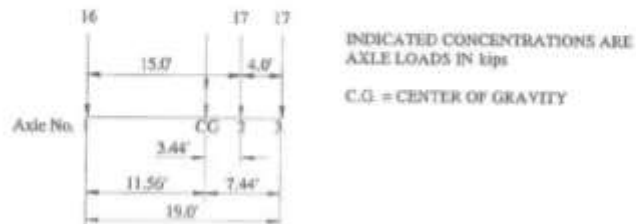a. *AASHTO Trucks*—Apply for all span lengths and load effects.

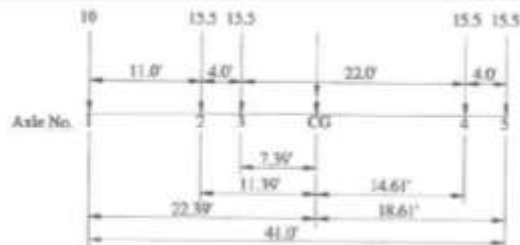Figure D6A-1—Type 3 Unit; Weight = 50 kips (25 tons)

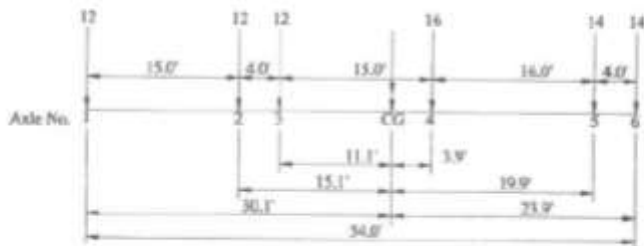Figure D6A-2—Type 3S2 Unit; Weight = 72 kips (36 tons)

Figure D6A-3—Type 3-3 Unit; Weight = 80 kips (40 tons)

Figure 64: AASHTO Legal Loads (source: *The Manual for Bridge Evaluation*, 2nd ed. 2011).

Table 13: Load Factors for Load Rating (source: *The Manual for Bridge Evaluation*, 2nd ed. 2011). γₚ=1.0 (MBE Article 6A.2.2.3)

APPENDIX B6A—LIMIT STATES AND LOAD FACTORS FOR LOAD RATING

Table B6A-1—Limit States and Load Factors for Load Rating (6A.4.2.2-1)

Bridge Type	Limit State*	Dead Load DC	Dead Load DW	Design Load Inventory LL	Design Load Operating LL	Legal Load LL	Permit Load LL
Steel	Strength I	1.25	1.50	1.75	1.35	Tables 6A.4.4.2.3a-1 and 6A.4.4.2.3b-1	—
	Strength II	1.25	1.50	—	—	—	Table 6A.4.5.4.2a-1
	Service II	1.00	1.00	1.30	1.00	1.30	1.00
	Fatigue	0.00	0.00	0.75	—	—	—
Reinforced Concrete	Strength I	1.25	1.50	1.75	1.35	Tables 6A.4.4.2.3a-1 and 6A.4.4.2.3b-1	—
	Strength II	1.25	1.50	—	—	—	Table 6A.4.5.4.2a-1
	Service I	1.00	1.00	—	—	—	1.00
Prestressed Concrete	Strength I	1.25	1.50	1.75	1.35	Tables 6A.4.4.2.3a-1 and 6A.4.4.2.3b-1	—
	Strength II	1.25	1.50	—	—	—	Table 6A.4.5.4.2a-1
	Service III	1.00	1.00	0.80	—	1.00	—
	Service I	1.00	1.00	—	—	—	1.00
Wood	Strength I	1.25	1.50	1.75	1.35	Tables 6A.4.4.2.3a-1 and 6A.4.4.2.3b-1	—
	Strength II	1.25	1.50	—	—	—	Table 6A.4.5.4.2a-1

*   Defined in the *AASHTO LRFD Bridge Design Specifications*.

Shaded cells of the table indicate optional checks.

Service I is used to check the $0.9F_y$ stress limit in reinforcing steel.

Load factor for *DW* at the strength limit state may be taken as 1.25 where thickness has been field measured.

Fatigue limit state is checked using the LRFD fatigue truck (see Article 6A.6.4.1).

6.1 Development of Distribution Factors

Bridges are designed and evaluated by examining typical sections. Girder analysis for a beam-slab bridge involves looking at a typical composite section of deck and beam and evaluating the loads on it. In order to perform the load rating, distribution factors for dead and live load are needed to determine the percentages of load that go to a bridge member. For girders, the dead load distribution factor is calculated as 1 divided by the number of girders. The live load distribution is determined from tables in the AASHTO Bridge Code. Early versions of the code, the Standard Specifications for Highway Bridges used simple S-over equations for calculating live load distribution to bridge beams. For example, in Table 3.23.1 of the 1992 AASHTO Standard Specifications the live load distribution factor for moment on a steel stringer with a concrete deck 6" or thicker and two or more traffic lanes is calculated as S/4.5, where S is the beam spacing. If S exceeds 7' then the load on each stinger is taken to be the reactions due to the wheel loads if the deck were simply supported by the stringers. In 1994 new equations for calculating distribution factors were introduced with the adoption of the LRFD Specifications. The LRFD equation for the moment distribution factor for a steel beam with a concrete deck and two or more lanes loaded

64

is shown in Equation 14, where S is the beam spacing, L is the span length, K_g is the longitudinal stiffness parameter, and t_s is the slab thickness. The LRFD equations are intended to account for various parameters, not just the beam spacing, that affect load distribution, and provide more accurate distribution factors.

$$0.075 + \left(\frac{S}{9.5}\right)^{0.6} \left(\frac{S}{L}\right)^{0.2} \left(\frac{K_g}{12.0 L t_s^3}\right)^{0.1} \qquad (Eq:14)$$

Table 14 shows an example of a table from Section 4.6.2.2 of the AASHTO LRFD Bridge Design Specifications. It shows the complexity involved with calculating the distribution factors. The values obtained from this table have been questioned by engineers (Cai 2005); (Eamon and Nowak 2002); (Yousif and Hindi 2007) who have called for taking into account more parameters such as diaphragms and sidewalks. DIC offers a way to calibrate a model and more accurately determine the live load distribution of an in-service bridge without adding to the complexity of the LRFD equations. Ideally DIC would be used to directly determine the load distribution; however, with the camera system available, this was not possible in this research. DIC data from GoPro® cameras was collected at the Bagdad Road Bridge in June 2015 to demonstrate the direct distribution measurement. The results will be submitted as an addendum to this report.

Table 14: Sample table of AASHTO live load distribution factors to show complexity of calculation (source: _LRFD Bridge Design Specifications_, 6th ed. 2012). The equations applicable to this research are boxed in red.

Table 4.6.2.2.2b-1—Distribution of Live Loads for Moment in Interior Beams

Type of Superstructure	Applicable Cross-Section from Table 4.6.2.2.1-1	Distribution Factors	Range of Applicability
Wood Deck on Wood or Steel Beams	a, l	See Table 4.6.2.2a-1	
Concrete Deck on Wood Beams	l	One Design Lane Loaded: $S/12.0$ Two or More Design Lanes Loaded: $S/10.0$	$S \le 6.0$
Concrete Deck, Filled Grid, Partially Filled Grid, or Unfilled Grid Deck Composite with Reinforced Concrete Slab on Steel or Concrete Beams; Concrete T-Beams, T- and Double T-Sections	a, e, k and also i, j if sufficiently connected to act as a unit	One Design Lane Loaded: $$0.06+\left(\frac{S}{14}\right)^{0.4}\left(\frac{S}{L}\right)^{0.3}\left(\frac{K_g}{12.0Lt_s^3}\right)^{0.1}$$ Two or More Design Lanes Loaded: $$0.075+\left(\frac{S}{9.5}\right)^{0.6}\left(\frac{S}{L}\right)^{0.2}\left(\frac{K_g}{12.0Lt_s^3}\right)^{0.1}$$	$3.5 \le S \le 16.0$ $4.5 \le t_s \le 12.0$ $20 \le L \le 240$ $N_b \ge 4$ $10{,}000 \le K_g \le 7{,}000{,}000$
		use lesser of the values obtained from the equation above with $N_b = 3$ or the lever rule	$N_b = 3$
Cast-in-Place Concrete Multicell Box	d	One Design Lane Loaded: $$\left(1.75+\frac{S}{3.6}\right)\left(\frac{1}{L}\right)^{0.35}\left(\frac{1}{N_c}\right)^{0.45}$$ Two or More Design Lanes Loaded: $$\left(\frac{13}{N_c}\right)^{0.3}\left(\frac{S}{5.8}\right)\left(\frac{1}{L}\right)^{0.25}$$	$7.0 \le S \le 13.0$ $60 \le L \le 240$ $N_c \ge 3$ If $N_c > 8$ use $N_c = 8$
Concrete Deck on Concrete Spread Box Beams	b, c	One Design Lane Loaded: $$\left(\frac{S}{3.0}\right)^{0.35}\left(\frac{Sd}{12.0L^2}\right)^{0.25}$$ Two or More Design Lanes Loaded: $$\left(\frac{S}{6.3}\right)^{0.6}\left(\frac{Sd}{12.0L^2}\right)^{0.125}$$	$6.0 \le S \le 18.0$ $20 \le L \le 140$ $18 \le d \le 65$ $N_b \ge 3$
		Use Lever Rule	$S > 18.0$
Concrete Beams used in Multibeam Decks	f	One Design Lane Loaded: $$k\left(\frac{b}{33.3L}\right)^{0.5}\left(\frac{I}{J}\right)^{0.25}$$ where: $k = 2.5(N_b)^{-0.2} \ge 1.5$	$35 \le b \le 60$ $20 \le L \le 120$ $5 \le N_b \le 20$
	g if sufficiently connected to act as a unit	Two or More Design Lanes Loaded: $$k\left(\frac{b}{305}\right)^{0.6}\left(\frac{b}{12.0L}\right)^{0.2}\left(\frac{I}{J}\right)^{0.06}$$	

6.2 Examination of LRFD Distribution Factors

(Mabsout, et al. 1997) found that sidewalks and railings could be taken into consideration to increase the strength of weak bridges. For instance, if sidewalks and parapets are properly reinforced to act integrally, then they will increase the load carrying capacity of interior girders by 5-30 percent (Mabsout, et al. 1997). It is important that the sidewalk be cast integrally with the deck for it to be considered in the strength of the bridge. Non-integral sidewalks may contribute

66

stiffness to the exterior girder at lower loads, due to composite action from friction. However, at higher loads the friction force may be overcome and composite action lost (NCHRP 2009).

In addition, Professors Christopher Eamon of Mississippi State University and Andrzej Nowak of the University of Michigan conducted research evaluating the effects of secondary elements (diaphragms, sidewalks, and barriers) on distribution of load. They found that the number of diaphragms does not significantly reduce the maximum moment a girder experiences. Diaphragms make their largest impact when the girder spacings are large and the spans are long (Eamon & Nowak, 2002). According to the results of the study, diaphragms reduce the maximum girder moment by an average of 4 percent, barriers an average of 10 percent, and sidewalks an average of 20 percent. This study found that, in regard to diaphragms, it is the ratio of interior girder stiffness to diaphragm stiffness that contributes to a reduction in the distribution factor. This is particularly the case when the ratio is less than 100. The relationships between secondary elements and increased stiffness are not linear, and there is a limit to the increase in stiffness.

C.S. Cai of Louisiana State University has proposed a new equation that not only includes the effects of diaphragms on load distribution factors but also simplifies the existing code. The new equation, shown below, is expressed such that only one equation is needed for moment or shear for either one lane or two lanes loaded. This would simplify the current tables and reduce them to a single table (Cai, 2005), see Equation 15.

$$LDF = C_1 + \frac{S}{C_2} + C_3 \left(\frac{S}{L}\right)^{0.75} \left(\frac{K_g}{12Lt_s^3}\right)^{0.25} \qquad \text{(Eq: 15)}$$

And if $R = \left(\frac{S}{L}\right)^{0.75} \left(\frac{K_g}{12Lt_s^3}\right)^{0.25}$ then equation reduces to Equation 16.

$$LDF = C_1 + \frac{S}{C_2} + C_3R \qquad \text{(Eq: 16)}$$

Where C1, C2, and C3 are constants based on scenario (moment, shear, etc).

To account for the added effects of the diaphragms to the load distribution, Cai proposes using a diaphragm modification factor, R_D, as shown in Equations 17 and 18.

$$R_D = 1 - C_{T1} \frac{R_{sk}}{R} \left(\frac{I_T}{I_T + 12Lt^3}\right)^{C_{T2}} \qquad \text{(Eq: 17)}$$

Where:

$$I_T = I_{Diaph} + A_{Diaph}e_{offset}^2 \qquad \text{(Eq: 18)}$$

$$C_{T1} = 0.03 \qquad C_{T2} = 0.6$$

$$R_{sk} = per\ AASHTO\ LRFD\ Code$$

R_D would be used to calculate the LDF instead of R. This could help avoid low ratings and subsequent postings, by taking into account the full effect of secondary elements on load distribution. It could also avoid unnecessary rehabilitation or replacement.

Researchers Zaher Yousif and Riyadh Hindi, similar to Cai, investigated the correlation between the distribution factors from the LRFD code and those from a finite element model. Their study looked at Beam slab bridges with AASHTO PCI girders. Using SAP2000®, they created finite element models to analyze the moment distribution factor. The study found that in comparison

to the finite element analysis the AASHTO LRFD Specification overestimated live load distribution in most cases (Yousif & Hindi, 2007). There were some cases where the AASHTO LRFD Specification underestimated the live load distribution. The discrepancies occurred at the limits of the applicable parameters (span length, etc.). The addition of camera data to calibrate a computer model could increase the accuracy of the distribution factors obtained from a model. Though the computer model in this research was calibrated using deflection, the distribution factors from the computer model were calculated using girder moments. The idea was to separate out any shear effects that may contribute to the deflection, since the distribution factors for shear and moment are calculated differently.

6.3 Distribution Factors for Bagdad Road Bridge

Distribution factors were not calculated directly from DIC data, since data was not collected for the exterior girders during the load test. It was assumed that exterior girders would not deflect significantly enough for the imaging software to detect. Therefore the distribution factors were calculated using the deflections from Calibrated FEM. The distribution factors can be found in Table 15. For an interior girder two lanes loaded controlled the distribution factor. The average experimental moment distribution factor for an interior girder was calculated to be 0.408. The value calculated from the AASHTO LRFD Specifications Section 4.6.2.2 was 0.671. For an exterior girder one lane loaded controlled the distribution factor. The average experimental distribution factor for an exterior girder was calculated to be 0.290. The value from the AASHTO code was 0.222.

Table 15: Moment distribution factors from AASHTO LRFD Specifications and Calibrated FEM.

	Distribution Factors			
	Exterior Girder (One Lane Loaded)		Interior Girder (Two Lanes Loaded)	
	Positive Moment	Negative Moment	Positive Moment	Negative Moment
mg (AASHTO)	0.222	0.222	0.671	0.671
mg (FEM)	0.316	0.263	0.411	0.405

This is consistent with previous findings for interior girders (Peddle, 2011). The measured distribution factors are lower than code based distribution factors for steel girder bridges. More research is needed in this area to evaluate the accuracy of the AASHTO LRFD code.

6.4 Load Ratings

The Bagdad Road Bridge over US Route 4 was load rated for moment using the LRFR method. The bridge was load rated twice using two different sets of distribution factors. The first set was calculated using the AASHTO LRFD Bridge Specifications, and the second set was calculated based on girder moments from Calibrated FEM. The load ratings can be found in Table 16 highlighted in yellow.

**Table 16: Bagdad Road Bridge over US Route 4 load ratings for moment. Load ratings are highlighted in yellow.**

		Exterior Girder				Interior Girder			
		Positive Moment		Negative Moment		Positive Moment		Negative Moment	
		Inventory	Operating	Inventory	Operating	Inventory	Operating	Inventory	Operating
Capacity		3848.6	3848.6	2241.2	2241.2	4018.6	4018.6	2241.2	2241.2
γ_{DC}DC (AASHTO)		264.4	264.4	492.8	492.8	264.4	264.4	492.8	492.8
γ_{DW}DW (AASHTO)		29.2	29.2	56.3	56.3	29.2	29.2	56.3	56.3
γ_L(1 + IM)(LL) (AASHTO)	Units are in ft-kips	319.4	246.3	228.8	176.6	966.5	745.6	692.5	534.2
γ_{DC}DC (FEM)		264.4	264.4	492.8	492.8	264.4	264.4	492.8	492.8
γ_{DW}DW (FEM)		29.2	29.2	56.3	56.3	29.2	29.2	56.3	56.3
γ_L(1 + IM)(LL) (FEM)		455.4	351.3	271.5	209.5	592.3	456	418.3	322.6
LRFR (AASHTO)		11.13	14.43	7.40	9.58	3.85	5.00	2.44	3.17
LRFR (FEM)		7.81	10.12	6.23	8.08	6.29	8.17	4.05	5.25
mg (AASHTO)		0.222	0.222	0.222	0.222	0.671	0.671	0.671	0.671
mg (FEM)		0.316	0.316	0.263	0.263	0.411	0.411	0.405	0.405

The results for load ratings show that AASHTO is conservative for interior distribution factors. In the case of the Bagdad Road Bridge, it is the interior negative moment that controls the rating. Calculations for the load ratings are in Appendix J. For Bagdad Road, AASHTO appears to be conservative which may result in an unnecessary load posting in the future. The conservatism may come from not taking diaphragms and sidewalks into account for the load distribution. Diaphragms distribute load more evenly between girders, and sidewalks increase the stiffness of exterior cross-sections and therefore may attract more load. This research into distribution factors is not in-depth, and a more rigorous review of AASHTO's distribution factors should be conducted. This is an excellent opportunity to use digital image correlation to help bridge owners determine the true load distribution in a bridge system.

6.5 Digital Image Correlation for Bridge Condition Assessment

An evaluation of load distribution can be applied to the load rating process. If DIC data was already collected during an inspection prior to load rating, then distribution factors from the data can be used at the Design Load Rating level. If data was collected during the most recent inspection, then a special load test could be performed to determine the distribution factors. A special load test would only be justified if the bridge has a load rating of less than one at the Legal Load Rating level. It would be part of the higher level of evaluation as prescribed by AASHTO's Manual for Bridge Evaluation, see Figure 65.

APPENDIX A6A—LOAD AND RESISTANCE FACTOR RATING FLOW CHART
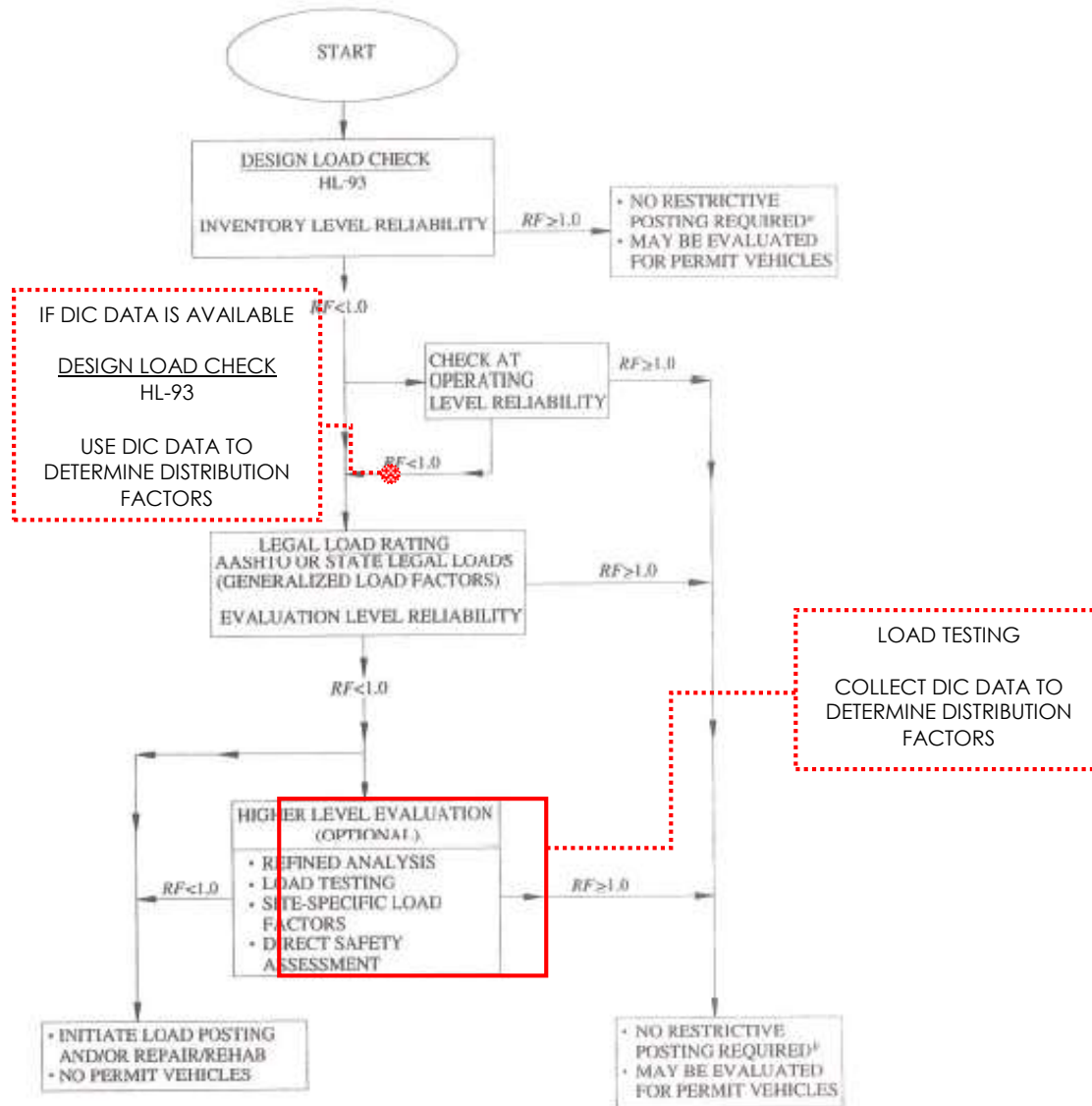
Figure 65: Flow Diagram of Load Rating Process. Proposed use of DIC in dashed lines. (credit: *Manual for Bridge Evaluation*, 2nd ed. 2011)

DIC can be used to determine load distribution, which will aid in assessing bridge safety. This chapter addresses where DIC fits into the inspection and load rating process. Some inspections will be natural candidates for DIC, while others have little use for the technology. There are seven types of inspection: Initial, Routine, In-Depth, Damage, Fracture-Critical, Underwater, and Special.

6.5.1 Initial Inspection

An Initial Inspection is the first inspection an owner has done on a bridge. This may be the first inspection after a bridge is constructed or following a change in configuration. It may also be done on change of ownership. DIC could be a part of this inspection in order to get a baseline of the bridge's behavior and determine its load distribution.

6.5.2 Routine Inspection

A Routine Inspection is a regularly scheduled inspection that looks for changes from the previous inspection. It is carried out every two years and involves making observations from the bridge deck and ground level. While staging and man lifts may be used to gain closer access to the bridge, observations are made at a distance further from the bridge and in less detail than In-Depth Inspections. See Figure 66 for an example of the level of detail involved in a routine inspection. DIC use during Routine Inspection has potential, and is recommended if an under-bridge inspection vehicle is used.

Figure 66: PennDOT inspector assesses an abutment using binoculars during a Routine Inspection (Scranton Times Tribune).

6.5.3 In-Depth Inspection

Areas of concern discovered in a Routine Inspection that require a more close-up, hands-on inspection are often subject to an In-Depth Inspection. This type of inspection almost always requires special equipment, such as an under-bridge inspection vehicle, to allow access to the member(s) of concern. Figure 67 shows an In-Depth Inspection performed with an under-bridge inspection vehicle.

Figure 67: Inspectors use an under-bridge inspection vehicle during an In-Depth Inspection (STRUCTUREmag.org).

A load rating is typically performed to assess the load carrying capacity of the member(s). Nondestructive field tests, such as a load test, may be performed to better assess load carrying capacity. In summary, a Routine Inspection is intended to be broad and is aimed at identifying possible trouble areas, while an In-Depth Inspection is designed to investigate those trouble areas identified by Routine Inspection. An In-Depth Inspection could make excellent use of DIC. An under-bridge inspection vehicle is large enough induce deflections that DIC can measure. In addition, having a truck of known weight produces verifiable deflections. Inspectors could place targets as they inspect the bridge. Traffic could be temporarily stopped and the truck could be driven over the bridge several times once the inspection is finished. Ambient data may also be collected as a baseline to remove noise from vehicle passes.

6.5.4 Special Inspection

A Special Inspection is an inspection scheduled at the bridge owner's discretion. It is designed to assess a known trouble area, such as foundation settlement. It is different than an In-Depth Inspection because it focuses on a single issue. For this type of inspection more detail or information, such as accelerations, may be needed. It is likely that more tools will be required than simply DIC in this instance.

6.5.5 Other Types of Inspection

A Damage Inspection is conducted to assess a bridge's structural state after an environmental or human incident, such as flooding or vehicular impact. DIC is not likely a tool for such an inspection, as it requires a significant load on the bridge. If damage is significant, the bridge will likely be closed to traffic until deemed safe. It would not be safe to apply a large load to determine a change in load distribution.

A Fracture Critical Inspection is an inspection specifically designed to evaluate fracture critical members (FCM). It involves a very detailed hands-on inspection of certain members. It is essentially an In-Depth Inspection of FCMs. Nondestructive test measures, such as dye penetrant, are often used for discovering cracks. DIC for deflection is an optimal tool for this type

of inspection. There is ingoing research at UNH in the use of DIC for strain measurement, as presented in Chapter 7. This strain measurement DIC application may be suited to fracture critical inspection.

An Underwater Inspection is designed to evaluate the substructure for deterioration and scour. If water is shallow the inspection may be performed from the surface using waders, but if the water is deep then an inspector with diving experience is required. Underwater Inspections have no use for DIC.

7. Digital Image Correlation for Structural Strain Measurement

The goal of this chapter is to present, describe, and explain the experimental apparatuses and procedures used to test the accuracy and effectiveness of GoPro® cameras as DIC sensors for strain measurement. This involves selecting and presenting the cameras and auxiliary equipment necessary for creating an experimental DIC strain sensor, describing settings used in testing the DIC sensors for strain measurements, describing the experimental lab test apparatus that the sensors were tested on, and describing both the testing and post-processing methods and procedures used in collecting and analyzing the DIC strain data.

7.1 Experimental DIC Sensors

GoPro® cameras were chosen for use in this study because they meet the requirements of being durable, waterproof, compact in size, having long battery life, and are capable of storing mass amounts of data (depending on the size of the storage card used). Other considerations were that GoPro® has a large support base, both in customer service and the community of users. There is a seemingly endless variety of accessories, attachments and mounting options available for purchase, making modifying an experimental setup as simple as shopping online for a new piece or attachment. Lastly, and maybe most importantly, they have excellent mobile and communication abilities. Through the use of their built in wireless network, the cameras are capable of being remotely controlled either individually using the GoPro® mobile phone app and a smart phone, or many cameras can be synchronized and controlled at once with one master wireless remote. The ability for each individual GoPro® to perform both as a sensor and its own data acquisition system while still being controlled as a unit of a synchronized sensor array make it far cheaper and easier to deploy than any of the alternative options. Due to their performance capabilities, mounting options, interconnectivity, and reasonably low price, GoPro® cameras were selected as the camera to be used in the experimental DIC strain sensor.

When purchasing a GoPro® camera, the package includes the camera, a protective case, battery, charger, wireless remote, and a few adhesive mounts. The adhesive mounts were not considered suitable for the purposes of this test, so the only additional items necessary to complete the sensor were the mounting mechanism and an SD card for data storage. The GoPro® Clamp and Gooseneck attachments were used as the mounting mechanism for this testing. The clamp is able to firmly secure onto objects ranging from 0.25"-2.5" thick, thanks to its rubber-padded feet and high spring rate clamp mechanism. This made it ideal for attachment to any structural member with a flange. The Gooseneck attachment connects the GoPro® camera to the clamp, and allows the camera to be adjusted in full range of motion, while holding the camera still once its position has been set. This allowed the camera to be set at varying heights above the target surface. Figure 68 below shows the collection of parts needed for assembling the typical 2D GoPro® DIC sensor.

The pieces used include: a GoPro® Hero 3+ Black Edition camera with protective case and battery pack, a GoPro® Clamp, a GoPro® Gooseneck, and a 32GB SanDisk® Ultra micro SDHC card. Larger capacity SD cards could be used in 2D testing, but it was found that 64GB cards were not compatible for use in the Dual Hero System (used in the 3D sensor introduced below). The GoPro® Clamp does come with a short gooseneck when ordered, but it was found that these varied in length after a few were purchased. The GoPro® Gooseneck (not the stock goosenecks that came with the clamps) was used in testing for consistency purposes.

Figure 68: The collection of parts necessary for assembling the 2D GoPro® DIC sensor

There were a few different variations of sensors used during lab testing. The 2D DIC GoPro® sensor was created using all of the pieces described above. This 2D GoPro® DIC sensor is shown assembled in Figure 69 below attached to the lab testing apparatus.

Figure 69: Assembled GoPro® DIC sensor for 2D strain collection

The other main sensor variation tested was a 3D GoPro® DIC strain sensor. It requires all the same parts, but uses a second GoPro® Hero 3+ Black Edition camera, and the stock protective case is traded out for the GoPro® Dual Hero System case. This system holds both cameras together and uses a "sync cable" that synchronizes the two cameras together, which allows for the

coordinated image capture necessary for 3D DIC analysis. Even though two cameras are present in this setup, the sync cable creates a "master and slave" camera system, where everything operates through the "master" camera and the "slave" camera copies its actions. For use, this means that if controlled via the GoPro® App, it operates through the "master" camera's wifi network, and if controlled via the wifi remote, this sensor will appear as one camera. The parts for the 3D DIC sensor are shown in Figure 70 below and the fully assembled unit in the lab environment is shown in Figure 71.

Figure 70: The collection of parts necessary for assembling the 3D GoPro® DIC sensor

Figure 71: Assembled GoPro® DIC sensor for 3D strain collection

7.2 Experimental Lab Apparatus

An experimental lab apparatus needed to be designed that would allow an easy comparison between the measurements from the experimental GoPro® DIC strain sensors and the control strain measurement method of foil strain gauges. The experimental apparatus for the tests had to be a simple set up that could apply a controllable amount of strain and be easily repeatable. Ideally, this would have involved performing simple tension tests on fabricated specimens using a programmable loading mechanism. What was designed was a simply supported beam subjected to four-point bending. The final designed test apparatus can be seen under loading in Figure 72 below.

Figure 72: Experimental test apparatus as seen while loaded

The "beam" used as the test specimen in this apparatus is a 72"x 3"x 0.25" Grade 50 steel plate with six pairs of notches machined at specified locations along its length. The notches were machined symmetrically with respect to the length of the beam, such that when load was applied to each side, the center span between load applications would be a region of constant strain. Load was applied to the beam by hanging two 50lb steel blocks with rope on the beam. The notches allowed the ropes to slot into position, meaning the loads could be applied consistently at the exact location of the notches as well as preventing the ropes from slipping under deflection. The supports were constructed from sections of W8x24 steel pieces welded together that were available from previous testing. They provided a stable support for the beam while raising the apparatus high enough to allow the weights to hang without touching the floor. To create the simply supported condition, two steel roller sections were placed under the beam.

Three sets of notches, consisting of four notches per set (two per location on length of beam, symmetrically about its center), were chosen. This would allow three distinct strain levels to be observed during testing. After considering the space requirements for the application of both strain measurement systems, and using the structural analysis software SAP2000 to create a finite

element model of the test beam, the test structure was designed to have a center span of 24" with consecutive 3" center-center offsets of the notches, allowing for a reasonable range of applied strains. It was determined that in order to avoid fatiguing and yielding at the notch locations, the test beam needed to be supported 9" in from both ends, giving it a total span from support to support of 54". For more details on the design and verification of the test structure, see Appendix K. Figure 73 below shows the machined notches on one side of the beam. These notches are mirrored on the other side of the beam, symmetrically about its center.

Figure 73: Photo showing the machined notches on one side of the test beam

The simply supported four-point loading conditions of the test allowed for simple calculations of the expected stress and strain. As mentioned above, symmetrical four point bending was chosen as the load configuration because it creates a zone of constant moment, which means that zone is also under constant strain. Calculating the strain in the beam was as simple as combining Hooke's Law and the equation for bending stress to calculate the predicted strain.

To calculate the moment applied to the test apparatus, shear and bending moment diagrams were used, as shown in Figure 74 and Figure 75 below, respectively. Note in the moment diagram that the entire center span is a constant moment value.
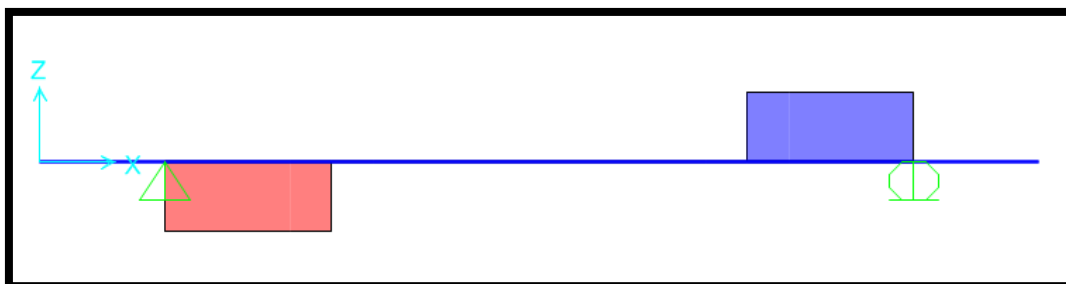
Figure 74: Shear diagram of the laboratory test apparatus (SAP2000, 2014)

Figure 75: Moment diagram of the laboratory test apparatus (SAP2000, 2014)

Table 16 below summarizes the strains that should be measured during testing under the three different levels of loading. Note that as L_i decreases, the expected strain increases. This is because as the loads are applied closer to the center of the beam, the greater the applied moment becomes. These values were calculated using the above equations and verified using the SAP2000 model.

Table 16: Summary of expected strains in the simply supported test apparatus under the different levels of applied load

Strain Level	L_i (in)	Applied Moment (lb-in)	Expected Strain ($\mu\varepsilon$)
Strain 1	36	450	496.6
Strain 2	30	600	662.1
Strain 3	24	750	827.6

In order to increase the versatility of the test apparatus, a second variation of the apparatus was created by fixing the supports, instead of leaving them simply supported. In order to achieve this fixity, C-clamps were used to limit the rotation at the supports, as shown in Figure 76. Clamps were applied in this fashion to both supports.

Figure 76: Picture displaying the clamps used to create fixed conditions for the supports of the test apparatus

It is very difficult to create fully fixed conditions in the lab, but this attempt at fixity worked to some extent. Looking closely at Figure 77, one can see the point of inflection in the curvature of the beam, which is highlighted by the red box. This indicates that the support was providing some rotational resistance. It can also be seen that the rotation at the support is not equal to zero, meaning that the support was not perfectly fixed either. Therefore the support conditions provided by the clamps created a partially fixed scenario.

Figure 77: Photo showing the point of inflection in the curvature of the test beam under fixed conditions

Since the support conditions provided rotational resistance somewhere between simply supported and fixed conditions, the measured strains under these partially fixed-fixed conditions should be expected to fall somewhere between the values measured under simply supported conditions and those strains expected under perfectly fixed conditions. A model of the test apparatus was created in SAP2000 with fixed support conditions. Table 17 below shows the predicted strains from that model.

Table 17: Summary of expected strains in the fixed-fixed test apparatus under the different levels of applied load as predicted by SAP2000 (2014)

Strain Level	L_i (in)	Applied Moment (lb-in)	Expected Strain (με)
Strain 1	36	73.2	79.3
Strain 2	30	131.1	144.8
Strain 3	24	206.1	227.6

7.3   <u>Data Collection Methods</u>

During laboratory testing, there were two data collection methods used: experimental strain measurement using the GoPro® DIC sensors and the control form of strain measurement using foil strain gauges. The installation and operation of these two data collection methods is described below.

7.3.1   *Operating the GoPro® DIC Sensor*

Operating the GoPro® DIC strain sensor is as simple as operating a camera. To deploy the sensor, it is simply clamped to the test specimen, with the camera facing down perpendicular to the speckled test surface. Special care was taken to be sure the camera was attached perpendicular to the surface, and the view was parallel with the length of the test beam. This was important because if the view was not parallel with the length, then the measured strain by the DIC sensor in the x-direction (the longitudinal strain in the beam) would not match the measured strain from the foil gauges. To aid in setting the camera perpendicular to the surface, bubble levels were used.

The cameras were operated exclusively using the GoPro® App on a smart phone during all lab testing. The instructions for the setup of the camera's wireless network and connecting to the app was conducted following the standard procedures provided in the HERO 3+ Black Edition User Manual (2014) and any further questions were answered using the GoPro® Support webpage (2015). To use the app to control the GoPro® camera, simply turn on the camera's GoPro® App wifi, connect to the camera's wireless network with the smart phone, open the GoPro® App on the phone, and select "Connect and Control" at the top of the screen. Once connected, the user has full control over that camera as if it were in their hand. All settings can be adjusted, and the phone displays a live feed of what the camera is seeing. This display was used to ensure the view of the camera was properly set before conducting the testing. The wireless capabilities allowed the camera to remain in place for the entire duration of the session of testing, ensuring consistent placement for all tests in a trial. To collect data using the GoPro® DIC sensor, it is as simple as pressing the "Record" button (big red button) on the GoPro® App to begin recording video. To stop collecting data, press that button again.

7.3.2   *Operating the Foil Strain Gauges*

The control method of strain measurement of which the DIC strain measurements would be compared to was measured using foil strain gauges. The exact model of strain gauges used was Omega KFH-6-120-C1-11L3M3R quarter bridge gauges. These are fully pre-wired quarter bridge strain gauges with a gauge length of 6mm and resistance of 120Ω. These foil gauges were applied and wired into a Type-I Full Bridge circuit configuration, which is the most accurate configuration for measuring bending strains. For all laboratory tests, the foil gauges were operated using a sampling rate of 10Hz. For more accurate data, two of these configurations were wired onto the test apparatus, one to the left and right of the DIC speckle pattern on the center span. For details on how the strain gauges were applied, see Appendix C. Figure 78 below shows the placement of the strain gauges on the test apparatus. To complete the Full Bridge Type-I circuit, each pair of foil gauges is mirrored on the underside of the beam.

Figure 78: Top-down view of the test apparatus showing the placement of the foil gauges on either side of the speckle pattern on the center span

Once everything was fully assembled and connected, the final test apparatus looks as shown in Figure 79. Note the simplicity of the GoPro® DIC sensor compared to all the wires, laptop, and DAQ (hidden behind the laptop) needed for operation of the foil gauges. It should be noted that although the laptop can be used on its own battery power, the DAQ system requires an external power source.

Figure 79: Fully assembled lab testing apparatus showing both the GoPro® DIC and foil gauge strain measurement systems

7.4   __Laboratory Testing Procedure__

The first step before starting each test was to adjust the test parameters to the predetermined settings. Every laboratory trial was designed to test different parameters of the set up, and each individual test within the trials used different settings of the test parameters. The sets of test parameters and their settings will be provided for each trial in their respective sections below. Always be sure the camera SD card is empty before starting testing.

Once both systems began collecting, the weights were carefully lifted off of the supports and applied one at a time to the test beam. When lifting the weights, do not slide them off the support, as this will cause the beam to vibrate, which reduces the accuracy of the DIC measurements. The weights were applied by placing the hanging rope into the correct notch of the beam that corresponded to the predetermined strain level for that particular test. Once the rope was notched, the weight was slowly lowered until its full weight was supported by the beam, making sure to not drop the weight and keeping vibrations to a minimum. Once one weight was applied, the other was applied following the same procedure.

After both weights were applied, they were allowed to hang on the beam for a period of at least five seconds. This allowed both systems to collect a constant, maximum strain measurement during that time. After the five second application had elapsed, the weights were removed in opposite order of which they were applied (the first weight on was the last weight off). Once the weights were returned to their positions on the supports, then both data collection systems were stopped, signifying the end of that test. Then the settings were changed for the next test, and this process was repeated until all tests in the lab trial were completed. Each test ran for approximately 30 seconds.

The easiest way to understand the test is to view a plot of the data. Figure 80 is a sample plot from one of the lab tests showing measured strains from both foil gauge circuits. The six labeled zones in the plot correspond to distinct occurrences during the test.
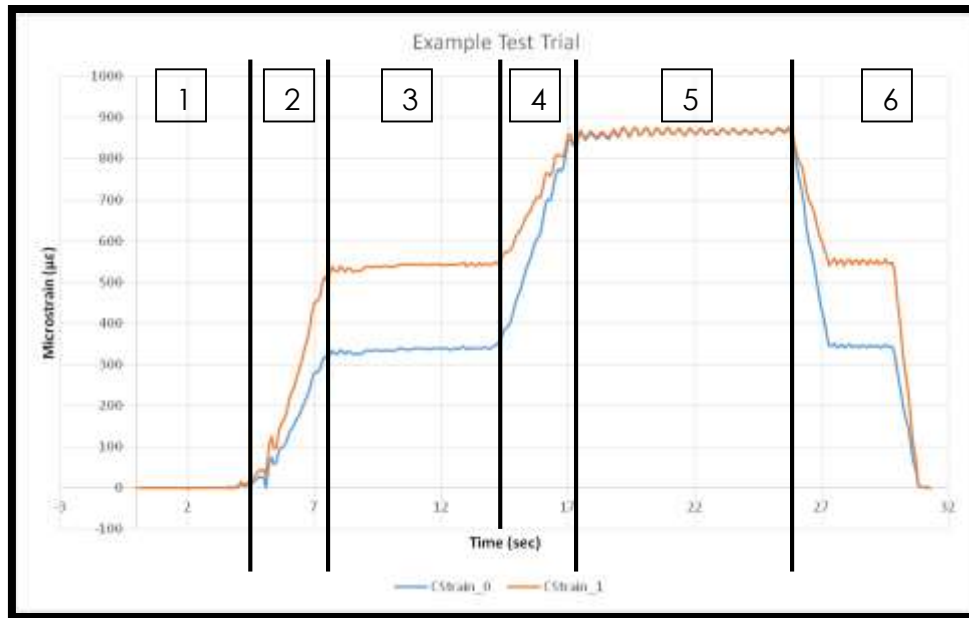
Figure 80: Example laboratory test plot correlating the different regions to what is happening during the test

Zone 1 is the time directly after data collection is started, but no weight has been applied. This is why the strain reading remains constant at zero. Zone 2 corresponds to when the first weight is applied to the beam. Due to the asymmetric loading, the strain measured by the foil gauges diverges, with higher strains being measured in the circuit closest to the location of the applied load. Zone 3 is the time between the application of the first and second weight, which is why the measured strains are constant. Zone 4 is when the second weight is applied to the beam. Zone 5 is the five second application of both weights. The slight oscillation in measured strains indicates that the second weight was not gently applied, and the beam was vibrating. Note how both foil gauge circuits measure identical strains during this time. This indicates that the test apparatus really is symmetric, and the center span is experiencing constant stress. Zone 6 shows the removal of the weights and the stoppage of data collection.

7.4.1   *Procedure for Performing a 3D DIC Calibration*

The above procedure was the standard load testing procedure followed whether a 2D or 3D strain analysis was being performed. The only difference in procedure between the two is that a 3D calibration must be performed at the start of a test involving 3D DIC analysis. Correlated Solutions (the producer of the Vic DIC analysis software used in this study) created a YouTube tutorial on how to perform a 3D DIC calibration (Correlated Solutions 2015). The procedure introduced in that tutorial was the one used in testing.

The basic premise of performing the 3D calibration is that by analyzing images of a calibration target grid in various positions in the field of view of both cameras, the software can triangulate the camera positions in relation to the target, and create a 3D model of the surface (Correlated Solutions 2015). The procedure for performing the calibration is the same procedures as for collecting 2D strain data, but instead of having the camera take a video of a speckled surface, a

video is taken of a calibration grid as the grid is moved and rotated in the field of view of the two synchronized cameras. The calibration grid should remain roughly same distance away from the cameras as the speckle pattern will be during testing. The grid should cover as much of the field of view as possible. Special care should be taken to be sure the grid points do not leave the field of view, as the software will show poor calibrations for images with missing grid points. When recording the calibration video, all settings should be the same as the test video, as any changes in condition will impact the accuracy of the calibration.

Correlated Solutions does produce a set of varying sizes of calibration target grids, but for this testing, a calibration grid was fabricated using Correlated Solutions' "Target Generator" software. Once the correct target size was established by printing sample grids, the proper sized grid was printed and securely taped to a stiff plastic plate. Figure 81 below shows the calibration target grid used in performing the 3D calibrations. Note how the grid is on the same plane as the speckle pattern to ensure that the calibration was performed correctly. A calibration did not need to be performed before every 3D test. One was performed at the start of the trial, and then that calibration could be used for all tests, so long as there were no changes in camera positions or properties.
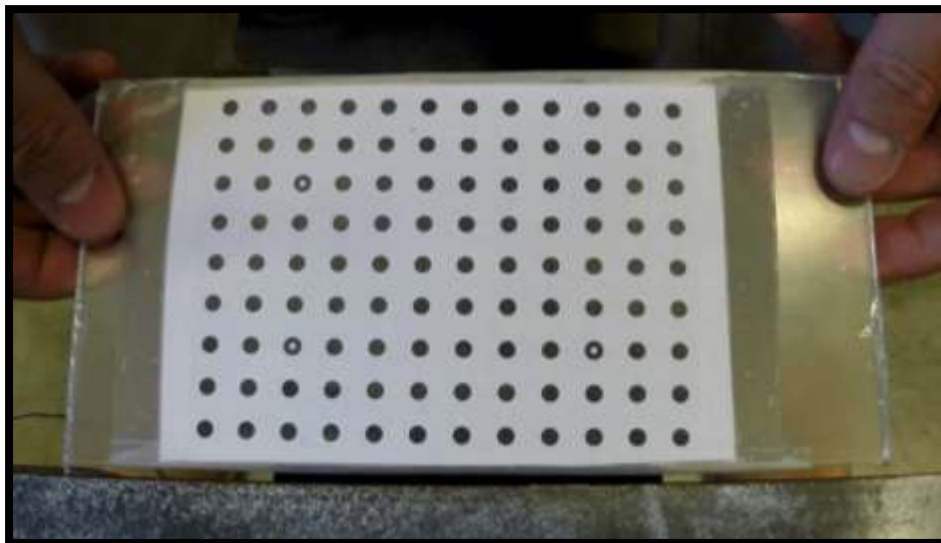
Figure 81: Sample photo of the calibration target grid used in testing

7.4.2   _Procedure for Post-processing DIC Test Images_

Once the test videos have been recorded, then the videos need to be imported, stored, and dissected into individual frames before they can be post-processed using the DIC software. To import the test videos from the camera, the SD card is removed from the camera and an SD to USB connector is used to transfer the files off of the SD card and onto the hard drive used for storage. Once on the storage device safely, the files are renamed appropriately to match the respective test number. This step requires special care, because the videos are not named when they are created by the GoPro® camera, they are simply given a generic number in a sequential order. The operator must know and keep track of the order of which the tests are conducted. Once the files are properly saved and named, the files can be deleted from the SD card to make room

for the next test trial, and the SD card is returned to the camera. If using multiple cameras, never remove more than one SD card at a time to prevent the accidental switching of SD cards.

Once all the test video files are named and organized, then the videos need be broken into individual frames. The video files are in the .MP4 video file format, but Vic DIC analysis software requires .TIFF image files for post processing. This is accomplished using a simple MATLAB code to convert the video files into individual frames.

7.5   Data Editing and Post-processing Techniques

After viewing the output strain fields in Vic-2D from the first few tests, it became apparent that the test apparatus was not performing as intended. The theory behind the test apparatus was that by attaching the GoPro® DIC strain sensor directly to the beam in bending, it would eliminate the out-of-plane displacement associated with the beam's deflection, and the strain measurements would be easily collected. When viewing the strain fields calculated in Vic-2D, the contours on the strain plot should all be the same color, so long as the measured strain was constant. One look at the strain fields from the testing, such as that shown in Figure 82, and it is obvious that this theory was not holding true.
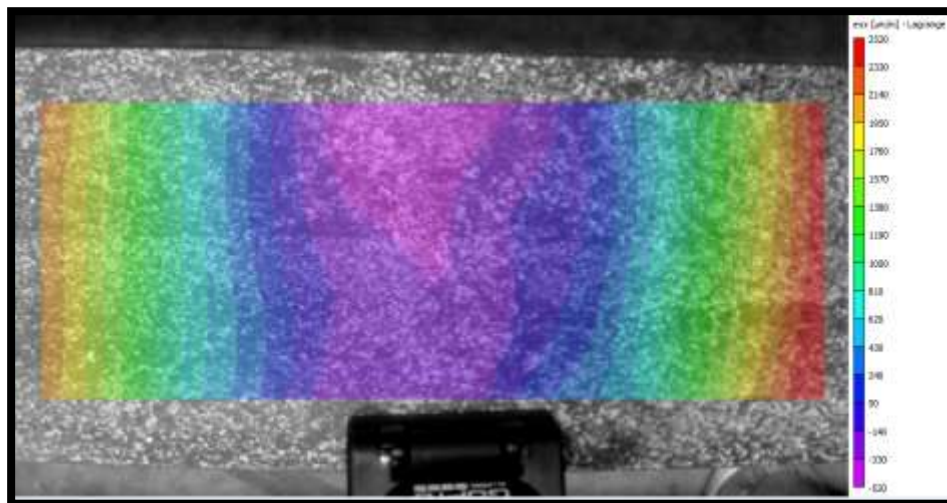
Figure 82: Sample strain field calculated from the lab test showing the unexpected strain distribution

The rainbow of contour colors and the legend going all the way up to positive 2500 με (tension) indicates that the measurements are impacted by the out-of-plane displacement caused by the curvature of the beam. This was not expected in the initial designs. As the beam deflects under loading, the beam gets closer to the DIC sensor at the edges of the images, and therefore is interpreted by the software as tension. If the contour range is adjusted to only show the areas undergoing compression (which was originally expected, as the top face of a beam in positive bending should be in compression), then the region of very small to no motion can be seen. Figure 83 below shows this adjustment. The color red indicates the areas that are measured to be in tension.
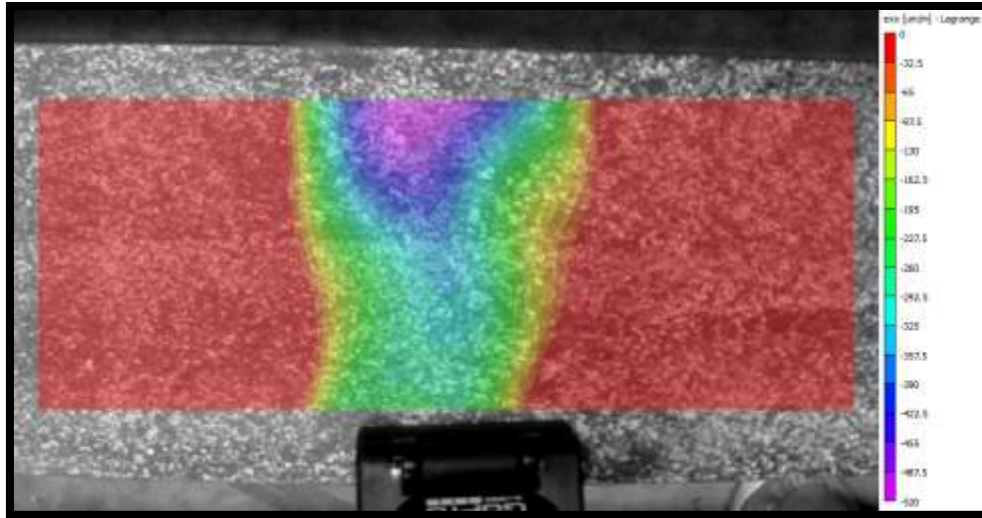
Figure 83: Sample strain field with the contours adjusted to only show the regions in compression

Although these were unexpected results, it also showed that the DIC sensors were operating according to existing theory. The regions where out-of-plane motion were impacting the measurements showed to be reading tension because they were getting closer to the camera, and the regions that remained a constant distance from the camera (the area directly under it where it was secured to the beam) were reading compression, which was expected from the design of the test. To adjust for these findings, instead of extracting the data from the entire area of interest (AOI) as initially planned, the data was extracted from selected areas of extraction (AOE). Figure 84 below shows the AOEs used to illustrate this point. The larger AOE extracts data from the entire AOI that was initially selected for analysis, while the smaller AOE only extracts data from the compression region.
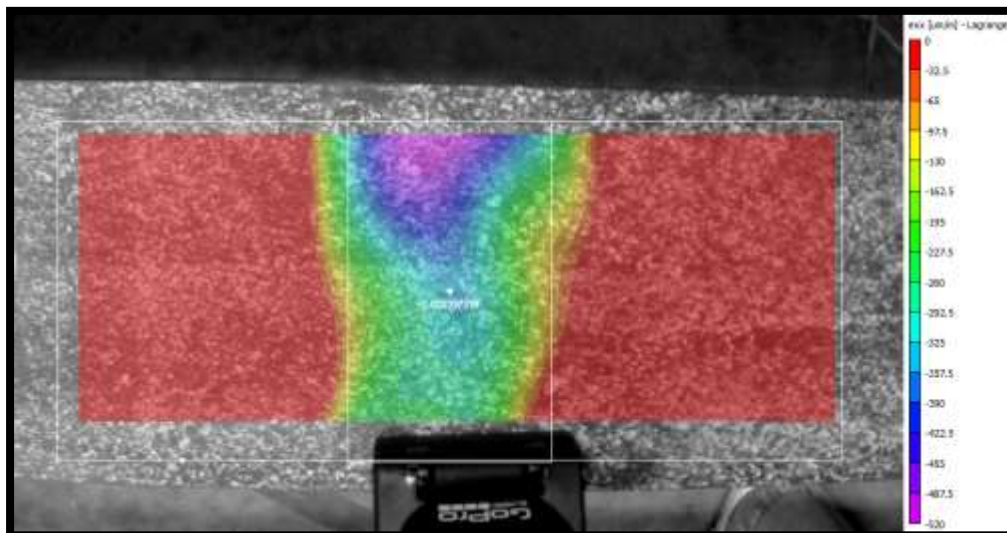
Figure 84: Snip showing the AOEs, shown as white boxes, used for data extraction. The larger one extracts data from the entire AOI, while the other only extracts from the region in compression

Figure 85 shows the unprocessed strain readings from both these AOEs in units of microstrain. This example was taken from a test that was subjected to a Strain Level 1 loading, so the expected strain was around 500 µε in compression. It is clear that the selected AOE showed results extremely similar to the expected measurements, while the entire AOI strain measurements were not close in either magnitude or direction. After it was established that this method of data extraction from the DIC software provided promising results, the testing and processing of data was continued with confidence.
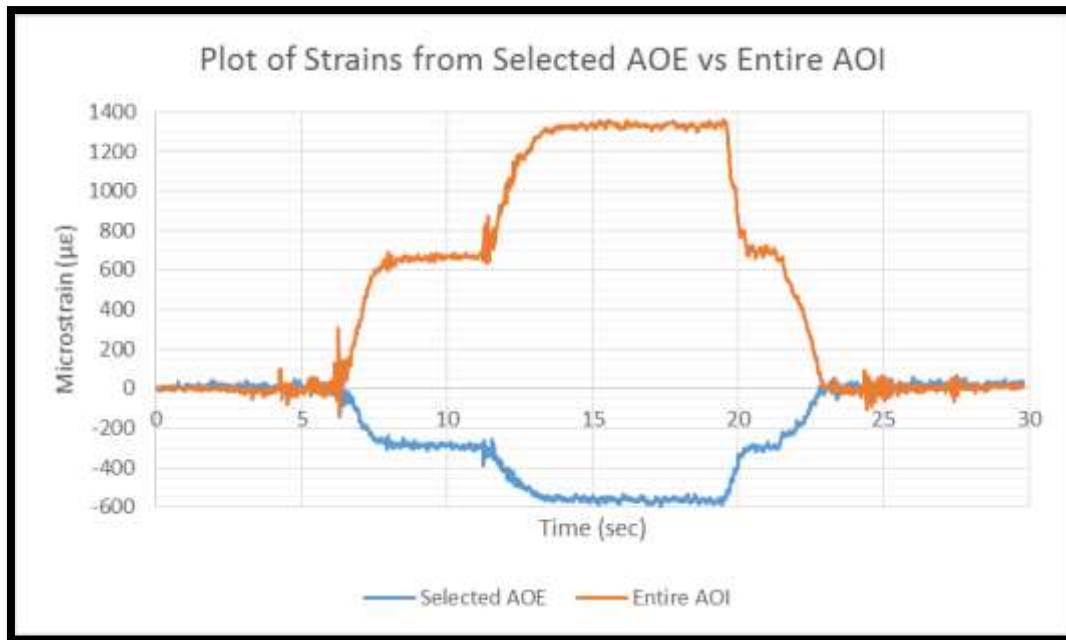
Figure 85: Plot showing the comparison of measured strains from DIC between using a selected AOE or the entire AOI

7.5.1 _Processing and Conditioning of Data_

After the data was extracted from the DIC software, then it needed some minor processing before being compared to the strain measurements from foil gauges. It should be noted that all data processing was conducted using Microsoft Excel.

One of the pitfalls of DIC strain measurement is that once the test videos are divided into frames, then the measurements have no time stamp associated with them. Therefore, in order for comparison to the foil gauge data, the time associated with each reading needed to be calculated. This is accomplished by knowing the frame rate used to record the test, as demonstrated in **Error! Reference source not found.**9.

$$t_n = t_{n-1} + \frac{1}{fps} \qquad \text{(Eq: 19)}$$

Where t_n is the time of the data point being calculated, t_{n-1} is the time of the previous data point, and fps is the frame rate in frames per second used to record the video. By appointing the first frame a time of zero seconds, then the time for all subsequent images can be calculated. If a

horizontal offset is necessary, like if there was a large time difference between the starting of the DIC sensors and the foil gauges, then an adjustment can be made simply by changing the time assigned to the first point such that the data curves align.

The first and most obvious change that was needed when viewing the strain data was that the foil gauge data was measured as positive and DIC strain data was measured as negative. This is because the full bridge foil gauge circuits were wired to measure strains caused by bending. Since the beam was undergoing positive bending, the strains were reported as positive. The DIC sensor was measuring strains on the compressive face of the beam in bending, which the software reports as a negative value. To remedy this, the strain values measured by DIC were all multiplied by negative one, as demonstrated in **Error! Reference source not found.**o.

$$\varepsilon_{DIC,edit} = -1 * (\varepsilon_{DIC,raw}) \qquad \text{(Eq. 20)}$$

Where $\varepsilon_{DIC,edit}$ is the edited strain measured by DIC, and $\varepsilon_{DIC,raw}$ is the raw strain output from Vic software.

The next change made to the data was to convert all the strain values from units of strain to units of microstrain. This simple conversion is showed in Equation 21. This adjustment was performed on measurements from both systems.

$$\varepsilon_{edit} = 10^6 * (\varepsilon_{raw}) \qquad \text{(Eq: 21)}$$

A correction for initial jump in measurement values was made to all strain values measured by both DIC and foil gauges. This involved simply subtracting off the average of the first second of recorded measurements, calculated as shown in Equation 22.

$$\varepsilon_{edit,i} = \varepsilon_{raw,i} - \frac{1}{n}\sum_{i=1}^{n} \varepsilon_{raw,i} \qquad \text{(Eq. 22)}$$

Where $\varepsilon_{edit,i}$ is the edited strain for either DIC or foil gauges, $\varepsilon_{raw,i}$ is the raw strain from either DIC or foil gauges, and n is the value of the sampling rate of either system (10Hz for the foil gauges, or the fps for the DIC sensors).

A rolling average was used to smooth the strain data measured by DIC. By using this, every edited strain value from DIC is really the average of n other raw strain measurements. The formula for calculating the rolling average is shown in Equation 23.

$$\varepsilon_{DIC,edit,i} = \frac{1}{n}\sum_{j=i}^{i+n-1} \varepsilon_{DIC,raw,j} \qquad \text{(Eq. 23)}$$

Where n is the number of measurements averaged together. The value used for n was dependent on the frame rate used during the test. No set value was used throughout, but typically n ranged from 0.20*fps to 0.50*fps. The benefits of using the rolling average are demonstrated in Figure 86 below. Employing a rolling average does get rid of higher frequency data, but this was deemed acceptable since this test was quasi-static in nature and only interested in the magnitude of strain measurements.
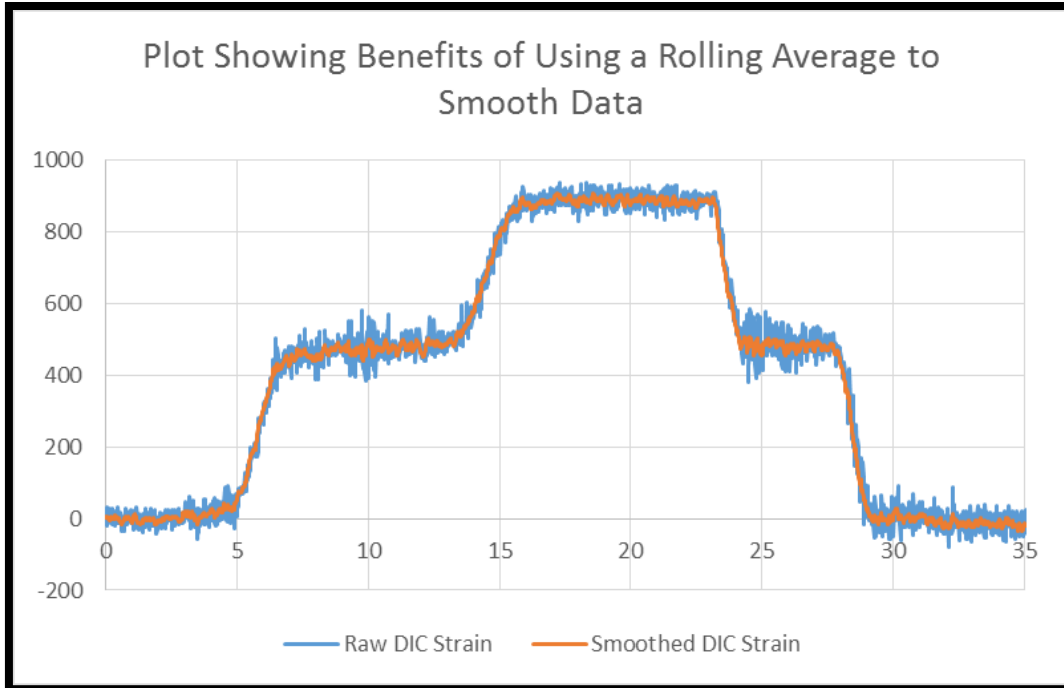
Figure 86: Plot showing the effects of using a rolling average on the DIC strain measurements

The last type of correction employed was a correction for linear drift. For some unexplainable reason, sometimes the DIC software calculated the strain measurements as having a constant increasing or decreasing slope. To remedy this, the slope of this linear drift was calculated over a time not undergoing some form of loading (an area that should have a slope of zero), and that slope was systematically subtracted from the strain measurements. This calculation is shown in Equation 24.

$$\varepsilon_{DIC,edit,i} = \varepsilon_{DIC,raw,i} - mt_i \qquad \text{(Eq: 24)}$$

Where m is the slope of the linear drift, and t_i is the time at the point being edited. Figure 87 below shows an example plot illustrating the effects of both the linear drift correction and the smoothing effects of the rolling average. The trend labeled CStrain_1 is the measurement by a foil gauge during that test. Note the amount of error between the plots before and after the data corrections are made.
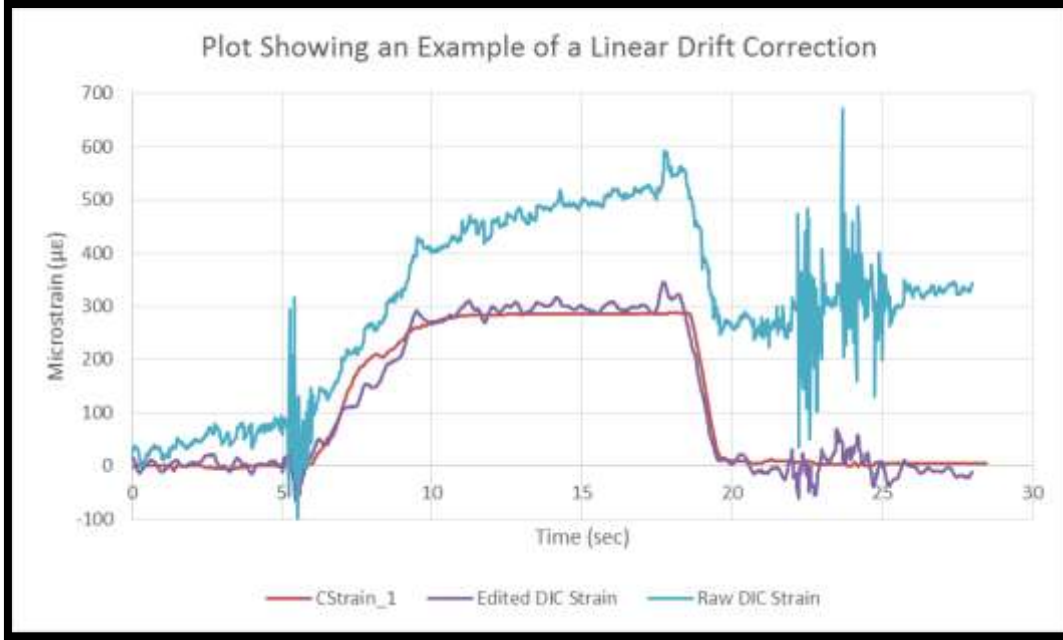
Figure 87: Plot showing the effects of using the combination of the rolling average and the linear drift correction

The final correction equation used to condition the strain data measured by the experimental GoPro® DIC strain sensor is provided in Equation 25.

$$\varepsilon_{DIC,edit,i} = -10^6 \left(\frac{1}{n} \sum_{j=i}^{i+n-1} \varepsilon_{DIC,raw,j} - \frac{1}{h} \sum_{i=1}^{h} \varepsilon_{DIC,raw,i} \right) - m t_i \qquad \text{(Eq:25)}$$

Where n is the number of measurements used in the moving average as explained above, h is the frame rate used to record the test video, and all other variables are the same as previously explained.

The above corrections were applied on an as-needed basis. Sometimes linear drift corrections were necessary, other times they were not. Corrections were made such that the DIC data matched that produced by foil gauges as closely as possible. In some rare cases where the test apparatus was clearly bumped during a test and there were noticeable jumps in the data from the DIC not caused by loading (these instances could be verified by watching the test video), the data was adjusted to correct for this data jump. An example of this is provided in Figure 88. At around the ten second mark during the test, the test apparatus was jarred, causing the DIC sensor to read a jump in strain. This is corrected by subtracting off the vertical offset at the end of the test from all points after the jump.
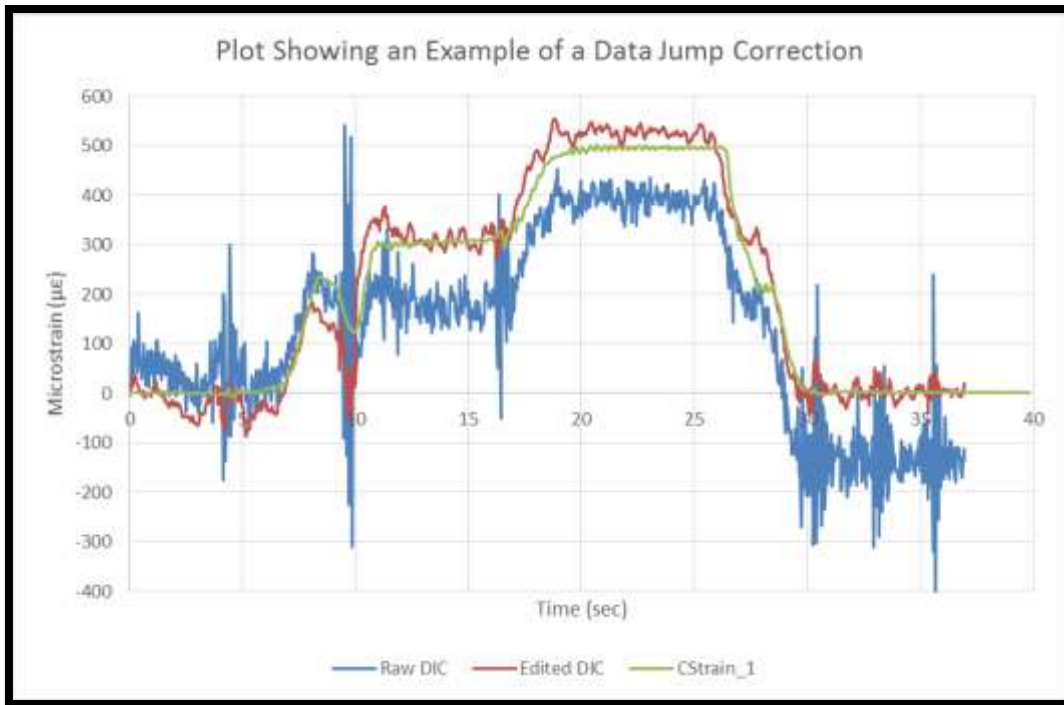
Figure 88: Plot showing an example of a correction for a data jump caused by bumping the test set up

7.6   3D DIC Lab Testing

Both 2D and 3D lab testing were conducted using the GoPro camera. The 2D results are included in Appendix K. The 3D results are presented here. 3D DIC analysis has all the benefits of 2D DIC, but it is not susceptible to the effects of out-of-plane movement. By performing a stereoscopic calibration, and recording the test surface with two synchronized cameras, then the 3D DIC software can calculate strains on the 2D surface, but also measure deflections in all three dimensions as well as automatically correct for lens distortion effects. Since the experimental test apparatus was causing a great deal of hassle due to out-of-plane movements and GoPro® actually produces a specially designed system for collecting synchronized images intended for the creation of 3D content, then it made logical sense to try out an experimental 3D GoPro® DIC sensor. Three trials were conducted, only trial 3 is presented here. Trials 1 and 2 for the 3D GoPro® DIC Sensor testing are included in Appendix K.

7.6.1 Goals, Purpose, and Results of 3D Trial 3

In 3D Trial 3, six tests were conducted where strains were measured with both the 3D GoPro® DIC strain sensor and the foil gauges in order to perform a statistical analysis on their differences in measurement. Two tests were conducted at each strain level, as shown in the list of tests in Table 18. All other parameters were held constant. The tests were conducted with the camera about 7.5" from the test surface, Light setting 2 (overhead lights only), 1080p resolution, and a frame rate of 24fps. All trials were processed using the same set of calibration images.

Table 18: List of tests conducted in 3D Trial 3

Test	Strain Level
1	1
2	1
3	2
4	2
5	3
6	3

Table 19 below shows the sumary of the results for the strain measurements taken in 3D Trial 3. The reported average values were calculated by averaging the average maximum strains from each AOE.

Table 19: Summary of results for 3D Trial 3

Test	Expected Strain ($\mu\varepsilon$)	Avg Foil Strain ($\mu\varepsilon$)	Avg DIC Strain ($\mu\varepsilon$)	std,DICi ($\mu\varepsilon$)	%Diff,i	abs(%Diff,i)
1	496.6	497.65	493.67	10.69	-0.80	0.80
2	496.6	497.35	471.21	8.84	-5.26	5.26
3	662.1	655.09	682.09	20.04	4.12	4.12
4	662.1	655.73	619.77	11.88	-5.48	5.48
5	827.6	825.24	761.12	11.93	-7.77	7.77
6	827.6	825.04	778.36	13.33	-5.66	5.66

Table 20 shows the results of the statistical analysis conducted on the results of 3D Trial 3.

Table 20: Summary of the statistical analysis conducted for 3D Trial 3

%Diff,avg	4.85
std,%Diff	2.31
t,n-1	-0.161
p-value	0.50<P<0.60
Result:	Fail to Reject the Null

Figure 89 through Figure 91 are a representative sample of the results of this trial. Figure 89 shows the method of AOE selection used in this trial. Figure 90 shows an example of what the collected strain data from both measurement systems looks like. Figure 91 shows an example of the 3D projection of the test surface created during the 3D DIC analysis. To view these results and a summary of strain measurement for each individual test, see Appendix K.
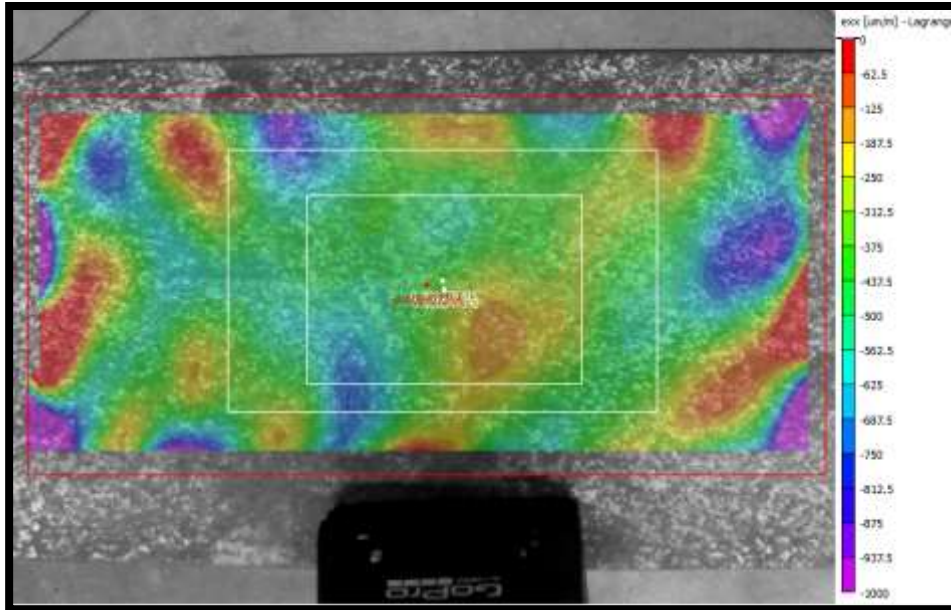
Figure 89: Snip displaying the method of AOE selection used in 3D Trial 3 (Vic-3D, 2012)
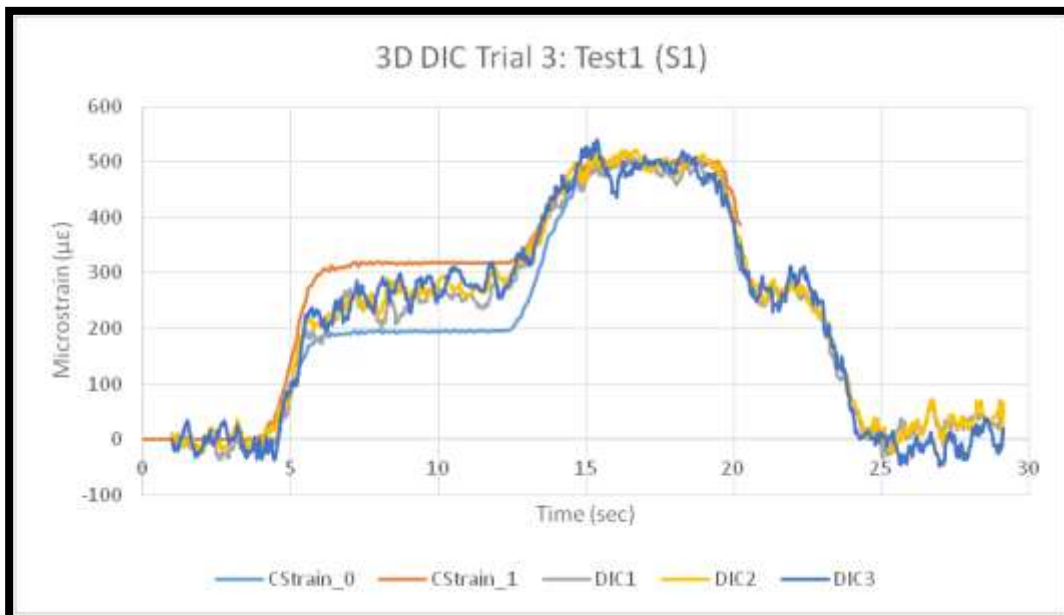
Figure 90: Sample plot of strain versus time from the data collected in 3D Trial 3
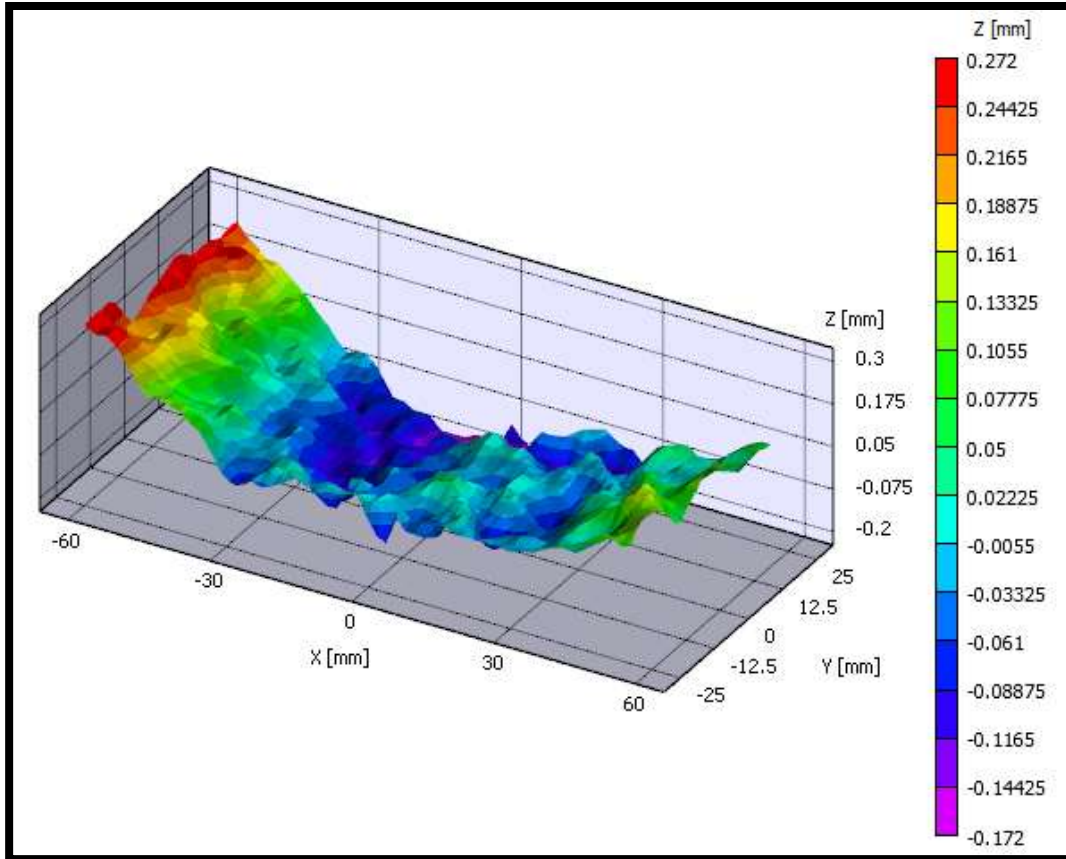
Figure 91: Snip showing a sample 3D projection of the beam surface under maximum loading (Vic-3D, 2012)

The results of this trial showed that the strain measurements by the 3D GoPro® DIC sensor are statistically significant when compared to the measurements by the foil gauges. By using the parameter settings that were established as the appropriate settings from the 2D Lab Trials, it was found that those same settings should be used when performing 3D DIC with the experimental sensor.

By observing the strain measurements plotted from the different AOEs, it is clear that the 3D GoPro® DIC sensors are not impacted by the out of plane movement. All three AOEs from every test measured very similar strains, despite each varying drastically in the area that they cover. These experimental 3D DIC sensors can accurately measure strains, even in situations with out of plane movement.

Every test was successful in predicting the 3D projections of the test surface undergoing deformations. Even though the surface is noisy, the overall trend of the deflection throughout the test matches the real trend. The deflection measurements shown in the contours of the projections represent the relative change in distance between the camera and the surface. The trends in the relative magnitude of these deflections match the magnitudes of the strains. The deflections are

larger in tests with larger strains. This shows that the 3D DIC sensor is also relatively accurate in measuring the curvature on the test surface.

7.7   **Conclusions of Lab Testing**

Overall, the trials conducted in the laboratory testing of both experimental 2D and 3D GoPro® DIC sensors showed great success. The strain measurements from both experimental DIC sensors were found to be statistically significant within 5% when compared to the control measurement method of foil gauges. The proper settings of the parameters impacting the accuracy of the DIC sensors were established.

It was found that light did have a significant impact on strain readings. There is a minimum amount of light that is necessary in order for the DIC software to make accurate measurements. Once that minimum amount was reached, then any additional increase in light did not impact the overall accuracy, but instead allowed an increase in data density by allowing a finer subset mesh. These results show that GoPro® DIC sensors deployed in the field may require an external light source.

It was found that camera height did not have a significant impact on the strain measurements. So long as the test surface has an adequate speckle pattern, then the GoPro® DIC sensors can be set to any reasonable height allowed by the gooseneck and still record accurate measurements. The recommended camera heights are anywhere around six to eight inches away from the test surface.

It was also found that camera resolution did not have a significant impact on the measurement accuracy. Similar to decreasing the height or increasing lighting conditions, increasing the resolution allowed for greater amounts of spatial resolution (ratio of pixels to surface area). This could be necessary in tests requiring a fine mesh and dense strain fields, but if only coarse measurements are needed (like in these tests), then lower resolution will work fine. It should be noted that only camera resolutions of 720p and 1080p could be tested because these were the only resolutions that had the option to record in the "Narrow" field of view. Any field of view wider and then the effects of camera distortion become larger.

Once the proper parameter settings were established, the 2D GoPro® DIC sensor was successful in measuring the trends and relative magnitudes of the strain induced in the test surface. Due to the out-of-plane movement caused by the curvature in the beam, a specialized data extraction process was necessary in order to calculate accurate measurements from the 2D DIC strain fields. By observing the measured strains from different AOEs, it was established that by extracting data using AOEs that covered the compression zone and part of the tension zone, then the measured strains closely matched those produced by the foil gauges.

The 3D GoPro® DIC sensor was successful in measuring the trends and magnitudes of strains as well as the curvature of the test surface. A proper method of performing the 3D calibration was established. It was found that AOE selection was not as significant for data extraction due to the 3D DIC sensor not being sensitive to errors from out-of-plane movement. With experimental DIC sensors showing that they were capable of collecting accurate measurements under proper testing conditions in the laboratory environment, then their performance capabilities could then be tested in the field. Preliminary field testing occurred in June 2015.

8. Outcomes and Recommendations

8.1 Outcomes

Through this research effort, foil strain gauges were installed on the Bagdad road over US Route 4 Bridge in Durham, NH. The strain measurements collected from these sensors was used to determine the location of the neutral axis for the composite girders. Digital imaging correlation was used at the Bagdad Road over US Route 4 to measure girder deflection. This collected data was then used to calibrate a detailed three-dimensional structural model for load rating. The resulting load rating were compared with AASHTO load ratings.

Prior to field deployment of either measurement technique, extensive laboratory tests were conducted to determine testing parameters and deployment and post-processing protocols. These tests and parameters are included in the appendices to this report.

The potential uses of digital imaging in bridge monitoring was expanded to include strain measurements through laboratory experiments and field deployment that was conducted in June 2015 and will be submitted as an addendum to this project.

Goals and Outcomes

- Provide a detailed manual for strain gauge selection, installation and operation.
- Demonstrate the value of structural health monitoring for structural condition assessment via load rating.
- Develop a procedure to calculate neutral axis location for a composite girder using collected strain readings.
- Develop a procedure to calculate live load distribution factors for an in-service bridge using collected bridge responses.
- Recommend foil strain gauge type, installation and data acquisition methods
- Demonstrate the robustness of digital image correlation for collection of bridge deflections and strains

Activities

- Detail the importance of structural health monitoring, specifically foil strain gauges and digital image correlation, for bridge management (Chapter 1)
- Design an instrumentation plan for the Gilford Bridges (Appendix A)
- Design an instrumentation plan for the Bagdad Road over US Route 4 Bridge, including sensor selection (appendix B), sensor installation procedures (Appendix C), data acquisition system (Appendix D) and full instrumentation plan (Chapter 2 and Appendix G)
- Deploy an instrumentation plan at the Bagdad Road over US Route 4 Bridge and use collection strain measurements to determine the in-service neutral axis location (Chapter 2 and Appendices E and H)
- 2012 Loading Testing of the Bagdad Road Bridge over US Route 4, including digital image correlation testing parameters (Appendix F), truck positioning and data collection (Chapters 3 and 5).

- Post-processing of collection information for neutral axis location and live load distribution factor calculation (Chapters 4 and 6 and Appendix H)
- Use of collected structural data for condition assessment and load rating (Chapter 6 and Appendix J)
- Develop and calibrated a 3D structural model of a in-service bridge for load rating and condition assessment (Chapter 6)
- 2015 Laboratory Data Collection via GoPro® cameras (Chapter 7 and Appendix K)
- Recommendations (8)

8.2 Recommendations

The results of research demonstrate the benefit of structural monitoring for short-term bridge monitoring and the potential benefit for long-term monitoring, specifically the use of a calibrated 3D structural model for bridge decision making. The application procedure required for the foil strain gauge may its application but the non contact nature of the digital imaging lends itself to wide application to New Hampshire bridges. This research supports the expansion of digital image correlation as a tool for finding load distribution within a bridge and the results load rating.

GoPro® cameras for digital imaging for strain measurement proved useful for in-service monitoring. Structural modeling is growing acceptance are the preferred means of structural response prediction. The combination of these two emerging field could potentially provide a significant increase the effectiveness and efficiency of bridge management. This technology is low-cost and ease to use with ubiquitous technology, which would facilitate its inclusion into routine bridge inspections and overall bridge management.

The Bridge Engineering Center at Iowa State University performed diagnostic load testing on 12 bridges that were posted as a reduced load capacity. The results of the diagnostic tests and subsequent post-processing showed that six of 12 bridges did not require load posting. See http://www.bec.iastate.edu/bridgeembargoes/Hosteng_BridgeEmbargoes_T2.pdf for additional details. The use of GoPro® camera of structural modeling would reduce the cost of diagnostic load testing without decreasing the benefit.

References

American Society of Civil Engineers. 2013. *2013 Report Card for America's Infrastructure.* Washington, D.C.: ASCE.

Attanayake, U., P. Tang, A. Servi, and H. Aktan. 2011. "Non-Contact Bridge Deflection Measurement:." *Structural Engineeringand Construction Management 2011.* Kandy, Sri Lanka: ICSECM. 11-63.

Barr, P., and M. Eberhard. 2001. "Live-load Distribution Factors in Prestressed Concrte Girder Bridges." *Journal of Bridge Engineering* 298-306.

Brogan, P. 2010. *Digital Image Correlation Application to Structural Health Monitoring.* Durham: University of New Hampshire.

Brownjohn, J. 2006. "Structural Health Monitoring of Civil Infrastructure." *Philisophical Transactions: Mathematical, Phsyical and Engineering Sciences* 589-622.

Busca, G., A. Cigada, E. Mazzoleni, E. Zappa, and M. Franzi. 2012. "Cameras as displacement sensors to get the." *6th International Conference of Bridge Maintenance, Safety and Management.* Stresa: IABMAS. 2835-2841.

Cai, C. S. 2005. "AASHTO LRFD Load Distribution Factors for Slab-on-Girder Bridges." *Practice Periodcal on Structural Design and Construction*, 171-176.

Cardini, A., and J. DeWolf. 2009. "Implementation of a Long-term Weigh-in-Motion System for a Steel Girder Bridge in the Interstate Highway System." *Journal of Bridge Engineering* 418-423.

Cardini, A., and J. DeWolf. 2009. "Long Term Structural Health Monitoring of a Multi-Girder Steel Composite Bridge Using Strain Data." *Structural Health Monitoring* 47-58.

Correlated Solutions. 2015. *Youtube.* January. Accessed July 6, 2015. https://www.youtube.com/watch?v=1J6U5NOgF20 .

DeWolf, J., M. Culmo, and R. Lauzon. 1998. "Connecticut's Bridge Infrastructure Monitoring Program for Assessment." *Journal of Infrastructure Systems* 86-90.

Eamon, C. D., and A. S. Nowak. 2002. "Effects of Edge-Stiffening Elements and Diaphragms on Bridge Resistance and Load Distribtuion." *Journal of Bridge Engineering* 258-266.

EO-MINERS. 2013. *Overview of Remote Sensing.* Accessed July 2, 2015. http://www.eo-miners.eu/earth_observation/eo_eof_rst_techniques.htm.

Farrar, C., and K. Worden. 2007. "An Introduction to Structural Health Monitoring." *Philosophical Transactions: Mathematical, Physical and Engineering Sciences, Vol. 365* 303-315.

Farrar, C., D. Doebling, and D. Nix. 2001. "Vibration-based Structural Damage Identification." *Philisophical Transactions: Methematical, Physical and Engineering Sciences* 135.

Farrar, C., D. Doebling, and D. Nix. 2001. "Vibration-Based Structural Damage Identification." *Philisophical Transactions: Mathematical, Physical and Engineering Sciences, Vol. 359* 135.

French, C., C. Shield, H. Stolarski, and B. Hedegaard. 2011. "I35W Collapse, Rebuild, and Structural Health Monitoring - Challenges Associated with Structural Health Monitoring of Bridges." *AIP Conference Preceedings Vol. 1335*. American Institute of Physics. 9-30.

García-Palencia, A., and E. Santini-Bell. 2012. "A Two-Step Model Updating Algorith for Damped Structures."

Geo Instruments. 2009. *Embedment Vibrating Wire Strain Gauge*. November 01. Accessed July 12, 2012. http://www.geo-instruments.com/products_HTML/data_Sheets/strain/embedment_Strain_Gauge.pdf.

Graybeal, B.A., B. M. Phares, D. D. Rolander, M. Moore, and G. Washer. 2002. "Visual Inspection of highway bridges." *Journal of Nondestructive Evaluation* 67-83.

Greene, L. 2001. *St. Petersburg Times*. Feb 16. Accessed July 2, 2015. http://www.sptimes.com/News/021601/TampaBay/Face_scans_match_few_.shtml. .

Harrison, D. 2007. *Bridge of Medieval England: Transport and Society 400-1800*. Oxford, GBR: Oxford University Press, UK.

Hearfield, J. 2015. *John Hearfield*. July 2. http://www.johnhearfield.com/History/Breadt.htm.

Howell, D., and H. Shenton. 2006. "System for In-Service Strain Monitoring of Ordinary Bridges." *Journal of Bridge Engineering* 673-680.

Johnson, G., and I. Robertson. 2007. *Structural Health Monitoring Systems for Civil and Architechtural Structures: LVDT-Taut-Wire Baselines, Crack Monitoring Devices, & Strain Based Deflection Monitoring Algorithms*. Honolulu: University of Hawaii.

Kuntz, M., M. Jolin, J. Bastien, F. Perez, and F. Hild. 2006. "Digital image correlation analysis of crack behavior in a reinforced concrete beam during a load test." *Canadian Journal of Civil Engineering* 1418-1425.

Lefebvre, P. 2010. *The Instrumentation, Testing, and Structural Modeling of a Steel Girder Bridge for Long-Term Structural Health Monitoring*. Durham, NH: University of New Hampshire.

Liu, C., J. Olund, A. Cardini, P. D'Attilio, E. Feldblum, and J. DeWolf. 2008. "Structural Health Monitoring of Bridges in the State of Connecticut." *Earthquake Engineering and Engineering Vibration vol. 7, No. 4* 427-437.

Mabsout, M. E., K. M. Tarhini, G. R. Frederick, and A. Kesserwan. 1997. "Influence of Sidewalks and railings on Wheel Load Distribution in Steel Girder Bridges." *Journal of Bridge Engineering* 88-96.

Murray, W., and W. Miller. 1992. *The Bonded Electrical Resistance Strain Gage*. New York: Oxford University Press.

National Instruments. 2010. "Compare NI DAQ Products." *ni.com*. Accessed July 14, 2012. http://www.ni.com/data-acquisition/compare/.

—. n.d. *Deploying from USB to Embedded with NI C Series Hardware*. Accessed July 10, 2012. http://www.ni.com/white-paper/6418/en#toc6.

NCHRP. 2009. *Bridge Management Systems for Transportation Agency Decision Making*. Synthesis No. 397, Washington, D.C.: NCHRP.

NH DOT Bureau of Bridge Design. 2010. "Bridge Reconstruction Notes." *State Project 14461*. Concord , NH.

O'Haver, T.C. 2008. *Wheatstone Bridge*. Accessed July 14, 2012. http://terpconnect.umd.edu/~toh/ElectroSim/Wheatstone.html.

Olund, J., and J. DeWolf. 2007. "Passive Structural Health Monitoring of Connecticut's Bridge Infrastructure." *Journal of Infrastructure Engineering* 330-339.

Omega Engineering Inc. n.d. *Introduction to Strain Gauges*. Accessed July 12, 2012. http://www.omega.com/prodinfo/straingages.html.

Omega Engineering, Inc. n.d. *Thermocouple Connector Standard Size Round 2 Pin includes Integral Cable Clamp Cap*. Accessed July 12, 2012. http://www.omega.com/pptst/OSTW-CC.html.

Peddle, J. 2011. *Digital Image Correlation as a Tool for Bridge Load Rating and Long Term Evaluation*. Durham NH: University of New Hampshire.

PXISA. 2012. *The PXI Systems Alliance*. Accessed July 10, 2012. http://www.pxisa.org/.

Radio-Electronics.com. n.d. Accessed July 11, 2012. http://www.radio-electronics.com/info/t_and_m/pxi/pxi.php.

Santini-Bell, Erin, Paul Lefebvre, Masoud Sanayei, Brian Brenner, Jesse Sipple, and Jason Peddle. 2012. "Pbjective Load Rating of a Steel Girder Bridge Using Structural Modeling and Health Monitoring." *Journal of Structural Engineering* TBD.

Sipple, J. 2007. *Structural Modeling and Monitoring of the Rollins Road Bridge for Condition Assessment*. Durham NH: University of New Hampshire.

Suhun, K., P. Shamin, D. Culler, J. Demmel, G. Fenves, S. Glaser, and M. Turon. 2012. *Structural Health Monitoring of the Golden Gate Bridge.* http://www.cs.berkeley.edu/~binetude/ggb/.

Sutton, M. 2009. *Image Correlation for Shape, Motion, and Deformation Measurements: Basic Concepts, Theory and Applications.* Washington, D.C.: Springer.

Taylor, R. M. 2002. "Tiber River Bridges and the Development of the Ancient City of Rome." In *Waters of Rome*, 1-20.

Waterfall, P. W., J.H. G. MacDonald, and N. J. McCormick. 2012. "Targetless Precision Monitoring of Road and Rail Bridges using Video Cameras." *6th International Conference on Bridge Maintenance, Safety and Mangement.* Stresa: IABMAS. 3976-3982.

Weather Underground. 2012. *History.* Accessed March 22, 2012. http://www.wunderground.com/history/airport/KPSM/2012/7/24/DailyHistory.html?req_city=Durham&req_state=NH&req_statename=New+Hampshire.

WSDOT. 2005. *Tacoma Narrows Bridge.* http://www.wsdot.wa.gov/TNBhistory/Machine/machine3.htm.

Yoneyama, S., A. Kitagawa, S. Iwata, K. Tani, and H. Kikuta. 2007. "Bridge Deflection Measurement using Digital Image Correlation." *Experimental Techniques* 34-40.

Yousif, Z., and R. Hindi. 2007. "AASHTO-LRFD Live Load Distribution for Beam-and-Slab Bridges: Limitations and Applicability." *Journal of Bridge Engineering* 765-773.

APPENDIX A: Gilford Structural Health Monitoring System Design

This section includes the considerations and design for the Gilford Bridge SHM system. Strain monitoring was chosen to support long-term monitoring by locating neutral axis and for research related to sensor supported construction by providing data to calculate curvature.

A.1 General Considerations

A set of instruments under each panel was initially considered. With more gauges, better information about load distribution and curvature could be detected; however, the costs of equipment and times required for installation can quickly become unreasonable. Ultimately, locations under 3 of the 9 panels were selected. The most valuable location was at the center span of each beam. Because damage to the system was possible during the demolition of the old deck and no repairs could be made between that time and the time panels were placed, redundancy for the most valuable location was needed. By incorporating extra pairs of gauges at the center span of each beam, the total pairs of strain gauges on each beam rose to 4.

Temperature measurements would also be required for calibration of the strain measurements. By measuring temperature at the two exterior beams of the bridge and at the center beam, temperature variations across the width of the deck could be detected. Temperature gauges would also be placed in pairs at location to detect a linear variation throughout the depth of the superstructure. This evaluation led to a total of 56 strain gauges and 6 temperature gauges.

In addition to creating a need for redundancy in the sensor network, the demolition of the existing deck also placed a unique demand on connectivity. Typically, conduit used to carry wires for SHM systems are designed to hide wires and provide some basic environmental protection. At the Gilford Bridge the network would also have to provide protection from falling debris. Schedule 40 PVC pipe was chosen as a relatively inexpensive conduit system to carry wires. Each piece of the PVC system would include a quarter inch slit for placing wires after the conduit was installed, and to provide access needed for any repairs that may be required during the lifetime of the SHM system. When the pipe was installed the slit would be angled slightly downward to prevent debris or water from falling and accumulating in the pipe as shown in Figure A-1.
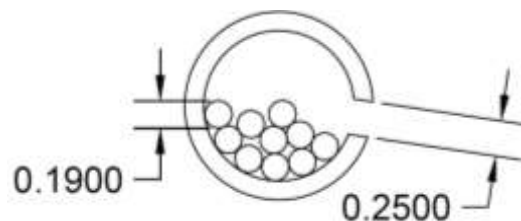
Figure A-1: Illustrated Proposed Hard Conduit Cross Section

A.2 Proposed Long-term Monitoring Network Design

This section refers to drawings that are included at the end of this appendix

Figure A-5 shows the plan view of the proposed sensor network with labeled sensors. The labels are formatted so that each gauge has a unique ID that captures the beam and station the gauge is on. The first number represents the station, and the letter represents the beam. The second number represents the number of the sensors that would then be locatable in a reference document. Figure A-6 and Figure A-7 are beam elevations for locating the stations when facing west or east from the center of the bridge.

Figure A-8 shows cross sections of all proposed gauge locations on interior and exterior beams. Note that the maximum number of gauges is shown only for dimensioning and that, as shown in Figure A-5, most stations have fewer gauges. In the case of exterior beams where stations 1 and 3 have fewer gauges, the proposed strain gauge locations closest to the beam web are recommended for instrumentation so that out-of-plane bending has a lower effect. In the cases of interior beams, the face of the beam being instrumented may be affected by confinement issues, which are detailed below.

The distance between the top of the bottom stringer flanges and the bottom of the connections to the diaphragms is not specified on the original plans. Therefore, several diameters of conduit are under consideration for Gilford. Smaller diameters will have a better chance of fitting under the connectors but will leave less room inside of the pipe for wires, which could make repairs to the system more difficult. Figure A-9 shows the varying proposed diameters with the number of THX-400 wires. The wires are illustrated as both distributed throughout the section of pipe and as they would rest on the bottom. The distributed graphic aims to display how much room might be available between wires, which might be of concern when trying to remove wires during maintenance.

Figure A-10 shows the conduit as it would fit under the most confined conditions that could be extrapolated from the original plans. The most confined conditions are defined by the 3" minimum between the bottom of the bottom flange and the bottom of the channel that is the diaphragm, which means the diaphragm could be close to the bottom flange. Furthermore, since the connection isn't detailed, the rectangular plate could be as close to the bottom as the top of the fillet, which is roughly an inch for W36x194 beams. Given tolerances in manufacturing, this could create a space confined to just 1", which would not allow for even ¾" diameter PVC, which has an outside diameter of 1.050".

It can be seen in Figure A-10 that the stepped elevations of beams to create the crown in the deck means that the confinement only affects one side of the beam and that any proposed size pipe could comfortably fit on the opposite beam face, with the exception of the center girder. This means that for stations 1 and 3, the side of the beam facing the inside of the bridge can be instrumented on 6 of the girders to avoid confinement. As for station 2, where redundant gauges are recommended, both beam faces should be instrumented to capture possible out of plane

bending, with the exception of the exterior girder, where all gauges will be installed on the inside face to preserve aesthetics. This means that clearance issues may arise in 7 locations; at 1 diaphragm connector on the exterior faces of beams B, C, E, and F, as well as 3 diaphragm connectors on beam D.

Figure A-2 through Figure A-4 show potential solutions where confinement issues may be inevitable. They include using flexible conduit or leaving the wire bare at the location of the diaphragm connectors.
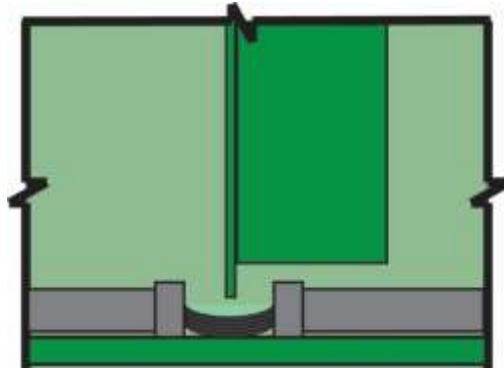
Figure A-2: Gilford Bridge – Illustration of Exposed Wired Option for Dealing with Hard Conduit Clearance Issues
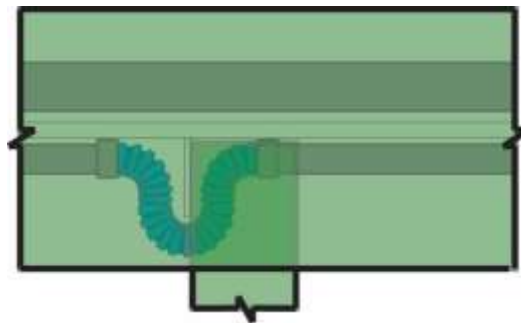
Figure A-3: Gilford Bridge – Illustration of Flexible Conduit Option 1 for Dealing with Hard Conduit Clearance Issues
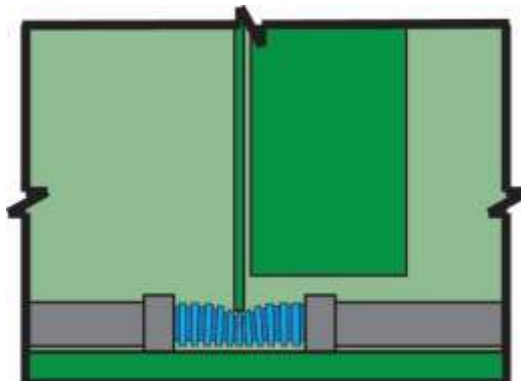
Figure A-4: Gilford Bridge – Illustration of Flexible Conduit Option 1 for Dealing with Hard Conduit Clearance Issues

Figure A-11 shows a proposed method of protecting strain gauge locations. The method would use a piece of cold formed steel bent in a Z shape to cover the location where the conduit is discontinuous and the gauge is bonded to the steel. Figure A-12 shows a version of the same method where the netting obstacle has resulted in the conduit being raised and attached to a location higher on the beam web. As shown in the figure, a hole would be required in the plate for the lead wire. Furthermore, the discontinuity in the pipe would no longer be covered, however, at a high enough location the top flange may be able to provide enough protection from construction debris.

Table A-1 and Table A-2 show the proposed designations for DAQ equipment purchased for this project. Two 8 card chassis are recommended for permanent installation at Gilford. The tables show the proposed connectivity of each channel, in each card, of each chassis in 2 scenarios. The first is prior to construction where 4 strain reading cards would be used at UNH to experiment with the equipment and prepare for construction. In this scenario, 4 of the card slots are used for varying purposes including testing the redundant gauges by switching them out with primary gauges, evaluating quarter bridge gauges and gauge effects on the web, and potential dynamic research with accelerometers. The second scenario occurs during construction where all redundant gauges must be read, which will require all 14 strain cards.

The following labels are used in the table:

- QTR: reserved for investigating quarter bridge gauges
- Web: reserved for investigating strain gauges on web
- Switch: used to test redundant gauges
- Accelerometer: used for dynamic research
- Gauge ID: previously described gauge ID (see Figure A-5), for example 1D1
- Dummy1 & Dummy2: thermocouple channels for use to be decided

A.3 Considerations for proposed Gilford SHM systems based on this research

A reduced sensor network has been proposed for Gilford. Although the system would be installed in a significantly shorter period, there would be several sacrifices. The reduction would place gauges only on the bottom of the bottom flange of the stringers, avoiding the netting obstacle and providing enough cover to negate the need for a complicated hard conduit system. Figure A-13 illustrates the gauge as installed on the bottom of the bottom flange. The system would only be capable of short term monitoring as the instrumented locations could be struck by vehicles in the future, and the location of the wires and gauges would be visible, affecting the aesthetics of the bridge. The system would not be capable of determining neutral axis location so it could not verify things like composite action.

Installing the system solely to predict curvature has not been proven and, therefore, the risk of installing it for no benefit reduces the worth of the system compared to the more complicated installation of the larger system. However, if the system is still reduced to just the bottom flange,

106

this research suggests that either 2 gauges should be installed or the gauges should be installed at the neutral axis of weak bending because both beams D and E showed differences in measurements on the bottom flange. 2 gauges might be able to pick up an off-center placement of a leveling screw because of warping due to eccentric loading but will require the placement of 42 gauges if all the original intended locations are to be instrumented.

The long term monitoring system has several potential benefits that should be considered when deciding the fate of the sensor network that will ultimately be installed in Gilford. The system would certainly be useful after construction as it could be used to prove that the new deck installation procedure improved the overall condition of the bridge. The continuous monitoring system could be used in the following decade to show that the risk of using new construction processes did not come at the price of a structure that degrades at an accelerated rate. Lastly, the sensor network would provide valuable data about steel behavior before, during, and after maintenance. That data could be used to evaluate the location of the neutral axis in a severely deteriorated structure versus a rehabilitated structure using the same equipment in a short period of time and the stress on the steel from the placement of slabs on the old steel.

Table A-1: Proposed Equipment Configurations Prior to Gilford Construction Project

Chassis1		
Card	Channel	Gauge
1	0	1A1
	1	1A2
	2	2A1
	3	2A2
2	0	3A1
	1	3A2
	2	1B1
	3	1B2
3	0	2B1
	1	2B2
	2	3B1
	3	3B2
4	0	1C1
	1	1C2
	2	2C1
	3	2C2
5	0	3C1
	1	3C2
	2	1D1
	3	1D2
6	0	2D1
	1	2D2
	2	3D1
	3	3D2
7	0	UNH
	1	UNH
	2	UNH
	3	UNH
8	0	UNH
	1	UNH
	2	UNH
	3	UNH

Chassis2		
Card	Channel	Gauge
1	0	1E1
	1	1E2
	2	2E1
	3	2E2
2	0	3E1
	1	3E2
	2	1F1
	3	1F2
3	0	2F1
	1	2F2
	2	3F1
	3	3F2
4	0	1G1
	1	1G2
	2	2G1
	3	2G2
5	0	3G1
	1	3G2
	2	QTR
	3	QTR
6	0	Web
	1	Web
	2	Switch
	3	Switch
7	0	Accel.
	1	Accel.
	2	Accel.
	3	Accel.
8	0	1A3
	1	1A4
	2	3A3
	3	3A4
	4	1D3
	5	1D4
	6	2D5
	7	2D6
	8	3D3
	9	3D4
	10	1G3
	11	1G4
	12	3G3
	13	3G4
	14	Dummy1
	15	Dummy2

Table A-2: Proposed Equipment Configurations during Gilford Construction Project

Chassis1		
Card	Channel	Gauge
1	0	1A1
	1	1A2
	2	2A1
	3	2A2
2	0	3A1
	1	3A2
	2	1B1
	3	1B2
3	0	2B1
	1	2B2
	2	3B1
	3	3B2
4	0	1C1
	1	1C2
	2	2C1
	3	2C2
5	0	3C1
	1	3C2
	2	1D1
	3	1D2
6	0	2D1
	1	2D2
	2	3D1
	3	3D2
7	0	2A3
	1	2A4
	2	2B3
	3	2B4
8	0	2C3
	1	2C4
	2	2D1
	3	2D4

Chassis2		
Card	Channel	Gauge
1	0	1E1
	1	1E2
	2	2E1
	3	2E2
2	0	3E1
	1	3E2
	2	1F1
	3	1F2
3	0	2F1
	1	2F2
	2	3F1
	3	3F2
4	0	1G1
	1	1G2
	2	2G1
	3	2G2
5	0	3G1
	1	3G2
	2	2E3
	3	2E4
6	0	2F3
	1	2F4
	2	2G3
	3	2G4
7	0	Accel.
	1	Accel.
	2	Accel.
	3	Accel.
8	0	1A3
	1	1A4
	2	3A3
	3	3A4
	4	1D3
	5	1D4
	6	2D5
	7	2D6
	8	3D3
	9	3D4
	10	1G3
	11	1G4
	12	3G3
	13	3G4
	14	Dummy1
	15	Dummy2
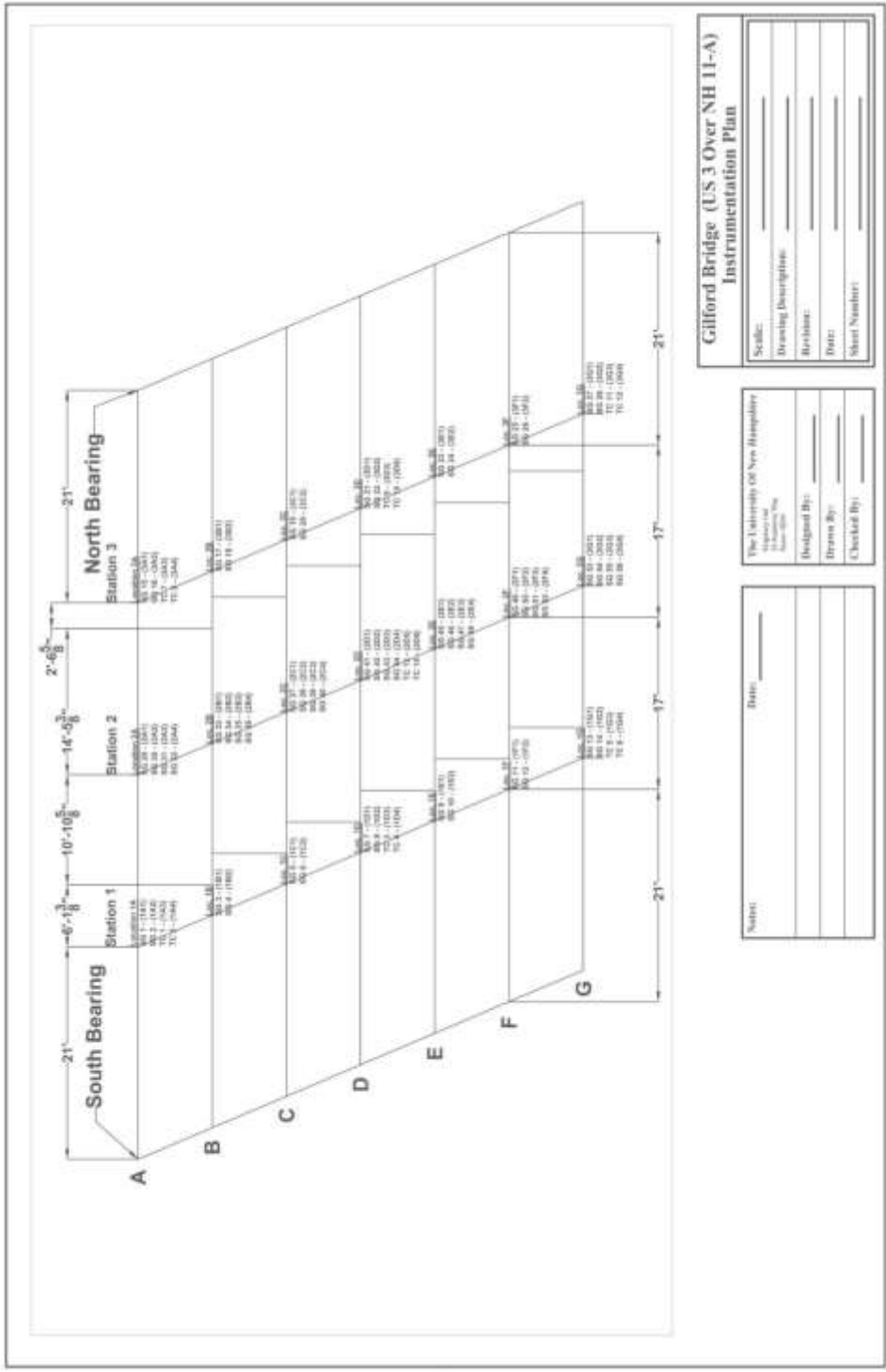
Figure A-5: Gilford Bridge – Proposed Instrumentation Plan View

110
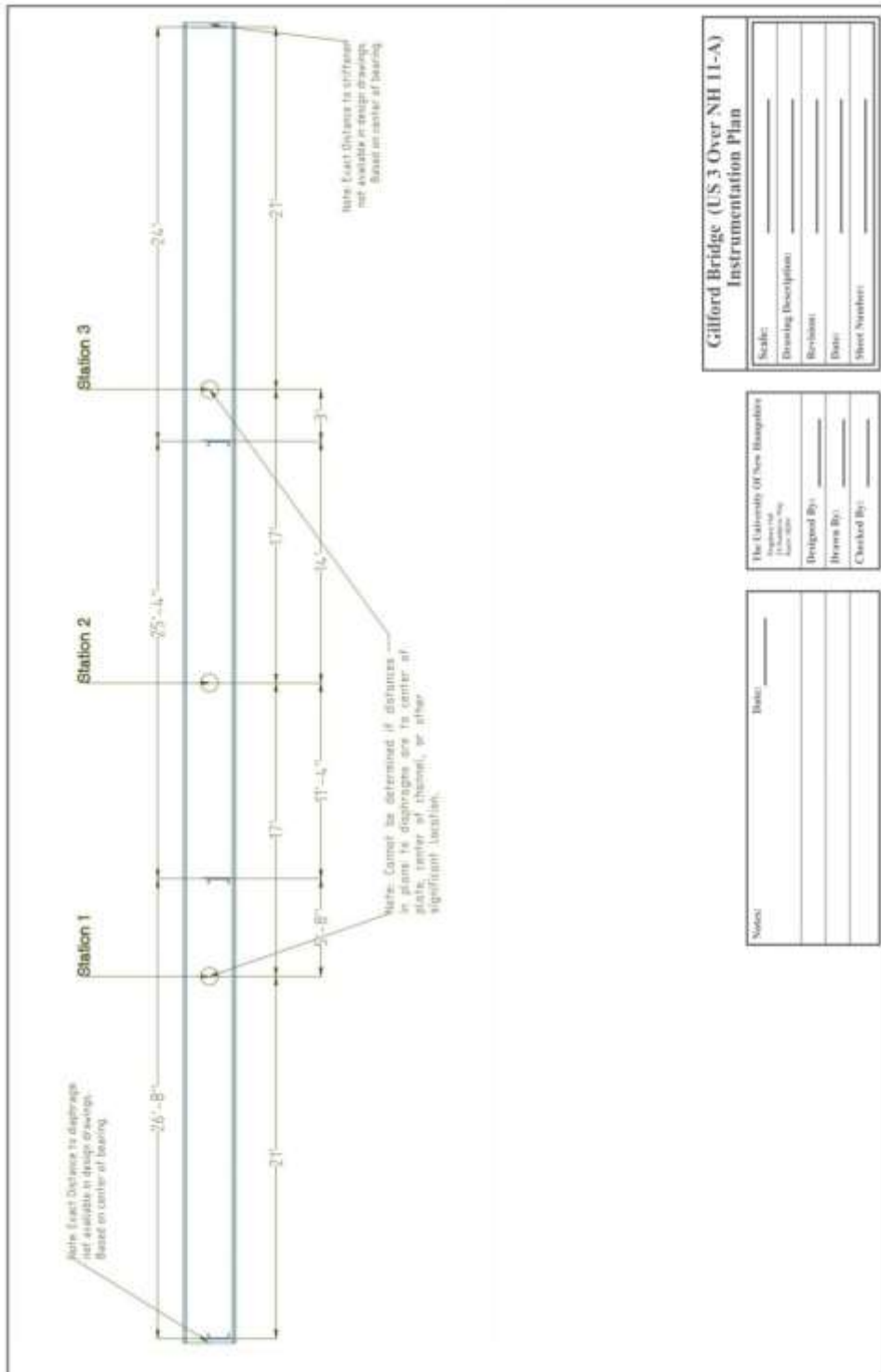
Figure A-6: Gilford Bridge – Proposed Instrumentation Beam Elevations, Facing West from Bridge Center
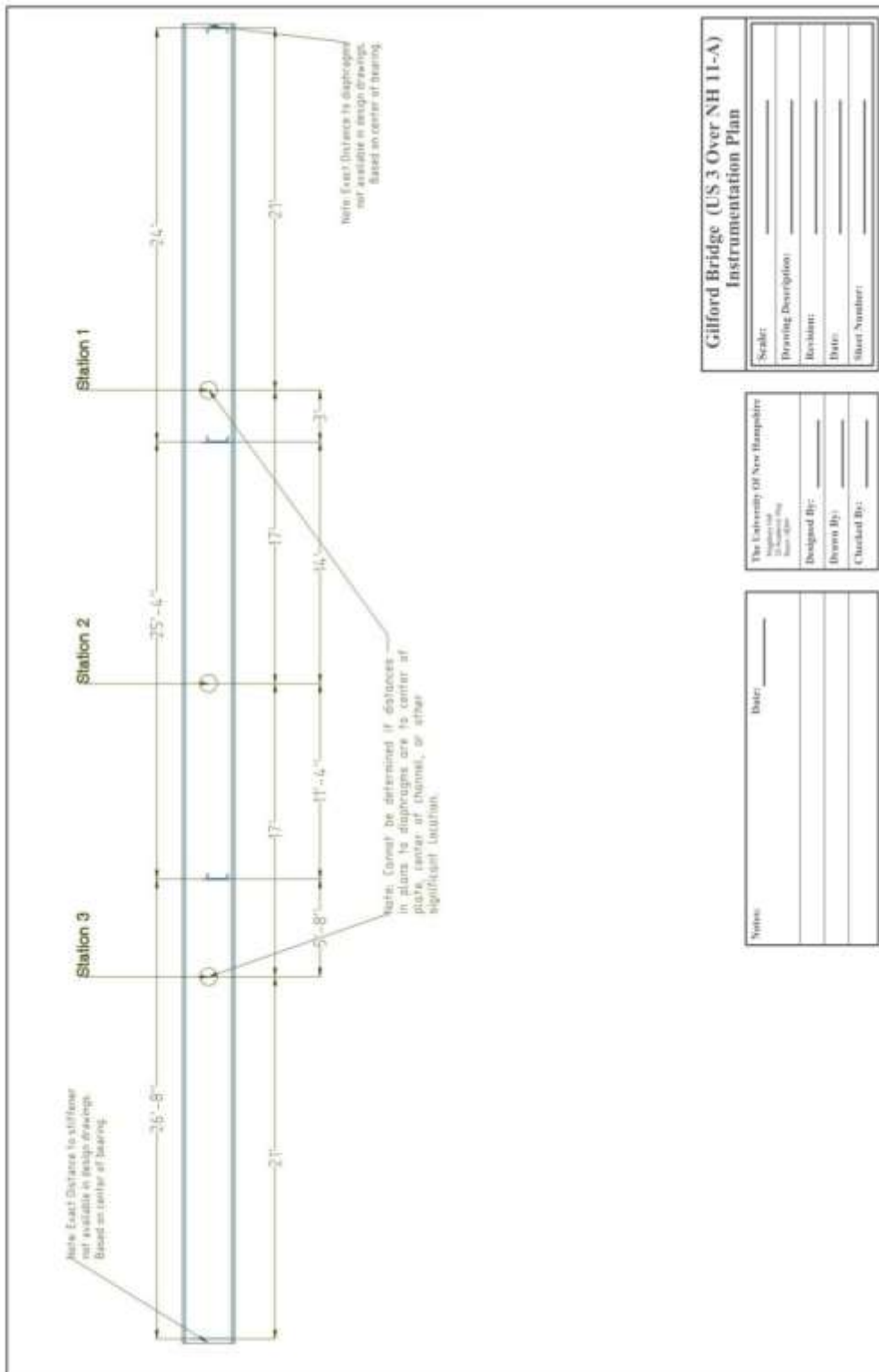
Figure A-7: Gilford Bridge – Proposed Instrumentation Beam Elevations, Facing East from Bridge Center
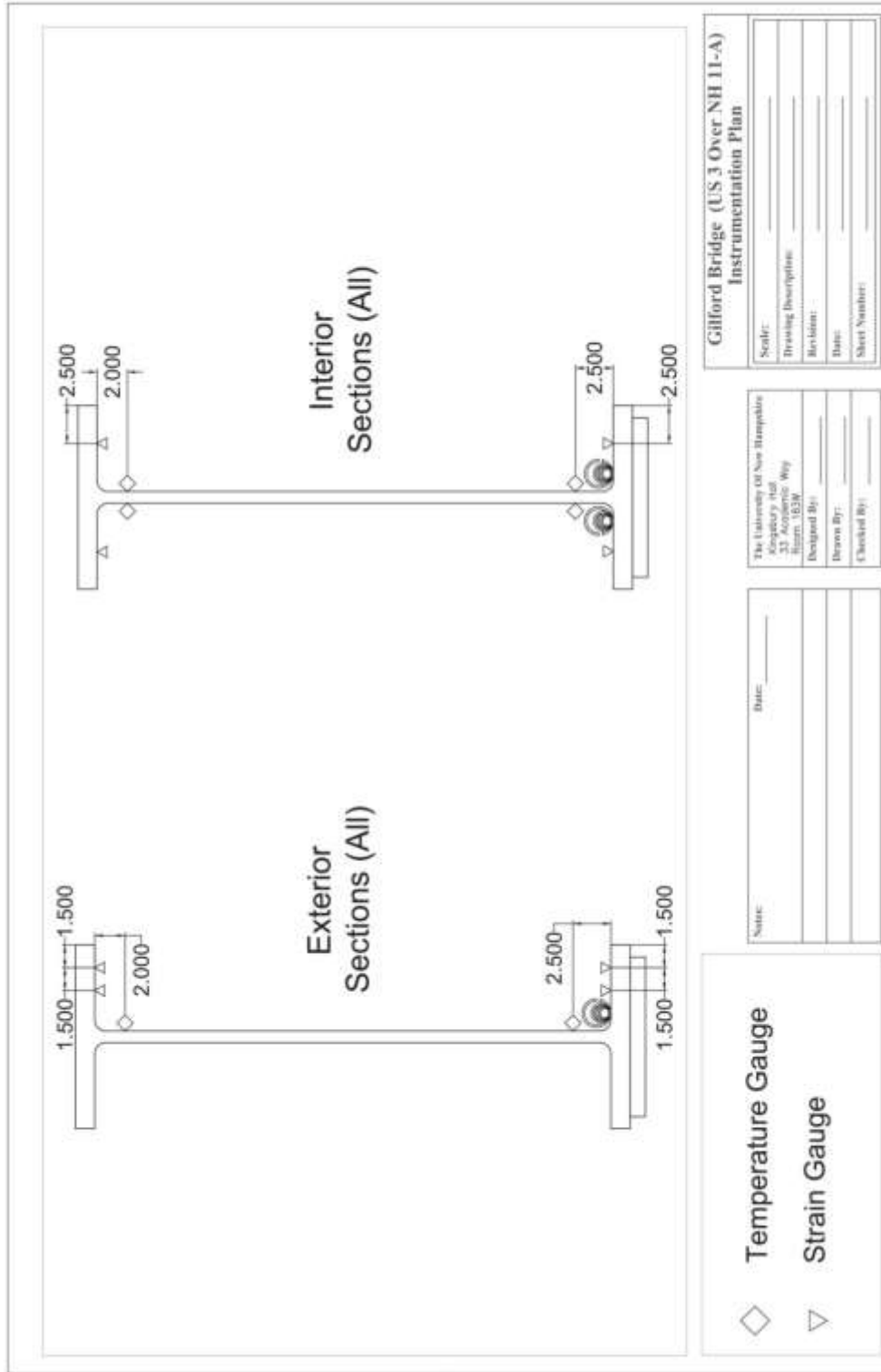
Figure A-8: Gilford Bridge – Proposed Cross Sections of Stations on Interior and Exterior Beams
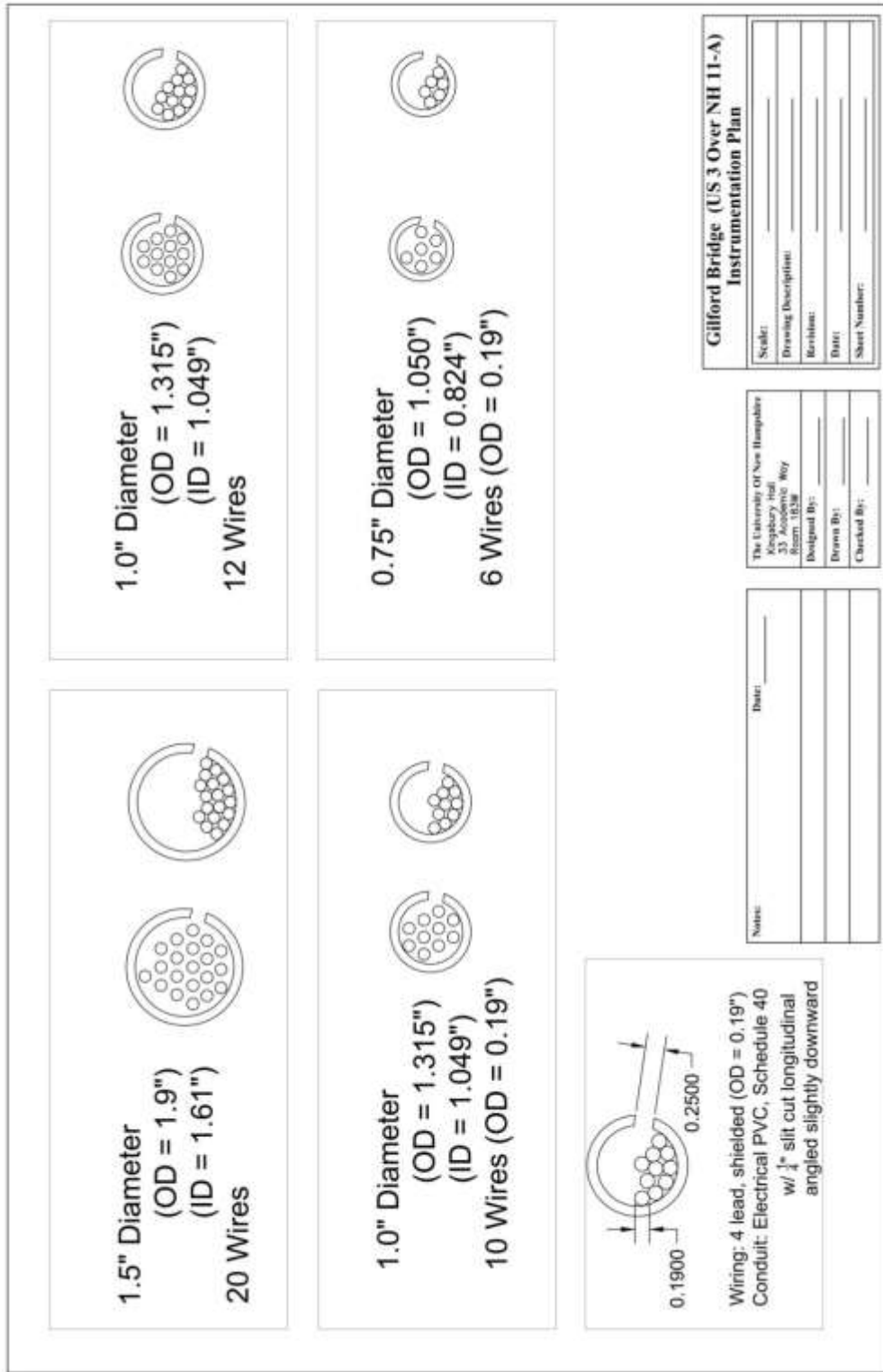
Figure A-9: Gilford Bridge – Drawing of Hard Conduit Diameter Options
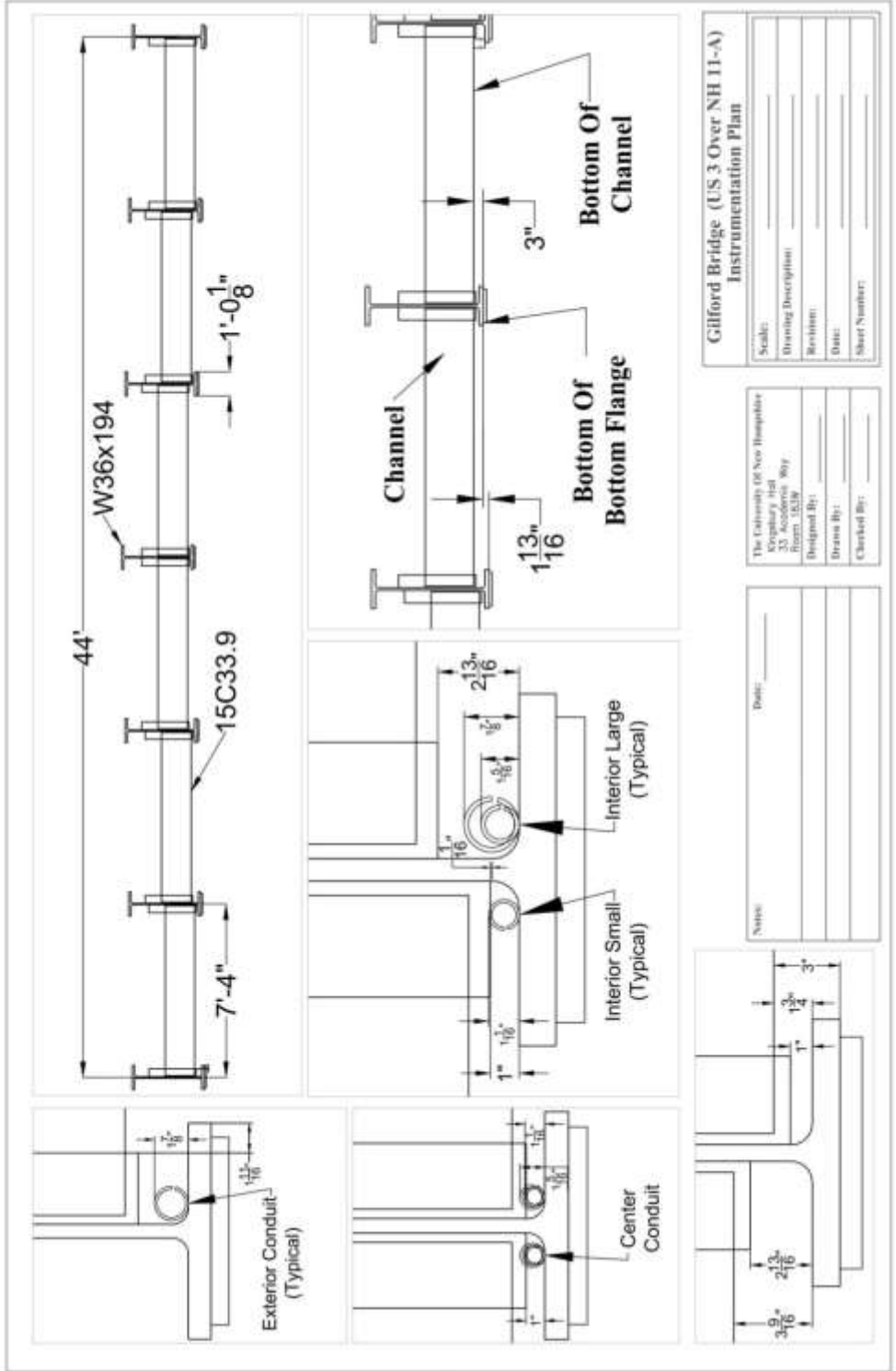
Figure A-10: Gilford Bridge – Drawing of Hard Conduit Options Displayed on Structural Steel Bridge Section
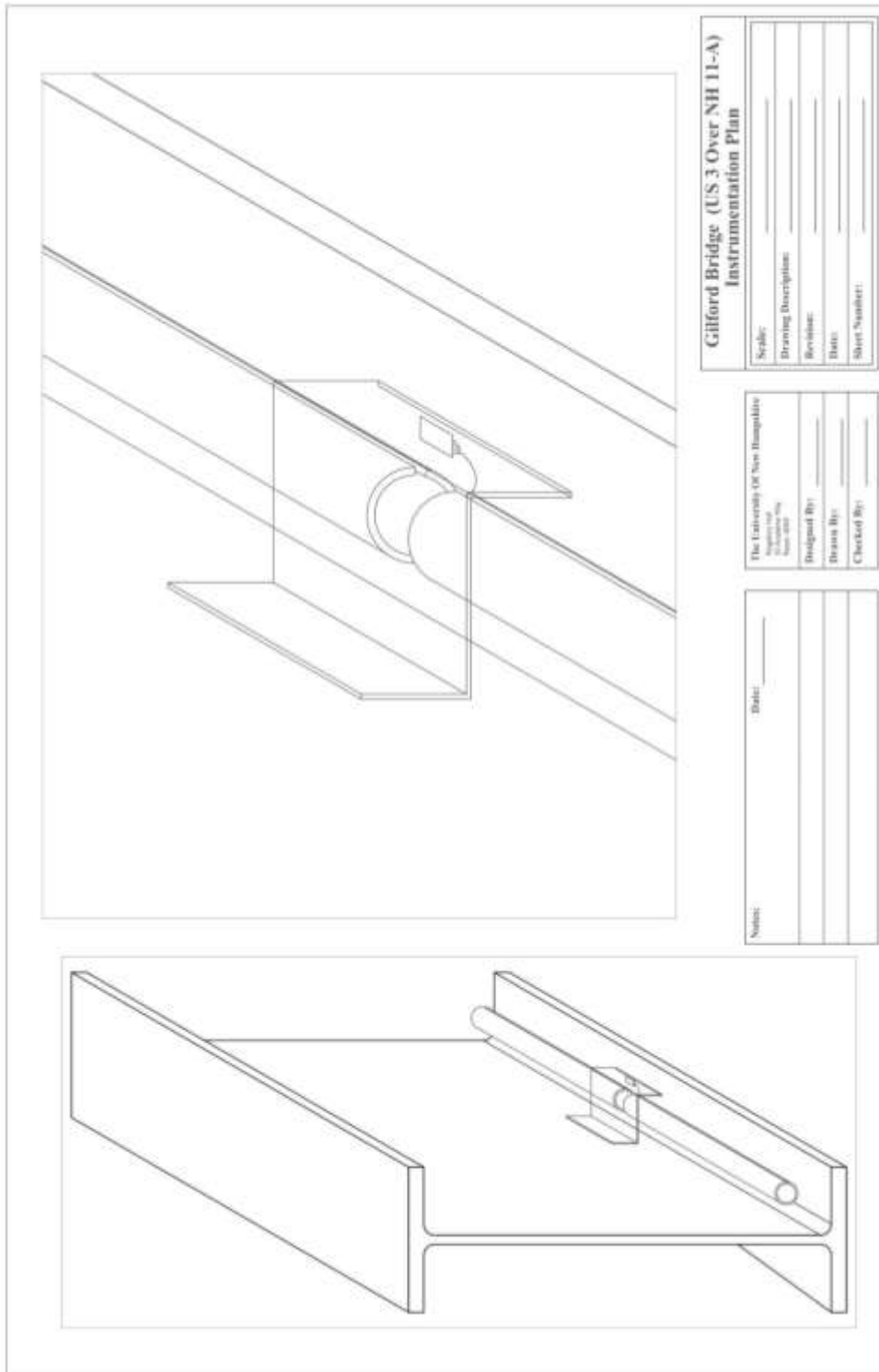
Figure A-11: Gilford Bridge – Drawing of Original Proposed method of Protecting Strain Gauged Location
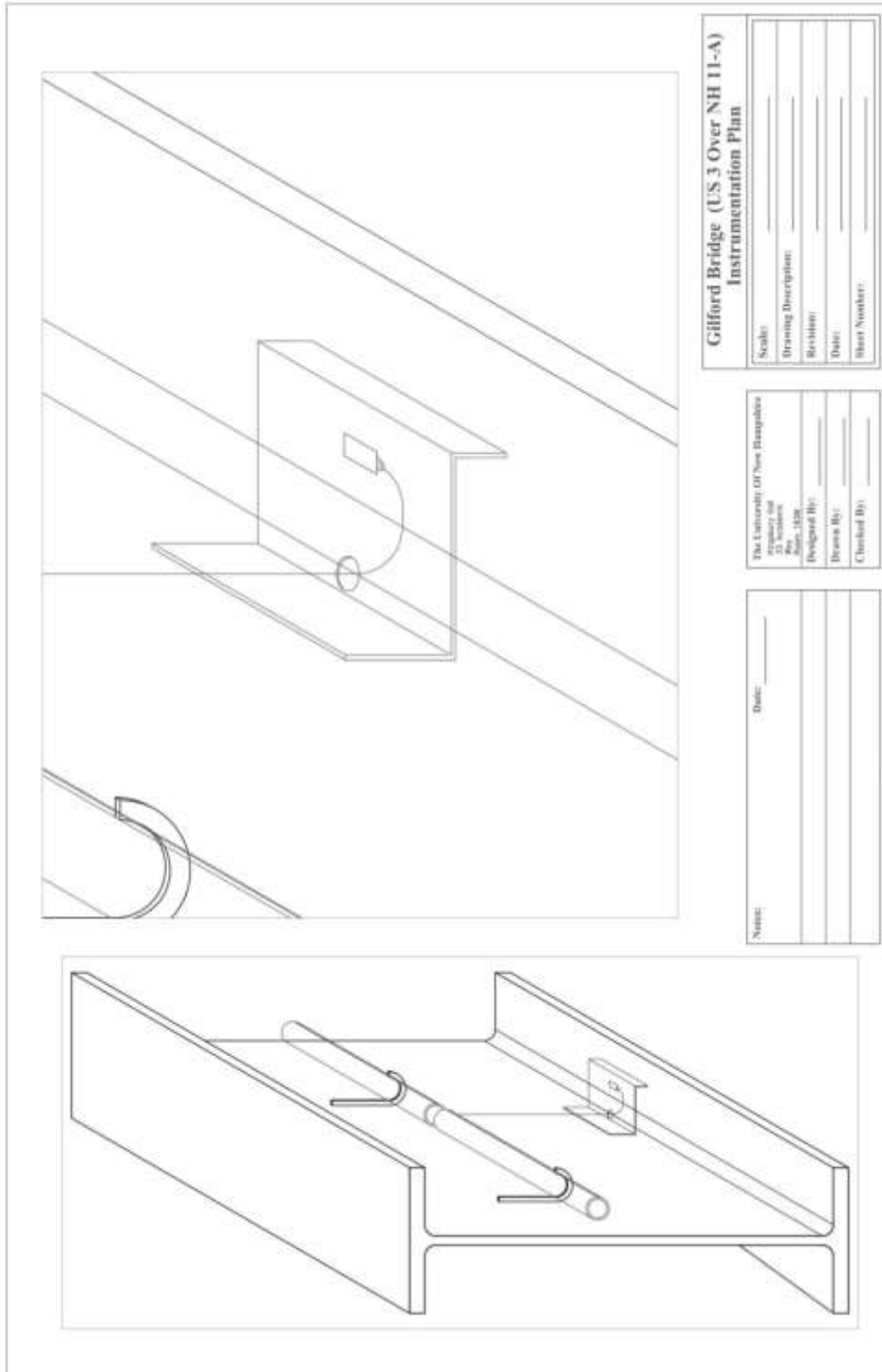
Figure A-12: Gilford Bridge – Drawing of Proposed Method for Raising Conduit above Netting
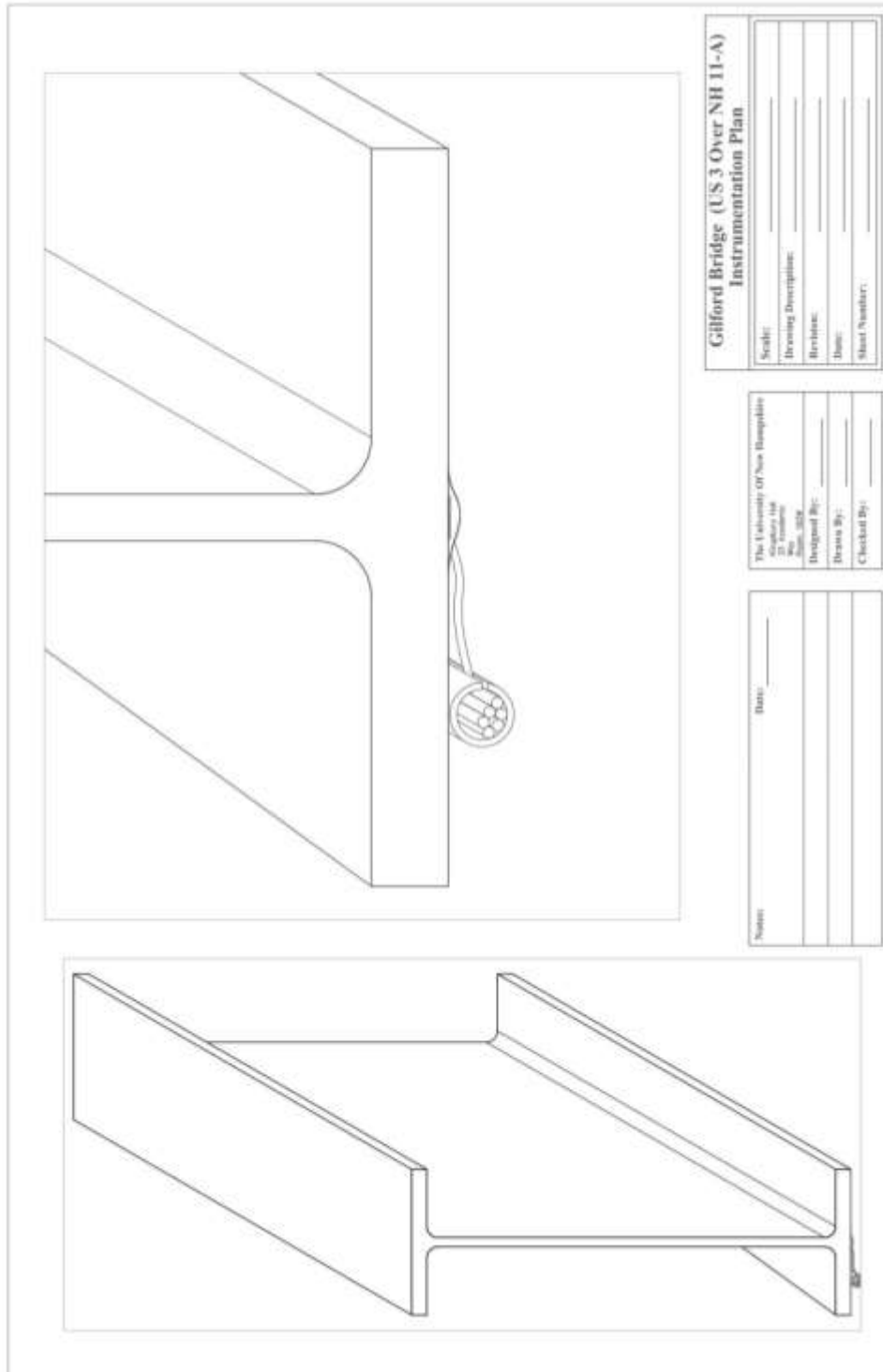
Figure A-13: Gilford Bridge – Drawing of Proposed Conduit Location for Short Term Monitoring at Gilford

APPENDIX B: Foil Strain Gauges

Foil strain gauges are traditional means for strain measurement, especially for in-service structures, such as bridges. This appendix will detail the inner working and mechanics of a foil strain gauge.

B.1 Basic Voltage Measurements Using Variable Resistance

Electrical resistance gauges function by using the change in conductivity a material will undergo as it deforms. An understanding of how the measurement is made is needed to identify and understand sources of error and make informed decisions during the gauge selection process.

Basic electrical measurements take advantage of Ohm's law. The law states that voltage (V) is the product of current (I) and resistance (R). The relationship is shown in equation B-1.

$$V = IR \qquad \text{(Eq: B-1)}$$

Figure B-1 illustrates a simple circuit featuring an excitation source and a single resistor. Current has been labeled with corresponding arrows to illustrate that it flows through the circuit.
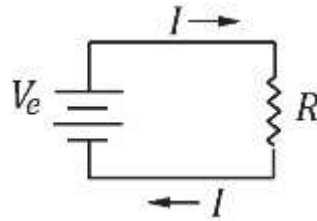
Figure B-1: Illustration of a Basic Circuit with 1 resistor

The hydraulic analogy is a widely used analogy for describing electrical circuits. The analogy describes energy as a type of fluid that flows through a circuit like pipes. In this analogy, the excitation is a source of pressure, or head as it's referred to in fluid mechanics. Current is the flow of this fluid. Similar to how flow in pipes and closed channels is constant, flow throughout the circuit is as well. If flow wasn't constant, fluid or electrons, would build up in the system which would require reservoirs or capacitors. Storing electrical fluid is not required for strain-based measurements so it won't be discussed further. Therefore, circuits mentioned here will feature a constant I.

When two resistors are connected in line with each other, what is known as "in series", their resistance values are additive as shown in equation B-2.

$$V = I(R_1 + R_2) \qquad \text{(Eq: B-2)}$$

Considering current is constant throughout a circuit, the equation highlights that voltage changes as it drops between resistors. Strictly speaking, voltage is the potential difference between two locations in an electrical circuit. That is what is also known as the electrical potential difference. Similar to how head pressure falls as fluid travels through clogged pipes or filters, voltage drops

across each resistor. The drop between resistors is also highlighted in the diagram of a voltage divider shown in Figure B-2.
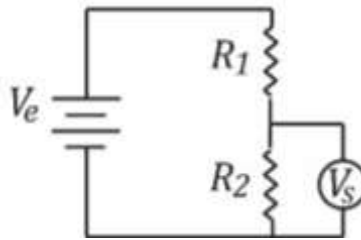
Figure B-2: Basic Voltage Divider 1

In equation B-3, V_s is a measure of voltage across the second resister, or the voltage signal. The measure of voltage signal relates to the excitation and the values of the resistors by the following equation:

$$V_s = \frac{R_2}{R_1 + R_2} \cdot V_e \qquad \text{(Eq: B-3)}$$

Looking at the equation for voltage signal, it can be seen how changes in resistance in either resistor can be determined if one resistance and the excitation is known or how both could be measured if they are related by some proportion. A bonded foil strain gauge essentially replaces one or more resistors in a circuit similar to this.

A bonded foil strain gauge functions when the filament within the gauge is subjected to the same elongation as the specimen that it is bonded to. Strain is transferred by shear forces in the rigid epoxy. The filament elongates, which changes the electrical conductivity of the filament for two reasons; both the physical elongation and the change in cross section of the filament due to Poisson's effect. Considering the hydraulic analogy, this is similar to how water pressure drops flowing through a longer and thinner pipe compared to a wider and shorter geometry.

B.2 The Wheatstone Bridge

The problem with measuring the voltage through the voltage divider described in the previous section is the measured value is that of both the voltage across the resistor, and the change in voltage as shown in Figure B-3:
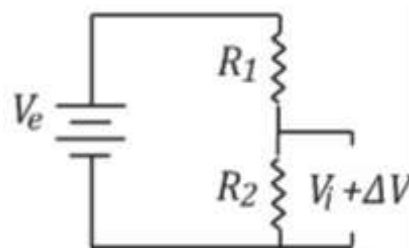
Figure B-3: Basic Voltage Divider 2

Because bonded foil gauges produce small changes in resistance, the change in voltage ΔV is relatively small. Thus the voltage across R_2, referred to as the steady state voltage (V_i), is typically much larger and subsequently errors in its measurements that would seem relatively small have a large impact on observations of ΔV. The influences of error in observing the steady state voltage make it desirable to isolate ΔV and measure that separately.

The Wheatstone bridge was not the first electronic circuit developed to isolate ΔV. Other circuits were developed that used auxiliary source to add voltage to the system in ways that reduced the steady state voltage, eventually low enough that it could be considered insignificant (Murray and Miller 1992). The Wheatstone bridge developed from those by using the same excitation voltage that powers the circuit to also supply the auxiliary voltage. The circuit is shown in Figure B-4:
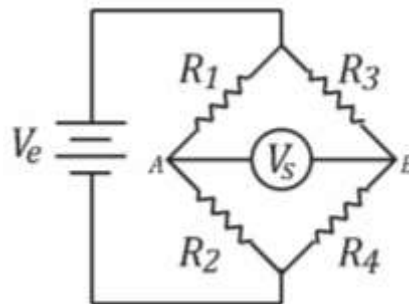
Figure B-4: Wheatstone Bridge Circuit

The Wheatstone bridge is essentially two voltage dividers connected in parallel. The voltage is measured between the two points that separately would be the initial point of voltage drop used in measuring voltage through a divider, points *A* and *B* (O'Haver 2008). The circuit can be used to completely eliminate the steady state voltage as is the case when the bridge is said to be balanced. When the bridge is unbalanced the steady state voltage is on the scale of the change in voltage and, therefore, errors in its observation do not cause unacceptable error.

To prove how voltage across the two points is equal to zero when the bridge is balanced requires the use of Kirchhoff's first and second law; however, a satisfactory understanding can be achieved by again utilizing the hydraulic analogy. In the hydraulic analogy, the Wheatstone bridge would be visually represented as a system of pipes as shown in Figure B-5 and Figure B-6.

121
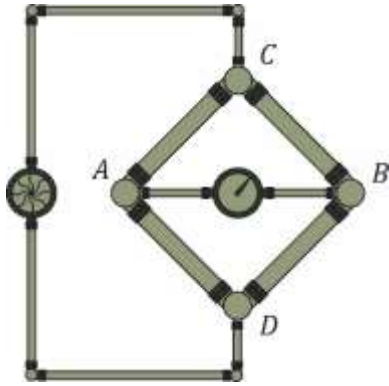
Figure B-5: Wheatstone Bridge in the Hydraulic Analogy
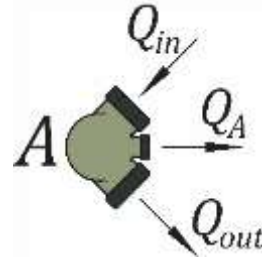
Figure B-6: Electrical Node in the Hydraulic analogy

In this analogy the source of excitation, or pressure, is a pump. If the head loss in all four pipes is the same, the meter between junctions A and B will not observe any flow. A closer inspection of the flow at either point A or B explains this. The summation of flows at this location must always equal zero. This is essentially Kirchhoff's first law. That is; the summation of current into any node equals the sum of the current out. If it does not then current would be stored at that location. If the resistance in any pipe changes, a potential across AB will form. The potential measured between junction A and B is a function of the two voltage dividers that make up the Wheatstone bridge. Equation B-4 shows the function for voltage across the meter.

$$V_s = \left(\frac{R_1}{R_1 + R_2} - \frac{R_3}{R_3 + R_4}\right) V_e \qquad \text{(Eq: B-4)}$$

A more detailed proof using Kirchhoff's first and second laws is follows and is based on Figure B-7.
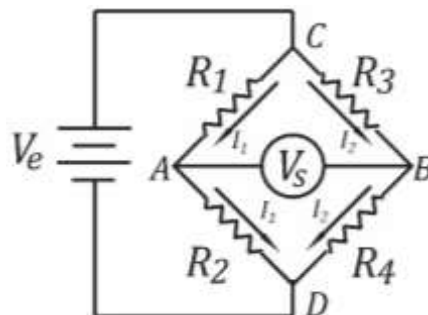
Figure B-7: Current Flow through a Wheatstone bridge Circuit

Kirchhoff's second law, otherwise known as Kirchhoff's loop law, states that the sum of potential around any closed network is zero. Because the current across AB is negligible due to the high

resistance of the meter, Kirchhoff's first law can be used to prove that the current across resistor 1, R_1, the current across resistor 2, R_2, the current across resistor 3, R_3, and the current across resistor 4, R_4, will be equal in a balanced bridge. Two closed loops exist in the Wheatstone bridge as shown in Figure B-7, the loop CAD and the loop CBD. The two loops provide the following equations:

$$V_e - I_1(R_1 + R_2) = 0 \qquad \text{(Eq: B-5)}$$

$$V_e - I_2(R_3 + R_4) = 0 \qquad \text{(Eq: B-6)}$$

Therefore:

$$I_1 = \frac{V_e}{(R_1 + R_2)} \qquad \text{(Eq: B-7)}$$

$$I_2 = \frac{V_e}{(R_3 + R_4)} \qquad \text{(Eq: B-8)}$$

The voltage V_s is a function of the difference in potentials in potential between AD and BD. That is:

$$V_s = V_{AD} - V_{BD} \qquad \text{(Eq: B-9)}$$

By using Ohm's law to convert voltages V_{AD} and V_{BD} yields:

$$V_s = R_2 I_1 - R_4 I_2 \qquad \text{(Eq: B-10)}$$

Substituting equations B-7 and B-8 into equation B-10 yields:

$$V_s = \frac{R_1}{R_1 + R_2} V_e - \frac{R_3}{R_3 + R_4} V_e \qquad \text{(Eq: B-11)}$$

Further simplifying equation B-11 by factoring out the excitation voltage V_e will yield equation B-4.

Equation B-4 shows how the steady state voltage can be eliminated with a balanced bridge. If each resistor in the bridge is equal, or if the proportion of R_1 to R_2 is equal to the proportion of R_3 to R_4, then the difference between statements is zero. The signal voltage would, therefore, be equal too:

$$V_s = (0)V_e$$

The only voltage being measured when the initial state is a balanced bridge is from a change in resistance of one or a combination of any of the resistors that make up the circuit.

B.3 The Bonded Foil Strain Gauge

The bonded foil strain gauge is a device that's been used to measure strains for various applications for many years. It functions by bonding to the surface of a material under strain with an application appropriate adhesive. The gauge has a thin filament inside of it that has a variable resistance. When the filament is stretched it both lengthens and becomes thinner due to Poisson's effect. The variable resistance is typically measured with a Wheatstone bridge. Changes in resistance are then converted into a strain value using a gauge factor. The general equation is

shown below. ΔR is the change in resistance, R_i is the initial resistance, GF is the gauge factor and ε is strain. The relationship is shown in equation B-12

$$\frac{\Delta R}{R_i} = GF \cdot \varepsilon \qquad \text{(Eq. B12)}$$

The filament inside of the gauge is made through a process known as etching. Typically etching involves covering a foil with an acid resistant chemical in a desired pattern. Then acid is poured over the foil until just the pattern remains. This creates a filament that is rectangular in cross section rather than cylindrical like in a wire (Murray and Miller 1992). The rectangular section has a larger surface area than a circular section would, which increases the area in contact with the carrier. The patterns can vary depending on the size of gauge and the type of strain the gauge will measure. Shown in Figure B-8, the pattern typically consists of several 180º turns that create several parallel filaments which further maximize contact area with the carrier matrix.
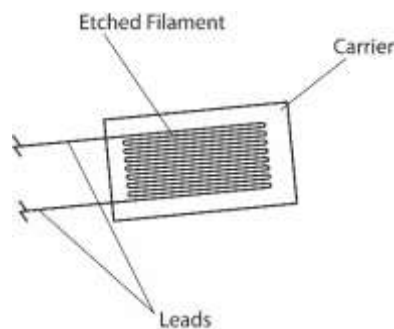
Figure B-8: Components of a Bonded Foil Strain Gauge

Figure B-9 illustrates an image of the Wheatstone bridge with a strain gauge used to replace the resistor between nodes C and B. Figure B-10 shows the circuit depicted using the hydraulic analogy. In the hydraulic analogy the change in resistance could equate to a depressed pipe that restricts flow. The restriction of flow causes an imbalance and more fluid, or electrons in the electric bridge, flow through the connection between C and A, which in turn causes fluid to travel across the meter.
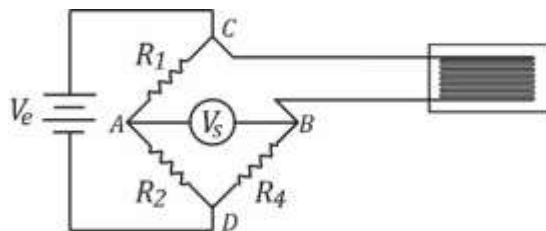
Figure B-9: Wheatstone Bridge with In-Line Strain Gauge
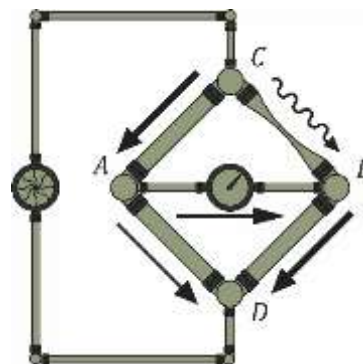
Figure B-10: Hydraulic Wheatstone Bridge with Impeded Flow

124

There are many types of bonded foil strain gauges that have been developed for different needs. Gauges have been designed to measure different types of strain; shear strain, axial strain, strain due to torque, etc. The filament inside the gauge can be made of various alloys and the grids made up of the filament can replace one, two, or four of the resistors in the Wheatstone bridge. Gauges that are made of one variable resistance filament, as shown in Figure B-9, are referred to as quarter bridge gauges, gauges that are made of two filaments are called half bridge gauges, and gauges that are made of four filaments are called full bridge gauges. Gauges can also be connected to a modified Wheatstone bridge (Murray and Miller 1992) adding even more options to the number of gauges available.

Temperature affects all bonded foil gauges for several reasons including expansion and contraction of the filament and carrier, and the effects of temperature on electrical conductivity. Temperature effects on electrical conductivity cause an imbalance in the Wheatstone bridge circuit when the gauge is located where temperature is different from the rest of the Wheatstone bridge. This can be an issue for SHM applications where the Wheatstone bridge is typically located inside the data acquisition hardware, which is typically housed in a climate controlled enclosure, and the gauge is located on a structure that fluctuates in temperature throughout daily and seasonal cycles. Effects of temperature on conductivity can be reduced to a negligible amount by use of full bridge gauges; however temperature effects on the gauge can only be mitigated.

Although the full bridge configuration chosen for this research has been shown to compensate for effects due to differences between the temperature at the gauge and the temperature in the data acquisition equipment where the quarter bridge gauges cannot, the effects of temperature on the carrier and alloy cannot be negated and are more pronounced in the full bridge gauges. Those effects are shown in Figure B-11 for the full bridge gauge and Figure B-12 for the quarter bridge gauge. The effects cause two distinct variations. The first is the linear variation on the gauge factor, which can be read using the y-axis on the right side scale of each graph. The second is a non-linear error represented by the curved line and can be read using the y-axis on the left of the graph. At room temperature both effects are equal to zero, allowing for accurate measurements with little post-processing achievable in laboratories environments. However in outdoor conditions, sensors readings must be compensated for temperature fluctuations.
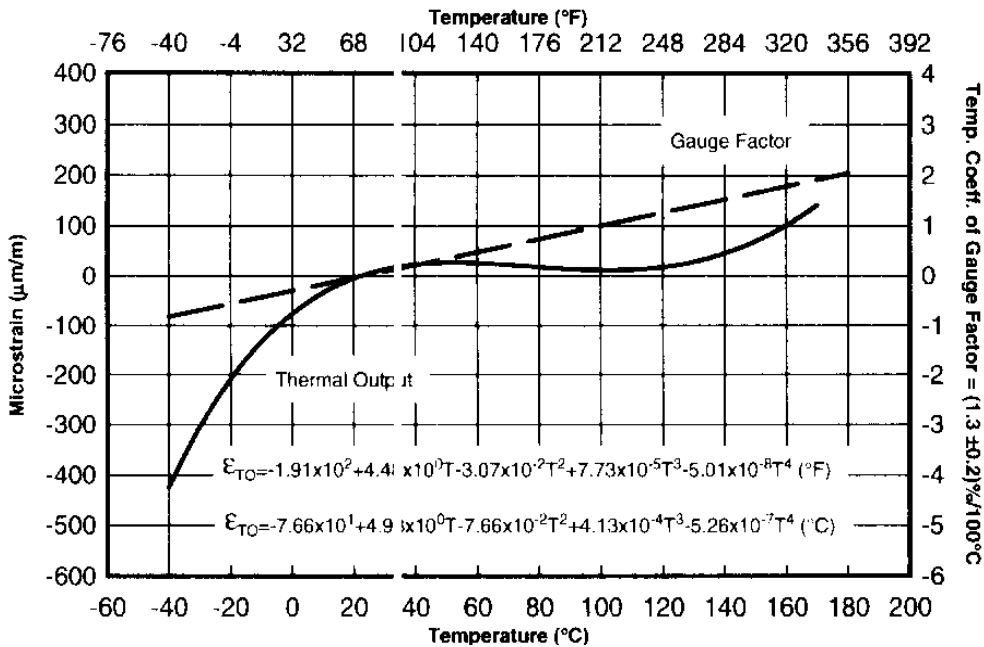
Figure B-11: Thermal Effects on Full Bridge Axial Strain Gauge
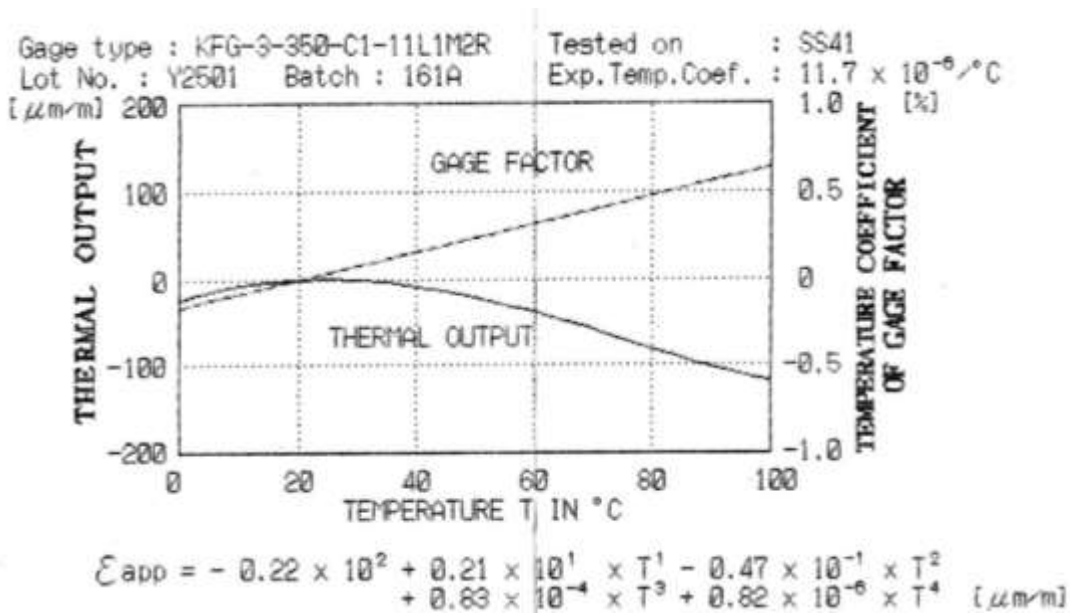
Figure B-12: Thermal Effects on Quarter Bridge Strain Gauge

The effects of temperature on the gauge factor can likely be neglected. The temperature expected in SHM projects in the New England area are expected to fluctuate between slightly below zero to slightly above 100 degrees Fahrenheit. Notice that the fluctuation between negative 4 degrees and positive 104 degrees results in a change of about 0.8% in the full bridge gauges. The second effect however cannot be neglected. It manifests as an apparent strain. In the same -4 to 104 degree F range the apparent microstrain can be seen to fluctuate from about -200 to 20 microstrains.

126

Figure B-13 shows the two apparent microstrain curves of the two gauges used in this research on the same graph. The lines are plotted using equations that are given with the graph by the manufacturer, shown in Figure B-11 and Figure B-12. It can be seen in Figure B-13, that temperature actually has a more pronounced effect on the full bridge gauges. This is likely because the resistance is higher at 1000 ohms over 350 ohms so temperature effects, as a multiplier, will create larger deviations when multiplied by the higher initial resistance of the full bridge gauges. In any event, manufactures provide these graphs as a tool to deal with these errors.
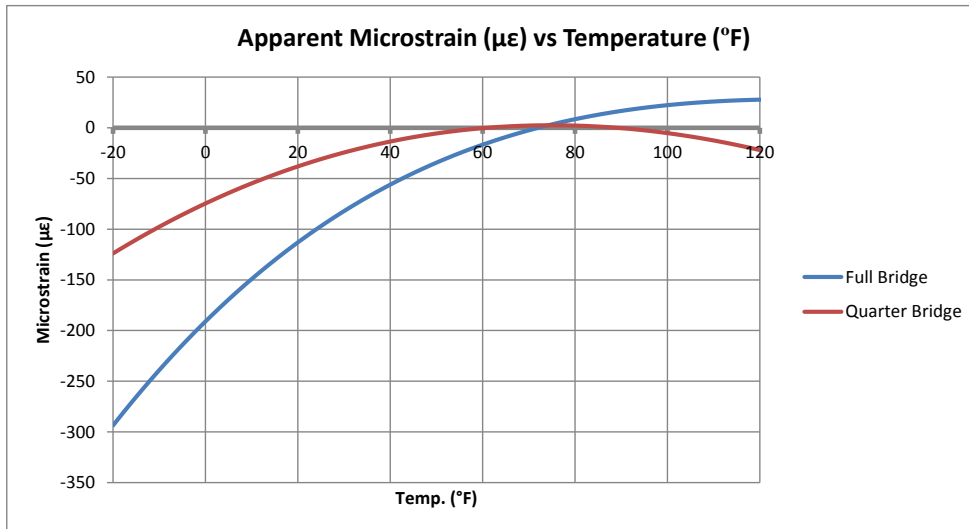
Figure B-13: Apparent Microstrain Curves of Full and Quarter Bridge Gauges

Because live load effects are expected to cause only single to double digit microstrain, the temperature effect can overshadow measurements when the observations are not at room temperature. When observations are short term and at constant temperature, the apparent micro-strain can be managed by zeroing the gauge, essentially subtracting the apparent strain at the start of the observation from each value recorded during the test. When observation periods occur over varying temperatures, such as throughout the course of a day, the apparent microstrain must be handled by measuring temperature at the gauge location and then subtracting the microstrain shown in the graph from each individual reading. This can also be handled using the formula at the bottom of the graph that represents a fourth order curve fit to the line.

APPENDIX C: Foil Strain Gauge Installation at BROUS4 Bridge

C.1 Installation Preparation

In preparing for the installation, a site evaluation was performed to assess how the beams could be accessed. The beams are approximately 17 feet off of the ground. The ground underneath the span was flat and stiff. A vehicle, such as a scissor or a boom lift, would have a good stable place to park under the span. However, a fairly long length of guardrail and the steep ditch between the road embankment of US Route 4 and the level surface under Span 3 prevents access from any vehicles that would arrive from the roadway under the bridge as shown in Figure C-1. Thick vegetation and a steep slope around the eastern abutment prevented vehicle access from the roadway above the bridge.

Figure C-1: Photo of Ditch Between Roadway and Underside of Span 3 at BRB

Figure C-2: Photo of Sloped Terrain and Vegetation Growing Around Eastern Abutment at BRB

Ultimately, scaffolding was rented from Seacoast Scaffolding of Concord, NH. The scaffolding included three five-foot bays, four leveling jacks, a ladder, guardrail, and several planks. The five-foot bays consisted of four columns and two cross braces. Leveling jacks served as the base of the system when the three bays were stacked, and were used to adjust the bearing elevation of the four columns creating a properly leveled structure. Three planks were placed on top of the scaffolding to create the platform, which provided access to the girders for sensor installation.

The gated guardrail system was around the top bay and locked into the columns for structural integrity. The ladder was fixed to one of the sides of the scaffolding not containing braces.

A practice run of assembling the scaffolding was conducted in the structural high bay (S-106) of Kingsbury Hall at UNH. The practice run allowed for identifying challenges in the assembly process without being distracted by environmental conditions or using valuable time out of the small window of daylight available at that time of year. A photo of the assembled scaffolding in the high bay is shown in Figure C-3. One challenge identified was a lack of planks. Prior to the practice run only three planks were rented. Placing planks on top of the third bay to build the working surface proved challenging without planks located on the second bay for access. For that reason, two more planks were rented prior to the actual installation.

Figure C-3: Photo of Scaffolding Assembled during Practice Run

Wires for the sensors were also prepared ahead of time. Preparation included cutting the wires and labeling them accordingly. The wires were cut to roughly 90-feet to account for the distance between the instrumented locations and the abutment, as well as enough slack to give flexibility to aspects of possible future configurations, such as locations for continuous data acquisition system housing. The labels were made from sticky file labels and were placed at roughly five-foot intervals down the entire length of each wire. They were placed with such frequency to allow for easy identification of the wire because ultimately the wires would be placed into a conduit of split wire loom and possible repairs may require extracting the wires out from a location not at the sensor or the abutment. The labels were numbered corresponding to a previous intended layout for the sensors and therefore are not necessarily in sequential order. Clear tape was placed over the labels to protect them from moisture. A photo of the installed labeled wires at the abutment is shown in Figure C-4.
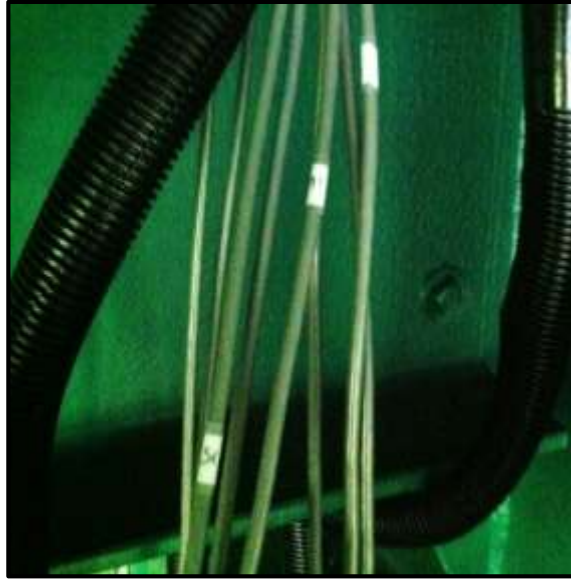
Figure C-4: Photograph of the Installed Labeled Wires

Other preparation for the installation involved gathering everything needed to installed the sensors in an instrumentation toolbox. A portable gasoline generator was made available by Dr. Jean Benoit of UNH for tools that require power, such as an electric grinder. The details about the equipment are included in Appendices B and D.

C.2 Installation Process

As noted, scaffolding was used to reach the instrumentation locations. After a discussion with Steve Mandeville the safety coordinator for the Bureau of Materials and Research at NHDOT, it was concluded that considering the relatively short height of the scaffolding, the only safety requirements would be guardrail and a ladder so that access to the top of the scaffolding would not involve climbing on the scaffolding itself. Also, because the location was significantly removed from the roadway by distance and a guardrail barrier, no traffic management was required. Hardhats and safety vests were worn during the entire installation process.

Figure C-5: Scaffolding Assembled at Bagdad Rd Installation Site

Scaffolding took roughly two hours to assemble on site. An image of the assembled scaffolding placed under girder D on the first day of installation is shown in Figure C-5. A significant portion of the time was spent transporting the parts of the scaffolding to the site given the previously mentioned terrain challenges.

The general process for installing each strain gauge involved prepping the surface, bonding the gauge, soldering the gauge to the wire, covering the installation for environmental protection, and securing the wire. The installation procedure followed in this research is based on recommendation from Omega© with field modification provided by Geocomp, INC. Thermocouples did not require surface preparation because it was assumed the temperature at the surface of the paint is the same as at the surface of the steel and therefore the thermocouples were bonded to the paint. They also did not require soldering because they use modular plug-style connections. An image from the manufacturer's website is shown in Figure C-6, model numbers OSTW-T-M and OSTW-T-F.
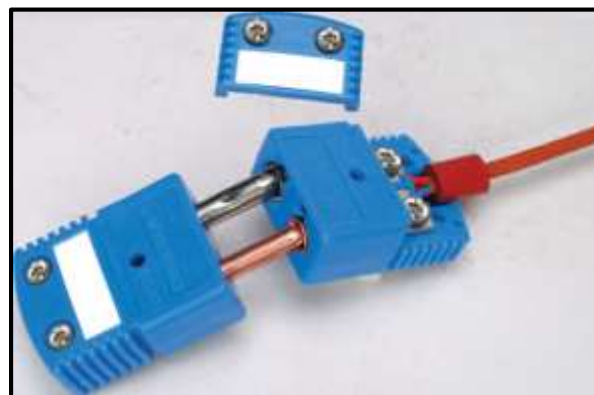
Figure C-6: Thermocouple Plug Connectors

131

Prepping the surface requires grinding the paint off to expose the steel and removing debris. Grinding is performed with a disk grinder as shown in Figure C-7, then coarser grit sand paper, and finally emery cloth to produce a smooth surface for the gauge to adhere to. The surface is then cleaned with acetone using individual rags until the rags do not show any debris from a single wipe.

Figure C-7: Photo of the Grinding Step of the Strain Gauge Installation Process at the BRB

When grinding and prepping the surface, special care was used to impact the smallest area possible because the paint protects the steel from moisture and gives the bridge an aesthetic appeal. The larger of the two gauges, the full bridge gauges, are only 0.583" x 0.437". However a larger surface area must be prepped due to the nature of the disk grinder. Affected areas were typically no more than 2" x 2", as shown in Figure C-8. Note that the location was marked with a permanent marker using a stencil to label the area the gauge would have to fit between. Figure C-9 is the same prepped area after a gauge has been bonded to the steel.
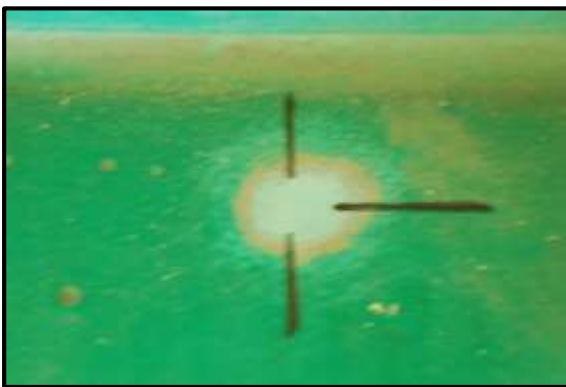
Figure C-8: Photo of Prepped Gauge Installation Site
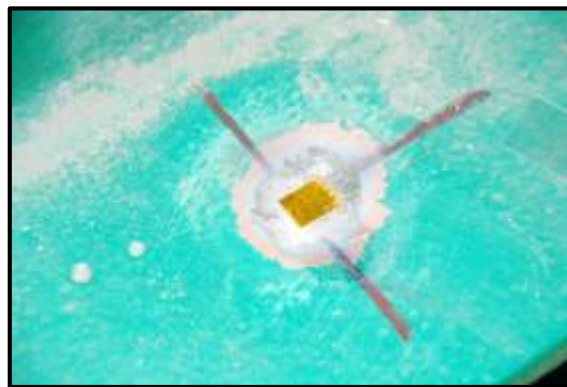
Figure C-9: Photo Full Bridge Gauge Bonded to Bottom Flange

The cold cure adhesive, Loctite 496, was used to bond the gauges to the beam. It is one of the most commonly used strain gauge adhesives according to Omega Engineering Inc. (omega.com), the strain gauge supplier. Bonding involves first placing the back of the gauge on the tacky side of a piece of translucent tape. Packing tape was used in these installations. Then a small amount of adhesive is dropped on the gauge. The gauge was then "taped" down and centered between the marks and uniform pressure was applied by hand for at least 1 minute as shown in Figure C-10. Then the tape was removed as shown in Figure C-11, which served as a quality assurance of the bond. While the tape was pulled back, the gauge was closely observed, if the gauge peeled back at all, it would indicate a delamination or air bubble in the adhesive, and the gauge would be removed and the application process restarted from the step of cleaning the surface with acetone. After removing the packing tape, electrical tape was carefully placed behind the gauge to insulate the leads, preventing the steel surface from shorting the circuit to the data acquisition equipment.
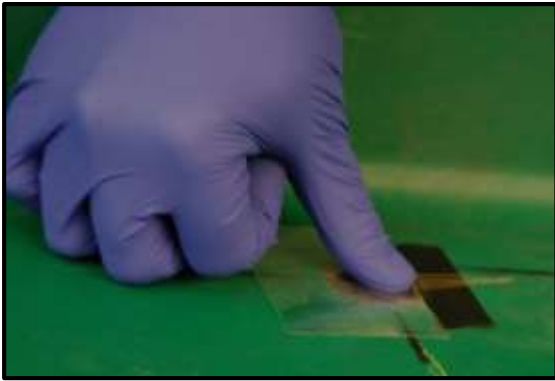
Figure C-10: Photo of Gauge Installation – Constant Pressure Applied

Figure C-11: Photo of Gauge Installation – Tape Removal

The next step involved soldering the gauge leads to the lead wires. The wire contains four separate tinned copper leads that are all the same except for the color of their coating. Each full bridge gauge requires a single wire of each individual strain gauge in the configuration. Quarter bridge gauges however only use two leads as opposed to the full bridge gauges four leads; therefore a single four lead wire accommodates a pair of quarter bridge gauges. Because the four wire leads are compatible with all leads on the gauges, the color coding scheme of connections are up to the installer. It is important to keep track of which color was used to connect to which gauge lead so that when the leads are later connected to the data acquisition equipment it will be configured correctly. Diagrams were created for the full and quarter bridge gauges to standardize the configurations. The wire configuration for both gauges is shown in Figure C-12.
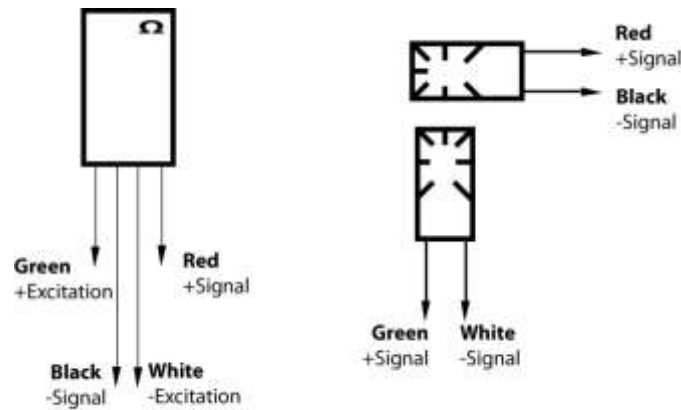
Figure C-12: Full (Left) and Quarter (Right) Bridge Strain Gauge Wiring Diagrams

Soldering involved taping the wire to the beam to reduce movement, heating the soldering iron, using it to place a small amount of solder on the leads from the gauge and the wire, and finally, heating the two soldered portions while they were in contact with the iron so that they would form together. Originally the intention was to use terminal strips that the gauges can be soldered to and the wire can be soldered to. The terminal strips provide a connection between the two leads without having to solder the flexible wires together, which can be a challenge. The strips, though, are bonded to the surface of the beam, similar to the strain gauge, and need to be heated to transfer the solder to the strips. The cold weather posed a challenge for the bonded strips because the thermal conductivity of the underlying beam and its cold temperature. Soldering to the strip when it was not bonded also proved to be a challenge as it severely warped the strip.

After the second gauge installation, the terminal strips were abandoned and then wires were directly soldered to each other. Although it was challenging and time consuming, the duration was reduced after the first day of installation by pre-soldering the wires prior to going to the site for further installations. Pre-soldering involved placing small amounts of solder on the wires and the gauge leads so that connections at the site could be formed by simply holding the two pre-soldered parts together and heating them. The images in Figure C-13 and Figure C-14 below show the comparison between an installation with terminal strip versus an installation where wires were soldered together.

Figure C-13: Photo of Gauge Installation – Soldered Using Terminal Strip
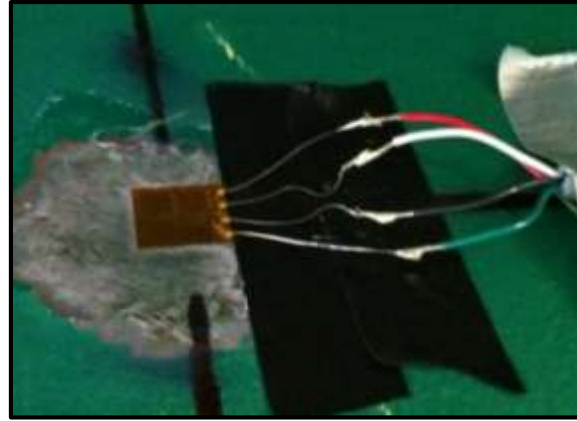
Figure C-14: Photo of Gauge Installation – Soldered Without Terminal Strip

When the soldering was complete, the entire affected area was covered with plumbers putty (Hercules® 25-101) to protect against moisture. The putty was first placed over the leads wires as shown in Figure C-15. Effort was made to ensure putty was placed between the wires, preventing them from possibly touching and shorting the circuit to the data acquisition equipment. Then the gauge and entire area that was affected by the paint removal process, plus a half inch buffer, was covered with the putty as shown in Figure C-16. Aluminum tape was used to further protect the installation from environmental effects as shown in Figure C-17. Lastly the wires were then clamped to the beam flange as shown in Figure C-18.

Figure C-15: Photo of Gauge Installation – Putty Placed Over Leads
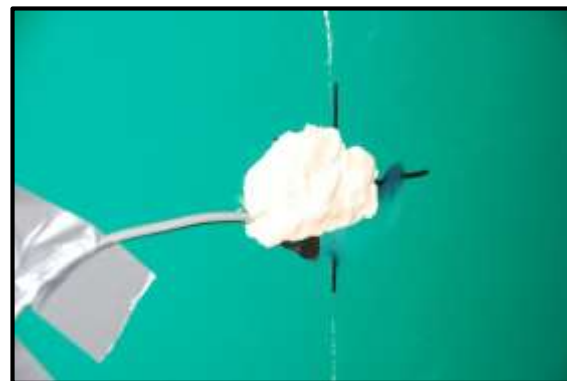
Figure C-16: Photo of Gauge Installation – Putty Placed Over Entire Installation

Figure C-17: Photo of Gauge Installation – Aluminum Tape Environmentally Protecting

Figure C-18: Photo of Gauge Installation – Wires Clamped to Bottom Flange

When all gauges were environmentally protected, the wires were secured to the beam flange with clamps. A voltmeter was used to evaluate the installation. The voltmeter measured the resistance of the circuit. The circuit in this case was the entire 90-feet of wire and gauge. If the resistance was infinite, it would indicate that something created a discontinuity, for example the solder or gauge was damaged. If the resistance was low it would imply that a short was created, for example if the leads had made contact with the steel beam or each other under the environmental protection. The resistances of the full bridge gauges are 1000 ohms and the resistances of the quarter bridge gauges are 350 ohms, both +/- 15%, according to the Omega, manufacturer. The resistance of the 90-feet of wire lead, on the other hand, was 5 ohms when tested prior to installation, so the difference would be easy to discriminate.

This general process was repeated on three other installation days. Significant differences between the processes were that thermocouples were only installed on the south face of Beam D, and that quarter bridge gauges were installed on the south face of Beam E. As previously noted, the thermocouples did not require surface preparation or soldering. Plumbers putty was also not used for environmental protection, as it was assumed that the aluminum tape would be sufficient environmental protection.

Installing quarter bridge gauges involved bonding six gauges rather than three. An image of a pair of quarter bridge gauges is shown in Figure C-20. However the installation took roughly the same amount of time because soldering was not required. The quarter bridge gauges were available "pre-wired" meaning that instead of having a two-inch lead as the full bridge gauges, they had a thirty-six inch wire attached to the gauges. The wire was taped together in a bunch under aluminum tape on the flange and gel splice connectors, type UY, shown in Figure C-19, were used to connect to the lead wires from the gauge to the lead wires for the DAQ. The gel splices function by inserting the two wires into holes and then squeezing the splice with pliers. The two halves of the splice crush a piece of metal foil around the wires to create continuity and gel surrounds the wires and protects the connection from moisture.

Figure C-19: Slice Type UY Connector (tekcomponenets.com)

Figure C-20: Photo of Gauge Installation – Quarter Bridge Gauges

Figure C-21: Photo of Gauge Installation – Area Covered With Green Tape

Each installation was later covered with green duct tape to hide the instruments as shown in Figure C-21. Considering the limited duration the scaffolding was rented and the weather conditions, the decision was made to secure the wires and return in the spring to run them to the eastern abutment for data acquisition. The wires were then secured with clamps for the duration of the winter. The wires from the north face of Beam D and the south face of Beam E were run under the flange and clamped to the opposite side so that later, when wires would be run to the abutment, they would all be entirely contained in the bay between the two beams.

Although the winter of 2011-2012 proved to be extremely mild and had little snowfall, there was no way of knowing that when the gauges were installed, and it was expected that at any time a significant snowfall could occur and impact accessibility at the site. Duct tape was used at roughly five-foot intervals to secure the split wire loom to the beam as it rests on the beam flange.

C.3 Significant Differences in Installation Conditions

Aside from the noted differences in sensor configuration, day to day conditions varied at the site. As shown in Table 5-1 of historical weather data retrieved from the nearest historic weather station in Portsmouth NH, (Weather Underground 2012), the first and third days were the most humid, and the second and fourth were the coldest. Humidity only seemed to pose a challenge on the third day. Condensation formed on the beam at a rate fast enough to trickle down the beam

137

face, and therefore, the area had to be wiped down several times throughout the instrumentation, as seen in Figure C-22.

Figure C-22: Photo of Condensation on Beam Surface

Cold temperatures seemed to have an effect on the adhesive, causing longer waits for the adhesive to cure. As a result, the type of pressure shown in Figure C-10 was applied for longer durations on subsequent days. Soldering was also a challenge on the second day in the cold temperatures. Not only did the soldering iron take longer to heat but posed other challenges in terms of handling and solder placement. Soldering such small wires is difficult to do effectively with gloves on. Without gloves, the cold impacted dexterity rather quickly, often quicker than would take to solder all four leads of a single gauge.   The cold caused minor numbness and shivering which posed obvious challenges when attempting to solder the thin leads.

Table C-1: Weather Conditions Mid-day during Installations

Day	Temp at noon	Dew Point	Humidity
11-29	55	51	91 %
12-1	46	25	58 %
12-5	50	43	92 %
12-9	45	28	67 %

Ideally, installations should occur during warmer time periods for both the comfort of the installers and the curing of the adhesives.

APPENDIX D: Data Acquisition Hardware

This appendix discusses the progression of data acquisition selection. As pointed out by (Cardini and DeWolf, Long Term Structural Health Monitoring of a Multi-Girder Steel Composite Bridge Using Strain Data 2009), continuous monitoring systems have 4 main components. Those components are control units, sensors, software, and communications. This chapter describes the software and control units. Control units include data loggers and the computers that read and manage them. Sensors selection is described separately in the following chapter so that emphasis can be placed on how the sensors function. Communication options were not thoroughly evaluated as part of this project because the decision of whether to continuously monitor at the Bagdad Road Bridge is pending.

The equipment selected included thermocouples and bonded foil strain gauges from Omega Engineering®, CompactDAQ® data acquisition chassis, and several modules that could be exchanged to fit various measurement needs purchased from National Instruments® (NI). SHM needs at Gilford were still under investigation while the need to procure equipment and evaluate its behavior outside of the lab was growing. Modular data acquisition hardware was sought because it would allow for adjustments during the sensor network design that develop as needs were identified. This would also allow for easier expandability in future SHM research projects at the bridge. Modular systems can read different types and numbers of instruments by purchasing modules. Ultimately NI hardware was chosen because of its compatibility with the data collection and processing software LabVIEW®.

D.1 Software: LabVIEW

LabVIEW is also a product of NI. Short for Laboratory Virtual Instrumentation Engineering Workbench, it's a developer's platform that can be used to create programs and graphical user interfaces for those programs. The programs can read and post-process data and present live calculations allowing for features to be interpreted in real time. This reduces the amount of software that needs to run as part of the SHM and experimenting process. Rather than having proprietary software supplied by the data acquisition system manufacturer to record data, then excel or a similar program used to post-process data, and then a third software platform to present the graphical interface, LabVIEW includes these functions in a single program. At the time of this writing, a standard license of the software costs $2,699. However, UNH has an Academic Site License and, therefore, no software costs were involved in this project.

Each LabVIEW executable file, including programs and subroutines, has a user interface called the front panel and the controlling "code" in the attached block diagram. These programs are called virtual instruments (VIs) because their appearance and operation is meant to model a physical instrument, like an oscilloscope. The user interface is created on the front panel when the program is not running by placing graphs, numerical indicators, and controls. The block diagram then programs the user interface by the placement of VIs and structures. The VI's and

components that are placed on the front panel appear as blocks in the block diagram. The blocks can then be wired together in a way that controls the flow of data and how it's processed.
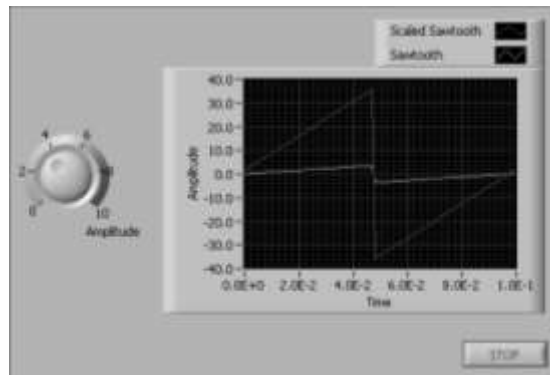
Figure D-1: Example VI Front Panel from "Getting Started with LabVIEW" Instructional Document.
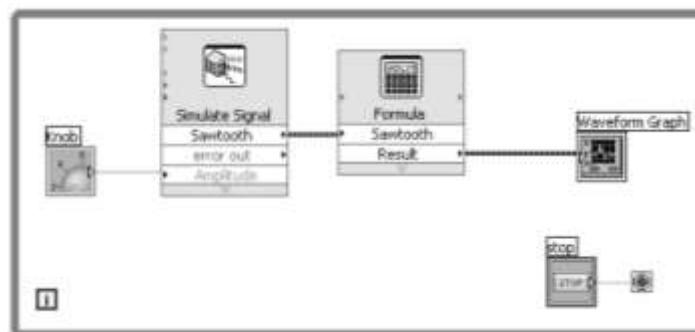
Figure D-2: Block Diagram for the Front Panel Shown in Figure D-1

Figure D-1 shows an example VI front panel and Figure D-2 shows the corresponding block diagrams. The rectangles in the block diagram labeled "Simulate Signal" and "Formula" are VIs and can be opened as programs to view or modify their own front panels and block diagrams. VIs that run on the block diagrams are often referred to as subVIs and, may or may not be opened during the operation of the front panel corresponding to the block diagram they are placed in. The squares labeled "Knob", "Waveform Graph", and "stop" are structures referred to as terminals that interact with subVIs in the block diagram when users interact with the front panel. Finally, the grey box around the block diagram is a "while loop," a structure that causes the program to keep running, once it's been started, until the user halts the program.

D.1.1 LabVIEW Tools Common to All Programs in this Research

LabVIEW has a wide variety of function and only a few were utilized in this research. The following pages show each program used, both the "front panel," which the user of the program

interacts with, and the "block diagram," which resides in the background and is where the general flow of the data and calculations are configured. An outline of each program is also included. Certain features are common to all programs and are described below:

- Items in the block diagram are called "VIs" short for virtual instruments.
- The grey box around the VIs in the block diagram shows that the program is contained in a while loop. The while loop causes the program to iterate continuously. Without the while loop, the program would collect 1 strain sample when the user clicked "run" and would halt.
- The grey hatched box around the "write to measurement" VI, labeled "write" in each block diagram, is a case structure. The case structure is attached to a Boolean switch that can be operated from the front panel when the program is running. When the case structure is on, the program runs the VIs in the structure, and will halt those operations when the case structure is turned off.
- The case structure receives a value of true from the switch when it is pressed, or latched, and turns on the VI that writes the measurement file stored on the controlling computer. When the button is unlatched, clicked on again, it stops the action of the write to measurement file.
- The "write to measurement file" VI is set to include only 1 header for each iteration. Otherwise, every sample would receive a new heading. Only 1 time column is configured because all gauges are configured to read at the same times. It is also configured to store the collected data in a tabular delimited file with a .lvm extension, and to rename an existing file if the intended file storage location already has a file in it with the same name.
- The "DAQ Assistant" is the VI that collects data from the equipment and moves it to the rest of the program. Its properties are adjusted by double clicking on it. Those properties include sampling rates, sensor configurations, and calibration information.
- Waveform charts are used instead of waveform graphs because the DAQ Assistant is set up to collect continuously and refresh the program after every sample. Not shown in the screen captures because they were captured when the programs were off, waveform charts display samples over a specified amount of time and therefore can display several of the samples at a time with lines between the data points. Waveform graphs, on the other hand, only display the last iteration and since the iteration is only 1 sample, no line would be drawn.
- Blue wires represent data that will change after each iteration as the DAQ assistant collects and feed new data to the program. Orange wires show the flow of constants, which do not have to be updated during iterations.
- Splitters divide or combine signals. Splitters can be used to show multiple strain signals collected by the 1 DAQ assistant on multiple charts or to combine signals that have been split so they appear on the same chart.

D.1.1 Flat Bar Test Program

This program collects strain data and, using inputted flat bar parameters, calculate the force of tension or compression applied to the bar. A screen capture of the front panel is located in Figure

D-3 and a screen capture of the block diagram is location in Figure D-4. An outline of the program is as follows:

- The user enters information about the flat bar in the numerical entry boxes on the left hand side of the front panel. These parameters are thickness, width, and the modulus of elasticity.
- The DAQ Assistant is shown on the block diagram. It is configured to collect 2 strain signals and then a splitter is used to display the strains on two different waveform charts on the front panel.
- As shown on the block diagram, the thickness and width are multiplied to produce a cross sectional area, which is then displayed under the left corner of the left chart on the front panel.
- The modulus, area, and strain data are then multiplied together to obtain a force value, and the values are displayed in two numerical display boxes on the front panel labeled force 1 and force 2. These represent the calculated tension or compression derived from each gauge on the specimen.
- The two force values are then added together and divided by two to generate an average value that is also displayed on the front panel in a numerical display box.
- At any point, the user can click on a "collect data" button that latches the Boolean switch, and the "write to measurement file" VI stores raw strain.   Note that the wire to the DAQ assistant is connected before the splitter so that it receives both strain signals.
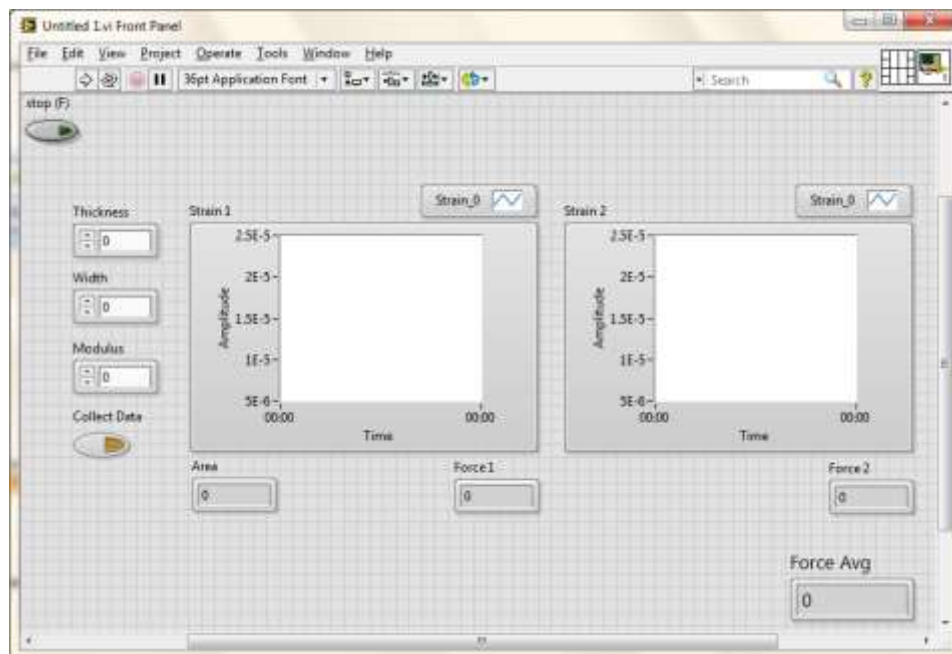
Figure D-3: Front Panel for the Flat Bar Test Program
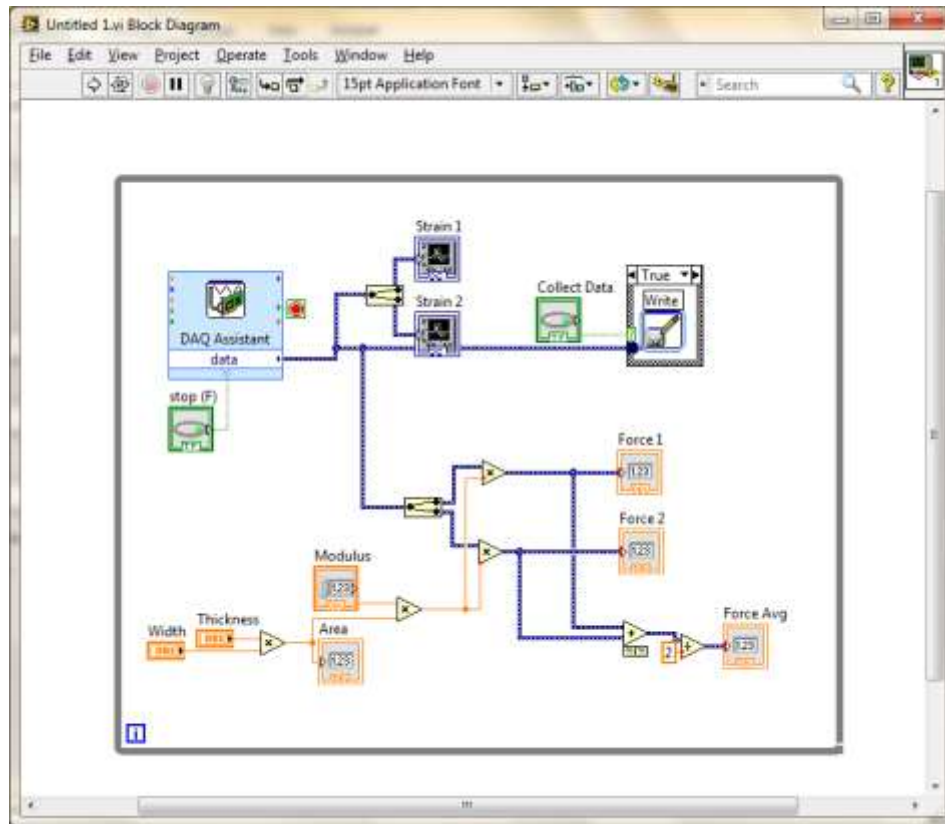
Figure D-4: Block Diagram for the Flat Bar Test Program

D.1.2 In-Field Gauge Diagnostic Program

This program was used to initially test each set of gauges on April 21st 2012. The front panel can be used to evaluate gauge behaviors and is shown in Figure D-5, and the corresponding block diagram is shown in Figure D-6. An outline of the program is as follows:

- Data is collected by the DAQ Assistant and sent to the large waveform chart, the splitter, and the write to measurement file vi enclosed in a case structure.
- A single waveform chart, which appears as the larger chart on the front panel, and the wire to the "write to measurement file" VIs are connected before the splitter and, therefore, receive data from all three gauges.
- By showing all signals on a single graph, gauge to gauge behavior could be evaluated. Significant deviations from zero when the bridge is unloaded or larger amounts of noise for example, could immediately be identified.
- The splitter receives data at the same time as the large waveform chart and divides the 3 signals and sends them to 3 waveform charts that appear smaller on the front panel. If the gauges began to significantly drift in different directions during an evaluation, the 3 charts would serve as a means to zoom in on each different signal.

143

- At any point, the user can click on a "collect data" button that latches the Boolean switch, and the "write to measurement file" VI stores raw strain.   Note that the wire to the DAQ assistant is connected before the splitter so that it receives both strain signals.
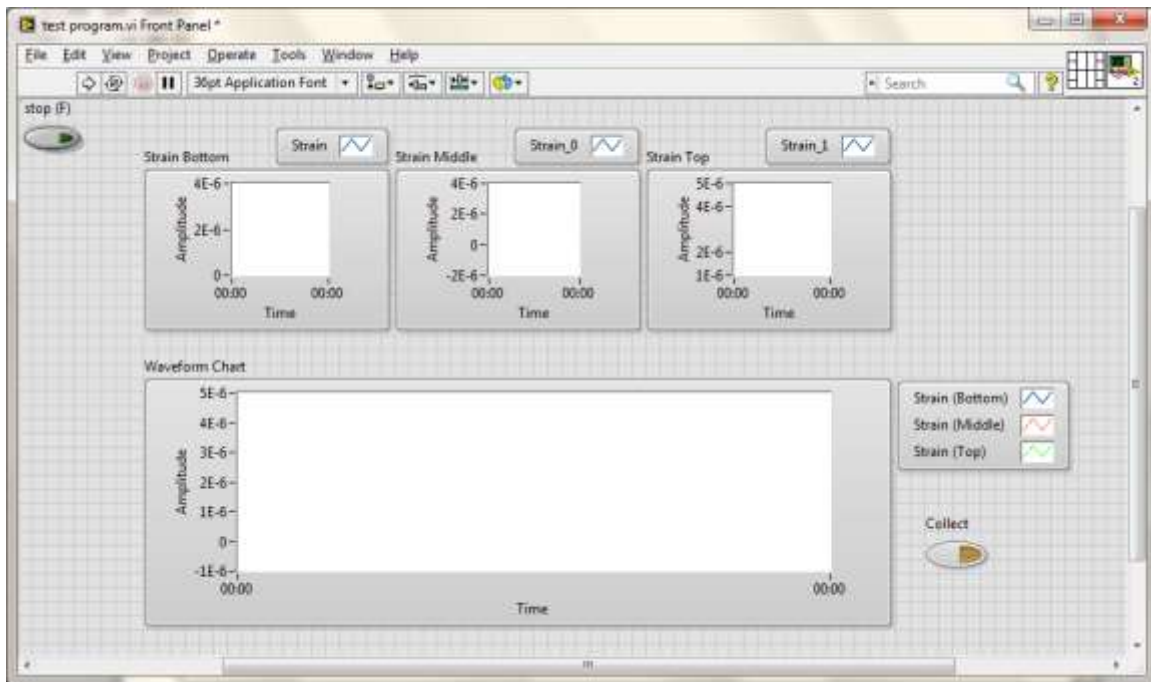
Figure D-5: Front Panel for the In-Field Gauge Diagnostic Program
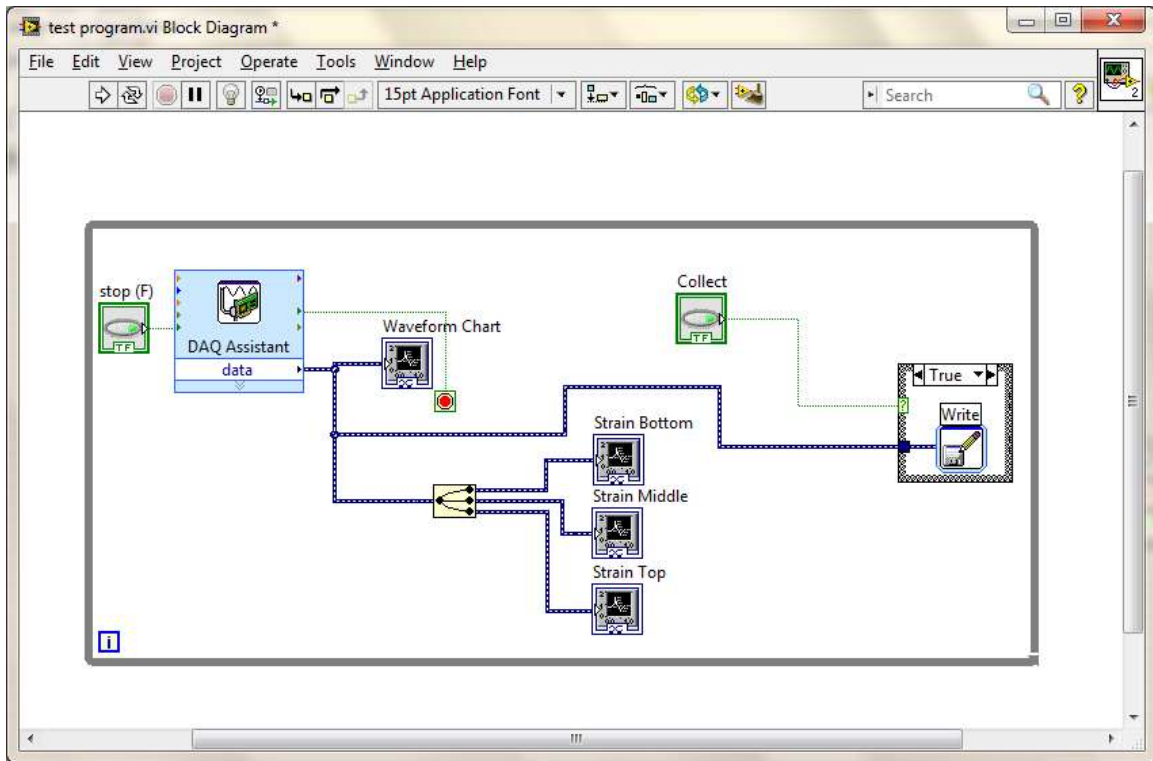
Figure D-6: Block Diagram for the In-Field Gauge Diagnostic Program

D.1.2 Program to Read All Gauges Currently Installed Simultaneously

This program was written to read all gauges installed as part of this research simultaneously. The front panel is shown in Figure D-7 and corresponding block diagram is shown in Figure D-8. An outline of the program is as follows:

- Data is collected by the DAQ Assistant and sent to a large splitter that divides the single stream of data that includes all sensors into multiple data streams, one for each sensor.
- Smaller splitters then combine the sensors into categories of longitudinal strains for each beam face, in section strains for the south face of Beam E, and temperature readings for the south face of Beam D.
- The data is displayed versus time, by category, in the waveform charts on the front panel. Each large waveform displays longitudinal strain values. The smaller chart on the bottom displays the in-section strains and the smaller chart on the top displays temperature values.
- At any point, the user can click on a "collect data" button that latches the Boolean switch and the "write to measurement file" VI stores raw strain. Note that the wire to the DAQ assistant is connected before the splitter so that it receives both strain signals.
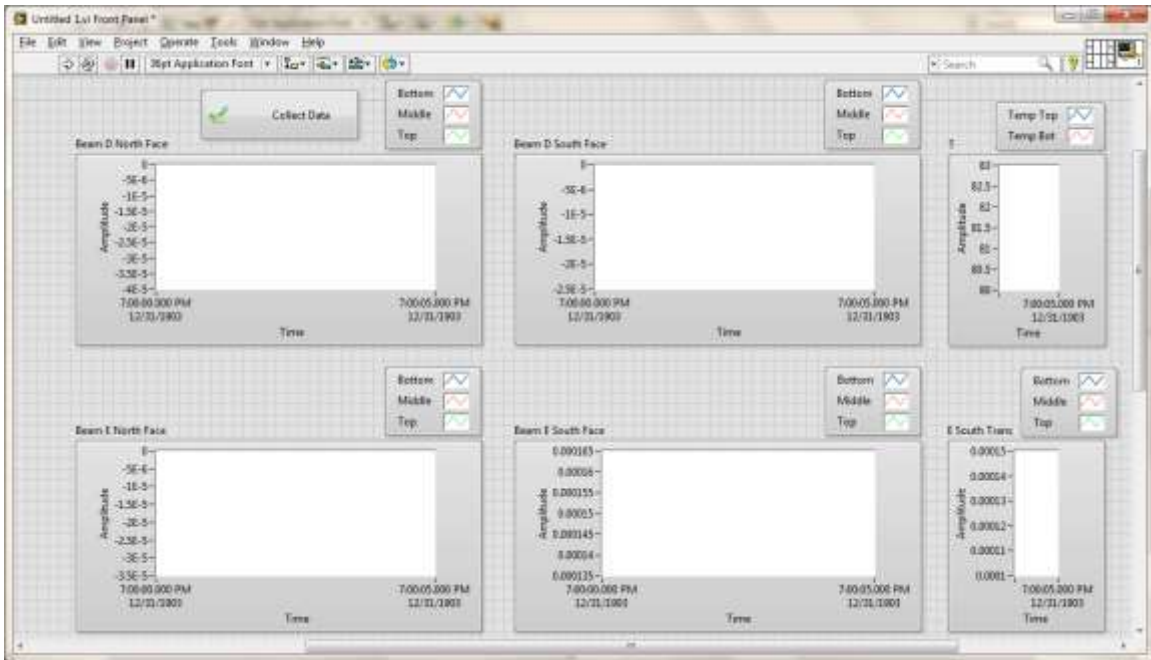
Figure D-7: Front Panel for the Current Bridge Monitoring Program
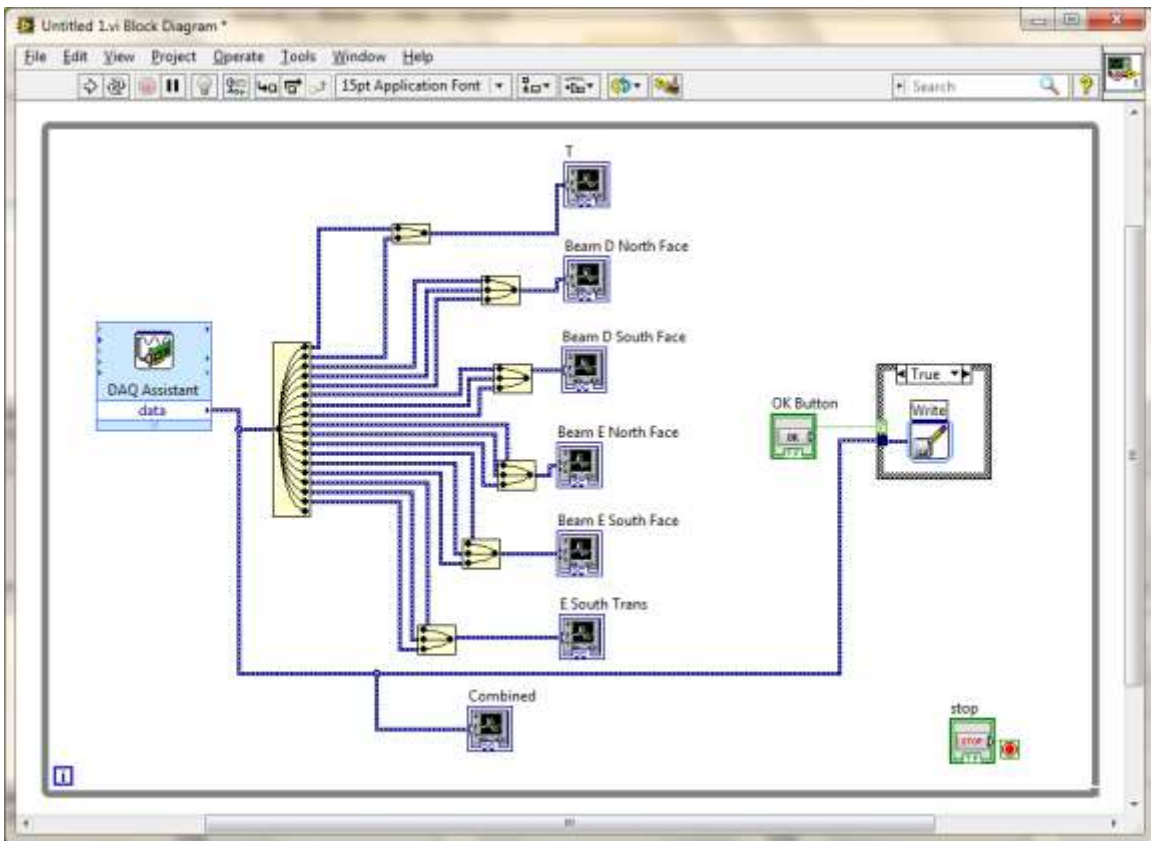
Figure D-8: Block Diagram for the Current Bridge Monitoring Program

146

D.2 Hardware

Rugged modular equipment was researched so the hardware would behave dependably in temperatures that exist at bridges in New England and could be easily expandable to meet developing research needs. Table D-1 shows different types of data acquisition loggers that National Instruments offers. (National Instruments 2010) These types of data loggers are common to the industry as other companies offer PCI, PXI, USB, Wi-Fi, and Ethernet devices.

Peripheral Component Interconnection (PCI) and PCI express equipment is connected to computers via slots in the motherboard, the same connections that would be used to connect video cards or modems. PXI stands for PCI eXtensions for Instrumentation and the equipment uses chassis to hold multiple modules. The PXI Systems Alliance (PXISA) is an industry consortium, founded in 1998, that promotes and maintains the industry standard (PXISA 2012). The PXI standard has become a "major force" in the data acquisition field because it is an open platform and the equipment is cross compatible (Radio-Electronics.com n.d.). That means PXI cards made by one manufacturer would work in a chassis produced by another.

Table D-1: Common Data Logging Hardware Standards

Features	Portable DAQ	Desktop DAQ	NI CompactDAQ	PXI Platform
Bus	USB, Wi-Fi, Ethernet	PCI, PCI Express	USB, Wi-Fi, Ethernet	PXI, PXI Express
Portability	Best	Good	Better	Good
Number of I/O Channels	1 to 100	1 to 100	1 to 250	1 to 1000+
I/O Configuration	Fixed	Fixed	Modular	Modular
Max Sample Rate	2 MS/s	10 MS/s	1 MS/s	10 MS/s
Built-In Signal Conditioning	Available	No	Yes	Available
Synchronization/Triggering	Good	Better	Better	Best
Programming Languages	LabVIEW, C, C++, VB .NET, C# .NET			
Operating Systems	Windows, Linux, Mac OS X	Windows, Linux, Mac OS X, Real-Time	Windows	Windows, Linux, Real-Time
Included Software	NI LabVIEW SignalExpress LE (Windows Only)			

Data loggers or data acquisition systems are commonly referred to as DAQs. Portable DAQ and Desktop DAQ systems were out of consideration because they are fixed systems and not as easily adaptable as the modular systems. Of the modular systems, the CompactDAQ was chosen for many reasons. Although it will not be compatible with other manufacturer's equipment, which was of no concern in this project, the equipment is less expensive and has built in signal

conditioning out of the box (National Instruments 2010). Better portability was an additional benefit that would result in smaller electrical enclosures because the portability comes in the form of smaller hardware.

The CompactDAQ equipment uses c-series modules. The carriers and chassis compatible with c-series modules are shown in Table D-2. Carriers were eliminated from consideration because they can only read one module at a time. From the available chassis, the CompactDAQ chassis was chosen because of cost, and it did not require significant LabVIEW expertise. The CompactRIO® uses a separate controller and a field programmable gate array (FPGA) system to manage timing and processing that requires additional programming experience to configure. In addition to expertise demands from FPGA programming, the R-series chassis were not in consideration because they are for expanding PXI systems (National Instruments n.d.).

Table D-2: Carriers and Chassis Compatible with NI C-Series Modules

	Carrier/Chassis	Applications	Recommended Programming Experience
	USB Carrier	Portable, small channel count	None needed
	Wi-Fi/Ethernet Carrier	Remote monitoring, structural monitoring, environmental monitoring, machine condition monitoring	None needed
	NI CompactDAQ (USB and Ethernet Chassis)	General-purpose mixed-sensor DAQ, control, high-speed DAQ, portable system up to 256 channels	None needed
	NI R Series Expansion Chassis	Large advanced test system, deterministic control and acquisition, manufacturing test	Comfortable with NI LabVIEW programming
	NI CompactRIO	In-vehicle logging, rapid control prototyping, advanced control unit, custom design deployment	Comfortable with LabVIEW programming

148

Because the costs of the CompactDAQ chassis are a fraction of those for CompactRIO, about $1000 versus $9000 for 8-slot chassis, the CompactDAQ provides for an excellent way to introduce the technology to UNH and local SHM stakeholders. The majority of the cost in equipment comes from the modules, approximately $1000 for 4-channel strain cards, see Appendix C, and the modules will be compatible with CompactRIO chassis should future researchers working with this equipment decide to upgrade. Table D- shows a quick comparison of C-series reading equipment. The table highlights that CompactDAQ chassis have cost savings with only a slight loss in ruggedness and performance. Both Table D-2 and Table D-3 are available at the National Instruments website, ni.com, with additional information about the specific functions of each.

Table D-3: Quick Comparison Table for C-series Module Reading Equipment

	Ruggedness	FPGA	Ease of Use	Performance	Cost	Programming
USB Carrier	***	No	*****	**	$	LabVIEW, ANSI C/C++, C#, Visual Basic .NET
Wi-Fi DAQ Devices	***	No	****	**	$	LabVIEW, ANSI C/C++, C#, Visual Basic .NET
NI CompactDAQ	****	No	*****	****	$$	LabVIEW, ANSI C/C++, C#, Visual Basic .NET
R Series Expansion	***	Yes	***	*****	$$$$	LabVIEW
CompactRIO	*****	Yes	***	****	$$$	LabVIEW

The number of C-series modules and chassis were selected based on the initial needs for a long term monitoring project at the Gilford Bridge. This resulted in three data acquisition chassis. Each of which can manage up to eight modules that read the cards and send data to the controlling computer. It was assumed two chassis would be located at the monitoring site permanently while one chassis would be used to expand on the system while conducting experiments at the site during load tests, but generally would be kept at the laboratories at UNH. Fourteen strain reading modules were purchased. Each reads up to four strain gauges meaning up to 56 gauges can be read when all 14 cards are utilized. These cards can be moved between bridge locations and UNH as research needs dictate. Two Thermocouple cards were purchased; the first card is capable of

measuring 16 thermocouples and is intended for long-term deployment, the second has four channels and is intended for measurements at UNH. One accelerometer card was purchased for potential dynamic research at the bridge or UNH.

A water resistant, durable, secure NEMA-4 enclosure was purchased, which will house the equipment at the bridge site during the permanent installation. A fanless computer for controlling the data acquisition equipment was also purchased. A photograph of the open enclosure with the pc, 2 chassis, and several modules is shown in Figure D-9. All of the strain gagues equipment is detailed in Appendix B.

Figure D-9: Photograph of Enclosure and DAQ Equipment

Table D-4: Summary of DAQ Equipment Available for the Gilford and BRB Projects

3 Data acquisition chassis	Manufacturer: National Instruments Model Number: NI-9178 • Each power up to 8 modules • Used to read modules and send data to the computer. • 2 chassis will be located at the monitoring site • 1 chassis will be used to conduct experiments at the University

14 Strain reading modules	Manufacturer: National Instruments Model Number: NI-9219 - Each reads up to 4 strain gauges - Can be moved between the bridge locations and the University as research needs dictate.
2 Thermocouple modules	Manufacturer: National Instruments Model Number: NI-9211 (4-channel) & NI-9213 (16-channel) - Up to 16 thermocouples can be read using the card for the bridge - Up to 4 thermocouples can be read using the card for the University
1 Accelerometer module	Manufacturer: National Instruments Model Number: NI-9234 - Used for potential dynamic research at the Bridge or University
1 NEMA-4 enclosure	Manufacturer: Omega Engineering, Inc. Model Number: OM-AMU2060 - water resistant, durable, and secure enclosure housing for the equipment at the bridge during permanent installation
1 Fanless PC	Manufacturer: Habey Model Number: MITX-6564 - 1 Computer: used to control the data acquisition hardware and access recorded data

Wiring	Manufacturer: Omega Engineering, Inc.
	Model Number: TX4

- Enough wiring has been purchased for the currently installed equipment and much of what is required for a Gilford
- 4-lead

Using data acquisition equipment that reads full bridge gauges comes at a small premium with respect to National Instruments products. Although a direct comparison can be difficult to make, because different cards have different features that researchers might feel adds or subtracts value, a general analysis can be performed. Considering only the chassis and modules, and neglecting the academic discount, the price of full bridge gauges was roughly $330 per channel compared to $210 per channel for quarter bridge gauges.

The costs per channel were taken from ni.com during the month of July 2012 and are presented in Table D-5. At the time of this research, the 2 c-series modules capable of reading full bridge gauges are the NI-9219, which was used in this project and can read at speeds up to 100Hz, and the NI-9237, which can run at a much faster 50 kHz. The NI-9219 costs $1,029 and the NI-9237 costs about $1,180. The module that reads Quarter Bridge gauges, NI-9235, costs $1,544, can read at speeds up to 10 kHz, and has 8 channels. All modules mentioned here can read at 24 bits of resolution. high speeds are not necessary in long term SHM because of data storage demands. However, to produce more level comparison, the costs of the higher speed full bridge channels are compared to the cost of the quarter bridge channels, which is only offered at high speeds. A full 8-slot chassis was used to produce the channel counts

Table D-5: Cost Difference for Full Bridge Channels versus Quarter Bridge Channels Based off National Instruments

Channel Type	Channel Count per card	Total Channels	Cost of Chassis per Channel	Cost of Module per Channel	Cost per Channel
Full Bridge (NI-9237)	4	32	34.38	$ 295	$ 329.38
Quarter Bridge (N-9235)	8	64	17.19	$ 193	$ 210.19

With respect to the sensors themselves, comparisons are even more difficult to make because a much broader selection of quarter bridge and full bridge gauges are available. The sensors are inexpensive compared to the cost of the channels so the cost was not a significant factor in the gauge selection process. The sensors used in the research were about $21.00 per full bridge gauge and about $12.00 per quarter bridge gauge. It should also be noted that half as much wiring is needed for 2-lead quarter bridge gauges as a single line contains 4 leads and therefore 2 gauges can be connected to the DAQ with a single line. The full bridge gauges on the other hand require all four leads and, therefore, require a dedicated line. The cost of wire is roughly $0.20 per foot. Based on 90' lengths of wire, this results in a cost per sensor of $39.00 for full bridge gauges and $21.00 for quarter bridge. The costs for gauges and wires were taken from omega.com during July of 2012. Considering that all other costs for the two systems are the same, including the computer, enclosures, software, personnel, installation, and overhead, the premium per channel for using full bridge over quarter bridge may be a small portion of the overall costs.

It should also be noted that the cards can read up to 100 samples per second per channel however they feature two modes, high speed and high resolution. The high resolution mode produces consistent values with a low noise to signal ratio but cannot be used above 2 Hz. The high speed mode on the other hand does not sacrifice any actual resolution but instead gives up a processing feature called delta-sigma ADC conversion that makes the high resolution collections so consistent. A correspondence regarding this is included in Appendix C. Another detail about the strain modules is that they cannot read three lead quarter bridge gauges, out of the box. Therefore, quarter bridge gauges used in this research are not the same as those used in another UNH SHM research project, the Powder Mill Bridge in Barre, MA. The monitoring system at the Powder Mill Bridge uses 3 lead quarter bridge gauges that feature an extra lead to compensate for temperature effects on the lead wires (Lefebvre 2010). However a working solution that would use resistors to modify the circuit was developed by engineers at NI and is also included in the Appendix B of this report.

153

APPENDIX E: Neutral Axis Determination from Strain Data Collected from an In-Service Bridge

The theoretical neutral axis of a beam represents a horizontal plane above which longitudinal stresses act tension or compression and below which stresses act in the opposite. In a doubly symmetric rolled shape with a consistent modulus of elasticity that is in pure bending, the plane is theoretically in the center of the section. Evenly dividing the geometry will balance tension and compressive forces in the beam. In a composite section, the added capacity of the deck moves the neutral axis upward, as shown in Figure E-1. The neutral axis is therefore of particular interest because it is a feature that can indicate changes in the capacity of the deck or the steel as well as changes in the level of composite action. If shear studs became corroded, for example, and the steel beams and concrete deck of a bridge were no longer in full composite action, the calculated neutral axis from strain gauge readings should shift indicating damage.

Figure E-1: Illustration of Neutral Locations in Composite and Non-Composite Sections

Figure E-1 shows a composite beam made of a concrete slab and steel rolled shape. When the beam is fully composite it is expected to have a neutral axis higher than half the depth of the beam and closer to the deck. When the beam is fully composite it has a single neutral axis, however, a non-composite beam will have two, a neutral axis for the deck and a neutral axis for the beam. The neutral axis of a rolled shape will be at half the depth of the beam, or lower in cases with an attached bottom cover plate like at the Bagdad Road Bridge. By instrumenting the steel, the location of the neutral axis can be watched over time to see if it moves suddenly from external events, such as impact, or slowly over time indicating degradation of the composite section or behavior.

Generally, the location of the neutral axis is assumed to be relatively static, meaning that it is in the same location regardless of load applied to the beam. The assumption holds true when the beam behaves linearly in the elastic range. However, mechanics show that materials do not behave entirely elastic. Concrete in particular has a non-linear and inelastic stress-strain relationship though it is usually assumed to be linear-elastic at smaller stresses. This indicates that as load increases, the neutral axis may move slightly. Other phenomena such as creep, or section loss, can also cause the location of the neutral axis to change over time. If this movement is tracked with instrumentation, it could be used to access the hidden deck or shear connector health.

154

Neutral axis research using two strain gauges in a cross section has been conducted by UNH and other universities. Lefebvre designed a system using quarter bridge bonded foil strain gauges at the Powder Mill Bridge in Barre, MA (Lefebvre 2010). Chakraborty and DeWolf used uniaxial strain gauges in pairs reading at high speeds to locate neutral axis during regular field monitoring. Their results showed the neutral axis moved suddenly for brief moments particularly when large trucks would pass over the bridge, sometimes as much as 12 inches, and suggested this could be the result of dynamic behaviors (2006).

This research expands on previous neutral axis based research by using multiple gauges in a cross section to investigate sensor behavior. A potential problem in measuring neutral axis locations is the presence of noise in the strain readings. Ideally only two strain values should be required because that is all that is needed to plot a straight line. Under elastic deformations, longitudinal strains will theoretically vary linearly throughout the depth of the section. Hence the assumptions that plane sections remain plane will hold true. However, using only two values carries the risk of noise or sensor malfunction causing erroneous neutral axis locations. This research uses an additional strain gauge, located at the center of the web, to produce more reliable results.

If noise causes significant difference between the calculated locations of neutral axis determined by different pairs of gauges, it could imply that more than just two gages in a cross section are required to determine a reliable neutral axis location. Requiring even just one more gauge at each location would result in 50% more strain gauges, data acquisition channels, storage demands, and installation times. This produces a potential cost to benefit ratio of two versus three gauges and is therefore an interest to SHM system designers and was chosen as an analysis portion of this thesis.

E.1 Neutral Axis Location Methods

The process of measuring neutral axis can be thought of in two ways that both rely on the assumption of linear strain distribution. The first is using similar triangles, and the second is plotting stain versus depth within the section and solving for the y-intercept of the line it creates. Using similar triangles may seem more intuitive, while plotting strain versus depth within the section is shown to prove the interchangeable nature of the neutral axis location without the need to re-derive or prove the equation for each pair of sensors that can be used. Both methods provide the same mathematical expression. The illustration in Figure E-2 shows the anatomy of the composite section that is used for this analysis.
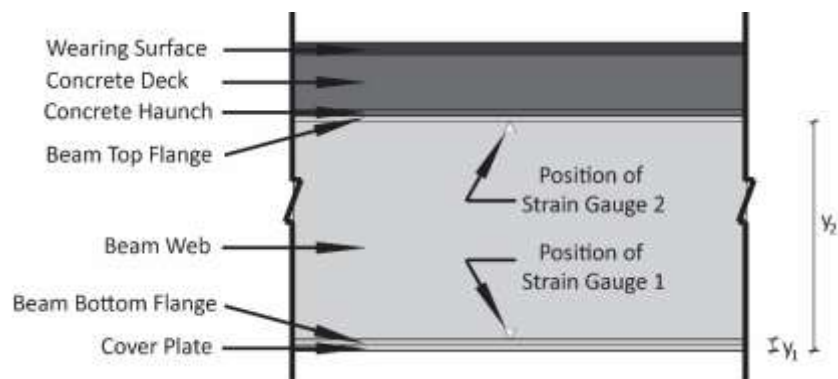
Figure E-2: Illustration of Composite Section Instrumented For Neutral Axis Detection

E.1.1 Method of Similar Triangles

If two strain values are available from any two locations in a composite section, the location of the neutral axis can be determined. To prove the method, consider an example with gauges installed on the top and bottom flanges as shown in Figure E-2. Using strain values the strain diagram shown in Figure E-3 can be generated. It can also be seen in Figure E-3 that the location of the neutral axis is the position of the top gauge minus the length shown on the strain diagram labeled c. If NA is the vertical position of the neutral axis measured from the bottom of the composite section, the formula for its position is shown in equations E-1.

$$NA = y_2 - c \qquad \text{(Eq. E-1)}$$
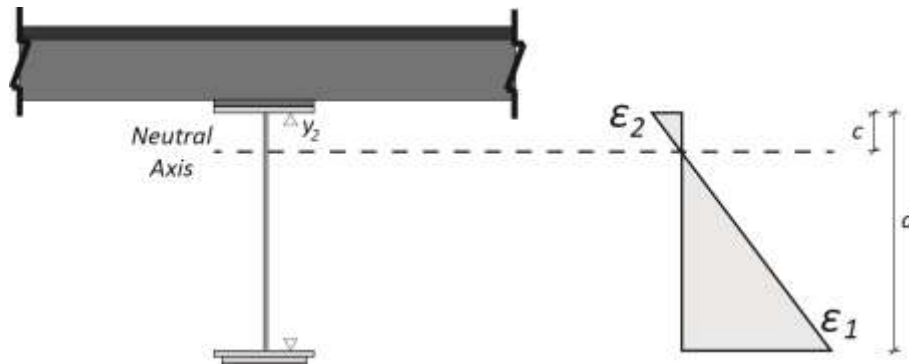
Figure E-3: Illustration of a Typical Strain Diagram for Composite Sections

The linear strain distribution is the basis for the relationship shown in Equations E-2 because of the properties of similar triangles.

$$\frac{-\varepsilon_2}{c} = \frac{\varepsilon_1}{d-c} \qquad \text{(Eq. E-2)}$$

The distance between the two gages is represented by d. Further simplifying for c will result in equation E-3.

$$c = \frac{d\varepsilon_2}{\varepsilon_2 - \varepsilon_1} \qquad \text{(Eq. E-3)}$$

Substituting c into equation E-1 yields the location of the neutral axis as measured from the bottom of the beam equation E-4.

$$NA = y_2 - \frac{d\varepsilon_2}{\varepsilon_2 - \varepsilon_1} \qquad \text{(Eq. E-4)}$$

E.1.2 Y-Intercept Method

Another approach to determining neutral axis location also involves the strain diagram and the equation of a line. If strains versus depths are plotted, the neutral axis corresponds to the y-intercept of the linear equation as shown in the Figure E-4.
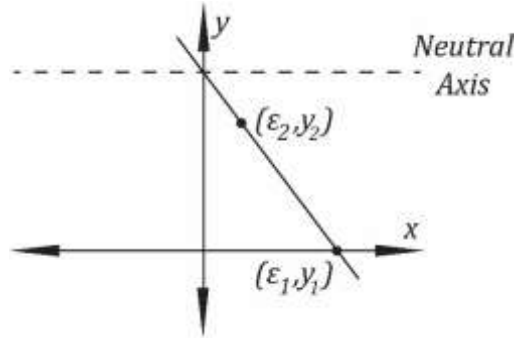
Figure E-4: Illustrated Neutral Axis Located on Cartesian Coordinate System

Equation E-5 is the equation of a line:

$$y = mx + b \qquad \text{(Eq. E-5)}$$

The equation solved for the y-intercept with the term b replaced with the neutral axis location:

$$NA = y - mx \qquad \text{(Eq. E-6)}$$

The slope of the line, m, is the difference in depth over the difference in strain values, as shown in Equation E-7:

$$m = \frac{\Delta y}{\Delta x} = \frac{y_2 - y_1}{\varepsilon_2 - \varepsilon_1} = \frac{d}{\varepsilon_2 - \varepsilon_1} \qquad \text{(Eq. E-7)}$$

Substituting equation E-7 into equation E-8 the equation for the neutral axis is found:

$$NA = y - \left(\frac{d}{\varepsilon_2 - \varepsilon_1}\right) x \qquad \text{(Eq. E-8)}$$

The position of the neutral axis can, therefore, be solved by substituting any pair of values from the position of gauges and corresponding strain values into Equation E-8. Either set of values, corresponding to the vertical height of the sensor and a strain reading from it, can be used for variables y and x. Note that if y_2 and x_2 are used the resulting equation, it will be the same as the equation derived using the method of similar triangles in the previous section.

E.1.3 Linear Regression

The process of using 3 gauges to measure the neutral axis will require a linear regression. Because of noise in the strain readings, the three pairs of strain and vertical position data will rarely fall on the same line. The linear regression, otherwise known as the best fit line, is the line that best correlates with data that is assumed to behave linearly. Overall the line produces the least amount of discrepancy, of any possible straight line, when the square of the differences between all data points is summed and minimized. The process is also known as the method of least squares.

Figure E-5 illustrates how noise in the measurements can cause a shift in the perceived neutral axis location. Besides the fact that the method of least squares introduces new equations, the method is the same in theory as the previously described y-intercept method. Strain values and vertical positions are plotted, and the intercept of the line with the y-axis is the location of the neutral axis, as shown in Figure E-4.

157
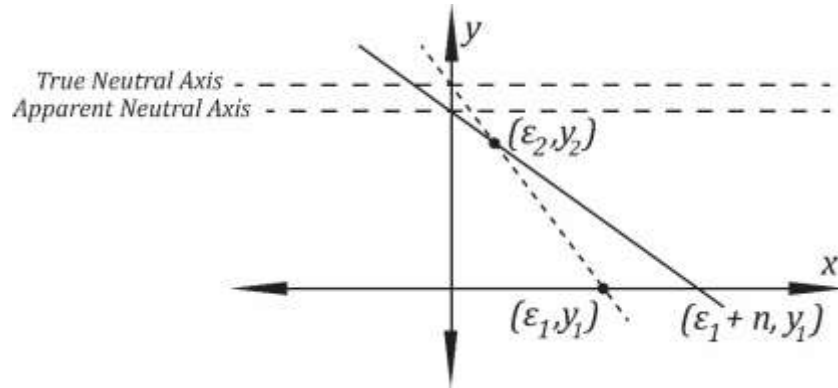
Figure E-5: Illustrated Effect of Noise on Apparent Neutral Axis Location

The slope of a regression is given in Equation E-9.

$$m = \frac{n(\sum xy) - (\sum x)(\sum y)}{n(\sum x^2) - (\sum x)^2}$$ (Eq. E-9)

The y-intercept, neutral axis, can then be solved for using Equation E-10.

$$NA = \bar{y} - m\bar{x}$$ (Eq. E-10)

E.2 Limitations of Live Load Strains

The exact dead load strain cannot be known for several reasons. Furthermore, gauges are placed with an inherent error, or imbalance, that can only be managed by calibrating the gauge to read zero. The gauges will therefore only measure change in strain from the time they are calibrated. The full bridge gauges will primarily measure live load induced strains where the quarter bridge gauges will measure live load strains and strains that are caused by the coefficient of thermal expansion of steel, as described in Chapter 3. If, however, temperature effects cause curvature as a response to restraints at the bearings that restrain thermal expansion, the full bridge gauges would be expected to capture effects from those strains.

The inability of measuring dead load strains means that neutral axis calculations can only be made when a bending load is placed on the beam. At other times the gauges should return to values close to zero, where the only deviation from zero are extremely small and caused by electrical noise and other errors, such as thermal effects. If the gauges actually read zero, it can be seen that the calculated value of the neutral axis would be the value of y used in Equation E-8. For example, if y_2 is used:

$$NA = y_2 - \frac{d(0)}{(0+0)} = y_2$$

Not knowing the dead load strains has no impact on the ability to measure neutral axis during live load events, assuming linearly elastic behavior. It can be seen in Figure E-6 that imposing the live load strains on dead load strain diagram or simply using the live load strain distribution will located the same position of a neutral axis.
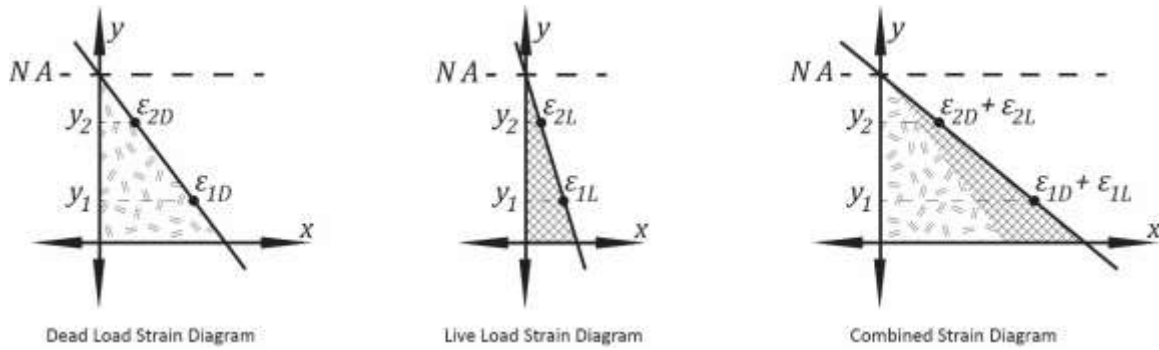
Figure E-6: Neutral Axis Locations from Dead Load, Live Load, and Combination of Dead and Live Loads

Because plane sections remain plane, strains will vary linearly throughout a section, and the ratio of dead load strains in two locations will be the same as the ratio of the live load strains in those same locations and therefore dead load strains are not required for measuring neutral axis locations.

E.3 Error Management

Several sources of error exist when using bonded foil strain gauges. These sources include multiple temperature effects on the lead wires and gauges, as described in detail in chapter 4, as well as effects of unprofessional soldering and not cleaning the flux off the solder, residual strain from the pressure of holding the gauge during installation, and any sources that might exist in the data acquisition equipment. Furthermore, potential issues that were not expected in installations at the Bagdad Road Bridge could affect strain measurements such as issues with the glue and gauge off-axis issues. These sources of error may cause researchers to be skeptical of all results derived from systems using bonded foil strain gauges.

These sources of error can be categorized by additive and multiplicative errors. The apparent strain is a constant that is added to the measured strain value, whatever that might be. The effect on the gauge factor will change what is multiplied by the voltage signal from the gauge and is therefore a multiplicative effect. The additive error is believed to be eliminated during calibrations. The multiplicative error is believed to be negligible because it cancels out of equations for apparent Poisson's ratio and neutral axis calculation.

The concept can be demonstrated by analyzing equations used in this research and including the sources of errors. The total of all multiplicative errors in this case is labeled E_M, and E_A is the total of all additive errors, the second subscript of each coefficient corresponds to the gauge the errors are affecting. Note that there is also a multiplicative effect on the additive error as well.

The equation for Poisson's Ratio Including Sources of Error:

$$v_a = \frac{(-\varepsilon_{transverse})E_{Mt} + E_{At}E_{Mt}}{(\varepsilon_{longitudinal})E_{Ml} + E_{Al}E_{Ml}} \qquad \text{(Eq. E-11)}$$

The equation for Neutral Axis Location Including Sources of Error:

$$NA = y_2 - \frac{d(\varepsilon_2 E_{A2} + E_{A2}E_{M2})}{[(\varepsilon_2 E_{A2} + E_{A2}E_{M2}) - (\varepsilon_1 E_{A1} + E_{A1}E_{M1})]} \qquad \text{(Eq. E-12)}$$

Figure E-7 shows the effect of the additive error on the strain measurements. Keeping in mind that the quarter bridge gauges cancel out strain due to thermal expansion and contraction,

159

any deviation from zero in an unloaded member is expected to be the result of additive (or subtractive) errors.
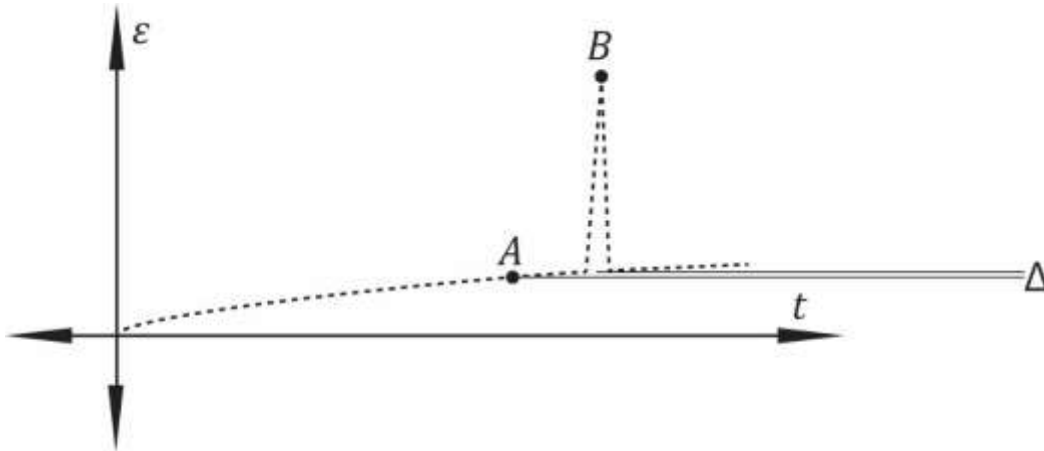
Figure E-7: Illustration of Typical Strain Reading over Time at the Bridge

Because all points on the line, such as point *A*, should be zero before the event occurs, values of strain at every point must be equal to $E_A E_M$. Then, during the event, the strain is equal to $E_A E_M + \varepsilon E_m$. In the analyses, a calibration value was subtracted from every event that was determined by averaging values over a period of time in every minute. Of course, there is a small difference between the value from calibration of and the value that occurs right at the event, this can be labeled Δ. If delta is small, close to zero, it can be negated from the equations. This produces equations E-13 and E-14:

$$v_a = \frac{(-\varepsilon_{transverse})E_{Mt} + E_{At}E_{Mt}}{(\varepsilon_{longitudinal})E_{Ml} + E_{At}E_{Mt}}$$

$$NA = y_2 - \frac{d(\varepsilon_2 E_{M2} + E_{A2}E_{M2})}{[(\varepsilon_2 E_{M2} + E_{A2}E_{M2}) - (\varepsilon_1 E_{M1} + E_{A1}E_{M1})]}$$

$$v_a = \frac{(-\varepsilon_{transverse})E_{Mt}}{(\varepsilon_{longitudinal})E_{Ml}} \qquad \text{(Eq. E-13)}$$

$$NA = y_2 - \frac{d\varepsilon_2 E_{A2}}{(\varepsilon_2 E_{M2} - \varepsilon_1 E_{M1})} \qquad \text{(Eq. E-14)}$$

If the multiplicative error can be assumed the same in both gauges, it can further be eliminated from the equations, first by factoring in the equation for neutral axis.

$$v_a = \frac{(-\varepsilon_{transverse})E_M}{(\varepsilon_{longitudinal})E_M}$$

$$NA = y_2 - \frac{d\varepsilon_2 E_M}{(\varepsilon_2 - \varepsilon_1)E_M}$$

And the original equations without errors are produced:

$$v_a = \frac{-\varepsilon_{transverse}}{\varepsilon_{longitudinal}} \qquad\qquad NA = y_2 - \frac{d\varepsilon_2}{\varepsilon_2 - \varepsilon_1}$$

The likelihood that multiplicative errors are close in both gauges is assumed to be high. The temperature correction curves showed that although minor changes in temperature had a large impact on the apparent microstrain, the effect on gauge factor was extremely small, less than 1% over the whole range of temperatures over the bridge. The small differences between temperatures at the gauges, with regards to multiplicative error, are negligible. The gauges on each face of each beam were installed on the same days so any multiplicative errors caused by installation might be similar, and furthermore, the wire leads are close in length and exposed to the same temperature, and they are all read by the same data acquisition equipment.

The same method of removing drift in the full bridge gauges also removes strain due to thermal expansion between the point of calibration and the event in quarter bridge gauge use. This may or may not be an issue for structural health monitoring. Thermal expansion may be able to tell certain things about the way a structure is behaving. However, eliminating thermal induced strain may help to focus on the way the structure is reacting to excitation. This may be all that is needed to produce values important to structural capacity such distribution factors and neutral axis locations.

APPENDIX F: Recommended Testing Parameters for Digital Image Correlation for Structural Response Measurements

Previous research at UNH was successful in obtaining deflection measurements using DIC, but the parameters used for testing confined the system to measuring only one displacement at a time and focused on keeping the cameras as perpendicular to the targets as possible. The testing parameters used by Peddle, 2011 produced repeatable results, but there was no research into how they affected the results obtained by DIC. There needed to be an investigation into those effects and the tolerable operating ranges of the parameters in order to increase the confidence level in DIC for in-service bridge field testing. This chapter addresses the range of operating parameters for DIC.

F.1 Testing Parameters and Setup

The parameters for this research were derived based on previous research and questions raised by bridge owners (NHDOT) and bridge engineers. Tests were performed in the structures laboratory to determine the effects of the target pattern, lighting conditions, and camera angle on the deflection results. The results of these tests decided the settings used to test an in-service bridge. An in-service bridge was used as verification of the recommended parameter settings.

Tests were performed on a shake table to determine the optimal settings for speckle pattern, lighting, and camera angle (Figure F-1).

Figure F-1: Lab testing setup using a shake table with a known displacement.

This setup eliminated the use of alternative methods for measuring displacement, such as a potentiometer or LVDT. The DIC results were compared directly to a known displacement. The shake table was set to run with an amplitude of 0.1002 in (2.545 mm) and a frequency of 0.29 Hz. The targets were rigidly attached to the shake table by clamping them to an angle that was bolted

to the table. Each testing scenario was repeated three times to provide confidence in the results. The three repeated tests are labeled "test a", "test b", and "test c" in the following figures.

F.2 Target Pattern

This research developed a Matlab® program to analyze the speckle pattern distribution and the percentage of black of a given target. Figure F-2 shows the distribution of speckles for each target evaluated. Each pattern had the same percentage of black, but had the speckle sizes making up that percentage varied. Figure F-2 shows a continuous curve for the speckle size despite the use of four discrete speckle sizes to create each pattern. This is because there is some overlap of the speckles and the Matlab® program finds an equivalent radius in this case. The targets were created in Microsoft Word® from four different size black circles of radius 0.05", 0.1", 0.2", and 0.4". Theses circles were added to each image such that the total area of circles was the same between the three images. For example, if a 0.4" circle was added to the large pattern, then four 0.2" circles were added to the medium pattern, and sixteen 0.1" circles were added to the small pattern. The three targets evaluated are shown in Figure F-3.
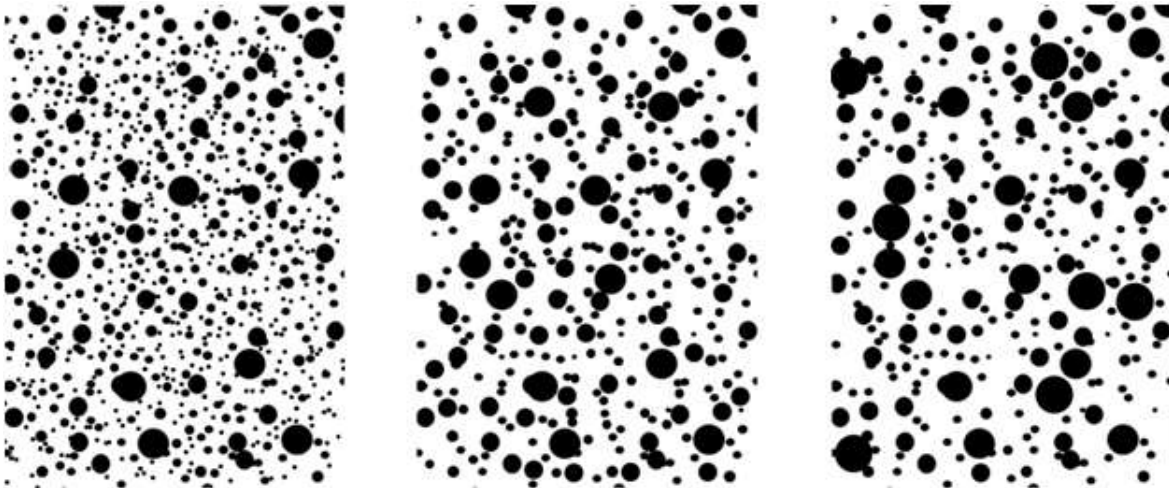
Figure F-2: Speckle size distribution produced using Matlab for small, medium, and large patterns.

163
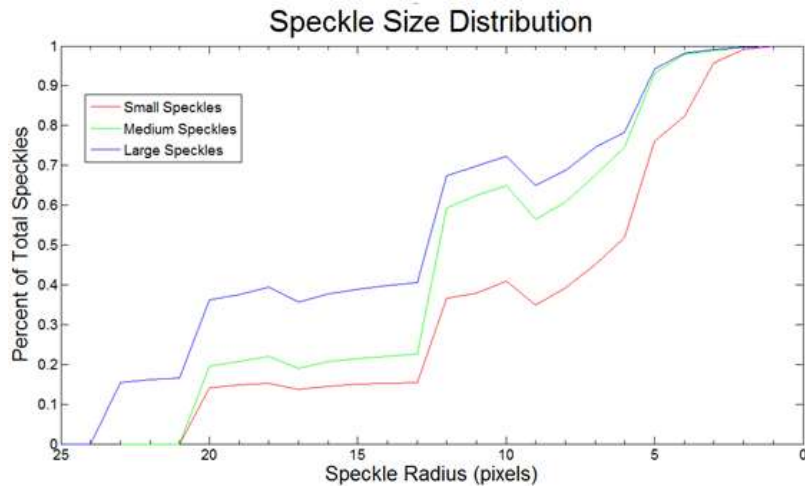
Figure F-3: Speckle targets evaluated in lab testing. From left to right: small, medium, and large speckles.

The speckle pattern had no effect on the results, as shown in Figure F-4, Figure F-5, and Figure F-6. There is a slight shift between the shake table and the measured data in Figure F-5. This occurred because the shake table was not reset at zero before each test (a, b, and c), and the plots of the measured data needed to be shifted over to match the table as closely as possible.
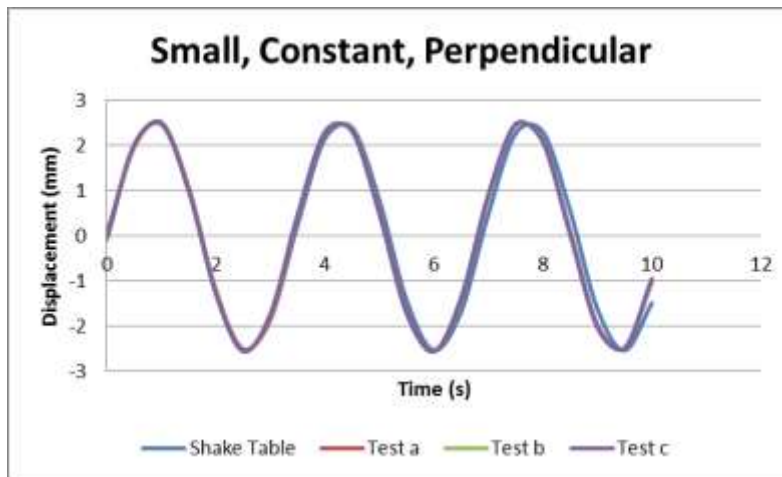
Figure F-4: Shake table test results for a small size speckle pattern, constant lighting, and the camera perpendicular to the target.
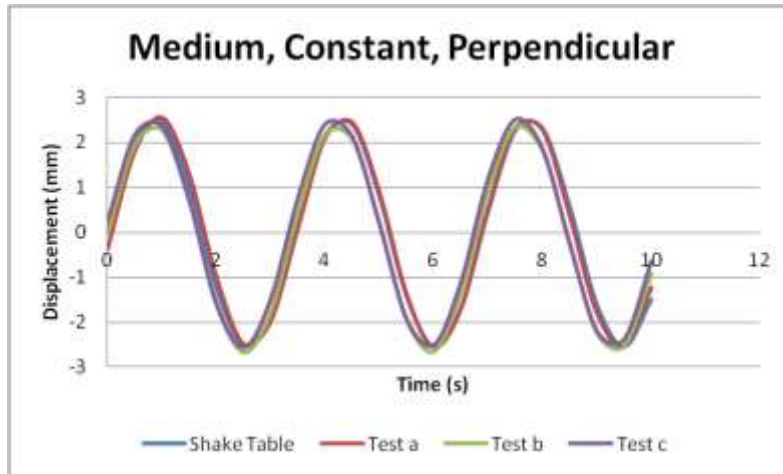
Figure F-5: Shake table test results for a medium size speckle pattern, constant lighting, and the camera perpendicular to the target.
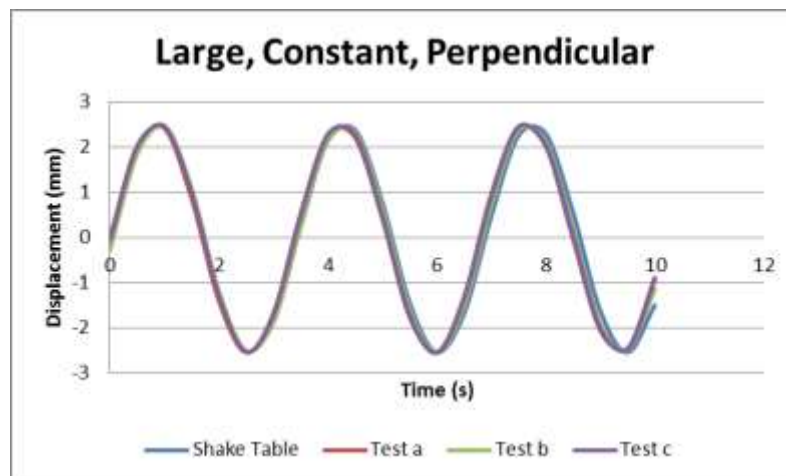
Figure F-6: Shake table test results for a large size speckle pattern, constant lighting, and the camera perpendicular to the target.

After reviewing the literature on the digital image correlation technique, the speckle pattern results make sense. In these tests there was no deformation to the specimen; there were only translational displacements. All pixels moved the same distance relative to one another, so it does not matter whether there is a single speckle on the specimen or a thousand. The software measures the same displacement of the specimen within the frame of view.

F.3 Lighting

The lighting conditions for a target were either constant or random. A pair of 1000 Watt halogen spot lights was used to provide the lighting on the targets. For the random lighting case, a piece of cardboard was waved in front of the lights in order to mimic the effect of clouds in front of the

165

sun. The results show that the lighting conditions had the largest effect on the accuracy of the DIC results. This is apparent in Figure F-7 and Figure F-8. When the lighting is constant, the image processing software is able to track the same subset of pixels from one frame to another. This is possible by assigning a gray value to a subset and then tracking the subset with that gray value from one frame to each subsequent frame. When the lighting varies, the gray value of a given subset changes from frame to frame and the software has difficulty tracking the subset.
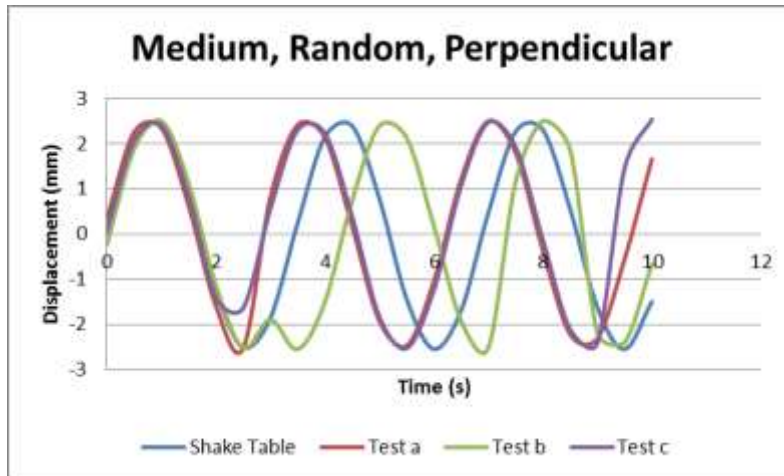
Figure F-7: Shake table test results for a medium size speckle pattern, random lighting, and the camera perpendicular to the target.
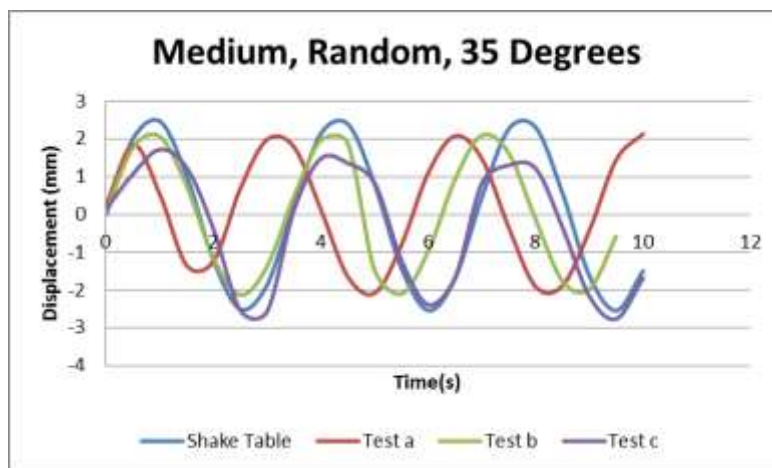
Figure F-8: Shake table test results for a medium size speckle pattern, random lighting, and 35 degree camera angle.

The best way to mitigate the effects of lighting on the results would be to perform a load test at night with artificial lighting. Since this was not practical for this research due to costs, bridge testing was performed with the cameras beneath the bridge looking from one abutment down to

166

the other. This minimized the effects of varying sunlight. Another practical method for daytime testing would be to illuminate the targets with artificial lights that are strong enough to counteract variations in sunlight.

F.4 Camera Angle

The results show that the DIC results are less than the actual displacements when the camera is on an angle. This effect can be seen clearly in Figure F-9.
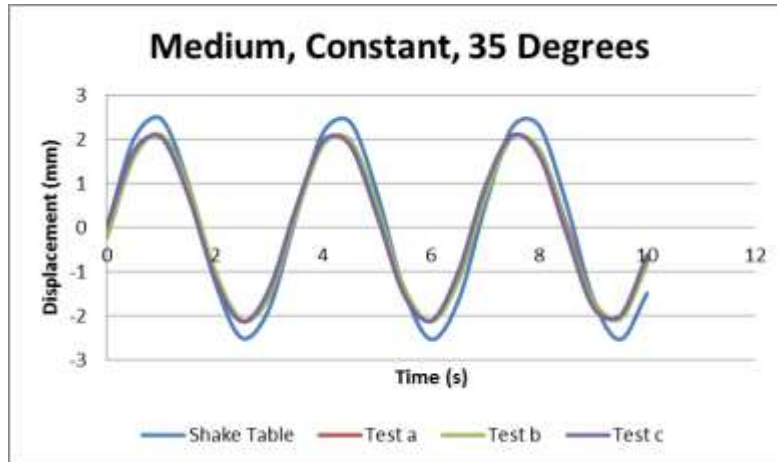
Figure F-9: Shake table test results for a medium size speckle pattern, constant lighting, and 35 degree camera angle.

The effect of the angle can also be seen by looking back and comparing Figure F-7 and Figure F-8. This discrepancy occurs because the software is measuring displacement perpendicular to the camera's line of action. If the angle is known, then the displacements can be corrected using trigonometry. For instance, the measured angle of 2.05 mm becomes 2.50 mm when corrected for the angle of 35 degrees from this lab test. Figure F-10 shows the trigonometry behind this calculation. The angle between the camera and the target is an issue in field testing because it is not always possible to be perpendicular to the targets. If the angle cannot be measured, then the camera angle should be as perpendicular as possible and as the camera placed reasonably far from the target in order to minimize the effects of angle.
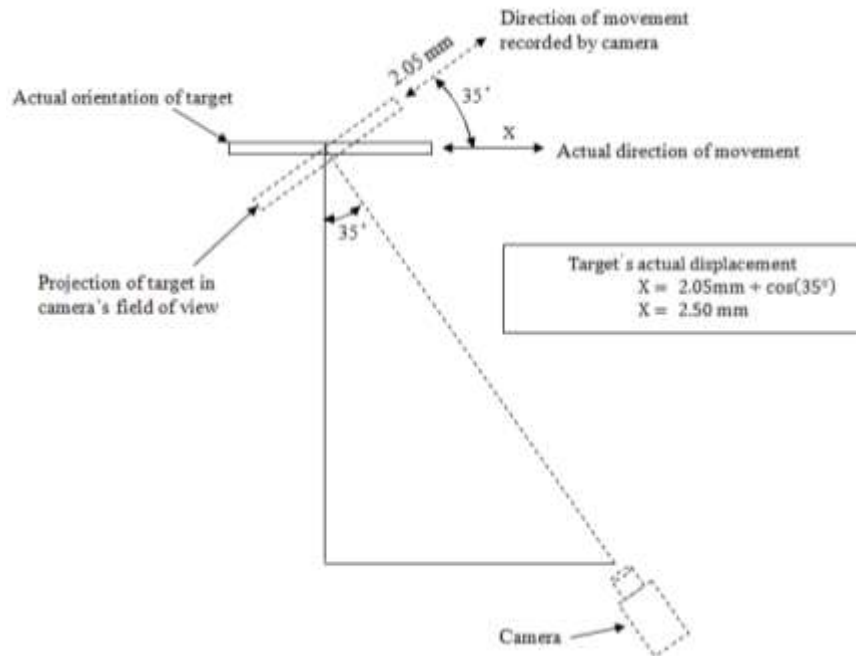
Figure F-10: Trigonometry to convert camera's measurement to objects actual measurement.

The camera angle becomes an issue in the field when the cameras have to be setup above or below a set of girders to be measured (Figure F-11). The cameras must be as level as possible to a target in direction of interest. For example, when measuring a displacement in the vertical direction it is ok for the cameras to be at an angle horizontally with the target, but not vertically.

Figure F-11: Cameras not setup level with girders. Note: this photo is of previous research performed at UNH.

F.5 Summary of Results and Recommendations

The results of this testing showed that the speckle pattern density is not as important to the accuracy of the collected data as proper lighting. The angle between the camera and the target is important, but errors from this source can be corrected for if the angle is known. See Table F-1 for recommended testing parameters.

Table F-1: Recommended testing parameters.

Parameter	Importance	Optimum Range	Avoid
Speckle Pattern	Low	Some form of distinguishable random pattern	No contrast between target and surroundings
Lighting Conditions	High	Constant; Slight variations are ok	Intermittent sun/clouds
Camera Angle	Medium	Perpendicular to target; Correct for known angle	Any angle, if unable to calculate it; Any acute angles

For field use, it is recommended that the target has a large enough speckle pattern such that it is distinguishable in the cameras field of view. Also, variations in lighting must be minimized by either testing at night with artificial lighting or keeping testing confined to the underside of the bridge and using a blind to block out light if necessary. The camera should be kept as perpendicular to the target as possible in order to minimize the angle between the two. If the camera cannot be setup perpendicular to the target, then measurements must be made to best estimate the angle between the camera and target. The camera data can then be corrected with the known angle.

APPENDIX G: Bagdad Road Strain Gauge Installation Procedure and Documentation

This section includes details related to the installation at the Bagdad Rd Bridge. The Initial Instrumentation Plan is included in section G.1. The document described the layout of sensors that were considered a first phase of instrumentation. The actual instrumentation that occurred is now considered the first phase, and when a second phase is planned, these proposed installation location should be evaluated for inclusion, if they still support research goals.

The application procedure document made for the initial installation is included in section G.2. Note that the strain relieving terminal strips were not used after the second gauge was installed. Drawings that represent the actual instrumentation, or the instrumentation conducted as phase 1, are included in section G.3. A list of equipment used during gauge application and lead wire installation is included in section G.4. Section G.4 includes documents related to the strain gauges. This includes the sheets that were filled out after the installation which may include notes for some sensors, as well photographs of each strain gauge. Note that because the thermocouples do not include any adhesion and are held to the face of the beam using tape, checklists were not used and photos of the uncovered gauges were not taken.

G.1 Initial Installation Plan

David Gaylord
11/25/2011
Erin Bell
UNH Department of Civil Engineering

Initial Instrumentation of the Bagdad Road over US Route 4 Introduction

On Monday Nov 28th we will be installing an initial batch of strain gauges. The station will require six strain gauges and two thermocouples. Observations from the initial installation will be used to plan installation of the remaining gages, which will be performed tentatively during the following weekend.

Schedule:

Transport and Set-up Scaffolding	8:30-10:00 am
Grinding and Prepping Surfaces	10:00-11:30 am
Glue Gauges in Place	11:30 am - 12:30 pm
Break for Lunch and Allow Time for 1-hour cure	12:30-1:30 pm
Solder Gauges and Apply environmental protection	1:30-3:00 pm
Secure Wires:	3:00-4:00 pm
Disassemble Scaffolding and transport back to UNH	4:00 – 5:00 pm

The schedule provides significant time to complete all tasks patiently and safely. If the times are far underestimated, and additional time is available to install at other stations, another station may be instrumented.

Instrumentation Layout:

The beam selected for the initial installation is the third interior beam from the southeast side of the bridge, labeled station D in the following figure. The particular location requires the most gauges out of all stations. It was chosen for the initial installation for two reasons. If significant weather conditions

prevent additional installation for an extended period of time, this location will provide the maximum amount of data of any station. Secondly, the station provides the most amounts of observations that can be made about the procedure without having to worry about reconfiguring the scaffolding.
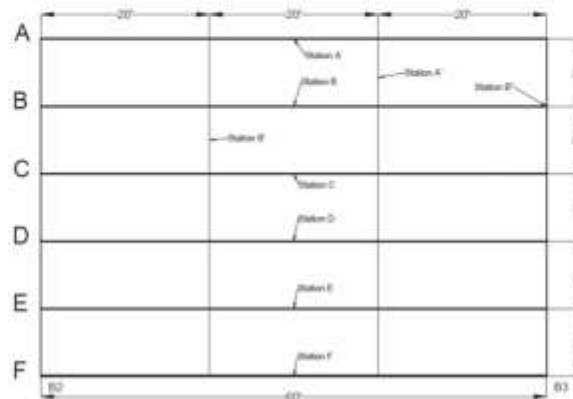
A single strain gauge will be installed each side of each flange 3" from the edge of the flange. Single strain gauges will be installed on each face of the web in the same section as the gauges on the flange at half the depth of the beam, 1' 5" from either flange.

172
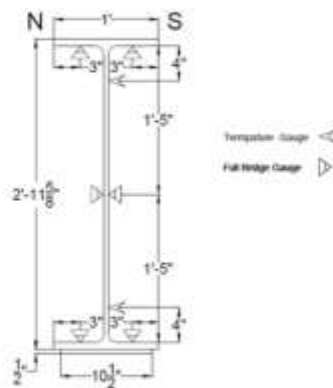
Gauging Procedure

Installing strain gauges will involve grinding a minimal amount of pain from the surface of the beam. The gauges measure 0.583" x 0.437". Care will be taken to remove the smallest amount of paint as possible, by limiting excess scrapes caused by the equipment outside the footprint of the gauge. The area will be given smooth surface with fine-grit sandpaper. The gauges will be glued with a cold curing adhesive, with tape applying pressure to the surface of the gauge for 1-hr.

An intermediate strain relieving strip will be glued to the surface of the beam 1" inch away from the bottom of the gauge. The wire that will run to the data acquisition system will be soldered to the strip and the leads from the gauges will then be soldered to the strip providing connectivity. The roll of wire for each gauge will then be sealed in plastic and taped to the flange till a time has been arranged to run the wires through split wire loom back to the data acquisition system.
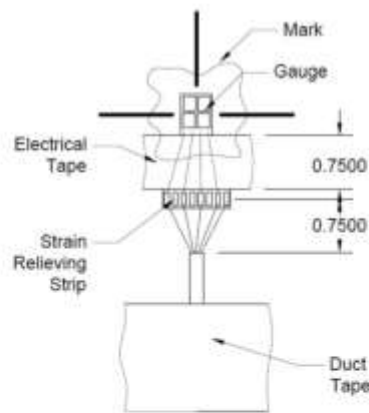
The gauge and strain relieving strip will be covered in paste to protect it from the environment. Then the area will be covered with aluminum tape. Later the tape will be painted to hide the entire installation. More details are available in the instructions included as an appendix to this document.

The thermocouples involve a much simpler instillation and no removal of paint. They will simply be taped with the aluminum tape on the web of the north face of the beam at 4" from each flange. The wire will be secured to the flange in the same manner as the wire connected to the strain gauges.

Scaffolding

OSHA compliant scaffolding has been rented from Seacoast Scaffolding in Concord NH. Scaffolding will be erected and used in accordance with DOT safety requirements. A meeting with Steve Mandeville, Safety and Environmental Coordinator for NHDOT Materials and Research was conducted to review the safety procedures and investigate any additional procedures that may be required caused by the close proximity to the road. All scaffolding will be level and platforms will be used to keep it from settling. All workers and non-workers at the site will wear hardhats and safety vests.

Debriefing

Following the installation a debriefing meeting will be held to discuss the installation and plan the remainder of gauge installation. Using the times for each step of gauge installation as well as scaffolding assemble and disassemble a schedule will be created to install the remaining 17 strain gauges and 4 thermocouples. Although the previous observed times will be used, methods of improving the installation procedure, for both accuracy and reduced duration, will be discussed.

Evaluations

By installing gauges on this member and other members, the methods to monitor strain values at locations on a steel beam for a period of time will be evaluated. This will include gauge selection, proper placement, installation procedures, programing, environmental protection, and duration of installation.

The installation of the 6 strain gauges described in this document will be used to analyze differences between using a linear interpolation between 2 strain values to calculate a neutral axis versus using a

174

linear regression from 3 gauge values. This important evaluation has a severe impact on the number of gauges and data acquisition channels that would be required for other structural health monitoring systems. Differences in strain values from gauges at the same height (in section) on the beam will be used to observe any potential strain value range in future installations. If this range grows over time it could indicate failure of the gauge, adhesive, or environmental protection.

Pre-cured sealed Gauges

Adhesives used to glue the gauges to the beams should be investigated, both in regards to the effect on measurement accuracy and lifespan of the installation. Recommended curing for typical strain gauge adhesives involves heating a specimen to a very specific temperature with a specific applied pressure that are not practical for instrumentation on civil structures. Pre-cured sealed gauges are manufactured by Vishay measurements with a bonded foil gauge similar to those that are to be used at both the Bagdad Rd and Gilford Bridge projects. Comparing values from gauges cured at the bridge to these gauges will be used to evaluate the chosen adhesives for the SHM systems.

The gauges are pre-adhered to a 0.005" thick shim in laboratory settings. The shim is then soldered to the surface of the beam at the location of interest. The heat given off by tools used for this type of measurement will not cause a measurable stress concentration and no heat distortion of the metal surface. The heat energy is measured in milli-joules is negligible compared to typical submerged arc welding which is typically measured in kilojoules.

175

G.2 Strain Gauge Application Procedure

Strain Gauge Application Procedure (11/25/2012)

1. Grind and prep a surface approximately 1"x1" centered at the designated location. Stencil the mark with a permanent marker with the center of the stencil located at the designated location. Do not fill in the center of the stencil.
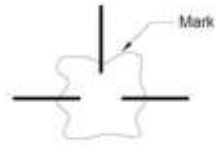
2. Glue the gauge at the center of the mark following the procedure for gluing strain gauges.
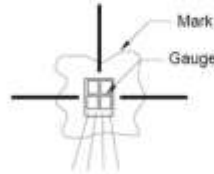
3. Apply a piece of electrical tape at the bottom of the gauge to shield the leads from the steel surface of the beam.
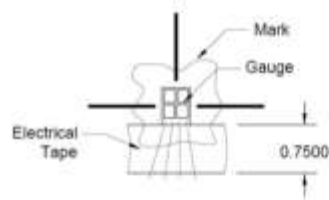
4. Glue the strain relieving strip at the opposite end of the tape. Be careful to glue the strip to the beam and not to the electrical tape.

176
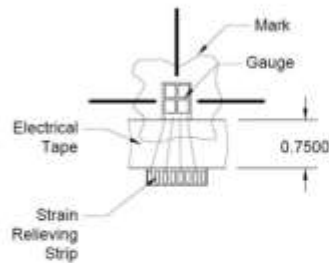
5. Use duct tape to secure the correctly labeled wire close to the gauge. The end of the shielded portion of the wire should be about ¾" away from the strain relieving strip. Secure the rest of the wire.
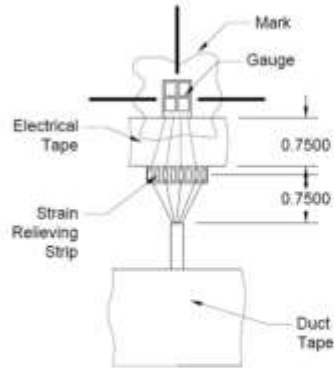
6. After the glue has cured solder the wires and leads to the strip at the correct locations. Then apply the environmental protection to the entire surface of the installation, including the full area of the ground surface, the soldered wires, strain relieving strip, and any portions of the wire extending past the duct tape.

7. Use aluminum tape to cover the entire area.
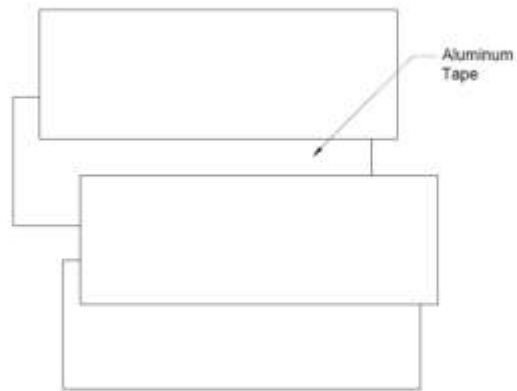
G.3 As-Instrumented Drawings
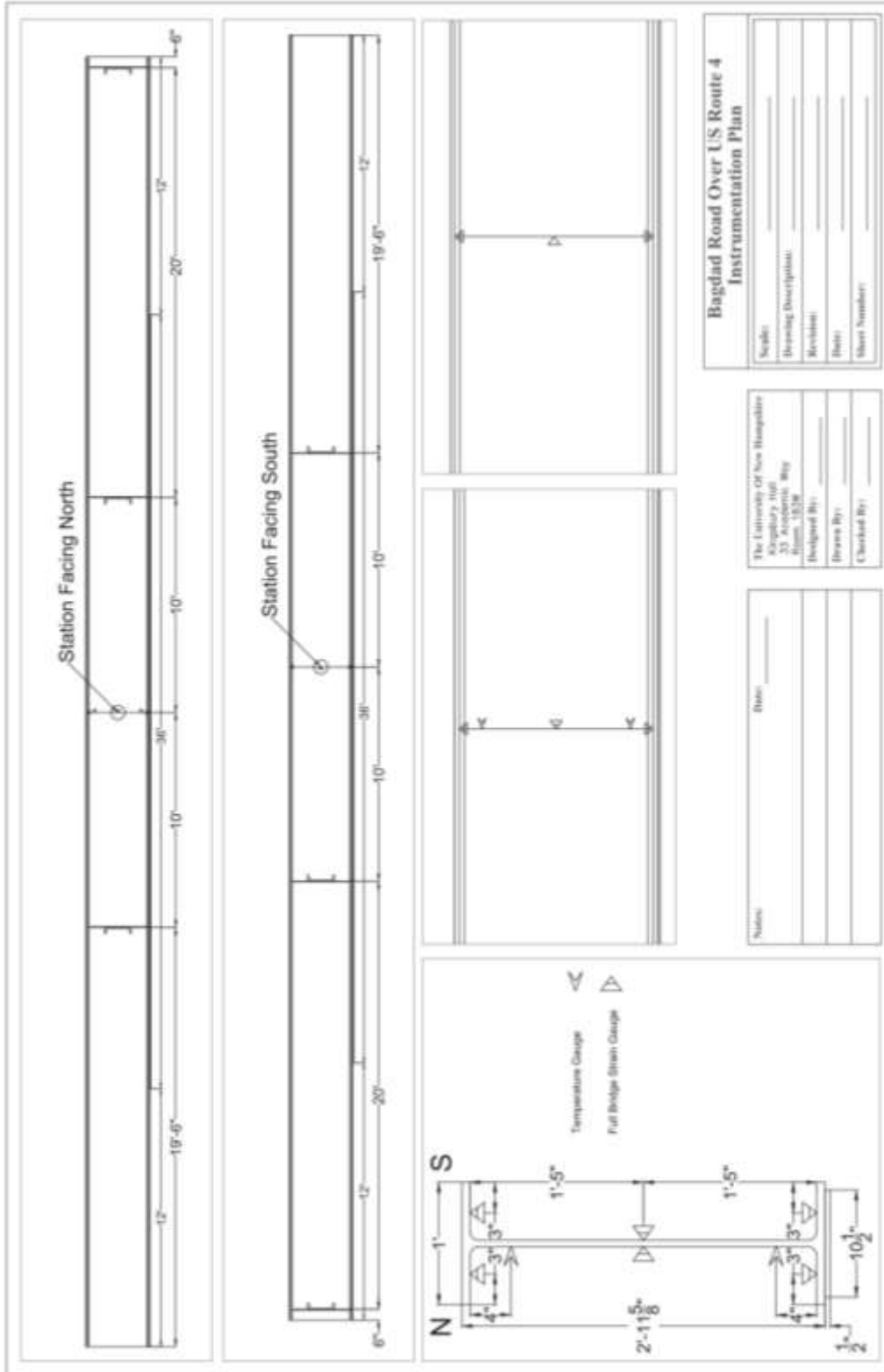
Station Facing North
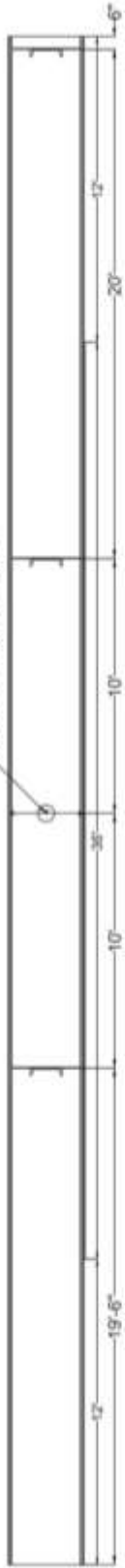
Station Facing South

Bagdad Road Over US Route 4
Instrumentation Plan

The University Of New Hampshire
Kingsbury Hall
33 Academic Way
Room 103W

Scale:
Drawing Description:
Revision:
Date:
Sheet Number:

Designed By:
Drawn By:
Checked By:

Date:

Notes:

Full Bridge Strain Gauge

Qtr Bridge Gauge

179
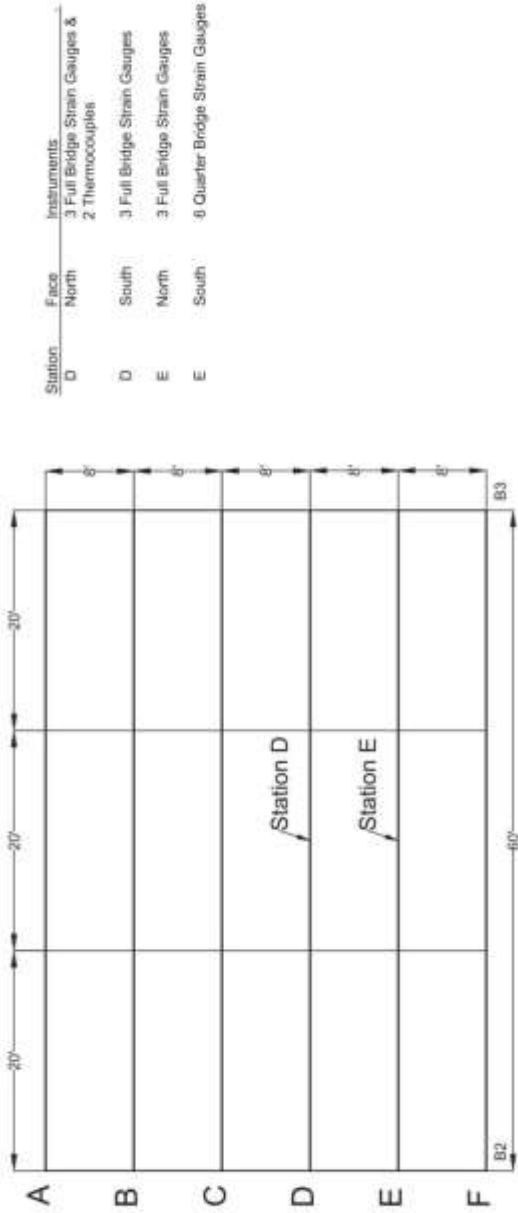
Station	Face	Instruments
D	North	3 Full Bridge Strain Gauges & 2 Thermocouples
D	South	3 Full Bridge Strain Gauges
E	North	3 Full Bridge Strain Gauges
E	South	6 Quarter Bridge Strain Gauges

Station D

Station E

A B C D E F

20' 20' 20' 20' 20'

8' 8' 8' 8' 8'

B2 B3

Span 1 Span 2 Span 3 Span 4

23' 22' 20' 20' 20' 20' 20' 22' 23'

45' 60' 60' 45'

B1 B2 B3

A B C D E F

8' 8' 8' 8' 8'
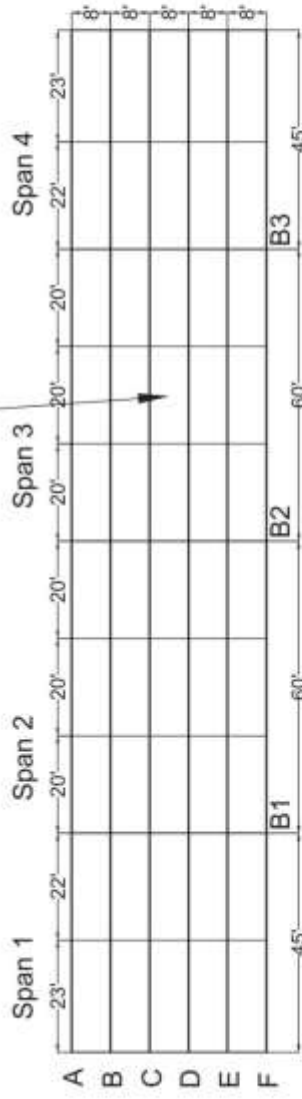
Bagdad Road Over US Route 4
Instrumentation Plan

Scale:

Drawing Description:

Revision:

Date:

Sheet Number:

G.4 Equipment Used during Gauge Instrumentation

The following tables include the items that were used during each installation. The items have been broken up into categories of surface preparation equipment, gauge adhesive and environmental protection, soldering equipment, and miscellaneous. It should be noted that an image of the stencil is not included because it was lost shortly after the installations. Surface preparation included a Ryobi AG402 grinder for removing paint, 80 grit sand paper and emery cloth to smooth the surface, acetone and tissues to clean residuals off the surface, and latex gloves that were worn when handling the acetone and would remain on through the application and bonding of the gauge.

Table G-1: Surface Preparation Equipment Used during Installation

4-in Angle Grinder	80-Grit Coarse Sandpaper	Emery Cloth Sandpaper	Container of Acetone
(homedepot.com)	(homedepot.com)	(homedepot.com)	(homedepot.com)
Latex Gloves		**Box of Plain Tissues**	
(homedepot.com)		(homedepot.com)	

Sensor adhesion and weather protection items included the Loctite 496 adhesive and packing tape used to bond the gauges to the exposed steel, the Hercules "Sta Put" plumbers putty (stock number 25-101) to cover the sensor and the area affected by the removal of the paint, electrical tape to isolate the lead wires from the conductive steel, foil tape (Nashua Tape Product 324A Cold Weather) to protect the installation from weather, and green tape to hide the installation and wires on the face of the beam.

Table G-2: Sensor Adhesion and Weather Protection Items Used during Installation

Loctite-496 Adhesive	Vinyl Electrical Tape	Foil Tape 324A Cold Weather	Scotch Masking Tape
(grainger.com)	(homedepot.com)	(homedepot.com)	(homedepot.com)

Plumbers Putty	Green Duct Tape

(homedepot.com)	(staples.com)

Soldering equipment and related items included a soldering iron (Radio Shack Cat No: 64-2055A), led-free solder (Radio Shack Cat No: 64-089), and water and rags to clean the soldering iron.

Table G-3: Soldering Equipment and Related Items Used during Installation

Soldering Iron	Led-free solder	Bottle Water	Rags
(Radioshack.com)	(radioshack.com)	(staples.com)	(Homedepot.com)

Miscellaneous equipment included the digital voltmeter used to ensure the installed gauge and lead wires were connected properly, the chalk used to mark the installation location, and the wire strippers that were used if repair needed to be made to the connection that would include cutting of the soldered portions of the lead wires and making another attempt. Lastly, the gel splice connectors were used to connect the quarter bridge gauges as described in Appendix C.

Table G-4: Miscellaneous Items Used during Installation

Digital Voltmeter	Chalk	Wire stripper	Gel Splice Connector
(sperryinstruments.com)	(staples.com)	(homedepot.com)	(tekcomponents.com)

AG.5 Installed Gauge Records

Details about each sensor are shown in Table G-5 including information about which number lead wire the gauge is connected to as well as information included in the calibration sheets, such as gauge factor and other information used to identify the specific sensor by the manufacturer. Photographs of each strain gauge and detail sheets are also included. Note that the bottom portion of the detail sheet is not filled out because it pertains to DAQ connectivity details that may vary each time the gauges are connected or may become established if long-term or continuous monitoring is established at the bridge.

Table G-5: Installed Strain Gauge Details

Gauge	Beam	Face	Location	Wire#	GF	Batch	CHT\lot No	Model No.
15	E	N	Bottom	15	2.12	5206	147	SGT-4/1000-FB11
16	E	N	Web	16	2.12	5206	147	SGT-4/1000-FB11
17	E	N	Top	17	2.12	5206	147	SGT-4/1000-FB12
12	D	S	Top	12	2.12	5139	147	SGT-4/1000-FB13
13	D	S	Middle	13	2.12	5139	147	SGT-4/1000-FB14
14	D	S	Bottom	14	2.12	5139	147	SGT-4/1000-FB15
9	D	N	Bot	9	2.12	5139	147	SGT-4/1000-FB16
10	D	N	Middle	10	2.12	5139	147	SGT-4/1000-FB17
11	D	N	Top	11	2.12	5139	147	SGT-4/1000-FB18
1	E	S	Top	1/2c	2.09	161A	Y2501	KFG-3-350-C1-11L1M2R
2	E	S	Top	1/2c	2.09	161A	Y2501	KFG-3-350-C1-11L1M2R
3	E	S	Middle	3/4c	2.09	161A	Y2501	KFG-3-350-C1-11L1M2R
4	E	S	Middle	3/4c	2.09	161A	Y2501	KFG-3-350-C1-11L1M2R
5	E	S	Bottom	5/6c	2.09	161A	Y2501	KFG-3-350-C1-11L1M2R
6	E	S	Bottom	5/6c	2.09	161A	Y2501	KFG-3-350-C1-11L1M2R

Table G-6: Installed Thermocouple Details

Termocouple	Beam	Face	Location	Wire#	QC #	INSP#	Model No.
6	D	S	Top	6T	PL2010/10	22302	5TC-GG-T-20-36
5	D	S	Bottom	5T	PL2010/10	22302	5TC-GG-T-20-36

Figure G-1: Photograph of Full Bridge Strain Gauge Installed on the Bottom Flange of Beam D, South Face

Figure G-2: Photograph of Full Bridge Strain Gauge Installed on the Web of Beam D, South Face

Figure G-3: Photograph of Full Bridge Strain Gauge Installed on the Top Flange of Beam D, South Face
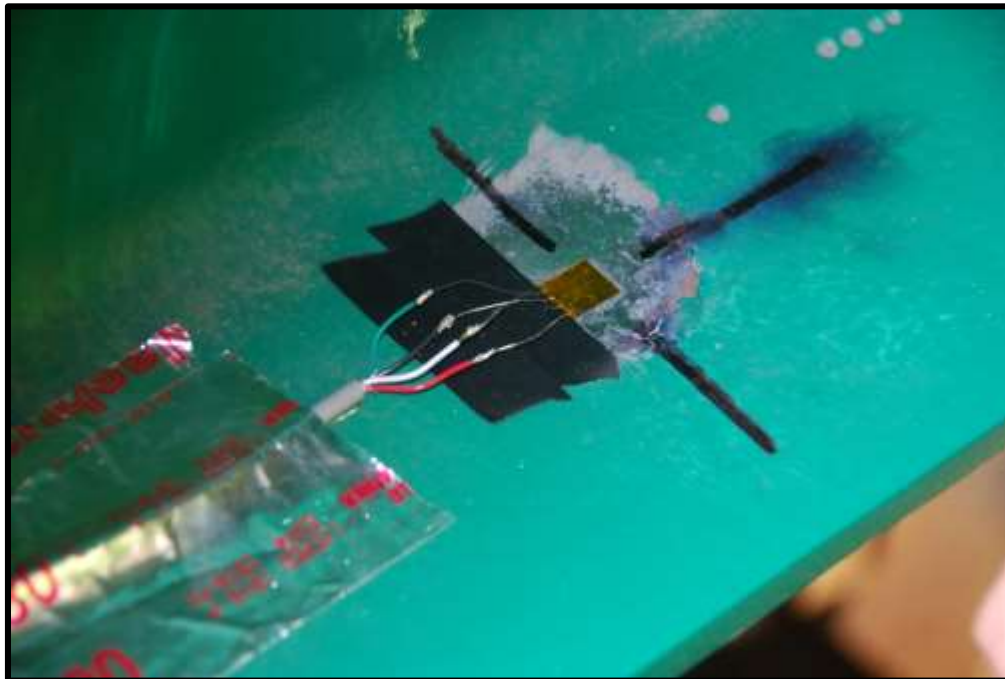
Figure G-4: Photograph of Full Bridge Strain Gauge Installed on the Bottom Flange of Beam D, North Face
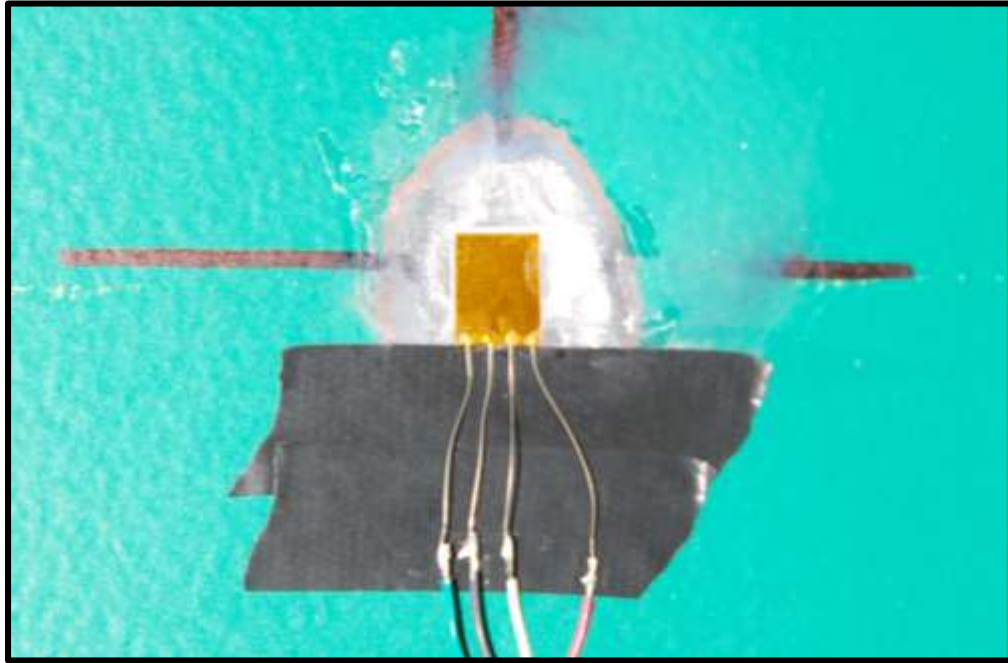
Figure G-5: Photograph of Full Bridge Strain Gauge Installed on the Web of Beam D, North Face
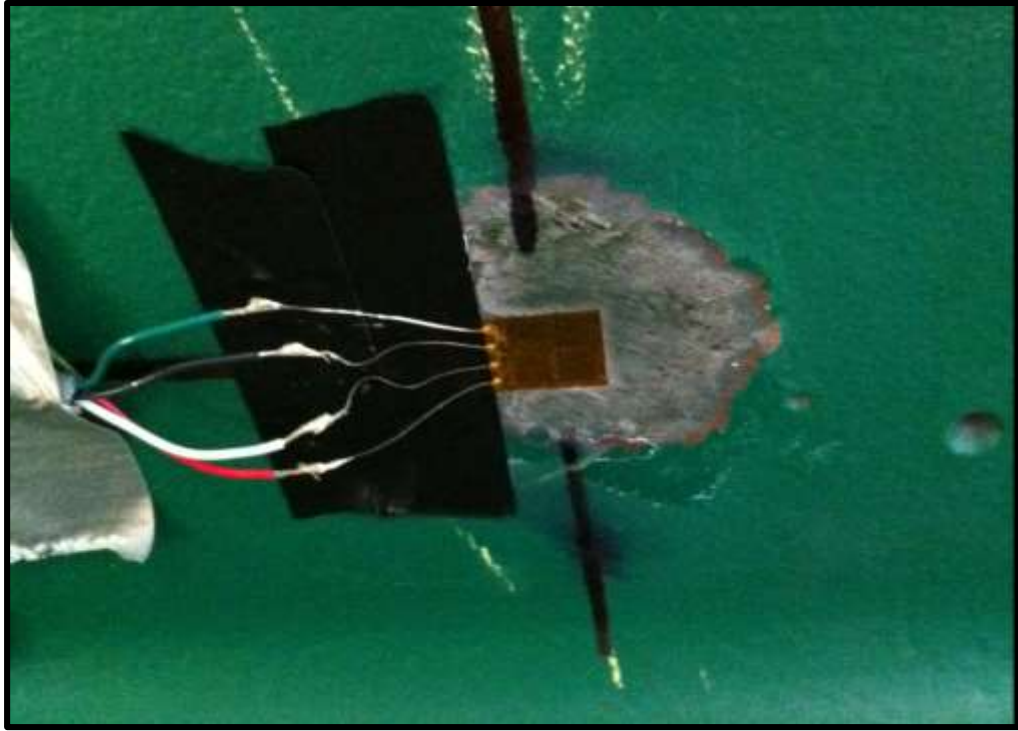
Figure G-6: Photograph of Full Bridge Strain Gauge Installed on the Top Flange of Beam D, North Face
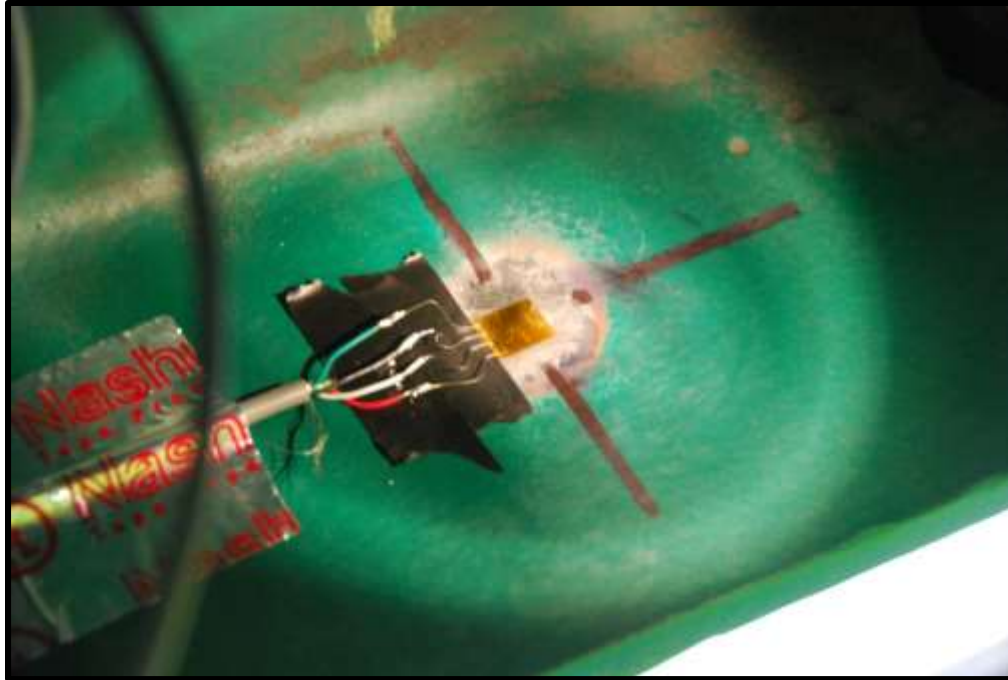
Figure G-7: Photograph of Full Bridge Strain Gauge Installed on the Bottom Flange of Beam E, North Face

Figure G-8: Photograph of Full Bridge Strain Gauge Installed on the Web of Beam E, North Face

Figure G-9: Photograph of Full Bridge Strain Gauge on the Top Flange of Beam E, North Face
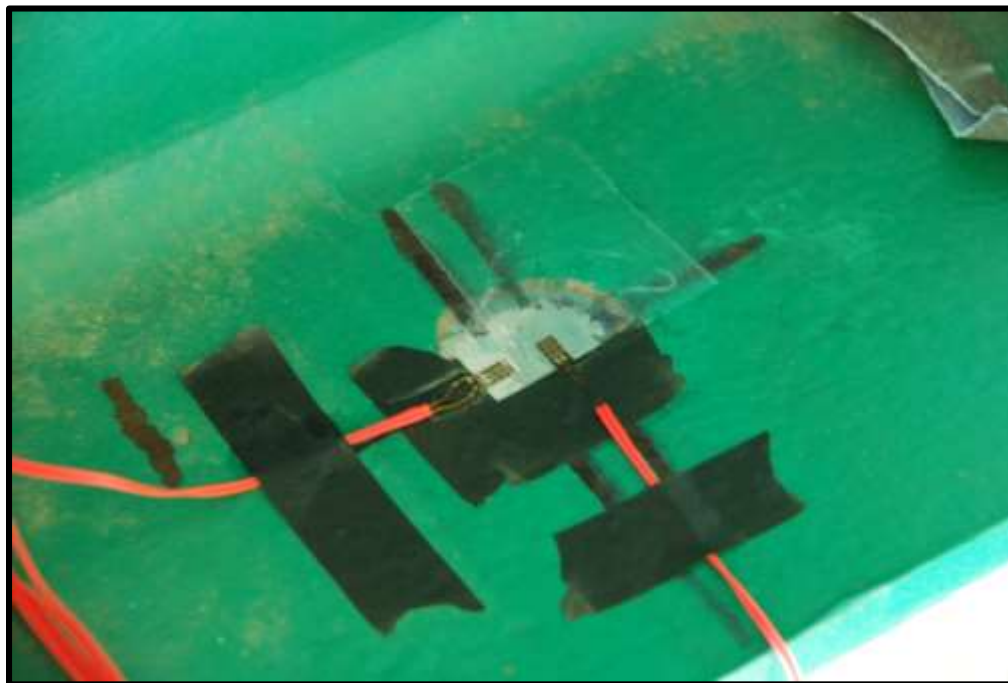
Figure G-10: Photograph of the Pair of Quarter Bridge Strain Gauges Installed on the Bottom Flange of Beam E, South Face
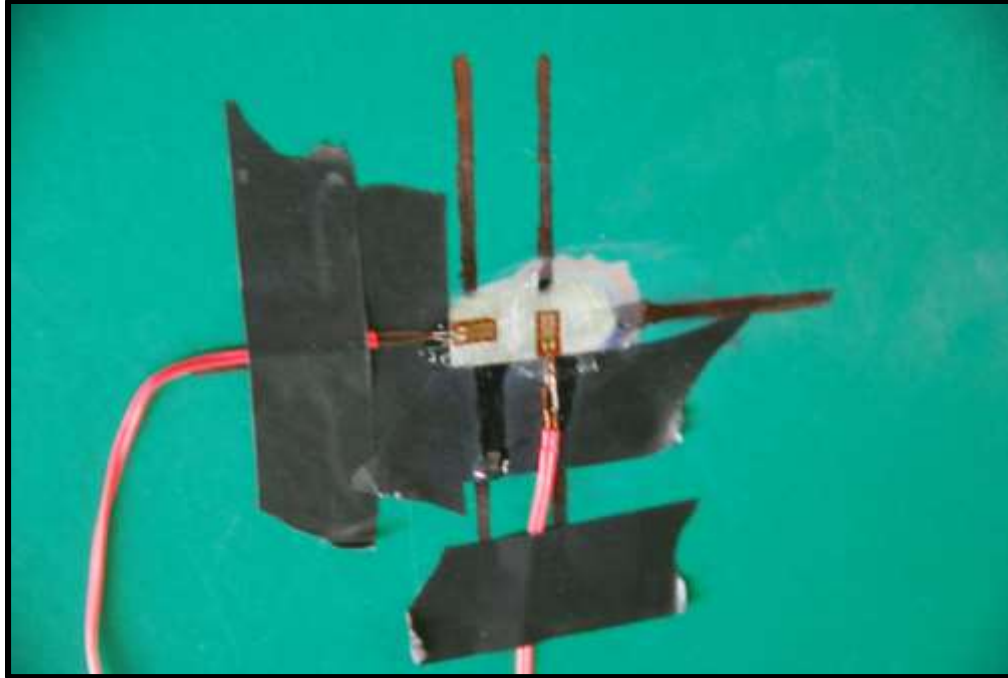
Figure G-11: Photograph of the Pair of Quarter Bridge Strain Gauges Installed on the Web of Beam E, South Face
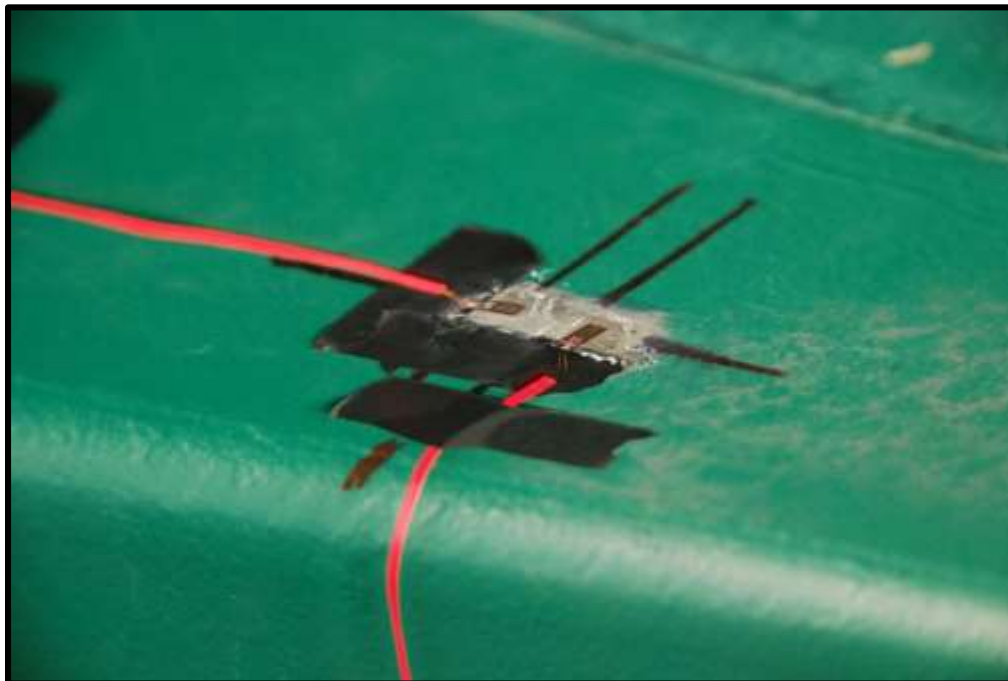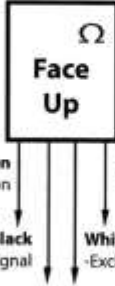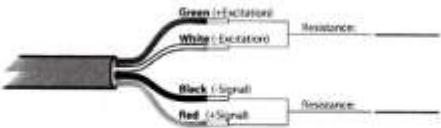
Figure G-12: Photograph of the Pair of Quarter Bridge Strain Gauges Installed on the Top Flange of Beam E, South Face

Figure G-13: Photo of Taped Sensor on South Face of Beam D, Showing Thermocouples

Figure G-14: Sample Strain Gauge Sheet for Full Bridge Strain Gauge on Bottom Flange of Beam D, South Face

Figure G-15: Strain Gauge Sheet for Full Bridge Strain Gauge on Web of Beam D, South Face

Bagdad Road over US Route 4 — Strain Gauge Sheet

Gauge ID # ___12___
Station Letter: ___D___

Ω Face Up

Installer's Initials: _____
Solder Intact: ☑
Process Complete: ☑

Location (to center of gauge)

Face	(South) / North
Location	(Top) / Bottom / Web
Distance To Edge	3"
Distance To Chan.	10'
Photo #	12
Photo Time	2 : 32

Green
+Excitation

Red
+Signal

Black
-Signal

White
-Excitation

Process

1. Grind Surface
2. Smooth / Clean
3. Mark Location
4. Apply Gauge
5. Apply Terminal Pad
6. Tape Surface
7. Tape Wire
8. Solder Connections
9. Apply putty
10. Tape / Label Gauge
11. Photograph Installation
12. Document Installation

Notes

No terminal pad was used

Gauge ID # _____
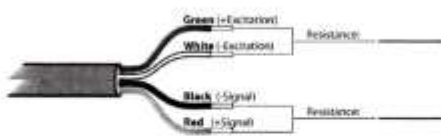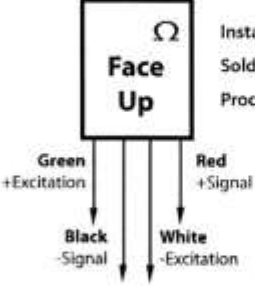Location _____
　Chassis # _____
　Mod # _____
　Channel # _____

Green (+Excitation) Resistance _____
White (-Excitation)
Black (-Signal)
Red (+Signal) Resistance _____

Notes

Testers Initials: _____

Figure G-16: Strain Gauge Sheet for Full Bridge Strain Gauge on Top Flange of Beam D, South Face

Bagdad Road over US Route 4 — Strain Gauge Sheet

Gauge ID # _____ 9

Station Letter: _____ D

Ω **Face Up**

Installer's Initials: _____

Solder Intact: ☑

Process Complete: ☑

Location (to center of gauge)

Face	South / (North)
Location	Top / (Bottom) / Web
Distance To Edge	3"
Distance To Chan.	10'
Photo #	9
Photo Time	2:25

Green +Excitation

Red +Signal

Black -Signal

White -Excitation

Process

1. Grind Surface
2. Smooth / Clean
3. Mark Location
4. Apply Gauge
5. Apply Terminal Pad
6. Tape Surface
7. Tape Wire
8. Solder Connections
9. Apply putty
10. Tape / Label Gauge
11. Photograph Installation
12. Document Installation

Notes

No terminal pad was used

Gauge ID # _____

Location _____

Chassis # _____

Mod # _____

Channel # _____

Green (+Excitation)

White (-Excitation)   Resistance: _____

Black (-Signal)

Red (+Signal)   Resistance: _____

Notes

Testers Initials: _____

Figure G-17: Strain Gauge Sheet for Full Bridge Strain Gauge on Bottom Flange of Beam D, North Face

Bagdad Road over US Route 4 — Strain Gauge Sheet

Gauge ID # _10_
Station Letter: _D_

Installer's Initials: _____
Solder Intact: ☑
Process Complete: ☑

Face Up Ω

Location *(to center of gauge)*

Face	South / **North**
Location	Top / Bottom / **Web**
Distance To Edge	_0_
Distance To Chan.	_10'_
Photo #	_10_
Photo Time	_2:47_

Green +Excitation
Red +Signal
Black -Signal
White -Excitation

Process

1. Grind Surface	5. Apply Terminal Pad	9. Apply putty
2. Smooth / Clean	6. Tape Surface	10. Tape / Label Gauge
3. Mark Location	7. Tape Wire	11. Photograph Installation
4. Apply Gauge	8. Solder Connections	12. Document Installation
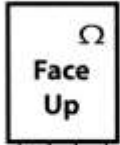
Notes

No terminal pad was used

Gauge ID # _____
Location _____
Chassis # _____
Mod # _____
Channel # _____

Green (+Excitation)
White (-Excitation)
Black (-Signal)
Red (+Signal)
Resistance _____
Resistance _____

Notes
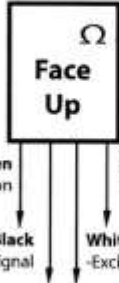
Testers Initials: _____

Figure G-18: Strain Gauge Sheet for Full Bridge Strain Gauge on Web of Beam D, North Face

Figure G-19: Strain Gauge Sheet for Full Bridge Strain Gauge on Top Flange of Beam D, North Face

Bagdad Road over US Route 4 — Strain Gauge Sheet

Gauge ID # _15_
Station Letter: _E_
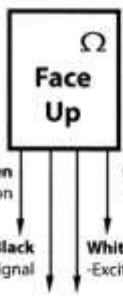
□ Ω **Face Up**

Installer's Initials: _[signature]_
Solder Intact: ☑
Process Complete: ☑

Location (to center of gauge)

Face	South / (North)
Location	Top / (Bottom) / Web
Distance To Edge	_3"_
Distance To Chan.	_10'_
Photo #	_15_
Photo Time	_2:32_

Green +Excitation
Red +Signal
Black -Signal
White -Excitation

Process

1. Grind Surface
2. Smooth / Clean
3. Mark Location
4. Apply Gauge
5. ~~Apply Terminal Pad~~
6. Tape Surface
7. Tape Wire
8. Solder Connections
9. Apply putty
10. Tape / Label Gauge
11. Photograph Installation
12. Document Installation

Notes

No terminal pad was used

Gauge ID # _____
Location _____

Chassis # _____
Mod # _____
Channel # _____

Green (+Excitation) — Resistance: _____
White (-Excitation)
Black (-Signal)
Red (+Signal) — Resistance: _____

Notes

Testers Initials: _____

Figure G-20: Strain Gauge Sheet for Full Bridge Strain Gauge on Bottom Flange of Beam E, North Face

Bagdad Road over US Route 4 — Strain Gauge Sheet

Gauge ID # ___16___
Station Letter: ___E___

Ω **Installer's Initials:** [signature]
Face Up **Solder Intact:** ☑
Process Complete: ☑

Location *(to center of gauge)*

Face	South / **North**
Location	Top / Bottom / **Web**
Distance To Edge	0
Distance To Chan.	10'
Photo #	16
Photo Time	1 : 58

Green +Excitation   Red +Signal
Black -Signal   White -Excitation

Process

1. Grind Surface
2. Smooth / Clean
3. Mark Location
4. Apply Gauge
5. Apply Terminal Pad
6. Tape Surface
7. Tape Wire
8. Solder Connections
9. Apply putty
10. Tape / Label Gauge
11. Photograph Installation
12. Document Installation

Notes

~ 5-10° off axis
No terminal pad was used

Gauge ID # _____

Location _____

Chassis # _____
Mod # _____
Channel # _____

Green (+Excitation)   Resistance: _____
White (-Excitation)
Black (-Signal)   Resistance: _____
Red (+Signal)

Notes

Testers Initials: _____

Figure G-21: Strain Gauge Sheet for Full Bridge Strain Gauge on Web of Beam E, North Face

Bagdad Road over US Route 4 — Strain Gauge Sheet

Gauge ID # _17_
Station Letter: _E_

Ω   **Installer's Initials:** _RR_
Face Up   **Solder Intact:** ☑
Process Complete: ☑

Location *(to center of gauge)*

Face	South / (North)
Location	(Top) / Bottom / Web
Distance To Edge	3"
Distance To Chan.	10'
Photo #	17
Photo Time	1:59

Green +Excitation   Red +Signal
Black -Signal   White -Excitation

Process

1. Grind Surface
2. Smooth / Clean
3. Mark Location
4. Apply Gauge
5. Apply Terminal Pad
6. Tape Surface
7. Tape Wire
8. Solder Connections
9. Apply putty
10. Tape / Label Gauge
11. Photograph Installation
12. Document Installation

Notes

No terminal pad was used

Gauge ID # _____
Location _____
    Chassis # _____
    Mod # _____
    Channel # _____

Green (+Excitation)   Resistance: _____
White (-Excitation)
Black (-Signal)   Resistance: _____
Red (+Signal)

Notes

Testers Initials: _____

Figure G-22: Strain Gauge Sheet for Full Bridge Strain Gauge on Top Flange of Beam E, North Face

Bagdad Road over US Route 4   –   Strain Gauge Sheet

Gauge ID # _5/6C_
Station Letter: _E_

Red → +Signal
Black → -Signal

Location (to center of gauge)

Face	South / North	Installer's Initials: _____
Location	Top / Bottom / Web	Solder Intact: ☑
Distance To Edge	_3"_	Process Complete: ☑
Distance To Chan.	_10'_	
Photo #	_5/6_	
Photo Time	_1:27_	

Green +Signal   White -Signal

Process

1. Grind Surface
2. Smooth / Clean
3. Mark Location
4. Apply Gauge
5. ~~Apply Terminal Pad~~
6. Tape Surface
7. Tape Wire
8. ~~Solder Connections~~
9. Apply putty
10. Tape / Label Gauge
11. Photograph Installation
12. Document Installation

Notes

No terminal Pad was used
No soldering, slice type UY was used

Gauge ID # _____

Location _____

Chassis # _____
Mod # _____
Channel # _____

Green (+Excitation)   Resistance: _____
White (-Excitation)
Black (-Signal)   Resistance: _____
Red (+Signal)

Notes

Testers Initials: _____

Figure G-23: Strain Gauge Sheet for the Pair of Quarter Bridge Strain Gauges Installed on the Bottom Flange of Beam E, South Face

203

Bagdad Road over US Route 4 — Strain Gauge Sheet

Gauge ID # 3/4 C
Station Letter: E

Red +Signal
Black -Signal

Location *(to center of gauge)*

Face	South / North
Location	Top / Bottom / (Web)
Distance To Edge	O
Distance To Chan.	10'
Photo #	3/4
Photo Time	1:28

Green +Signal   White -Signal

Installer's Initials:
Solder Intact: ☑
Process Complete: ☑

W
G
R B

Process

1. Grind Surface
2. Smooth / Clean
3. Mark Location
4. Apply Gauge
5. Apply Terminal Pad
6. Tape Surface
7. Tape Wire
8. Solder Connections
9. Apply putty
10. Tape / Label Gauge
11. Photograph Installation
12. Document Installation

Notes

No terminal pad was used
Note: drawing does not match layout. Red + Black
wires connected to transverse mounted gauge. White + Green
connected to longitudinal
No soldering, slice type UY was used

Gauge ID # _____

Location _____

Chassis #	_____
Mod #	_____
Channel #	_____

Green (+Excitation)   Resistance: _____
White (-Excitation)
Black (-Signal)
Red (+Signal)   Resistance: _____

Notes

Testers Initials: _____

Figure G-24: Strain Gauge Sheet for the Pair of Quarter Bridge Strain Gauges Installed on the Web of Beam E, South Face

Bagdad Road over US Route 4 — Strain Gauge Sheet

Gauge ID # 1/2C
Station Letter: E

Red → +Signal
Black → -Signal

Location (to center of gauge)

Face — ~~South~~ / North
Location — Top / ~~Bottom~~ / ~~Web~~
Distance To Edge — 3"
Distance To Chan. — 10'
Photo # — √2
Photo Time — 1 : 29

Green +Signal   White -Signal

Installer's Initials: ___
Solder Intact: ☑
Process Complete: ☑

Process

1. Grind Surface
2. Smooth / Clean
3. Mark Location
4. Apply Gauge
5. ~~Apply Terminal Pad~~
6. Tape Surface
7. Tape Wire
8. ~~Solder Connections~~
9. Apply putty
10. Tape / Label Gauge
11. Photograph Installation
12. Document Installation

Notes

No terminal pad was used
No soldering - slice type UY was used

Gauge ID # ___

Location ___
Chassis # ___
Mod # ___
Channel # ___

Green (+Excitation)   Resistance ___
White (-Excitation)
Black (-Signal)   Resistance ___
Red (+Signal)

Notes

Testers Initials: ___

Figure G-25: Strain Gauge Sheet for the Pair of Quarter Bridge Strain Gauges Installed on the Top Flange of Beam E, South Face

APPENDIX H: Strain Gauge Measurement Quality

Several analyses were conducted as part of this research that was discussed in Chapter 6. The first phase of analysis involves a small scale experiment conducted to evaluate the gauges. The second phase of analysis assesses the differences between the indoor behavior of the gauges on the small scale experiment and the outdoor behavior of the gages on the Bagdad Road Bridge. The third phase of analysis evaluates the use of the full bridge strain gauges on the web of the beam for neutral axis location. The fourth and final phase of analysis of this research focused on calculation of the neutral axis location from gauge readings during bridge excitation compared to the predicted and expected neutral axis location.

Data collection for the first part of the analysis was conducted on April 9th, 2012 in the UNH structural high bay (S106). Data for the remaining parts was largely collected on April 30th, 2012 at the Bagdad Road Bridge, with some preliminary data collections on April 15st and April 21st. The data was post-processed and normalized using procedures detailed in the following sections. Only strain values were collected for this research, leaving temperature effects as a priority for future researchers, Adam Goudreau and Samuel White, funded by this project at UNH. The strain values collected on April 15st and April 21st at the bridge were to diagnose any issues with the gauges and make sure they were functioning correctly. These collections were short in duration, lasting no more than two to three minutes. The strain values collected on April 30th were tallied over 37 minutes and were used to create a pool of live load events that could be used to extract out values necessary for the second and third phases of the analysis portion of this research.

H.1 The Flat-Bar Tests

The first small scale experiment was conducted solely to gain familiarity with the DAQ equipment, programming, and the gauge mechanics and application procedure. The gauge was placed on a specimen and strained uniaxially to simplify the mathematically evaluation. This step was important because there are several settings that can affect the way the equipment turns the electrical signal into a strain value, and simply observing a response does not mean that the settings or application is correct. On an in-service bridge, observations may be difficult to verify due to the complexity of the structure and sensor performance in environmental conditions. To make observations easy to verify, gauges were mounted on a small flat bar, as shown in Figure H-1 and Figure H-2. Placing the bar in tension and using the strain value, geometric, and material properties of the bar, the weight supported in tension by the bar was mathematically derived using easily determined parameters.

Figure H-1: Photo of Flat Bar Specimen
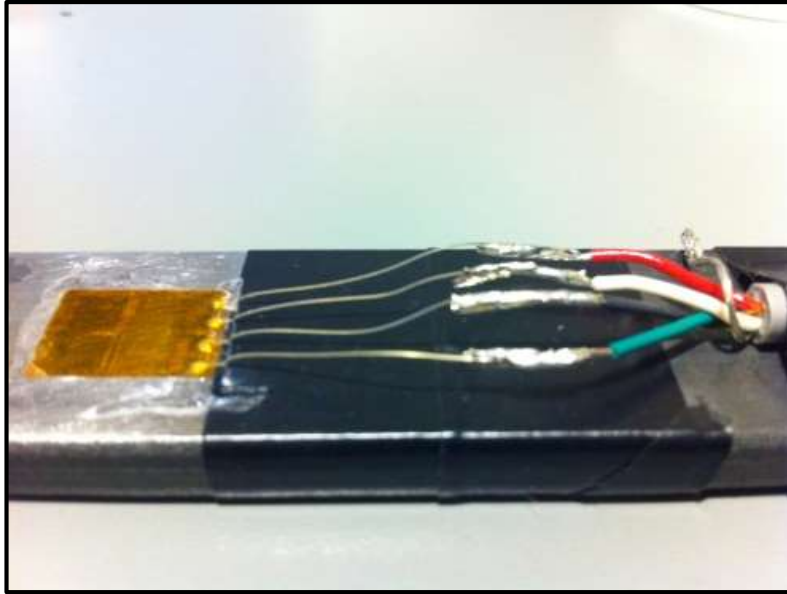
Figure H-2: Close Up Photo of Full Bridge Gauge Installation on Flat Bar Specimen

The steel flat bar shown in Figure H-1 and Figure H-2 measures 0.25 inches in thickness by 1.01 inch width, and is about 10 inches long. Two 3/8-inch holes were drilled into each end of the bar. The holes allow hooks to hold the bar and to suspend weights. It is instrumented with two of the full bridge gages described in Chapter 4, at mid-length. Using Equation H-1, which can be derived by substituting Equation 4-1 into 4-3, allows for the back calculation of the known weight for comparison.

$$P = \varepsilon E A \qquad \text{(Eq. H-1)}$$

Originally it was expected that a single gauge would be required to calculate the applied force. However, tests using a similar set up conducted by another graduate student at UNH, Jim Browne, showed that two gauges were required to capture the total strain due to tension in a flat bar. A program written in LabVIEW collected strain values using the NI 9219 C-series module and a NI 9162 USB chassis at 2 Hz. The DAQ stored the raw measurements and also multiplied them by user entered width, thickness, and modulus values, based on the test set-up shown in Figure H-3. A screen shot of the front panel of the program and a thorough description of its block diagram is in Appendix D.

Figure H-3: Illustration of Flat Bar Pull Experiment

The weight calculated from each strain gauge was displayed on the screen as well as the average of the two values. Three roughly 36 pound weights were hung from the bar one at a time adding

up to 108 pounds. The weights were loaded and unloaded roughly 10-15 seconds apart to gather a reasonable sample size of collected data at each total applied weight. The results are shown in Figure H-4 and Table H-1.   Looking at the calculated weight from each gage separately, it would appear the gauge is reporting a fluctuating incorrect value. However the average of the two values is a flat line that is close to the actual applied weight.
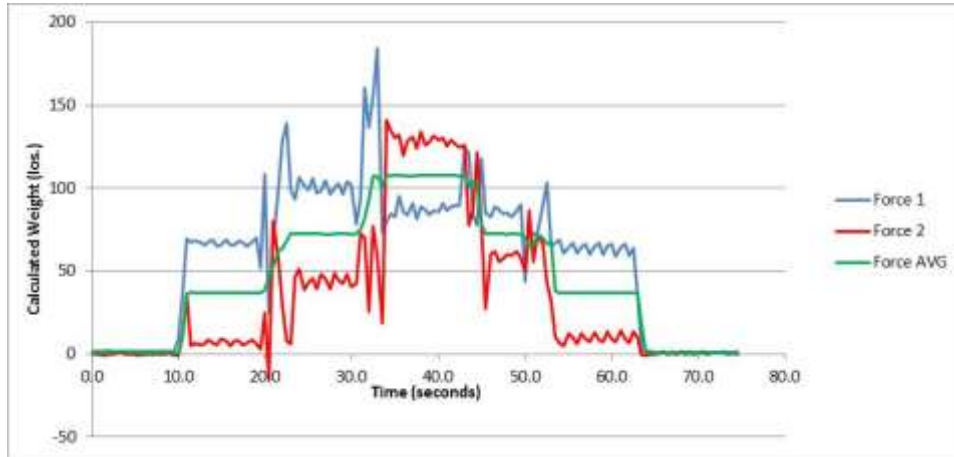

Figure H-4: Graph of Flat Bar Pull Test

Table H-1: Calculated Weight during the Flat Bar Tests

Step	Actual Weight (lb.)	Weight from Side 1 (lb.)	Weight from Side 2 (lb.)	Avg. Weight Applied (lb.)	Difference %
1 weight (+35.9 lb)	35.9	65.7	8.1	36.9	2.79%
2 weights (+35.8 lb.)	71.7	96.2	48.4	72.3	0.84%
3 weights (+35.5 lb.)	107.2	81.8	133.9	107.5	0.28%

Some interesting things can be observed in this test. It can plainly be seen that what is going on at the surface of the material is not representative of the global behavior. It was assumed that hanging the bar from a hook, and then hanging the weights of the bar with a hook had created a pinned-pinned connection and therefore the bar would be in pure tension. The most likely explanation for differences between the two faces is that there is a presence of bending. The bending is super-imposed on the bar, adding or subtracting from the tension effect. The gauge, however, is only capable of measuring the combination of effects.

Bending could occur for two reasons. The first is that the bar could initially be slightly bent, and that applying weight to the bar, straightens it out. Figure H-5 shows this phenomenon with an exaggerated deflected shape. Notice how bending, or unbending in this circumstance, places difference actions on the two gauges. The other explanation is that the holes drilled into the bar to create the pinned-pinned condition are not actually straight, or not perpendicular to the length of the bar. Hanging weight from the plane of the hole actually causes bending in this case.
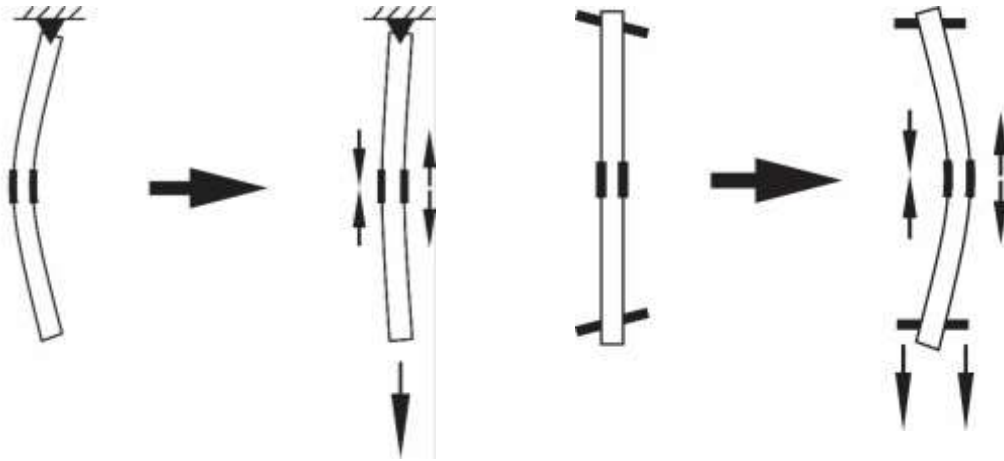
Figure H-5: Illustration of Flat Bar Figure 0-6: Illustration of Flat Bar Bending
Straightening

Hanging the third weight had an interesting implication to the bending and unbending scenarios. When hanging the first and second weight, the calculated force on side one consistently overestimated the known applied weight, and the side two consistently underestimated the known applied weight. However, when the third weight was hung, it produced the opposite result. The gauge on side one overestimated the applied weight while the second gauge on the other side underestimated the applied weight.   This may mean that the bar is not just bent in single curvature as shown in Figure H-5, and that varying weights, and the straightening of different curves causes multiple unbending scenarios. This switch could also indicate there are multiple non-perpendicular planes in the hole that the hook is suspended from, and that hanging the third weight caused the hook to dislodge and fall into a location that engaged a different uneven plane.

Another interesting observation from the pair of gauges is the suggestion that noise may actually be a much smaller portion of the signal than originally suspected. Noise is the fluctuation from one signal to the next that theoretically should be at the same value. The differences are caused by electronic and magnetic phenomenon in the equipment, lead wires, and the gauge itself. Examining the blue and red lines separately in Figure H-4, there appears to be a significant amount of noise indicated by variation in sensor reading. However, examining the green line on Figure H-4 that represents the average of the two strain gauge readings, there appears to be little fluctuation at all. The chances of noise in two gauges being consistently equal and opposite in magnitude from each other are likely small. The best explanations for the fluctuation from signal to signal in both gauges are that they are likely due to some sort of dynamic effect related to vibration in the bar and not measurement error.

The most significant observations from the small scale experiment is that what happens on the surface of a member may not be representative of the global behavior of the member as whole, and higher excitation in the mode of observation produces increasingly accurate results. The superposition of bending and the presence of dynamic effects during loading imply that effects out on the instrumented bridge, such as torsion or out of plane deflection, could also cause unexpected results. The manner that observations became closer to true values as more weight was hung implies that these unexpected results diminish as the phenomenon of interest increases. Therefore as one effect starts to greatly overshadow other effects, measuring the effect becomes

easier. This supports engineering judgment that suggest the most accurate observations at the bridge will occur at the highest loads.

H.2 Gauge Behavior at the Bagdad Road Bridge

A preliminary evaluation of the strain gauges at the Bagdad Road Bridge was conducted to compare the differences in gauge readings at the bridge versus at the UNH high bay. Differences between the sensor installations included significantly longer lead wires, varying temperatures, and covering in the form of environmental protection, as well as any differences that might have occurred during the outdoor installation, such as those derived from the glue curing in a cold and humid environment. Initial gauge readings showed that gauges at the bridge had no detectable difference in signal to noise ratio, however the sensor experiences significantly more drift. The drift is likely the result of apparent strain due to temperature effects.

H.2.1 Full-Bridge versus Quarter Bridge Sensors

Figure H-6 through Figure H-8 show readings from the full bridge strain gauges at the Bagdad Road Bridge versus the gauges installed on the flat bar specimen discussed in section H.1. Figure H-9 shows readings from the quarter bridge strain gauges located on the south face of Beam E compared to an ambient quarter bridge strain gauge readings. Note that the scale on Figure H- is approximately six times the scales on Figure H-6 through Figure H-8. The ambient gauge was used because mounting a quarter bridge strain gauge to a flat bar specimen, similar to the one mentioned in section H.1, was not conducted as part of this research. Instead, a small amount of confining pressure was applied to the ambient gauge to simulate an installation using a clip and a pad so that the gauge would not move from small air flows and strain. All figures show eight seconds of data collected at 2 Hz from unloaded conditions. Note the consistent small deviation from zero is to be expected and is likely due to temperature drift, and can be compensated for by calibration.
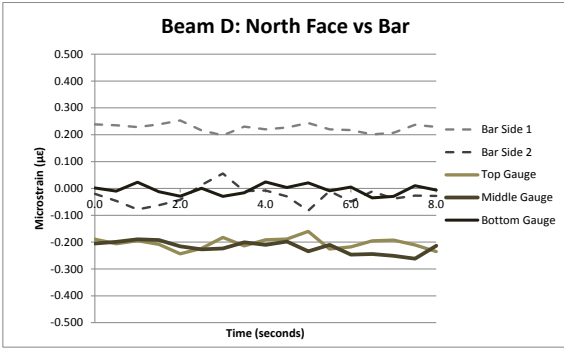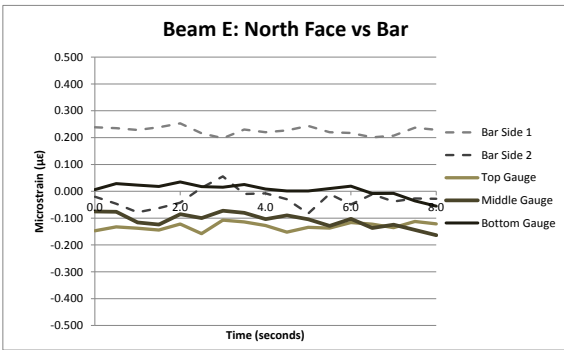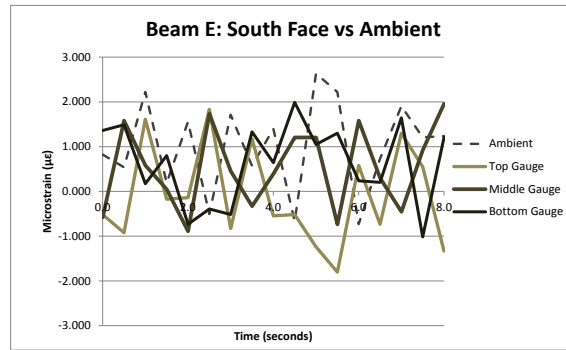
Figure H-6: Graph of Ambient Readings in North Face of Beam D versus Flat Bar
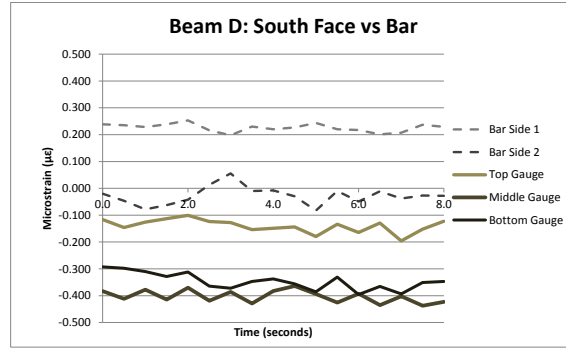
Figure H-7: Graph of Ambient Readings in South Face of Beam D versus Flat Bar

Figure H-8: Graph of Ambient Readings in North Face of Beam E versus Flat Bar

Figure H-9: Graph of Ambient Readings in South Face of Beam E versus Ambient Quarter Bridge Gauge

Figure H-6 through Figure H-9 show that gauge locations, indoors or outdoors, do not have a significant impact on noise. Variations in sequential readings were relatively the same in both installations. Table H-2 shows the standard deviations of the strain readings from all gauges. If the presence of noise had a larger influence on the gauge values it would be expected that the standard deviations would increase as variation from reading to reading. The standard deviations of the bar samples were 0.0150 and 0.0335 µε, respectively, and the standard deviations of the gauges at the Bagdad Road Bridge were between 0.0146 and 0.0317 µε. The ambient quarter bridge gauge had a standard deviation of 1.023 µε and the quarter bridge strain gauges at the Bagdad Road Bridge were between 0.905 and 1.091 µε.

Table H-2: Standard Deviations from Unloaded Gauge Readings at Indoor and Outdoor Locations

Standard Deviations (µε)									
Bars (Full & Ambient (Quarter)		Beam D: North Face (Full)		Beam D: South Face (Full)		Beam E: North Face (Full)		Beam E: South Face (Quarter)	
Bar Side 1	0.0150	Top	0.0209	Top	0.0246	Top	0.0146	Top	1.0905
Bar Side 2	0.0335	Middle	0.0220	Middle	0.0234	Middle	0.0267	Middle	0.9235
Ambient	1.0234	Bottom	0.0189	Bottom	0.0317	Bottom	0.0230	Bottom	0.9054

These observations also highlight the differences in noise that can be expected between the applications of full versus quarter bridge strain gauges. The standard deviations from these samples are roughly 42 times higher for quarter bridge strain gauges than for full bridge strain gauges. Howell and Shenton wrote about similar differences when discussing a strain monitoring system in 2006, pointing out that full bridge gauges in their system experience standard deviations of 0.5 µε for full bridge gauges versus 9.4 µε for quarter bridge (Howell and Shenton 2006). Although they experienced higher standard deviations, likely due to differences in hardware and collections speeds, the same pattern of significantly more noise in quarter bridge strain sensors is apparent.

H.2.2 Sensor Drift

During the initial diagnostic of the gauges, there was a slight drift that was not observed in the flat bar test and was observed in the sensors at the Bagdad Road Bridge, shown in Figure H-. The drift manifests itself as a changing trend in gauge readings that can not immediately be seen from one value to the next because it is small in comparison to noise at that scale. However, the trend is seen when looking at strain values over collection durations as small as a minute. Localized thermal expansion of the steel is not expected to be the cause of the trend as the gauges are designed to cancel out that effect and rather is expected to be caused by the apparent strain output of the gauge as temperature changes.

Figure H-10 shows the drift as it occurred over a 2 minute collection on the south face of Beam D. The gauges can be calibrated before a collection so that they initially all read zero, however, by the end of just 2 minutes of collection, the readings have trended away to a maximum deviation of -0.5 microstrain. The deviation is fairly small compared to the load induced strains, observed by the three large spikes in strain readings at 32, 84, and 108 seconds, but could grow to be much larger than strains resulting from typical traffic loads in collections lasting more than a few minutes. Deviations in large collections can be accounted for by calibrating frequently through the data collection periods or through post-processing.
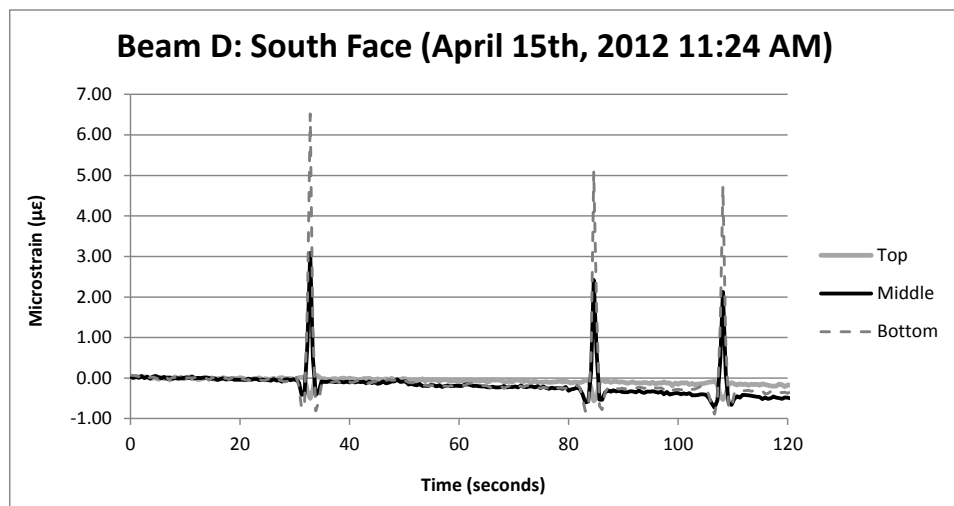

Figure H-10: Graph of Data Collected During Initial Gauge Evaluation after Installation

The method of post processing used in this research when collections lasted longer than a couple of minutes was to find a duration within a minute of data that appeared to experience no live load and take the average of it, then subtract that average from all samples within the minute. This

resulted in a line that centered at zero and still captured the behavior of the instrumented member. In addition to removing the apparent microstrain error, this method also removes any other potential additive errors.

Figure H-11 shows a comparison of gauge readings from Beam D on the bottom flange before and after the post-processing. The figure shows a minute worth of data taken from the fourth of five collections recorded on April 30th, 2012. The calibration had occurred roughly 30 minutes prior, before the start of the first collection. During the time between 380 and 390 seconds into the collection, no observable live load events had occurred, so the average of strain values for those 10 seconds were subtracted from all values within that minute of the record.
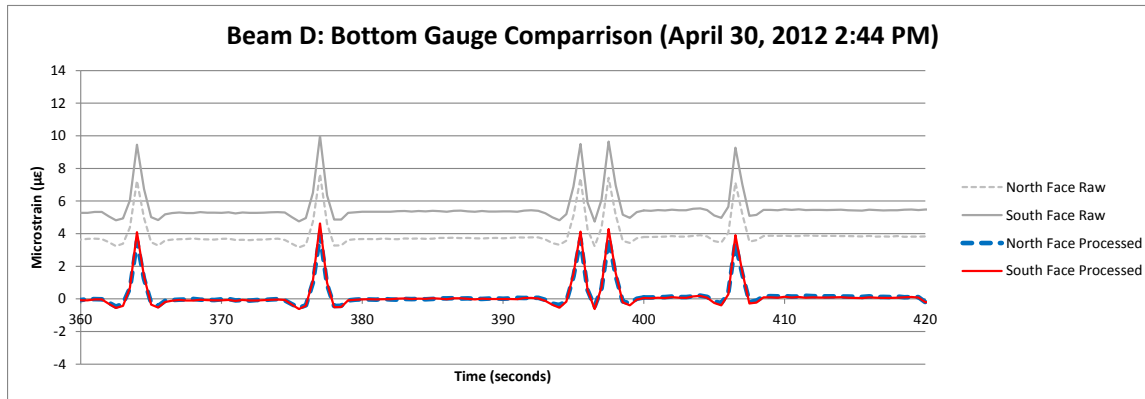
Figure H-7: Comparison of Measurements from Bottom Flanges of Beam D

Note that the drift in Figure H-10 is much more pronounced than in Figure H-11. That is because the drift in Figure H-10 occurs just 2 minutes after calibration where the drift shown in Figure H-11 occurred roughly 30 minutes after calibration. The x-axis depicts the time, in seconds, into the recording the figure corresponds with; several records were made after that initial calibration and will be described in detail in section H.3. The values subtracted from each value as part of this calibration were 3.7 and με.

Removing drift helps to isolate actual strain due to loading. Each time the bridge is loaded it is considered to be excited. Analyzing the bridge responses during excitations allowed for the full bridge behavior on the web to be analyzed and for neutral axis position to be researched without the need to focus on multiple sources and magnitudes of error. Eventually, detecting actual strain due to temperature may be helpful to SHM research at UNH. In fact, it may be necessary to collect temperature strain for determining such things as deflected shape using curvature. However, until temperature induced error can be successfully removed, it will be impossible to know what strain in an unloaded bridge is due to thermal expansion and contraction versus due to the several ways temperature produces error in the measurements using bonded foil gauges, which include effects on the sensors themselves, the lead wires, the DAQ hardware, and potentially the adhesive and environmental protection.

H.3 Generating the Live Load Event Database

To obtain a sample of strain values that were significantly more than those caused by noise in the sensors, a data collection was conducted that aimed to capture loads induced by school buses entering or leaving Oyster River High School. The proximity to the high school is shown in Figure H-12.

Figure H-8: Aerial Photo of Bridge Proximity to Oyster River High School (googlemaps.com)

Data was collected for over 37 minutes in 5 separate files called records. Each record was divided up into one minute segments, except for the last segment which was made of the remaining seconds in the record that did not sum to a minute. The minutes were then calibrated separately using the process described in the previous section. Using the full bridge gauges on bottom of Beam D, 156 live load events were identified. Histograms of peak strain from each beam face are shown in Figure H-13 through Figure H-16.
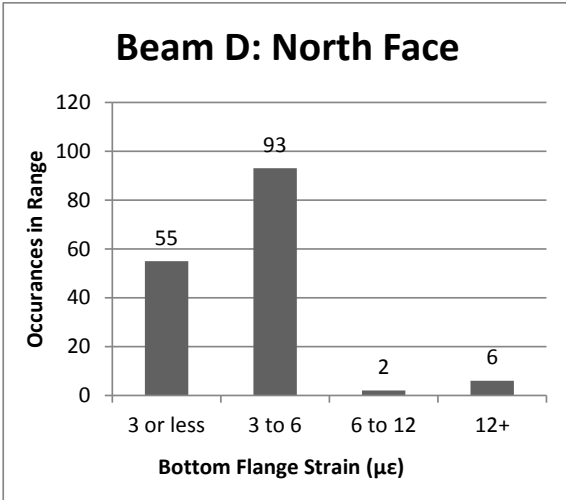
Beam D: North Face

Figure H-9: Histogram of Bottom Flange Strain Values on North Face of Beam D
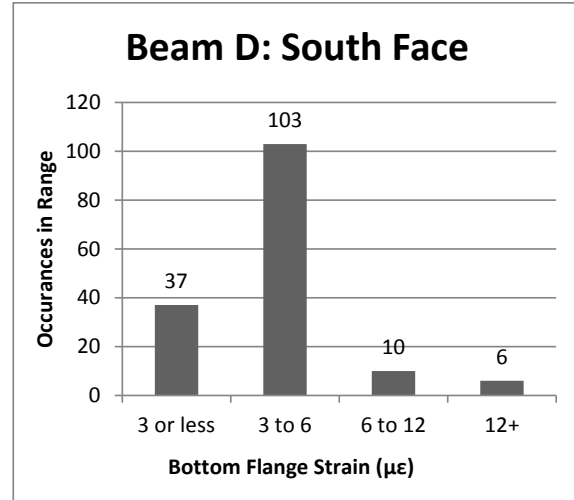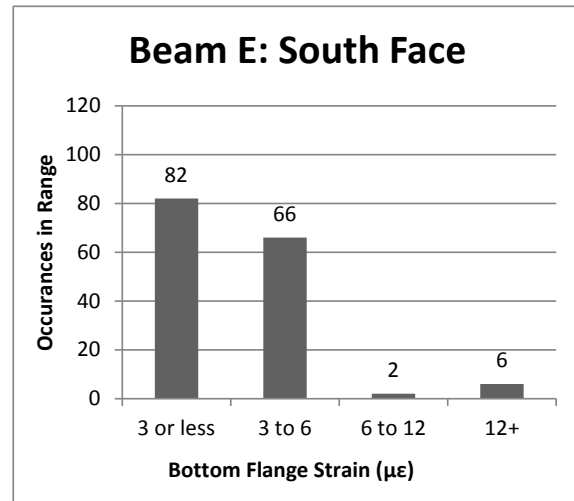
Beam D: South Face

Figure H-10: Histogram of Bottom Flange Strain Values on South Face of Beam D
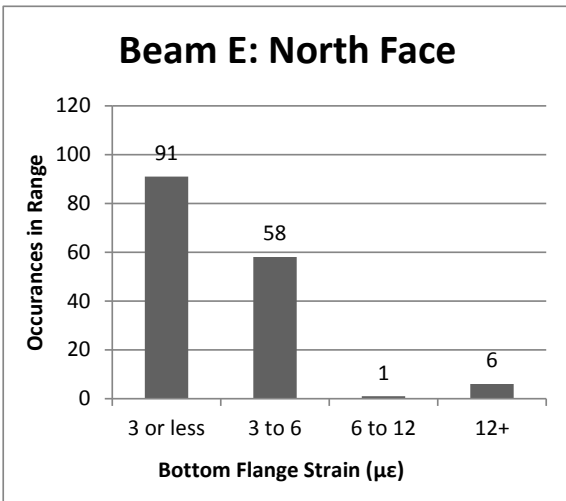
Beam E: North Face

Figure H-15: Histogram of Bottom Flange Strain Values on North Face of Beam E

Beam E: South Face

Figure H-11: Histogram of Bottom Flange Strain Values on South Face of Beam E

Some things are immediately apparent from the histograms. Only six events caused readings higher than 12 microstrains in the beams. Because that amount of strain, as compared to the typical values measured during the collection, was high they may have been caused by school buses. However, because nothing was used to record vehicle information as motorists crossed and researchers were positioned beneath the bridge, there are no observations to confirm this.

Analysis on all 156 events produced widely varying results in terms of comparisons and feature extractions. One example is shown in Figure H-17. The scatterplot shows the difference between values from bottom gauge readings on Beams D and E. Although Beam D generally experienced higher strain than Beam E, the amount varies much more widely at lower peak strains. The largest amount of scatter occurs during events when small strains occur in the bottom flange, particularly those less than 3 με.

When considering all events extracted from the sample, the bottom flange of Beam D was between -12% and 429%, excluding extraneous strain reading that were categorized as outliers. However, considering just live load events that produced measurements of at least 3 με in both sides of the bottom flange of Beam D, resulted in a significantly smaller range of 14-41%, a fraction of the range that occurred over all events.
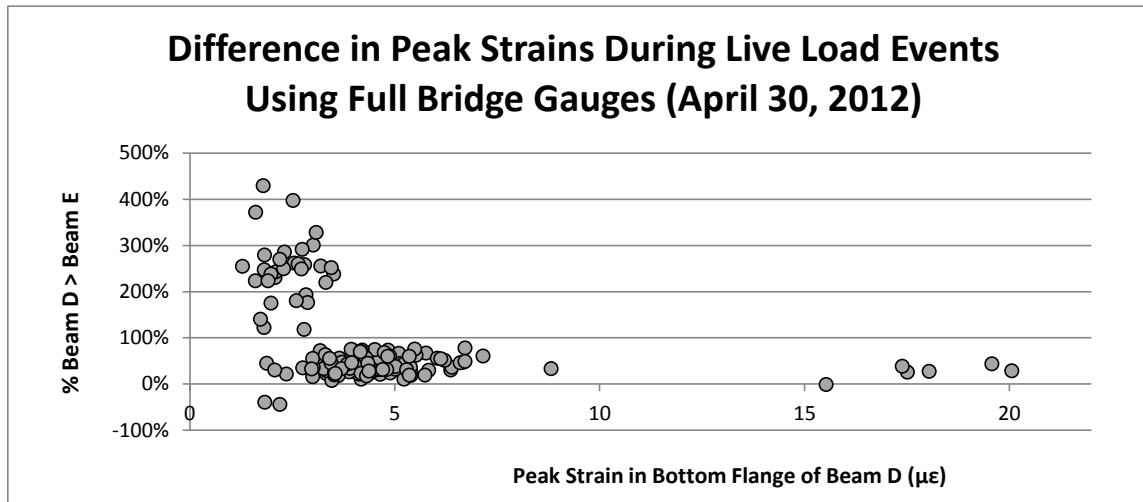
Figure H-12: Scatter Plot of Percent Difference between Peak Strains Beam to Beam

The same type of scatter appeared in feature extractions as well. The scatter existed in the pool of neutral axis locations determined from all events. An example is shown in Figure H-18 that plots peak strains in Beam D versus neutral axis location. The largest amount of scatter exists, again, below 3 με. Reducing the database by eliminating events that caused less than 3 microstrains in both sides of the bottom flange of Beam D produced a pool of samples with less scattered characteristics. The standard deviation for neutral axis locations on the north face of Beam D reduces from 1.16" to 0.55", and 0.62" to 0.42" on the south face when going from all events to events causing over 3 με.
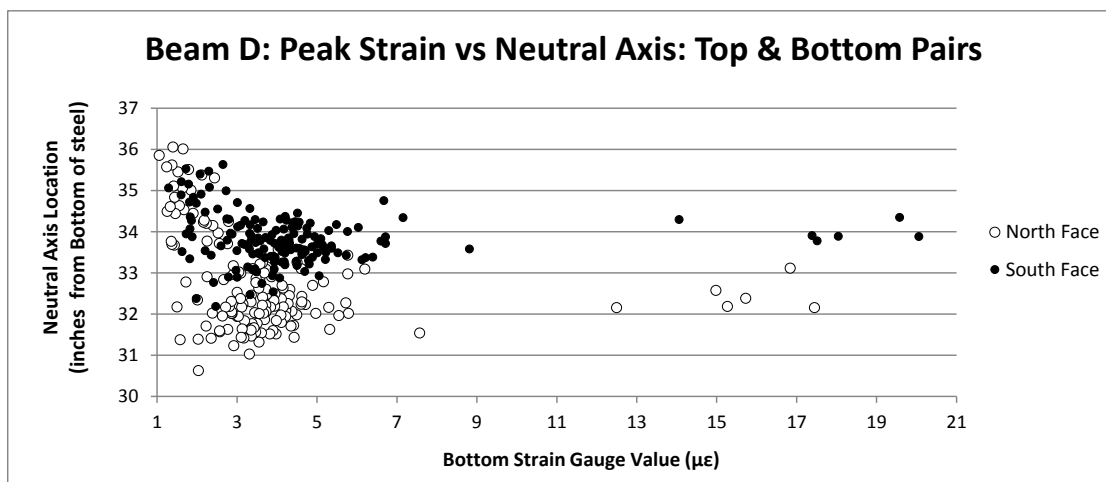
Figure H-18: Scatterplot of Neutral Axis Locations versus Peak Strains for All Live Load Events Using Top & Middle Strain Gauge Readings on North & South Faces of Beam D

For further analysis, only significant events are used. The pool of data was reduced from the original 156 events to 101 events using the criteria that the event had to cause strain of at least 3

216

με in both sides of the bottom flange of Beam D. The database of 101 events is hereby referred to as the Live Load Event Database. Small values excluded from the database may have been caused by traffic in the westbound lane, which is not above the instrumented girders. During the collections used for this research, there were no observations made regarding the vehicle crossing information including size and direction of travel. This information would have been extremely valuable in this post-processing and therefore, methods of recording vehicle size and position should be investigated.

Vehicles in the westbound lane will likely still induce a response in the gauges on Beams D and E, especially large vehicles, from a global deflection and twist of the superstructure. However, the significance of other types of responses, such as warping, torsion, or dynamic effects, likely contribute to a larger portion of the strains in the beams under the eastbound lane. One of the basic assumptions in developing the Live Load Event Database is that the largest possible strains from traffic loads will correspond to events where bending is predominant. Using larger strain values for analysis has the benefit of reduced effect from noise, because of a higher signal to noise ratio. Assuming the level of noise, in the form of variation in measurement to measurement, is expected to be constant regardless of the force applied to the girder.

H.3.1 Beam to Beam Comparison

As noted for the larger pool of all recorded events, the strain measurements collected on Beam D are generally higher than those collected on Beam E. In the Live Load Event Database, the average the ratio of Beam D strain measurements to Beam E strain measurements was 1.41 with a standard deviation of 0.18. The higher responses measured from Beam D may be due to the position of the vehicle as it drives across the bridge or additional stiffness from the curb and pedestrian sidewalk. Figure H-19 shows a cross section of the superstructure of the Bagdad Road Bridge. The center of the painted white line that indicates the breakdown lane or non-traffic lane is approximately 57 inches from the granite curb. Using the measurements of the deck section on the original plans, a distance of 3" to the inside of edge of Beam E was determined. Travelers are likely to follow typical traffic laws and stay evenly within the painted lines, indicated by the path shown with arrows in Figure H-19. This path places the vehicles closer to Beam D than Beam E.
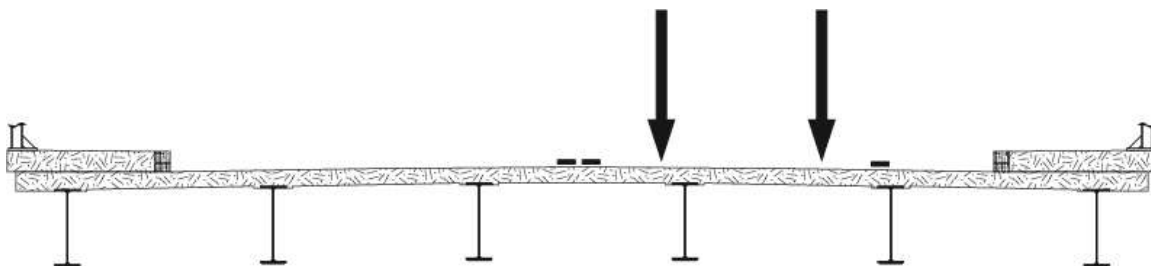
Figure H-139: Deck Cross Section with Highlighted Lane Lines and Likely Vehicle Path on the Bagdad Road Bridge

## H.4 Full Bridge Strain Gauge Use on the Web

The full bridge strain gauges used for this research function by mounting all strain sensing resistors of the Wheatstone bridge circuit on the specimen by placing two resistors in the direction of principle stress and two in the direction of Poisson's effect. This creates an additive effect as the two resistors in Poisson's direction have a negative effect on the Wheatstone bridge and are compressed; therefore, their resistance increases the voltage in to voltage out ratio and amplifies the signal.

H.4.1 Apparent Poisson's Ratio

As one means to investigate the possible interference from web compression, quarter bridge strain gauges were mounted on the south face of Beam E. In addition to placing a pair on the web, pairs were placed on both flanges to expand on the investigation of possible superimposed strains on measurements with the full bridge strain gauges. After noting how web compression could also affect strain measurement collected from the web, it is not difficult to see how torsion or warping could affect strain measurements collected from the flange.

An example of an Apparent Poisson's Ratio is shown below using event 5:110, and measurements were taken from the pair of quarter bridge strain gauges on the web. During the event, a strain of 8.38 με was measured by the gauge facing the longitudinal direction and a value of -2.47 με was measured in the transverse direction.

$$\nu_a = {}^{-\varepsilon_{transverse}}\!/\varepsilon_{longitudinal} = {}^{-(-2.47)}\!/_{8.38} = 0.295$$
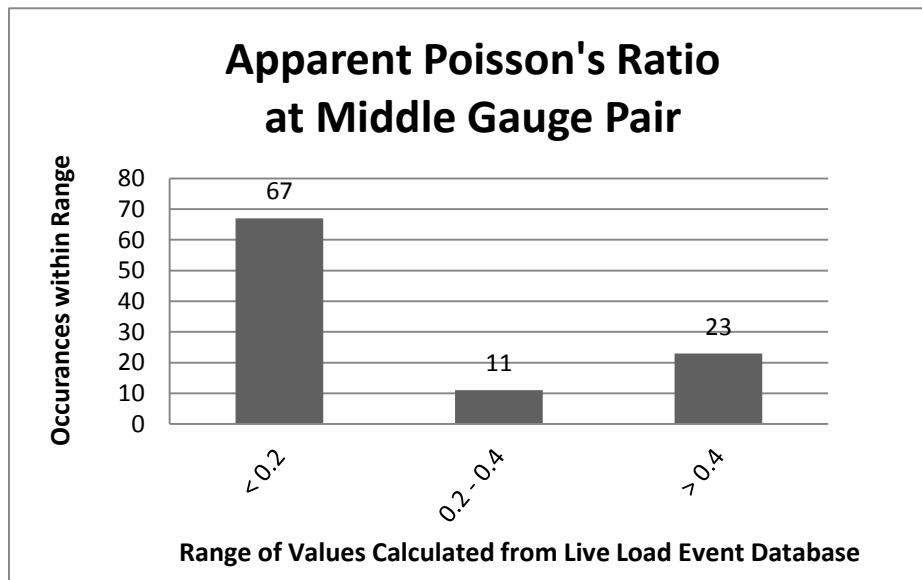
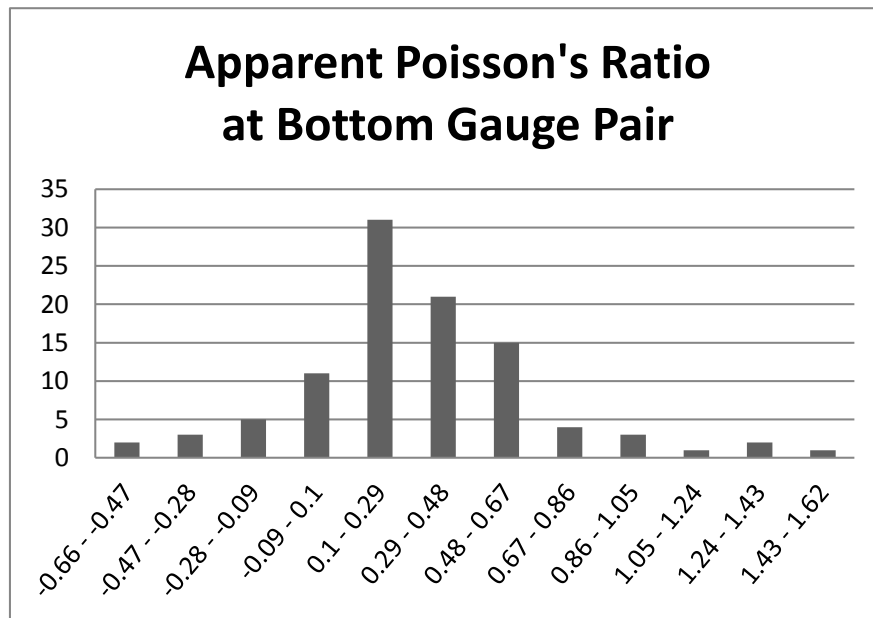**Figure H-20: Histogram of Apparent Poisson's Ratio Results Calculated from Gauges on the Web**

Results derived from the values that were obtained on April 21st were inconclusive. The event 5:110 that calculated values close to the expected ratio were uncommon. Figure H-20 shows a bar graph of apparent Poisson's ratios for the pair of gauges on the web. The average is 0.04, with a maximum of 7.10 and a minimum of -5.38, and a standard deviation of 1.15. The results do not make sense. Expectations are that a higher level of compression in the web, than would be caused by Poisson's effect during the longitudinal strains due to bending, will result from web compression as vehicles pass. That web compression would therefore result in a higher value than the well-known Poisson's ratio of 0.3 for steel material. In this case the majority of events caused an apparent Poisson's effect lower than 0.3.

Averaging close to zero initially implies that either the gauge measuring vertical effects on the web is reading close to zero or the gauge measuring horizontal effects is reading values that are too high. However, inspections of the measurements made by the middle gauge mounted in the horizontal direction were consistently reasonable as they fell between the values reported by the top and bottom sensors. Furthermore, the middle gauge mounted in the vertical direction

measured a wide range of values significantly away from zero, with a range of -2.55 to 2.65 and a standard deviation of 1.091. More research should be conducted that investigates the calculated ratios compared to the position of traffic, as well as further inspection of possible malfunctions in the gauge mounted in the vertical direction.

The apparent Poisson's ratio method does appear to function as expected on the bottom flange. Figure H-21 shows a histogram of apparent Poisson's ratios derived from the pair of quarter bridge strain gauges on the bottom beam flange, using the Live Load Event Database. The average apparent Poisson's Ratio for the bottom flange is 0.31, which is much closer to the expected value of 0.30 than with the middle gauge pair. This concludes that the full bridge gauges are appropriate for use on the bottom flange. However, as shown in the histogram, the values did trend to slightly lower than 0.30, so more samples should be analyzed to confirm the conclusion.

Figure H-14: Histogram of Apparent Poisson's Ratio Results Calculated from Gauges on the Bottom Flange

The top flange value results were largely meaningless. The noise to signal ratio of the strain gauges, coupled with values that are close to zero, created significantly varying results. The limited results that were close to expected values may have been just as likely due to coincidence as from meaningful gauge results. The range was -133.13 με to 13.41 με with an average of -1.18 με and a standard deviation of 14.74 με.

Figure H-22 shows calculated Poisson's ratios versus measured longitudinal strain value. It highlights that although lower strain values are part of the reason for the high amount of scatter in the sample of middle strain gauge pair values, low values are likely not the only cause. The bottom strain gauge values also are much more scattered at lower loads than at higher loads. However, the middle gauge values are generally more scattered, regardless of the loading. It can be seen in Figure H-22 that of the four live load events causing a greater than 8 με reading in the middle longitudinal gauge, only a single value was close to the true Poisson's ratio.
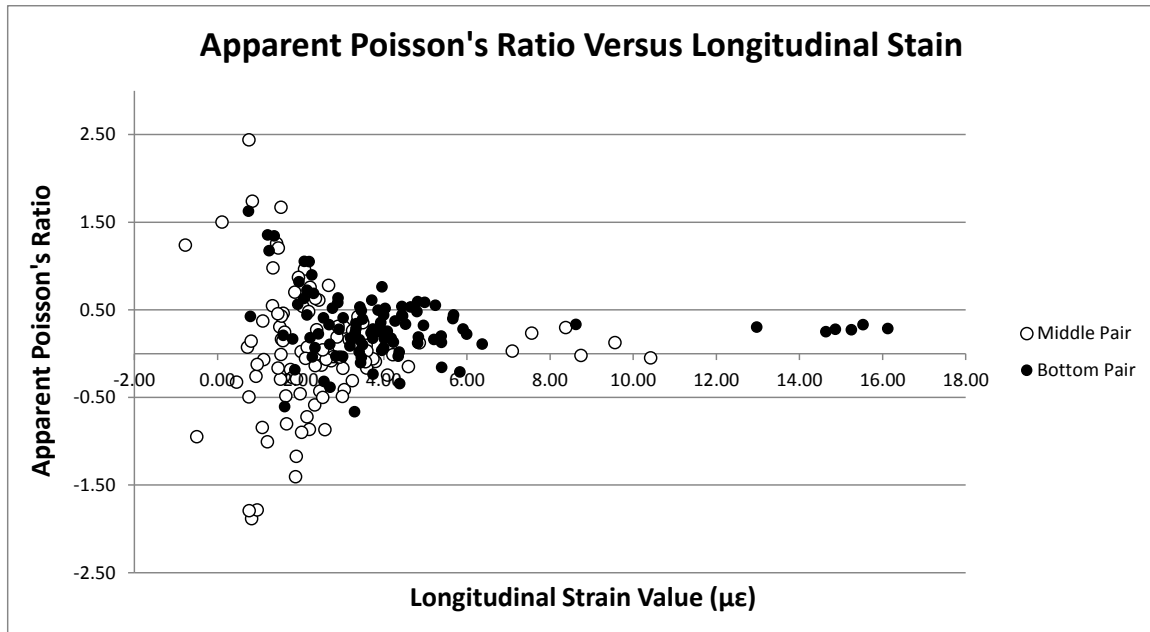
Figure H-15: Scatterplot of Apparent Poisson's Ratio's Versus Longitudinal Strains from Middle and Bottom Gauges

H.4.2 Middle Strain Reading versus Linear Interpolation

Considering the possible malfunctioning of the quarter bridge gauge on the web, another method was used on the samples to evaluate sensors on the web. A linear interpolation assumes that the strain gauges on the top and bottom flange are functioning correctly. Then, because the gauge on the web is located at half the height between the other sensors, each strain reading is expected to be halfway between the two measurements. The equation used to determine the expected value was then compared to the value is shown in Equation H-2.

$$\varepsilon_{expected} = \frac{\varepsilon_{bottom} - \varepsilon_{top}}{2} + \varepsilon_{bottom} \qquad \text{(Eq. H-2)}$$

The measured values were anticipated to be artificially higher due to the effects of web compression; therefore, the percentage that measured over expected was calculated using Equation H-3, where the measured strain is recorded by the middle gauge, located on the web.

$$\% \, over = 100 \, x \, \frac{\varepsilon_{measured} - \varepsilon_{expected}}{\varepsilon_{expected}} \qquad \text{(Eq. H-3)}$$

A sample calculation using the values from the northern face of Beam D during event 4:218.5, is provided, below. During this live load event, strain values of -0.65, 2.39, and 4.43 με were measured from the full-bridge strain gauges on the top flange, web, and bottom flange respectively.

$$\varepsilon_{expected} = \frac{4.43\mu\varepsilon - (-0.65\mu\varepsilon)}{2} + (-0.65\mu\varepsilon) = 1.89\mu\varepsilon$$

$$\% \, over = 100 \, x \, \frac{2.39\mu\varepsilon - 1.89\mu\varepsilon}{1.89\mu\varepsilon} = 26.5 \, \%$$

220

Table H-3 summarizes the results for the entire sample of 101 events in the Live Load Event Database. Note that 12 outliers were dismissed when considering measurements made with the quarter bridge gauges on the southern face of Beam E. Outliers were taken as values outside of a -200% to +200% range. The range for percentages over expected for all other beam faces was -16% to 42% which means that no events came close to the bounds used for dismissing outliers derived from quarter bridge readings on Beam E. The fact that outliers only needed to be excluded from measurements made with quarter bridge gauges, even in a range of values still an order of magnitude greater than those resulting from full bridge gauge measurements, highlights how scattered the features extracted from the quarter bridge gauges tended to be.

Table H-3: % Measured Value Greater than Expected Value

Beam / Face	Average	Standard Deviation	Outliers	Range
Beam D / North Face	22.7 %	7.33 %	0	1.59 – 41.7 %
Beam D / South Face	4.91 %	7.11 %	0	-13.3 – 20.7 %
Beam E / North Face	-0.38 %	5.77 %	0	-16.3 – 18.7 %
Beam E / South Face	13.87 %	61.8 %	12	-169.1 – 126.6 %

Table H-3 shows that middle strain gauge values, made with full bridge gauges, on the northern face of Beam E are consistently over expectations. In fact, the range was 1.59% to 41.7%. Therefore no values were equal to below zero in the entire sample. However, results were closer to expectations in other sets of strain gauges. Measurements on the web taken on the southern face of Beam D averaged around 5% over expectations, which could be expected in a small sample size. Measurements from the north face of Beam E are even closer to expected values, theoretically zero percent, averaging at less than a half percent.

The fact that measured strain values collected from the gauge on the web on the north face of Beam D are consistently higher than expected could be that the beam is deflecting in an unexpected manner or it could be that the strain gauge on the bottom flange is malfunctioning. This could be supported by the fact that, as shown in section 7.3, values from the bottom flange of the north face of Beam D were consistently lower than those measured on the opposite side of the flange. A possible beam distortion scenario is illustrated in Figure H-23. In this scenario, the web is placed into a small amount of curvature from the effect of web compression. The strain gauge would then measure artificially higher because the bending strain is superimposed on the strain due to Poisson's ratio, as both would be acting in the same direction. The scenario is similar to what caused exaggerated values on one side of the flat bar in the analysis described in section H.1.

Figure H-16: Illustration of Beam Distortion
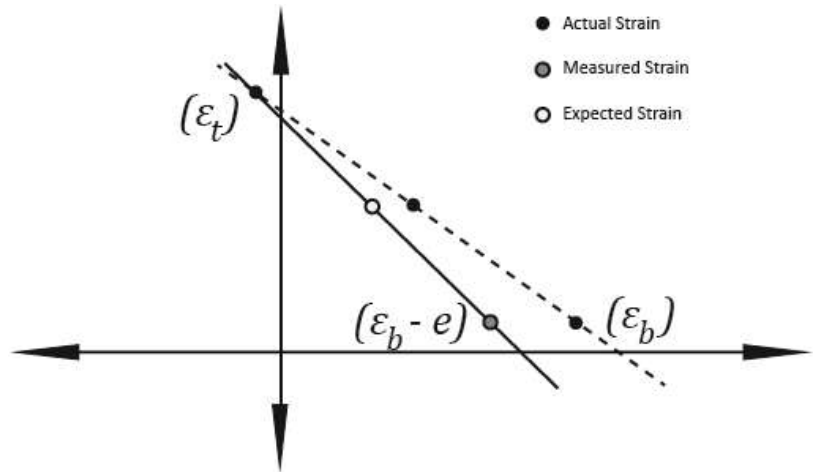
Figure H-17: Illustration of Gauge Error on Strain Diagram

Figure H-17 illustrates how a strain gauge malfunction in the bottom flange could affect the expected value of strain experienced by the web. The scenario could occur when an error causes the bottom strain gauge to read too low, which could easily happen if it was not bonded properly, for example if an air bubble existed in the adhesive. This would lower the expected values of strain between the bottom value and the top value, which in turn would make an accurate measurement in the middle appear to be exaggerated. An analysis of the differences for the sample used to evaluate apparent Poisson's ratio is shown in Table H-4. It excludes the 12 outliers previously mentioned that caused results from measurements made with quarter bridge gauges to be outside of a -200% to 200% range.

Table H-4: % Measured value on Bottom Flange of South Face of Beam is Greater than North face

Beam	Average	Standard Deviation	Range
Beam D	15.7 %	1.78 %	9.51 – 19.4 %
Beam E	11.6 %	31.1 %	-60.8 – 84.3 %

Table H-4 shows the bottom strain gauge readings on the southern face of Beam D were on average 15.7% higher than the strain gauge readings on the northern face of Beam D. The behavior was also fairly consistent, indicated by the relatively low standard deviation. This indicates the possibility of the gauge on bottom flange of Beam D is reading values too low. The possibility would explain why the expected values for the middle gauge are highest on that beam face.

Similar behavior also existed on Beam E, which could indicate that some global behavior, such as dishing, is causing the southern faces of the beams on the instrumented side of the bridge to strain more than the northern faces. However, the conclusion is difficult to draw because the results are much more scattered, indicated by the high standard deviation. The scatter is likely caused by a larger presence of noise in the quarter bridge strain gauges, described in section H.2. Additional data sets are required to draw this conclusion with a reasonable level of confidence. Recommendations include taking more samples with concurrent truck position data and to

specifically investigate the behavior of the full bridge gauge on the bottom flange of the north face of beam D.

### H.4.3 Interpolation during Negative Bending

Calculating expected strain values during negative bending is a potential opportunity to evaluate the behavior of the full bridge gauges on the web. Because negative bending will occur when the vehicle is in the span 2 or span 4 as shown in Figure H-18, the vehicle will not be in the instrumented span 3 to cause the web compression.
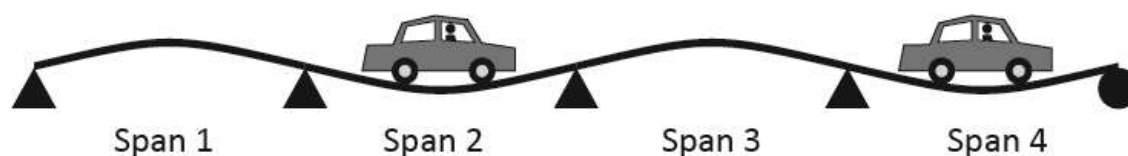
Figure H-18: Illustration of Vehicle Placements that Cause Negative Bending in Span 3

Figure H-19 shows two live load events captured on April 15th, 2012 during the initial evaluation of the sensors at the bridge. Negative bending is apparent in the figure, particularly in the top in middle gauges, as they can be seen going into compression just a moment before and after the peak tension values of the live load event. The top gauge appears to be going into the slightest amount of tension during these time as well, which is opposite of its typical behavior during the positive bending events.

It can also be seen in Figure H-19 that the excitation in the strain gauges during negative bending is small, compared to the magnitudes experienced during positive bending. For this reason, only the six events that caused readings over 12 με were analyzed. Because the vehicles have to travel through span 2 and span 4 to pass over span 3, two values from negative bending could be captured from each of these events. This created a database of 12 negative bending occurrences for the following analysis.
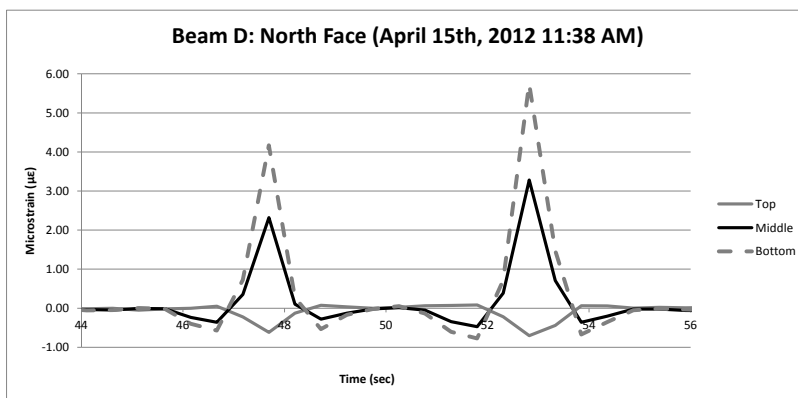
Figure H-19: Graph of Strain Measurements on North Face of Beam D during Initial Evaluation

The results are shown in Table H-5. The same range of ±200% was used to exclude two outliers in the quarter bridge strain gauge readings on the south face of Beam E. Higher standard deviations in all comparisons were likely the result of higher noise signal ratios. Although the sample size is too small to draw any significant conclusions, there is an indication that the measurements collected via the strain gauges are higher than expected on Beam D and lower on Beam E.

Table H-5: % Measured Value Greater than Expected Value (12 samples)

| Beam / Face	Average	Standard Deviation	Outliers	Range
Beam D / North Face	28.29 %	14.22 %	0	6.03 – 51.6 %
Beam D / South Face	10.49 %	9.84 %	0	-7.08 – 24.9 %
Beam E / North Face	-17.3 %	6.57 %	0	-4.37 – 27.1 %
Beam E / South Face	-9.50 %	69.6 %	2	-107.0 – 108.2 %

Further analysis could have implications similar to those described in 7.4.2. The first is that full bridge strain gauges on the web may be artificially raised due to both web compression and some other sort of out-of-plane movement from the global response of the bridge that causes local bending in the beam, similar to the shape shown in Figure H-16. Out of negative and positive live load induced bending, the average amount readings were in excess of expected values were actually higher during the negative events. This is counterintuitive as web compression is expected to increase when vehicles are closer to the instrumented location. However this could be due to the effect of higher noise to signal ratios. The second implication again points to the strain gauge on the bottom flange of the north face of Beam D as not functioning properly because it again collected values that resulted in the middle gauge readings to exceed expectations, more so than on the south face. If the readings in the web are consistently above expected values in both positive and negative bending, and sensor malfunction is not detected, than the web may go into compression from bending, regardless if a vehicle is above the instrumented location.

## H.5 Neutral Axis Calculation from Live Load Event Data

This section shows the resulting neutral axis locations calculated using the four previously describe pairings. In the analysis of full bridge strain gauges, installed on the north and south faces of Beam D and the north face of Beam E, practically all samples were included. In the analysis of the quarter bridge strain gauge values some results were excluded as outliers. Outliers, in this case, were results that calculated a neutral axis value outside the bounds of the beam: y < 0" or y > 43.73. The bins of the histograms divide each range of results into 12 equal sized ranges.

H.5.1 Results from the Top and Bottom Pairs

Figure H-27 through Figure H-30 are histograms of the neutral axis locations calculated from the collected strain readings for top and bottom flange gauges with events divided into twelve equal sized bins. Table H-6 shows the data ranges and standard deviations for each set. 30 outliers were excluded from the sample when calculating the values using reading from the quarter bridge gauges on the south face of Beam E that resulted in locations outside bounds of the composite section and, therefore, not practically applicable.
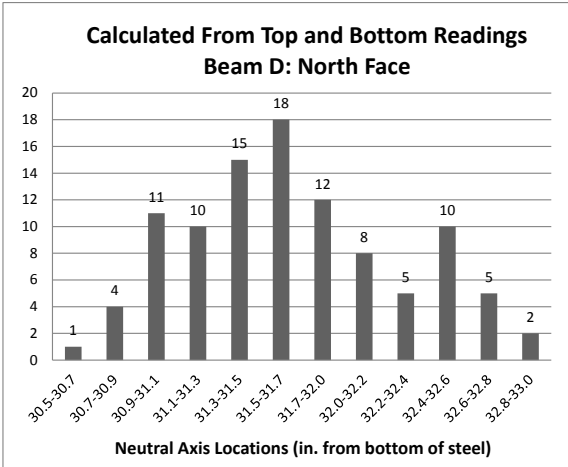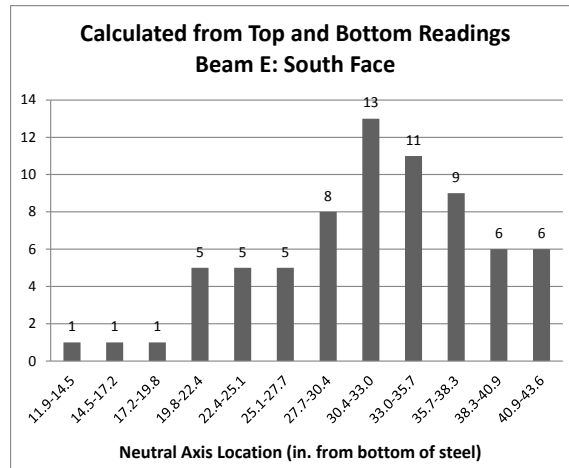
Figure H-27: Histogram Of NA Locations Calculated from Top & Bottom Gauges on North Face of Beam D
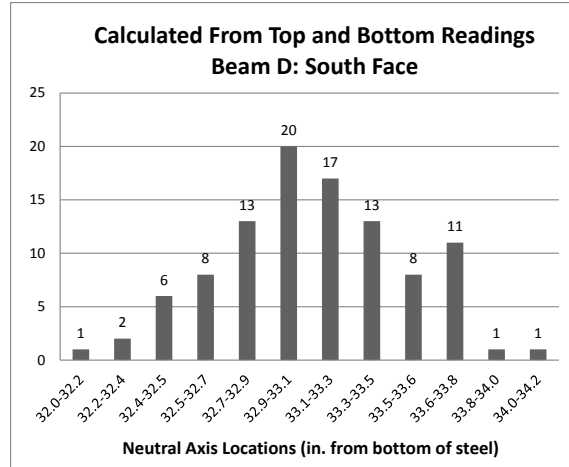
Figure H-28: Histogram Of NA Locations Calculated from Top & Bottom Gauges on South Face of Beam D
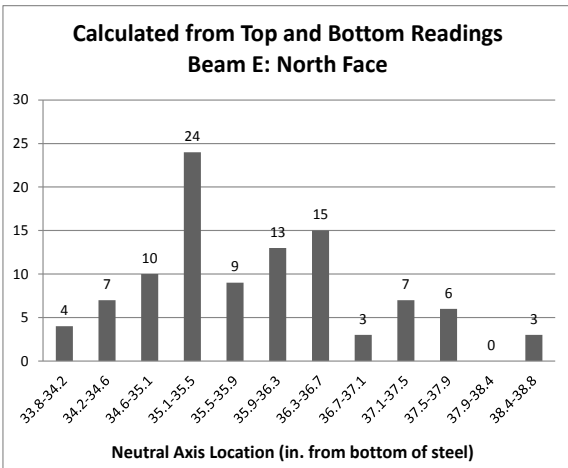
Figure H-29: Histogram Of NA Locations Calculated from Top & Bottom Gauges on North Face of Beam E

Figure H-30: Histogram Of NA Locations Calculated from Top & Bottom Gauges on South Face of Beam E

The results shown on the histograms indicate normal distributions with the exception of the north face of Beam E and possibly the north face of Beam D. Bimodal distributions could be the result of varying vehicle position having an effect on the beam. Also, although the south face of Beam E appears to be skewed to the right, this is likely a result of removing outliers. The predicted neutral axis location of 31.7" from transformed section calculations is closer to the upper bound in the range of acceptability. Referring to Figure , the upper bound, corresponding to the top of the concrete deck, is 12" away from the predicted value at 43.7", and the lower bound, corresponding to the bottom of the steel cover plate, is 31.7" away from the predicted values at 0". It is plausible that if values over 12 inches above the predicted value were also plotted, the histogram would appear more normally distributed.

Table H-6: NA Positions From Top and Bottom Gauge Readings

Beam / Face	Average (in.)	Standard Deviation	Range
Beam D / North Face	31.77	0.5530	30.53 – 33.07
Beam D / South Face	33.17	0.4077	32.04 – 34.25
Beam E / North Face	35.94	1.079	33.86 – 38.83
Beam E / South Face	31.81	6.918	11.91 – 43.64

The analysis using values from top and bottom pairings of gauges show relatively consistent behavior on 3 of the 4 beam faces. The locations derived for both faces of Beam D and the south face of Beam E are all within 1.5". Although the values from the south face of Beam E are more scattered than for other faces, this is to be expected as the values come from quarter bridge gauges. The major difference among beam faces occurs in the north face of Beam E which, on average, results in locations that are over 2.5" higher than in other beam faces. This could be interpreted as damage, for example section loss in the steel that results in movement upwards, however, the values from the south face agree with the transformed section properties of an undamaged section.

H.5.2 Results from the Top and Middle Pairs

Figure H-31 through Figure H-34 are histograms of the neutral axis locations calculated from the collected strain readings taken on the top flange and on the web of the two beams with events divided into twelve equal sized bins. Table H-7 shows the data ranges and standard deviations for each set. 29 outliers were excluded from the sample when calculating the values using reading from the quarter bridge gauges on the south face of Beam E that resulted in locations outside bounds of the composite section and, therefore, not practically applicable.
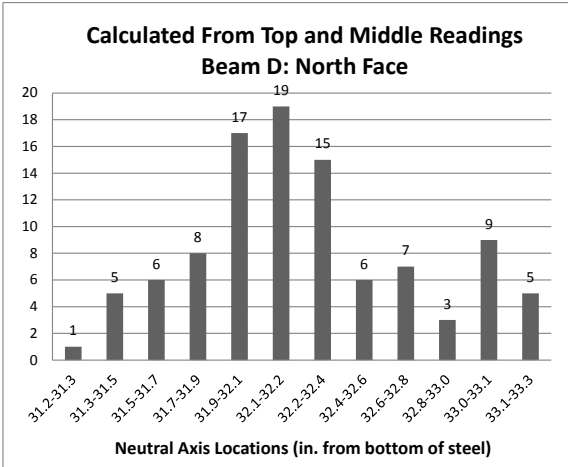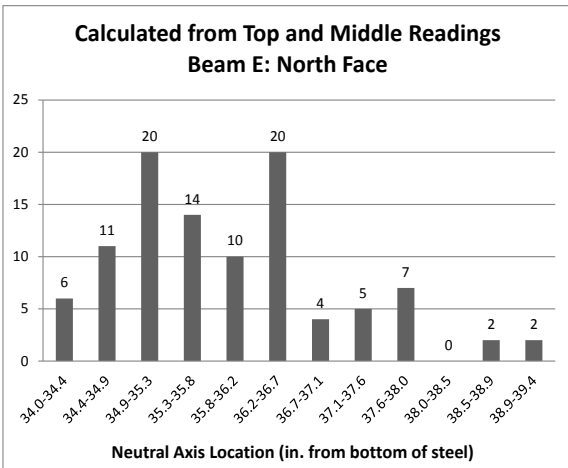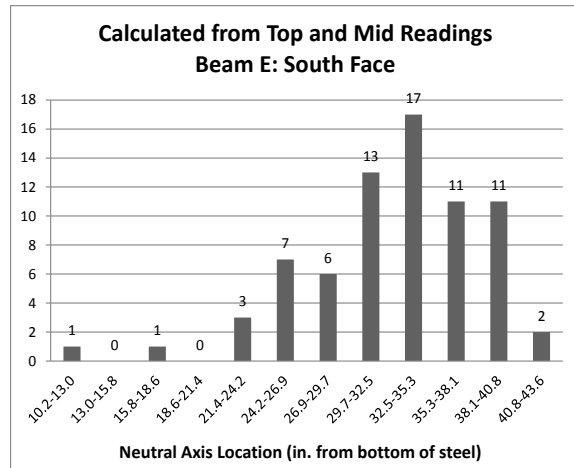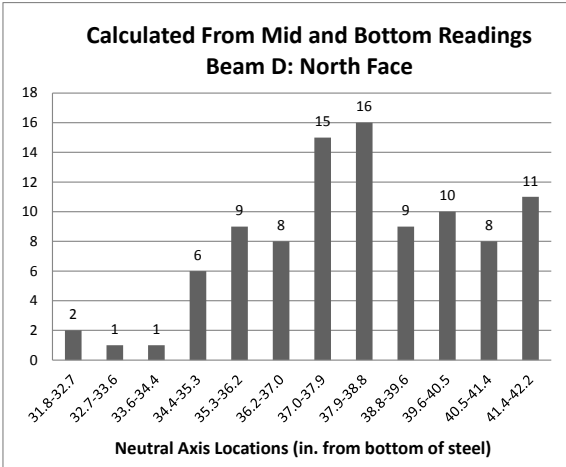
Figure H-31: Histogram Of NA Locations Calculated from Top & Middle Strain Gauges on North Face of Beam D
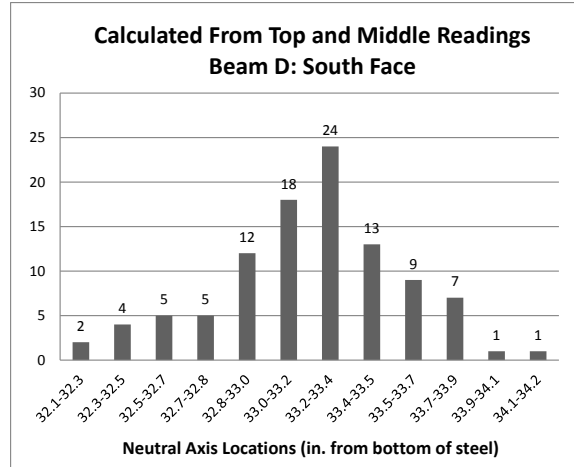
Figure H-32: Histogram Of NA Locations Calculated from Top & Middle Strain Gauges on South Face of Beam D

Figure H-33: Histogram Of NA Locations Calculated from Top & Middle Strain Gauges on North Face of Beam E

Figure H-34: Histogram Of NA Locations Calculated from Top & Middle Strain Gauges on South Face of Beam E

The histograms show similar results as the ones deduced using top and bottom pairings. Both faces of Beam D appear to have results that are normally distributed, although results from the north face may be trending slightly towards bimodal behavior. The north face of Beam E is more distinctly bimodal and the south face appears to be skewed to the right, again likely the result of including a larger range of samples below the expected value than above.

Table H-7: NA Positions From Top and Middle Gauge Readings

Beam / Face	Average (in.)	Standard Deviation	Range
Beam D / North Face	32.30	0.4868	31.22 – 33.38
Beam D / South Face	33.25	0.3841	32.20 – 34.28
Beam E / North Face	35.99	1.156	34.01 – 39.41
Beam E / South Face	32.54	5.913	10.30 – 43.68

The analysis using values from top and middle pairings were similar to the pairings for top and bottom gauges. The results show consistent behavior again in all beam faces except the north face of Beam E. The locations derived for both faces of Beam D and the south face of Beam E are all within 1.0", an even smaller range than occurred when using top and bottom pairings. Once again, the values from the south face of Beam E are more scattered than on other faces, likely a result of using quarter bridge gauges. Also repeated are unexpected values occurring in the north face of Beam E, which again on average are 2.5" over values from other beam faces.

H.5.3 Results from the Middle and Bottom Pairs

Figure H-35 through Figure H-38 are histograms of the neutral axis locations calculated from the collected strain readings taken on the bottom flange and on the web of the two beams with events divided into twelve equal sized bins. Table H-8 shows the data ranges and standard deviations for each set. An astounding 48 outliers were excluded from the sample when calculating the values using readings from the quarter bridge gauges on the south face of Beam E, and 5 outliers on the north face of Beam D that resulted in locations outside bounds of the composite section and, therefore, not practically applicable.
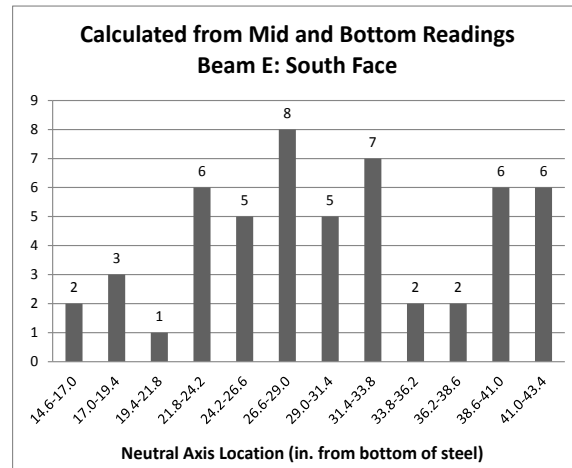
Figure H-35: Histogram Of NA Locations Calculated from Middle & Bottom Strain Gauges on North Face of Beam D
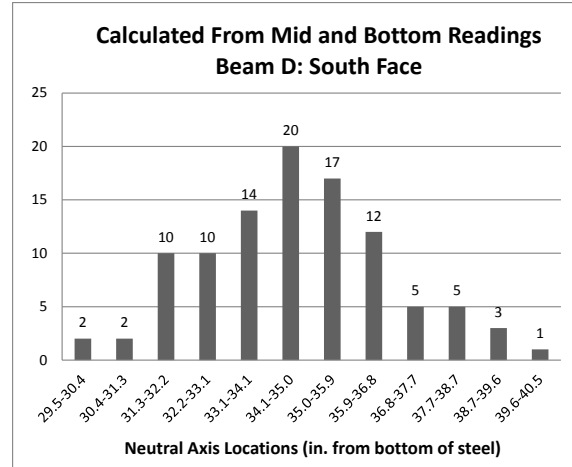
Figure H-36: Histogram Of NA Locations Calculated from Middle & Bottom Strain Gauges on South Face of Beam D
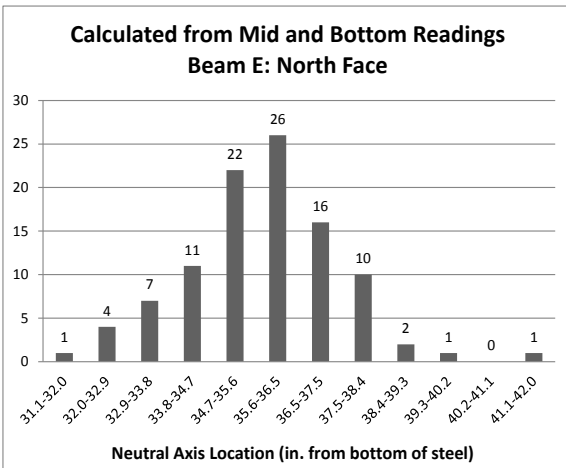
Figure H-37: Histogram Of NA Locations Calculated from Middle & Bottom Strain Gauges on North Face of Beam E

Figure H-38: Histogram Of NA Locations Calculated from Middle & Bottom Strain Gauges on South Face of Beam E

When using the middle and bottom gauges, the histograms for the north faces of each beam no longer appear bimodal. An explanation for the north face of Beam E is that including the five outliers that resulted in neutral axis locations above the deck would have changed the bin widths and added more sample to the right hand side of the chart making it appear more bimodal. The distribution on the south face of Beam E is difficult to draw conclusions from, likely a result of reducing the sample size so significantly. Note that the apparent peaks in Figure H-38 are between 6 and 8 occurrences where peaks in the other 3 histograms are 20 and over.

Table H-8: NA Positions From Middle and Bottom Gauge Readings

Beam / Face	Average (in.)	Standard Deviation	Range
Beam D / North Face	38.29	2.303	31.86 – 42.30
Beam D / South Face	34.71	2.080	29.51 – 40.55
Beam E / North Face	35.82	1.687	31.12 – 42.06
Beam E / South Face	30.38	7.631	14.64 – 43.44

The results from using middle and bottom gauges were much more varied than when using pairs that include the top gauge, indicated by much higher standard deviations, and in general, the calculated locations were significantly higher, with the exception of the south face of Beam E. Higher neutral axis locations in Beam D may be the result of web compression causing artificially high readings in the gauge on the web. These high readings would create diagrams with steep slopes and high y-intercept, as illustrated in Figure E-5. More results from the south face of Beam E could be used to further investigate this concept, as the quarter bridge gauges installed on that face will not be affected by web compression. This initial small batch of 53 samples has an average that is significantly lower than those derived from beam faces instrumented with full bridge gauges.

The highest average, at 38.6" taken on the north face of Beam D, may be a result of erroneously low values in the bottom gauge readings or erroneously high values in the middle gauge readings. Both notions are supported in chapter 7 where the ratio of readings on the bottom flange showed the north side had consistently lower values than on the south side, and the values at the middle gauge were consistently over expectations. The ratio of values from the southern side to the northern side was 1.41. The middle gauge reading on the north face of Beam D were, on average, 22.7% over expectations during positive bending events and 28.3% over expectations during negative bending events.

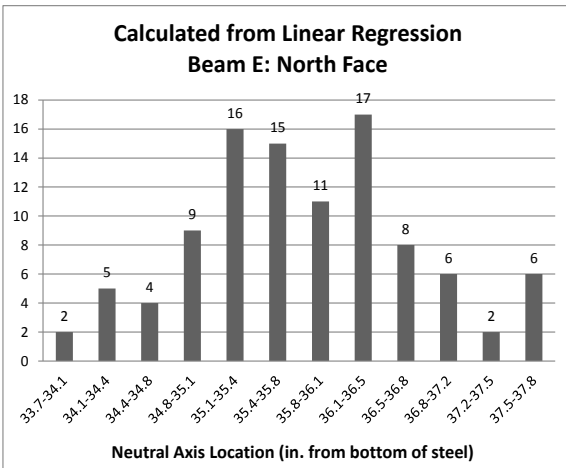### H.5.4 Results from the Linear Regression

Figure H-39 through Figure H-42 are histograms of the neutral axis locations calculated from the set of all strain readings on a beam face during events using linear regressions, again with results divided into twelve equal sized bins. Table H-9 shows the data ranges and standard deviations for each set. In this case, only 18 outliers were excluded from the sample when calculating the values using readings from the quarter bridge gauges on the south face of Beam E that resulted in locations outside bounds of the composite section and, therefore, not practically applicable.
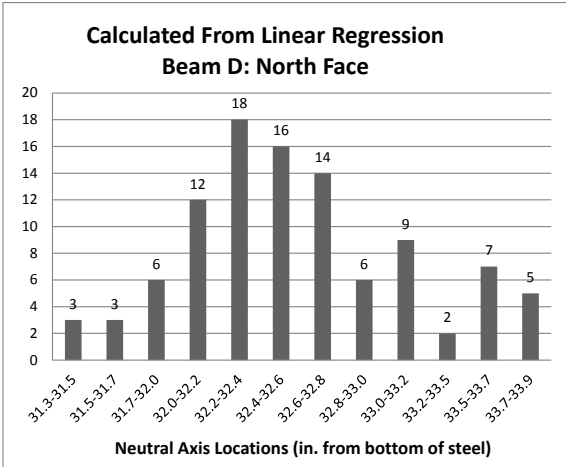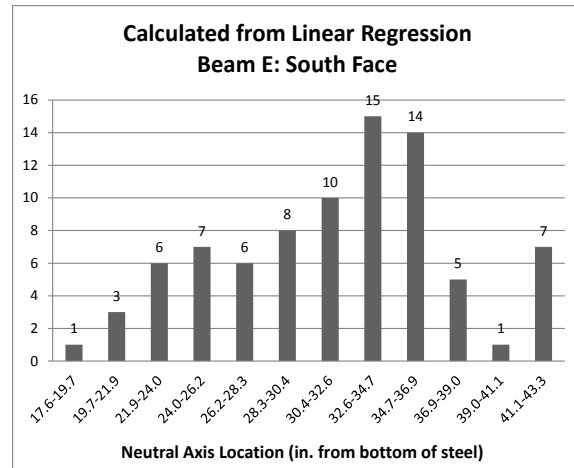
Figure H-39: Histogram Of NA Locations Calculated from Linear Regression of 3 Gauges on North Face of Beam D
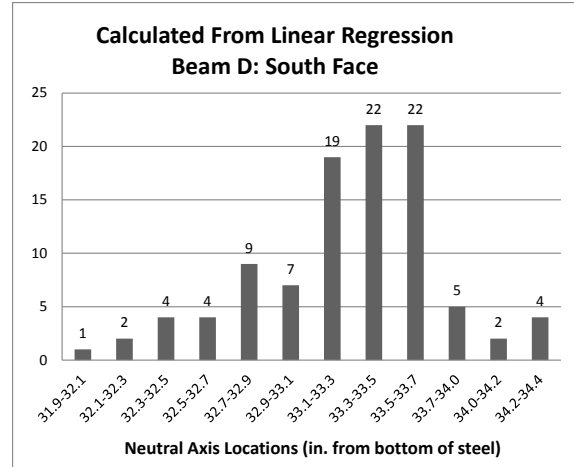
Figure H-40 Histogram Of NA Locations Calculated from Linear Regression of 3 Gauges on South Face of Beam D

Figure H-41: Histogram Of NA Locations Calculated from Linear Regression of 3 Gauges on North Face of Beam E

Figure H-42: Histogram Of NA Locations Calculated from Linear Regression of 3 Gauges on South Face of Beam E

The histograms show results that are much more similar to the results derived from using the pairs of top and bottom, and top and middle gauges, than the results from the previous section that used middle and bottom gauges. Possible bimodal distributions are again apparent in the north face of Beam E and less in the north face of Beam D.

231

Table H-9: NA Positions From Linear Regressions

Beam / Face	Average (in.)	Standard Deviation	Range
Beam D / North Face	32.62	0.5877	31.36 – 33.93
Beam D / South Face	33.38	0.4516	32.00 – 34.40
Beam E / North Face	35.88	0.9093	33.77 – 37.89
Beam E / South Face	31.78	5.954	17.66 – 43.33

Table H-9 reinforces the similarities between the linear regression and the pairs that contained the top gauge readings. The results again have the lowest standard deviations occurring from measurements taken on Beam D, and the north face of Beam E once again is more than 2.5" above other values. This implies that measurements from the top gauge have a large influence on the derived neutral axis location, as any set that utilizes the gauge shows consistent behavior.

APPENDIX I: Matlab® Code for Speckle Pattern Analysis and Data Filtering

I.1 Code for Analyzing Speckle Patterns

```matlab
%Enter the total number of pixels in the image


total_pixels = 65046;

%Define Structural Elements (speckle size diameters)
SE10 = strel('disk',10,6);
SE9 = strel('disk',9,6);
SE8 = strel('disk',8,6);
SE7 = strel('disk',7,6);
SE6 = strel('disk',6,6);
SE5 = strel('disk',5,6);
SE4 = strel('disk',4,6);
SE3 = strel('disk',3,6);
SE2 = strel('disk',2,6);
SE1 = strel('disk',1,6);
SE0 = strel('disk',0,6);

%Import Image
image1 = imread('c:\users\jason peddle\pictures\speckle_pattern_3.png');

%Convert to Black and White
image1bw = im2bw(image1);

%Image Morphology (Displays Only Speckles Equal to or Larger than the
%Structural Elemtnt)
im10pxl = imclose(image1bw,SE10);
im9pxl = imclose(image1bw,SE9);
im8pxl = imclose(image1bw,SE8);
im7pxl = imclose(image1bw,SE7);
im6pxl = imclose(image1bw,SE6);
im5pxl = imclose(image1bw,SE5);
im4pxl = imclose(image1bw,SE4);
im3pxl = imclose(image1bw,SE3);
im2pxl = imclose(image1bw,SE2);
im1pxl = imclose(image1bw,SE1);
im0pxl = imclose(image1bw,SE0);

%Determine the Percentage of Total Speckles of Each Diameter
px10 = 1-(((total_pixels-bwarea(im0pxl))-(total_pixels-
bwarea(im10pxl)))/(total_pixels-bwarea(im0pxl)));
px9 = 1-(((total_pixels-bwarea(im0pxl))-(total_pixels-
bwarea(im9pxl)))/(total_pixels-bwarea(im0pxl)));
px8 = 1-(((total_pixels-bwarea(im0pxl))-(total_pixels-
bwarea(im8pxl)))/(total_pixels-bwarea(im0pxl)));
px7 = 1-(((total_pixels-bwarea(im0pxl))-(total_pixels-
bwarea(im7pxl)))/(total_pixels-bwarea(im0pxl)));
px6 = 1-(((total_pixels-bwarea(im0pxl))-(total_pixels-
bwarea(im6pxl)))/(total_pixels-bwarea(im0pxl)));
px5 = 1-(((total_pixels-bwarea(im0pxl))-(total_pixels-
bwarea(im5pxl)))/(total_pixels-bwarea(im0pxl)));
px4 = 1-(((total_pixels-bwarea(im0pxl))-(total_pixels-
```

```
bwarea(im4pxl)))/(total_pixels-bwarea(im0pxl)));
px3 = 1-(((total_pixels-bwarea(im0pxl))-(total_pixels-
bwarea(im3pxl)))/(total_pixels-bwarea(im0pxl)));
px2 = 1-(((total_pixels-bwarea(im0pxl))-(total_pixels-
bwarea(im2pxl)))/(total_pixels-bwarea(im0pxl)));
px1 = 1-(((total_pixels-bwarea(im0pxl))-(total_pixels-
bwarea(im1pxl)))/(total_pixels-bwarea(im0pxl)));
px0 = 1-(((total_pixels-bwarea(im0pxl))-(total_pixels-
bwarea(im0pxl)))/(total_pixels-bwarea(im0pxl)));

%Plot Speckle Size Distribution
y = [px10,px9,px8,px7,px6,px5,px4,px3,px2,px1,px0]
x = [10,9,8,7,6,5,4,3,2,1,0]
plot(x,y)
```

I.2 Code for Filtering Data

```
%Clear Variables and Close Plots
clc
clear all
close all

%Import Unfiltered File: path 3 station 4 girder 4
[num,txt,raw] = xlsread('G:\Research\Bagdad rd Bridge
Test\path3station4girder4.xlsx');
%FILTER
order = 4;
%Butterworth Filter
[butter_b, butter_a] = butter(order, .1, 'low');
number_of_point = length(num);

%Freqz(butter_b, butter_a, number_of_point, sampling_freq)
y1 = filter(butter_b,butter_a,num(:,2));  %Filtering Displacement
x1 = filter(butter_b,butter_a,num(:,1));  %Filtering Frame Number
y2 = filter(butter_b,butter_a,num(:,5));  %Filtering Displacement
x2 = filter(butter_b,butter_a,num(:,4));  %Filtering Frame Number
y3 = filter(butter_b,butter_a,num(:,8));  %Filtering Displacement
x3 = filter(butter_b,butter_a,num(:,7));  %Filtering Frame Number
%--------END OF FILTER

%Plot Filtered Data
plot (x1,y1,'r');
hold on;
plot (x2,y2,'g');
hold on;
plot (x3,y3,'b');
hold on;
%Write Filtered Data to a File
xlswrite('G:\Research\Bagdad rd Bridge Test\Master_filtered.xlsx',[x1 y1 x2
y2 x3 y3],'Station4Girder4a')
%Clear Variables and Close Plots
clear all
close all
```

APPENDIX J: Load Rating Calculations

Interior Beam: Plastic Moment (Positive)

		units		coverplate		
Steel grade	36	ksi		b	10.5	in
tf	1.22	in		h	0.5	in
d	35.6	in				
bf	12	in				
tw	0.6	in				
f'c =	3.5	ksi				
Depth of slab	7.5	in				
c =	8.406	in				
β_1 =	0.85		for 3 ksi concrete			
a=	7.1451	in				
trib width	96	in				
abba =	685.9296	in^2				
Cslab	2040.641	kips				
Ctop_flg	-40.608	kips				
Ttop_flg	567.648	kips				
Tweb	716.256	kips				
Tbot_flg	527.04	kips				
T_cp	189	kips		T = C?	-0.08856	Negative: too much compression,
Moment Arms						
Cslab	4.83345	in				
Ctop_flg	-0.047	in				
Ttop_flg	0.657	in				
Tweb	17.894	in				
Tbot_flg	35.084	in				
T_cp	35.334	in				
Moments						
Cslab	9863.334	k-in				
Ctop_flg	1.908576	k-in				
Ttop_flg	372.9447	k-in				
Tweb	12816.68	k-in				
Tbot_flg	18490.67	k-in				
T_cp	6678.126	k-in				
$M_p = \Sigma$	48223.67	k-in				
	4018.639	k-ft				

Exterior Beam: Plastic Moment (Positive)

		units		coverplate		
Steel grade	36	ksi		b	10.5	in
tf	1.22	in		h	0.5	in
d	35.6	in				
bf	12	in				
tw	0.6	in				
f'c =	3.5	ksi				
Depth of slab	7.5	in				
c =	8.809	in				
β_1 =	0.85		for 3 ksi concrete			
a=	7.48765	in				
trib width	76	in				
abba =	569.0614	in^2				
Cslab	1692.958	kips				
Ctop_flg	133.488	kips				
Ttop_flg	393.552	kips				
Tweb	716.256	kips		Difference		
Tbot_flg	527.04	kips		T = C?	-0.597665	Negative: too much
T_cp	189					compression,
Moment Arms						
Cslab	5.065175	in				
Ctop_flg	0.1545	in				
Ttop_flg	0.4555	in				
Tweb	17.491	in				
Tbot_flg	34.681	in				
T_cp	34.931					
Moments						
Cslab	8575.127	k-in				
Ctop_flg	20.6239	k-in				
Ttop_flg	179.2629	k-in				
Tweb	12528.03	k-in				
Tbot_flg	18278.27	k-in				
T_cp	6601.959	k-in				
$M_p = \Sigma$	46183.28	k-in				
	3848.607	k-ft				

Negative Plastic Moment (Interior & Exterior)

		units			Rebar		
						Dia (in)	Space (in)	Area (in²)
Steel grade	36	ksi					

		units			Rebar		
Steel grade	36	ksi				Dia (in)	Space (in)	Area (in²)
tf	1.22	in		Top		0.5	12	1.242917
d	35.6	in		Bottom		0.625	8	2.91
bf	12	in						
tw	0.6	in						
Span Length	60	ft						
Depth of slab	7.5	in						
Beam Spacing	8	ft						
c =	21.841	in						
effective width	76	in						
Deck overhang	2.333333	ft						
Ttop_steel	44.745	kips						
Tbot_steel	104.8711	kips						
Ttop_flg	527.04	kips						
Ctop_flg	0	kips						
Tweb	283.4136	kips						
Cweb	432.8424	kips		Difference				
Cbot_flg	527.04	kips		T = C?	0.1872937	Positive: too much tension, increase c		
Moment Arms								
Ttop_steel	19.466	in						
Tbot_steel	16.2785	in						
Ttop_flg	13.731	in						
Ctop_flg	0	in						
Tweb	6.5605	in						
Cweb	10.0195	in						
Cbot_flg	20.649	in						
Moments								
Ttop_steel	871.0062	k-in						
Tbot_steel	1707.144	k-in						
Ttop_flg	7236.786	k-in						
Ctop_flg	0	k-in						
Tweb	1859.335	k-in						
Cweb	4336.864	k-in						
Cbot_flg	10882.85	k-in						
$M_p = \Sigma$	26893.98	k-in						
	2241.165	k-ft						

J.1 Sample Spreadsheet for Calculating Dead and Live Loads

User Input		Value	Notes	Code Reference
Span				
Number of Spans		4		
Span Length	(ft)	60	O.K.	Table 4.6.2.1.1b-1
X_{POI} from left abutment	(ft)	40	O.K.	Sec 1.3.3 (pg. 1-5)
eta (η)		1		
Trucks				
Number of Trucks		1	Short Truck (14 ft between middle and rear axle)	
Direction of Truck Travel		← (R2L)	Right to Left	
Distance from Left Abutment to Rear Axle of Lead Truck		89	O.K.	
Spacing Between Lead Truck's Rear Axle and Rear Truck'		na	for neg bending only; minimum of 50 ft	Sec 3.6.1.3.1
Beams				
Number of Beams		6	O.K.	
Beam Spacing	(ft)	8		
Beam Type		W36x135		
Concrete in Beams (f'c)	(ksi)	3.5		
Cross Sectional Area of Beam	(ft²)	0.28		
Deck				
Width of Deck	(ft)	44.667		
Thickness of Deck	(ft)	0.625		
Deck Overhang	(ft)	2.333		
d_e (dist from CL ext beam to edge of curb)	(ft)	-4		
Concrete in Deck (f'c)	(ksi)	3.5		
Haunch Thickness	(ft)	0		
Haunch Width (width of top flange of beam)	(ft)	1.00		
Additional Input				
Width of Parapet + sidewalk	(ft)	6.333		
Weight of Parapet + sidewalk	(klf)	0.774106563		
Wearing Surface Thickness	(ft)	0.166666667		
Utilities Dead Load	(klf)	0		
Positive or Negative Moment?		Positive		
Inventory or Operating Ratng?		Operating		
Interior or Exterior Girder?		Exterior		

Axle Positions			
Lead Truck: Position of Front Axle (X_{T1F})	(ft)	61.00	O.K
Lead Truck: Position of Middle Axle (X_{T1M})	(ft)	75.00	O.K
Lead Truck: Position of Rear Axle (X_{T1R})	(ft)	89.00	O.K
Rear Truck: Position of Front Axle (X_{T2F})	(ft)	0.00	O.K
Rear Truck: Position of Middle Axle (X_{T2M})	(ft)	0.00	O.K
Rear Truck: Position of Rear Axle (X_{T2R})	(ft)	0.00	O.K

Intermediate Values			Notes	Code Reference
Gamma (γ)	DC	1.25	Strength I load Case	Table 3.4.1-2
	DW	1.50	Strength I load Case	Table 3.4.1-2
	LL	1.35	Strength I load Case	Table 3.4.1-1
g for DL		0.17		
mg for live load		0.22		
Unfactored Total DL for Components ($w_{DL,C}$)	(klf)	8.12		
Unfactored Total DL of Future Wearing Surfaces ($w_{DL,W}$)	(klf)	0.75		
Factored Distributed DL (γw_{DL})	(klf)	11.28	gamma included	
Single Lane Factored Distributed Lane Load (γw_{LL})	(klf)	0.86	gamma included	
Lead Truck: Front Axle Load ($\gamma P_{axle\ F}$)	(kip)	10.80	gamma included	
Lead Truck: Middle Axle Load ($\gamma P_{axle\ M}$)	(kip)	43.20	gamma included	
Lead Truck: Rear Axle Load ($\gamma P_{axle\ R}$)	(kip)	43.20	gamma included	
Rear Truck: Front Axle Load ($\gamma P_{axle\ F}$)	(kip)	10.80	gamma included	
Rear Truck: Middle Axle Load ($\gamma P_{axle\ M}$)	(kip)	43.20	gamma included	
Rear Truck: Rear Axle Load ($\gamma P_{axle\ R}$)	(kip)	43.20	gamma included	
$W_{u,DL}$	(klf)	1.88		
$W_{u,LL}$	(klf)	0.19		
Dynamic Load Allowance (IM or I)		0.33		Table 3.6.2.1-1
Pu,LL Lead Truck Front Axle	(kip)	3.18		
Pu,LL Lead Truck Middle Axle	(kip)	12.73		
Pu,LL Lead Truck Rear Axle	(kip)	12.73		
Pu,LL Rear Truck Front Axle	(kip)	0.00		
Pu,LL Rear Truck Middle Axle	(kip)	0.00		
Pu,LL Rear Truck Rear Axle	(kip)	0.00		

60' Span

Note: these intermediate calculations are in feet

			Bent 3	Diaphragm	Midspan	Diaphragm	Bent 2
Girder 4	Raw Data		15.025	14.78	14.565	14.315	13.885
	Elevation Change due to Slope		1.3818	0.9212	0.6909	0.4606	0
	Elevation Change due to Cover Plate		0	0.0417	0.0417	0.0417	0
	Camber		13.6432	13.9005	13.9158	13.8961	13.885	0.3692 inches
Girder 5	Raw Data		15.068	14.631	14.42	14.165	13.746
	Elevation Change due to Slope		1.3818	0.9212	0.6909	0.4606	0
	Elevation Change due to Cover Plate		0	0.0417	0.0417	0.0417	0
	Camber		13.6862	13.7515	13.7708	13.7461	13.746
	Corrected for Crown		13.8112	13.8765	13.8958	13.8711	13.871	0.2972 inches

Moment Values			
Moment at POI due to Dead Load of Components	(ft-kip)	264.37	
Moment at POI due to Dead Load of Wearing Surface	(ft-kip)	29.16	
Most neg Moment from factored lane load	(ft-kip)	-21.02	
Most pos Moment from factored lane load	(ft-kip)	50.92	
Moment caused by axles	(ft-kip)	195.44	Be sure to enter Positive or Negative Moment in Input
Total Moment due to Live Load (positive)	(ft-kip)	246.36	
Most Negative Σ	(ft-kip)	467.95	
Most Positive Σ	(ft-kip)	539.89	

APPENDIX K: 2D Digital Imaging Correlation Laboratory Results

This section presents the results of the laboratory testing of the 2D GoPro® DIC strain sensor. Three research trials were performed using this setup, each with different goals. The summary of the major results and representative plots are provided here in this section, while the entirety of the results is provided in the respective appendices. In the test trials, parameter levels designated as 1 are low levels of that setting (low light, low height, low strain) and levels designated as 3 are the high levels (flood lights, highest height, highest strain). All 2D DIC analysis was performed using Vic-2D 2009, a DIC analysis software produced by Correlated Solutions, Inc.

K.1   2D Lab Trial 1

K.1.1   Goals, Purpose and Results of 2D Trial Lab 1

The first laboratory trial for the testing of the 2D GoPro® DIC sensor was designed to test the effects of height (distance between camera and target surface), light, and video resolution on the accuracy of the measured strain values. The strain induced in the system was varied by applying the loads to the notch locations corresponding to the assigned strain level and also by altering the fixity of the supports. Table K-1 below shows the settings used for all the tests in 2D Lab Trial 1. Table K-3 below is a summary of the statistical analysis conducted for 2D Lab Trial 1. Table K-2 below shows the summary of the results from the tests in 2D Lab Trial 1.

Figure K-1 shows an example plot from one test conducted in 2D Lab Trial 1. To see all the results from this trial, including snips showing the AOEs used for DIC data extraction, the data plots, and individual summaries for all the tests.

Table K-1: Parameter settings for the tests in 2D Lab Trial 1

|	Height	Light	Strain Level	Resolution	Fixity
1	1	1	1	1080	Simple
2	1	1	3	720	Fixed
3	1	2	3	720	Simple
4	1	3	1	720	Fixed
5	1	3	2	1080	Simple
6	2	1	1	720	Simple
7	2	2	2	1080	Fixed
8	2	2	2	720	Simple
9	2	3	3	1080	Fixed
10	3	1	2	720	Fixed
11	3	1	3	1080	Simple
12	3	2	1	1080	Fixed
13	3	3	1	1080	Simple
14	3	3	3	720	Fixed
15	2	2	2	720	Simple
16	2	2	2	1080	Fixed
17	2	2	2	720	Simple

Table K-2: Summary of results from 2D Lab Testing Trial 1

Test	Expected Strain (με)	Avg Foil Strain (με)	Avg DIC Strain (με)	std,DICi (με)	%Diff,i	abs(%Diff,i)
1	496.6	495.31	467.38	8.45	-5.64	5.64
2	227.6	542.57	505.70	33.38	-6.80	6.80
3	827.6	830.88	883.47	9.73	6.33	6.33
4	79.3	285.31	343.92	12.21	20.54	20.54
5	662.1	657.46	754.50	19.16	14.76	14.76
6	496.6	495.44	466.05	37.16	-5.93	5.93
7	144.8	390.59	483.79	7.02	23.86	23.86
8	662.1	661.69	707.73	10.36	6.96	6.96
9	227.6	527.20	595.85	16.67	13.02	13.02
10	144.8	430.91	277.18	52.73	-35.68	35.68
11	827.6	836.61	862.32	28.16	3.07	3.07
12	79.3	276.73	305.12	12.54	10.26	10.26
13	496.6	494.20	549.78	21.39	11.25	11.25
14	227.6	530.48	540.00	25.46	1.79	1.79
15	662.1	673.60	694.01	5.88	3.03	3.03
16	144.8	405.38	483.84	8.52	19.35	19.35
17	662.1	675.35	663.81	10.84	-1.71	1.71

Table K-3: Summary of the statistical analysis for 2D Lab Testing Trial 1

%Diff,avg	11.18
std,%Diff	9.22
t,n-1	2.761
p-value	0.01<P<0.005
Result:	Reject the Null
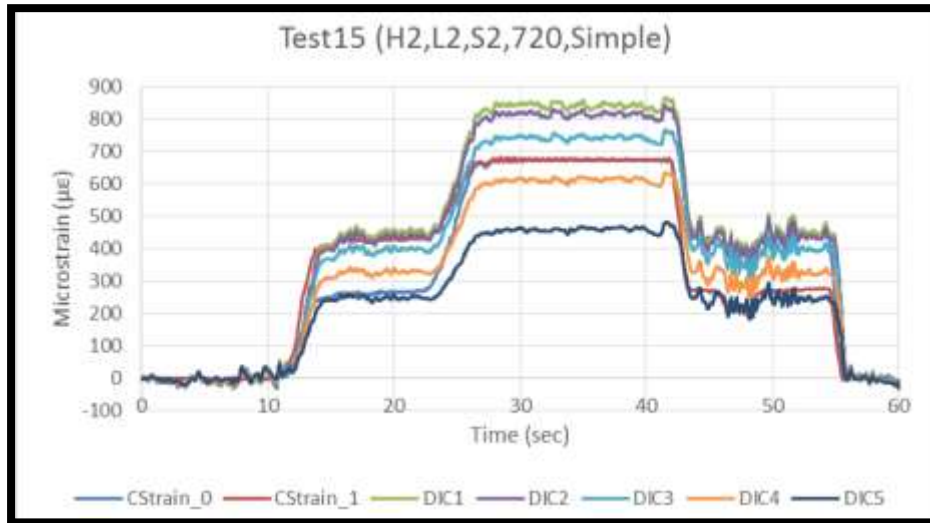
Figure K-1: Sample plot of the data collected for one test in 2D Lab Testing Trial 1

The overall result of the statistical analysis was to reject the null hypothesis, meaning that from this test, it could not be concluded that strains measured by the DIC sensors were accurate within five percent of the foil gauges. With that said, there were still several extremely valuable lessons learned from this first round of laboratory testing.

The most important lesson from this trial was the effects of height, light, and resolution on the DIC data. Overall, it was found that height and resolution had little impact on the accuracy of the measured strains, but did play an important role on the analysis. The combination of all three parameters impacts the subset size that can be used for analysis. These impacts will be discussed using figures showing the subset mesh as recommended from Vic-3D's Suggested Subset Size tool.

The effects of light on the accuracy of DIC data become relatively apparent when the standard deviations of the individual tests are observed. Tests conducted with Light Level 1, which was just ambient light (no overhead lights), have a much larger average standard deviation (32.0 με) when compared to the two other levels (9.3 and 19.0 με for Light 2 and Light 3, respectively). This indicates that low levels of light create more uncertainty in the strain data. This point is further emphasized when viewing the subset mesh recommended by Vic-3D in Figure K-2. The recommended subset size was 125, which is the largest size the software will recommend, for both resolution levels. This means that low light conditions do not provide enough contrast in the speckle pattern for the software to distinguish the pattern. From this trial, it appears that the GoPro® DIC sensors will need some form of external light in the field, as data collected in low light conditions is very poor.

As for the other lighting settings, the data from both appears to come out fairly well, although their standard deviations do differ. This could be caused by the other parameters, not necessarily the lighting conditions. Figure K-3 and Figure K-4 show the different recommended subset meshes for each setting. Those images are of the exact same speckle pattern, the only difference is that in Light 2, the overhead lights were used and in Light 3, construction flood lights were used. Just visually, the contrast created by the additional light is noticeable.
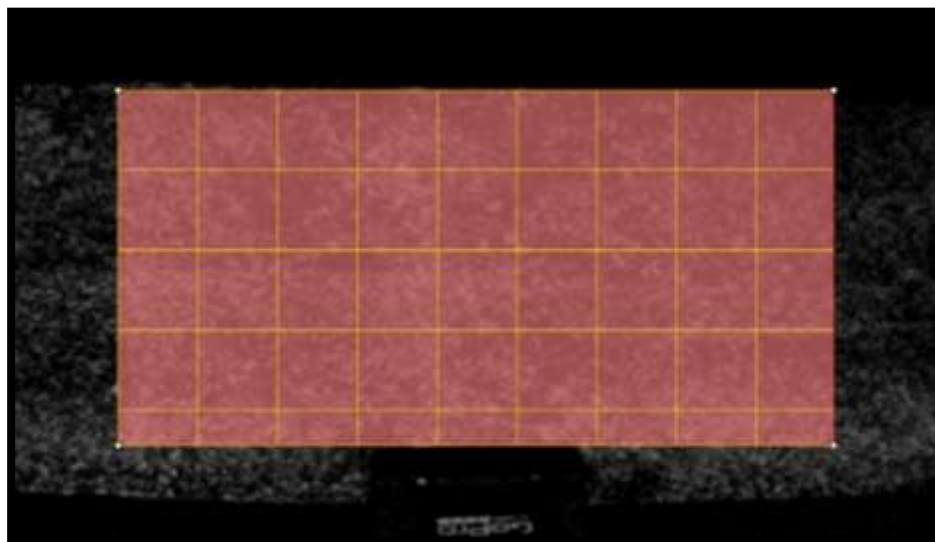
Figure K-2: Recommended subset mesh for 2D Trial 1 in Light 1 conditions
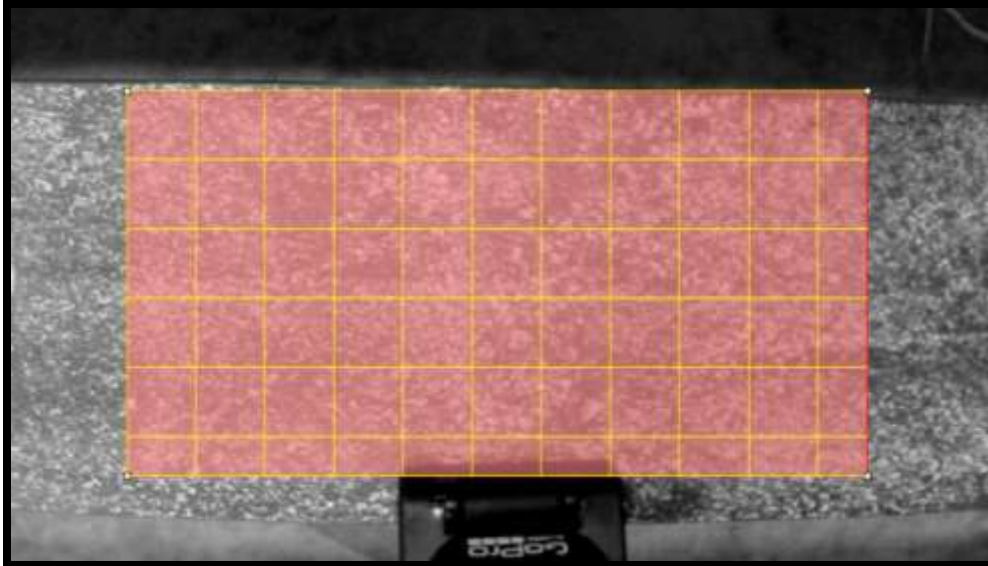
Figure K-3: Recommended subset mesh for 2D Trial 1 in Light 2 conditions at 720p resolution (Vic-3D, 2012)
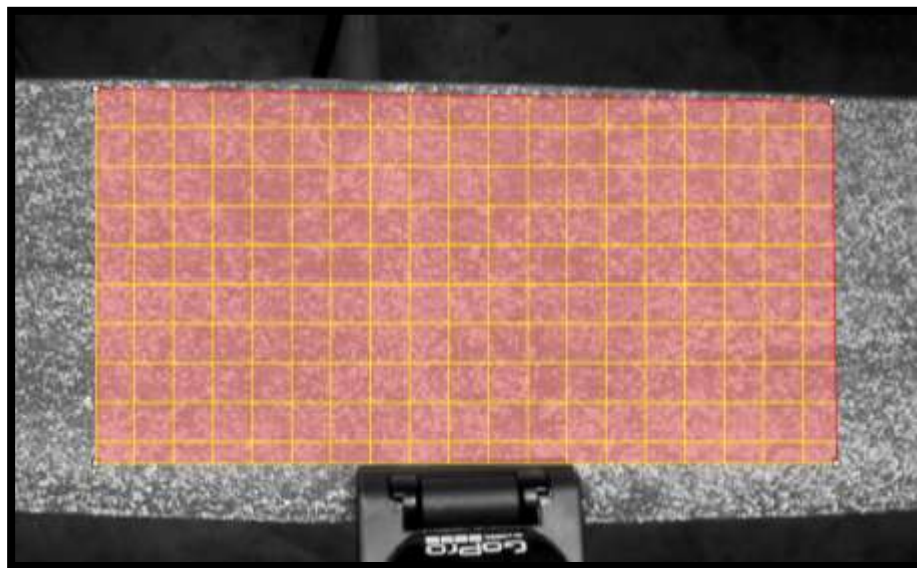
Figure K-4: Recommended subset mesh for 2D Trial 1 in Light 3 conditions at 720p resolution (Vic-3D, 2012)

This comparison illustrates the impact of light on the subset mesh. This exemplifies the FEM mesh analogy. So long as the speckle pattern has adequate fineness, then increasing light will allow the user to employ a finer mesh, which will provide more data in the strain field. But if a coarse strain field is adequate for the test being conducted, then there is a minimum amount of light that is required for accurate data.

Height has a similar effect on the subset mesh. Height settings of 1, 2, and 3 meant the camera lens was a distance of 7.0", 8.0", and 9.3" inches away from the test surface, respectively. Moving the camera farther from the test surface decreases the spatial resolution of the image. Spatial resolution is the ratio of image pixels per unit area in the image. So by moving the camera farther

from the test surface, there are fewer pixels per area of the test surface. This is illustrated in Figure K-5 and Figure K-6 below. These two figures show the recommended subset mesh at Height 1 and Height 3, respectively, while all other parameters were the same (Light 3, 720p). Figure K-5, showing the mesh with camera at Height 1, has a recommended subset mesh size of 55, while Figure K-6, at Height 3, has a recommended size of 39. Also note how the actual mesh sizes are very similar. This demonstrates that by moving the camera farther away, the spatial resolution of the mesh decreases (less pixels per area), but the actual mesh size stays similar in size. It is important to note that this will only hold true so long as the speckle pattern is adequate; if the speckle pattern is too fine, moving farther away will cause the speckles to blur together, thus decreasing the surface intensity of the pattern.

Figure K-5: Recommended subset mesh for 2D Trial 1 in Light 3 conditions at 720p resolution at Height 1 (Vic-3D, 2012)
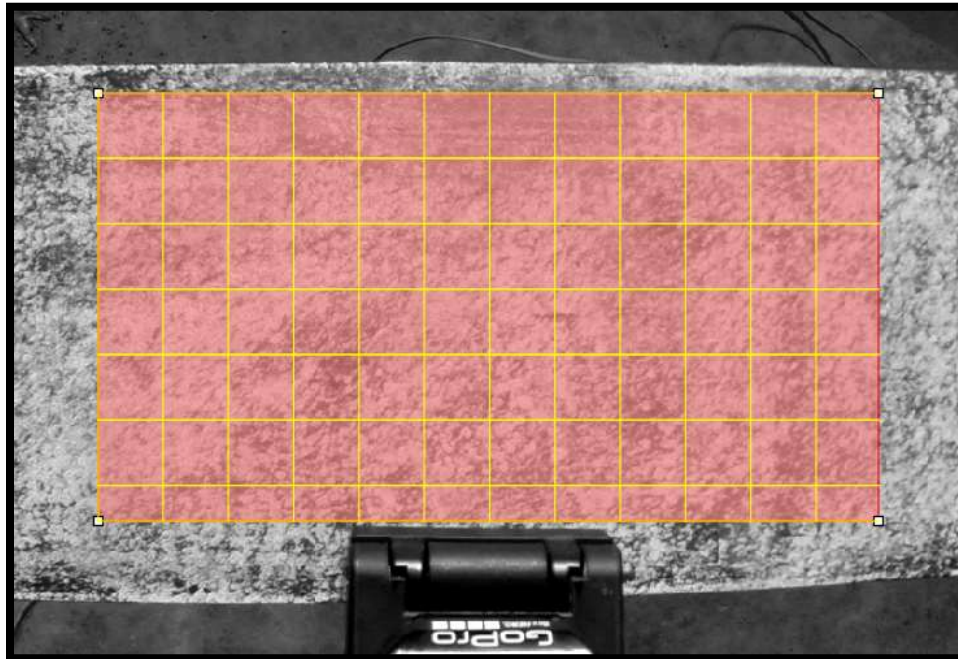
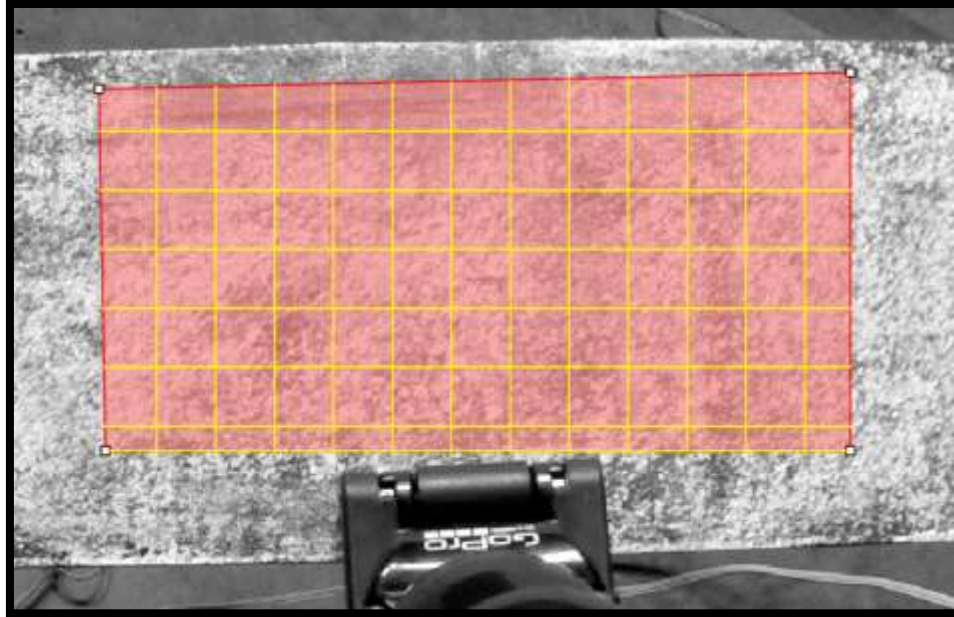**Figure K-6: Recommended subset mesh for 2D Trial 1 in Light 3 conditions at 720p resolution (Vic-3D, 2012)**

The main impact of camera resolution was also on the recommended subset mesh, and not entirely on the accuracy. Figure K-7 shows the recommended subset mesh for a reference image at Height 2, Light 2, and 1080p conditions. Compare this subset mesh to that in Figure K-3, which has the same conditions except it was taken in 720p resolution. Note how the 1080p resolution allows for a smaller subset than the 720p (for easy comparison, count the squares along the edge of the sensor footing). Now to counter what was just said, the recommended subset size is larger for 1080p at 75 pixels than at 720p, which was at 69 pixels. This is because the two different images have varying spatial resolution. In 1080p, the pixels are smaller than in 720p. Comparing the recommended subset sizes by number value is not relevant, because their pixels cover different sized areas. This trial was inconclusive on the effects of resolution on strain measurement accuracy, but it taught a valuable lesson on the impacts of light, height, and camera resolution on spatial resolution and subset mesh sizes.
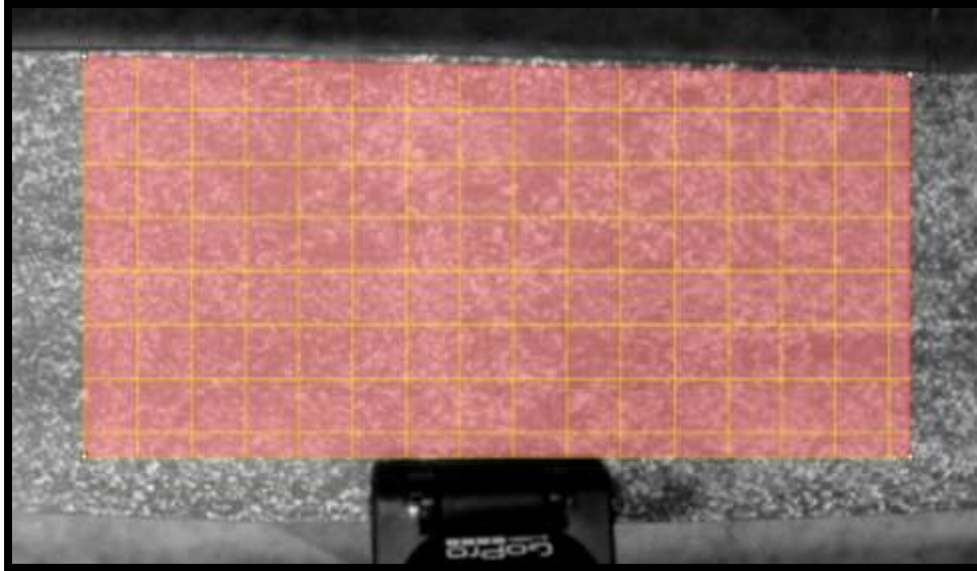
Figure K-7: Recommended subset mesh for 2D Trial 1 in Light 2 conditions at 1080p resolution (Vic-3D, 2012)

Another important lesson learned involved the AOEs used to extract data from the test images. If observing the figures showing the AOEs and the plots of the data, it is readily apparent that the center AOEs (plotted as DIC1 in all plots) are much greater in compression than the expected strain values. This can be explained by the curvature of the beam. Initially what was thought was that the center of the beam remained in plane with the original distance from the camera, but the resulting strain fields show that the center is far greater in compression, indicating the test surface moves away from the camera at the center of the beam. This causes the software to register the pixel movements in compression. The AOEs whose data most closely matched the measured strain from the foil gauges were those that included a little bit of the tension region. This is because the inclusion of the tension zone balanced out the increase in compression in the center. This test showed that for this particular experimental setup, data should be extracted using AOEs closely spaced around the transition zone between compression and tension.

Another observation about the AOE spacing was that equal spacing of the AOEs did not result in linear changes in maximum strain. As the AOE width increased, the rate of change in maximum strain increased. This can be explained by the rate of change in slope of the beam. The further away from the center of the beam, the more the curvature will impact the measurements.

Comments should be made about the performance of the experimental apparatus and foil gauges. In the simply supported condition, the strains measured by the foil gauges were extremely similar to those expected by the model and hand calculations. From this, it can be concluded that test apparatus is performing exactly as designed, and that the full bridge foil gauge circuits are calibrated and functioning properly.

As for the test apparatus under the fixed conditions, the measured strain values were not close to those predicted by the model under perfectly fixed conditions, but the measured values were in fact between the predictions for simple and fixed conditions. This shows that the original assumption that the clamped supports would provide some but not total rotational resistance was accurate. After this trial, it was deemed unnecessary to apply the fixed conditions to the apparatus. It added a great deal of time to the testing procedure, while providing very little meaning in the

248

testing of the GoPro® strain sensors. For those reasons, the fixed conditions were eliminated in all future trials.

K.2   2D Lab Trial 2

K.2.1   Goals, Purpose and Results of 2D Trial 2

The purpose of 2D Trial 2 was to verify the findings of 2D Trial 1 by eliminating the parameters of height and fixity. The goal was to show that accurate strain data could be collected with either resolution and at light levels 2 and 3. It also aimed to verify the finding that DIC performed in low light conditions was not accurate. Table K-4 below shows the tests and varying parameters for each test. All tests were performed with the camera about 7" from the test surface.

Table K-5 below shows the summary of results for 2D Lab Trial 2. To see all the results from 2D Lab Trail 2, including snips showing AOE selection, plots of strain over time, and individual test summaries. Table K-6 below is a summary of the statistical analysis conducted for 2D Lab Trial 1. Figure K-8 shows a sample plot representative of the tests performed in 2D Lab Trial 1.

Table K-4: Parameter settings for the tests in 2D Lab Testing Trial 2

	Light	Stress Level	Resolution
1	1	1	1080
2	1	2	720
3	1	3	720
4	2	1	720
5	2	2	1080
6	2	2	720
7	2	3	1080
8	3	1	1080
9	3	2	1080
10	3	3	720

Table K-5: Summary of results from 2D Lab Testing Trial 1

Test	Expected Strain (με)	Avg Foil Strain (με)	Avg DIC Strain (με)	std,DICi (με)	%Diff,i	abs(%Diff,i)
4	496.6	524.50	544.36	7.59	3.79	3.79
5	662.1	693.99	787.62	10.05	13.49	13.49
6	662.1	692.18	755.59	6.34	9.16	9.16
7	827.6	864.15	922.74	8.61	6.78	6.78
8	496.6	525.05	523.34	5.98	-0.32	0.32
9	662.1	693.42	708.00	12.44	2.10	2.10
10	827.6	866.02	930.21	11.98	7.41	7.41

Table K-6: Summary of the statistical analysis for 2D Lab Testing Trial 1

%Diff,avg	6.15
std,%Diff	4.49
t,n-1	0.678
p-value	0.40<P<0.25
Result:	Fail to Reject the Null
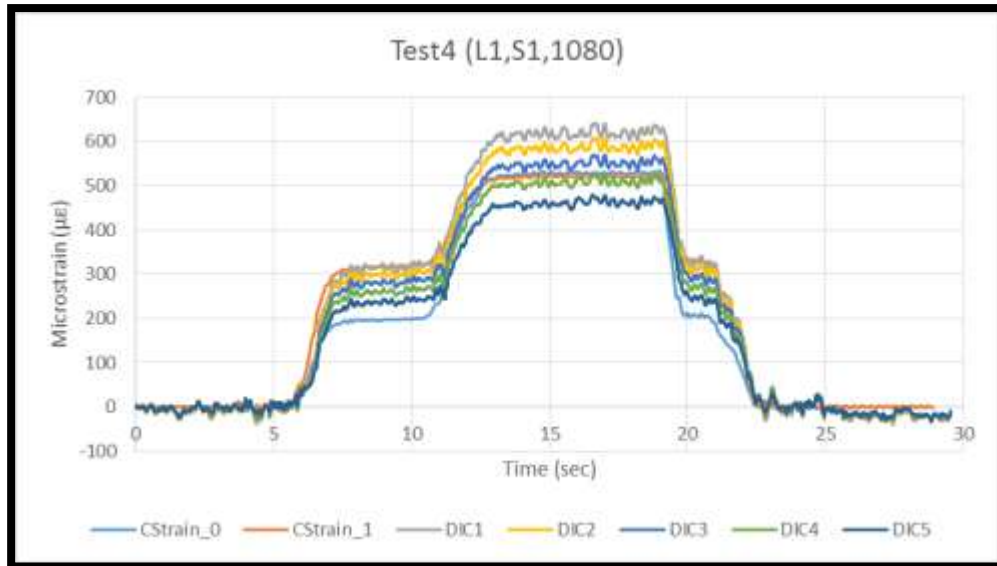
Figure K-8: Sample plot of the data collected for one test in 2D Lab Testing Trial 2

K.2.2   Lessons Learned in 2D Trial 2

The overall result of the statistical analysis of this trial was that it failed to reject the null hypothesis. This means that the strain measurements from the experimental 2D GoPro® DIC strain sensor are statistically significant when compared to the measurements by the foil gauges. Since Tests 1-3 were excluded from the statistical analysis (which will be explained below), then it can be said that DIC measurements taken in either 720p or 1080p resolutions and in medium to high levels of light should be accurate.

There are several factors that could have attributed to the overall success of this trial. The first and most hopeful reason is that the settings used during testing were close to ideal, and thus the results are accurate. With an adequate speckle pattern, the GoPro® Camera can be set 6-8" off the test surface in medium to high lighting conditions, record a test video at 720p or 1080p resolution using the narrow field of view setting, and the resulting strain measurements will be accurate. Another reason this trial was successful can be attributed to the experience of the operators in both conducting the test and performing the post-processing. If the test plots of 2D Lab Trial 1 and 2D Lab Trial 2 are compared, it can be seen that there are notably fewer spikes in strain caused from the test apparatus being bumped or jarred. Simply by practicing running the test, the results are better. Also, the experience gained in AOE selection can attribute to some success. After analyzing 2D Lab Trial 2, the understanding of the effects of AOE selection helped select better, more accurate areas of which to extract data.

This brings around a good point about conducting DIC analysis. Unlike other forms of strain measurement, where the installation of the sensor is arduous and requires knowledge of the structural system, but once installed measures the strain regardless of the user's abilities, DIC requires a knowledgeable user in both the installation and post-processing of the collected images. There is a definite learning curve involved in performing DIC, and requires an understanding of both the structural system and the DIC analysis process. The measured strains are highly dependent on the expertise of the user in the collection, post-processing, and analysis of the DIC data.

The most obvious lesson taken from 2D Trial 2 was that GoPro® DIC sensors do not perform well in low light conditions. The tests performed in Light 1 conditions yielded no useable results. Light 1 condition means that no light sources were on during the recording of the test. On the day and time during this particular testing, the sky was cloudy and the tests were performed in the afternoon, so there was very little ambient light (and the light was fading, which explains why the results got progressively worse from Test1 to Test 3). These results show that GoPro® sensors deployed in the field may require an external light source in order to collect accurate data, especially if it is used on a cloudy day.

As mentioned above, the results of this test were more accurate when compared to the foil gauge measurements not only because of the settings used in collection, but also because of the testing procedure. 2D Trial 2 had far fewer tests that were impacted by the test apparatus being jarred. This brings about one of the weaknesses of this strain sensor: the 2D GoPro® DIC sensor is highly susceptible to the impacts of vibrations. This setup would not fare well when used on test surfaces that undergo high levels of vibration.
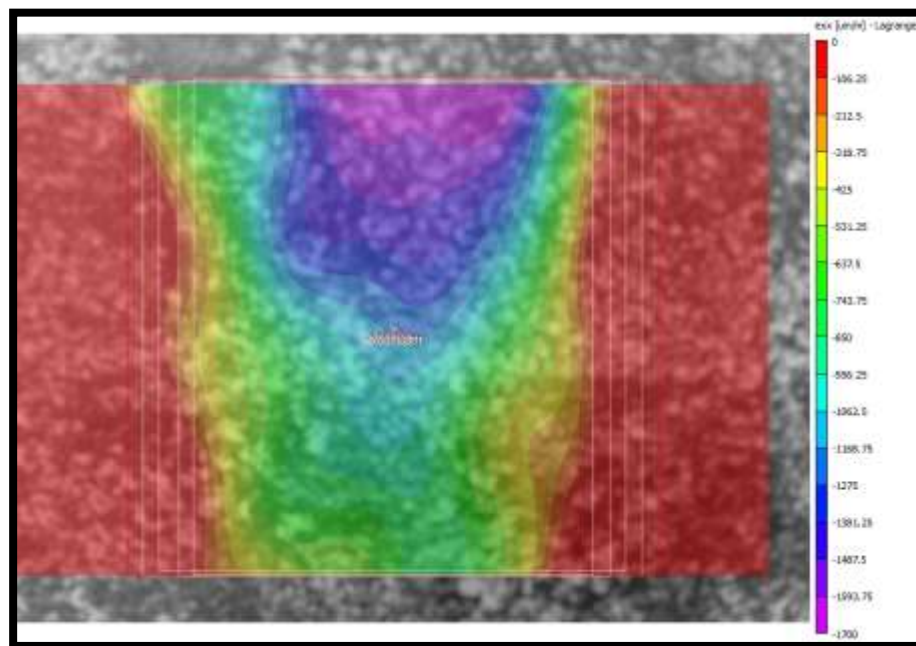
K.3   2D Lab Trial 3

K.3.1   Goals, Purpose, and Results of 2D Trial 3

This trial was conducted to see how the GoPro® DIC strain sensor would perform if it were applied much closer to the test surface. To accomplish this, the gooseneck attachment was removed and replaced with a short extender arm. This setup was then applied to the test beam just as the original sensor was. This experimental sensor can be seen in Figure K-9. The goal of this trial was to see if by shortening the distance between the test surface and the camera if it would lessen the out-of-plane curvature effects on the strain measurement. Three tests were run, one at each strain level, with normal overhead lighting (Light 2 in the previous tests) at 1080p. The following figure and three plots are the results from the three tests in this trial.
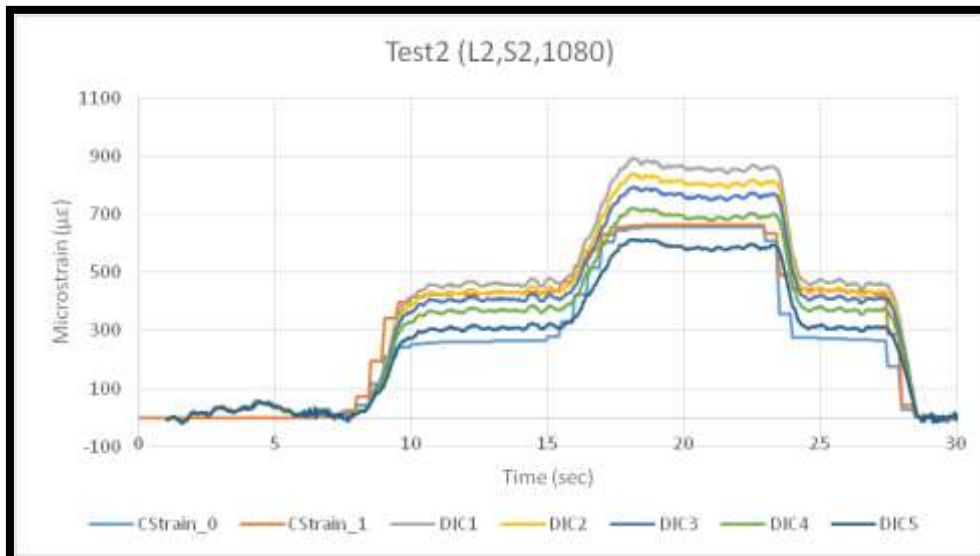
Figure K-9: Experimental DIC sensor that tests the short range capabilities of the GoPro® camera
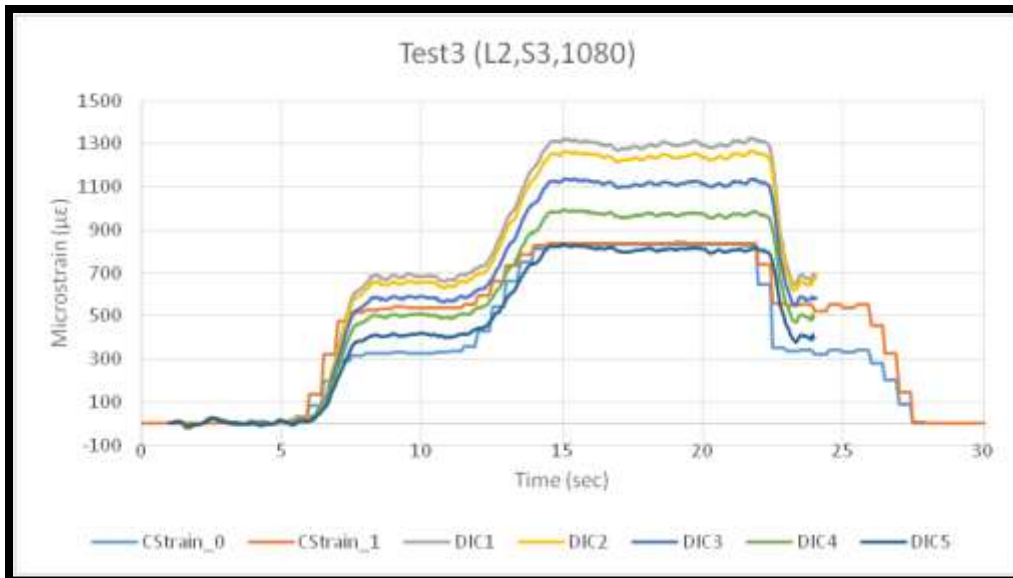

Figure K-10: Representative sample showing the five AOEs used for data extraction in 2D Trial 3
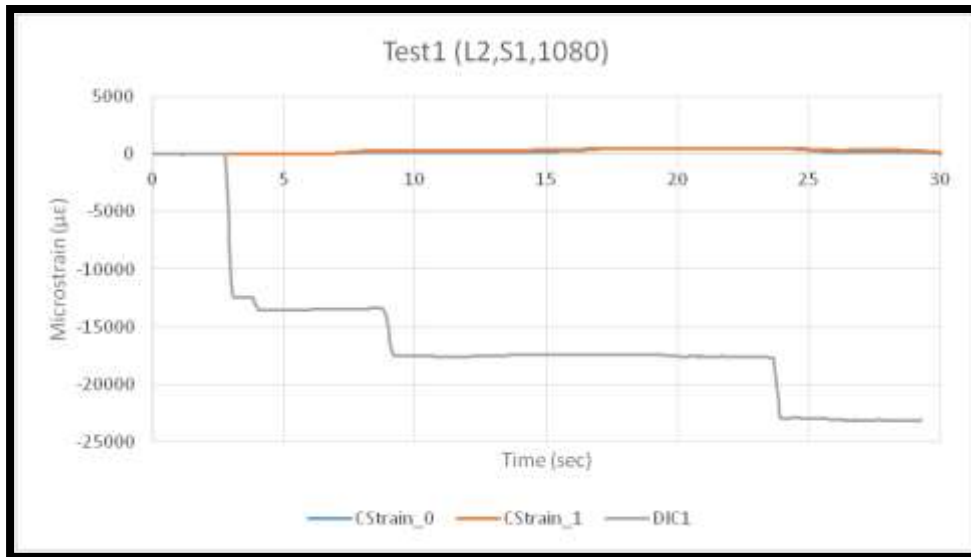
Figure K-11: Plot of strains vs. time measured during Test 1 of 2D Lab Trial 3

Figure K-12: Plot of strains vs. time measured during Test 2 of 2D Lab Trial 3

Figure K-13: Plot of strains vs. time measured during Test 3 of 2D Lab Trial 3

K.3.2   Lessons Learned in 2D Trial 3

Ultimately, this trial showed that moving the camera closer to the test specimen did not reduce the impact of curvature on the strain measurement. The five AOEs were selected in the same manner as the trials before, and the plots still show a wide range of measured strains due to the out-of-plane movement.

Although Test 1 was a complete failure at measuring strains, it does show some valuable lessons about using these DIC sensors. The data plotted in Figure K-11 is so poor because the camera rotated at the top joint in the extender arm. The camera lens got closer to the test surface, which was measured as tension, and then is plotted as negative because of the editing equation. Each jump in strain correlates to a time when the camera moved a little bit. This plot shows three important lessons. First, make sure all attachments and bolts are fully tightened before beginning a test. Second, if the measured strain makes a large permanent jump without returning close to what it was before, this is an indication that the camera moved during the test, not to be confused with jumps in measurement from the test specimen being bumped. And third, this illustrates one of the main setbacks in using DIC: it does not provide real time feedback during a test. The operators were unaware that the camera moved until the images were post-processed. After viewing the data, the test video was played back, at which point the camera rotation could be seen. When using the GoPro® DIC sensors, all pieces should be checked that they are tightened snug before beginning testing.

Another lesson learned was that even though this setup is still susceptible to curvature effects, the camera is still capable of collecting data this close to the test surface. In Figure K-10, it can be seen that the speckle pattern is not as crisp as in past trials, but it still provides enough surface intensity for DIC to be performed. Even if a speckle pattern is slightly out of focus, meaningful strain data can be collected.

254